

## Nonlinear dynamic atomic force microscopy

Chandrashekar, A.

**DOI**

[10.4233/uuid:431f98e1-3b0b-4c61-87ba-e6b458748428](https://doi.org/10.4233/uuid:431f98e1-3b0b-4c61-87ba-e6b458748428)

**Publication date**

2022

**Document Version**

Final published version

**Citation (APA)**

Chandrashekar, A. (2022). *Nonlinear dynamic atomic force microscopy*. [Dissertation (TU Delft), Delft University of Technology].

**Important note**

To cite this publication, please use the final published version (if applicable).  
Please check the document version above.

**Copyright**

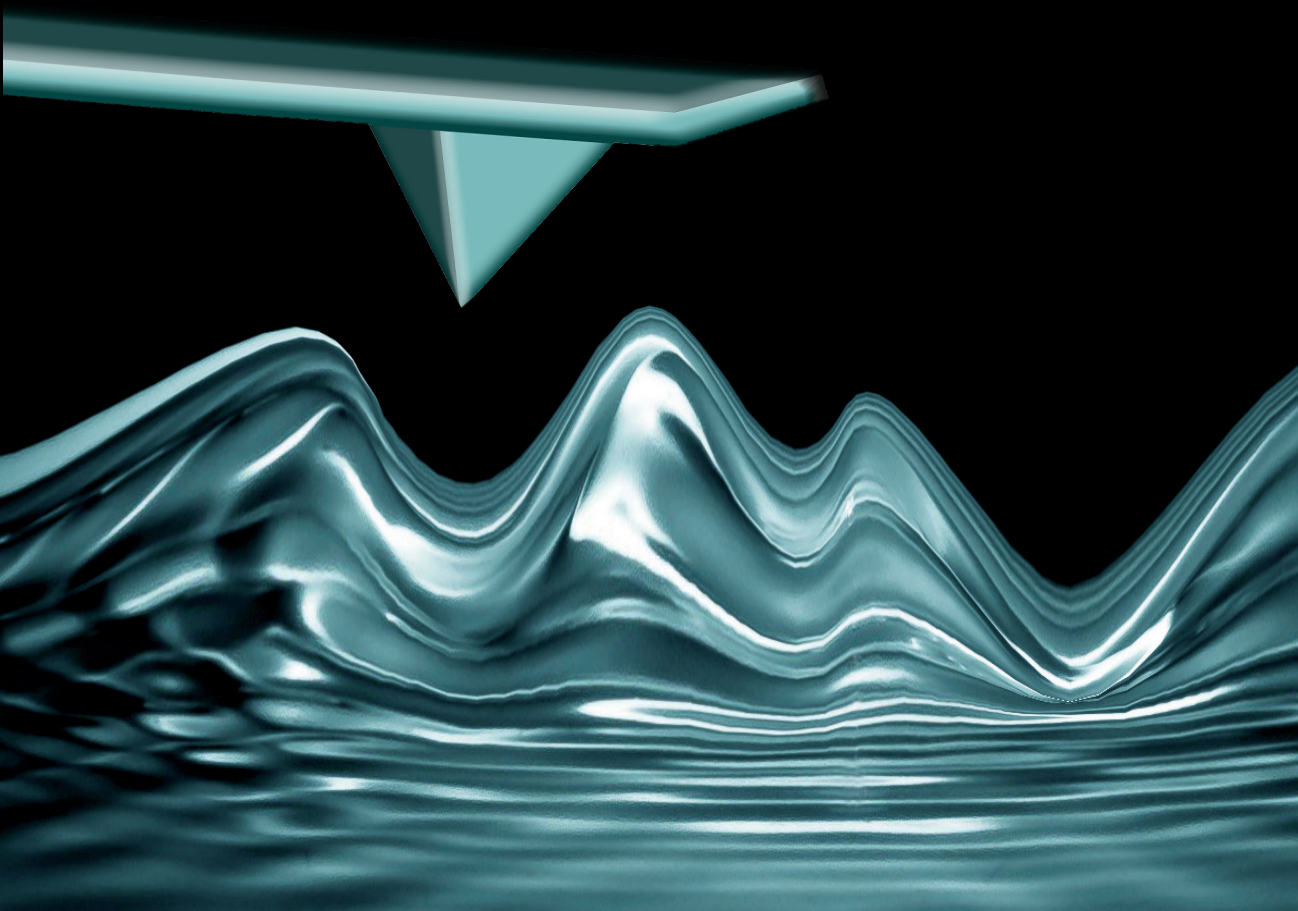
Other than for strictly personal use, it is not permitted to download, forward or distribute the text or part of it, without the consent of the author(s) and/or copyright holder(s), unless the work is under an open content license such as Creative Commons.

**Takedown policy**

Please contact us and provide details if you believe this document breaches copyrights.  
We will remove access to the work immediately and investigate your claim.

# **NONLINEAR DYNAMIC ATOMIC FORCE MICROSCOPY**

**Abhilash Chandrashekar**





# **NONLINEAR DYNAMIC ATOMIC FORCE MICROSCOPY**



# **NONLINEAR DYNAMIC ATOMIC FORCE MICROSCOPY**

## **Dissertation**

for the purpose of obtaining the degree of doctor  
at Delft University of Technology  
by the authority of the Rector Magnificus prof.dr.ir. T.H.J.J. van der Hagen,  
chair of the Board for Doctorates  
to be defended publicly on Wednesday 28 September 2022 at 15:00 o'clock

by

**Abhilash CHANDRASHEKAR**

Master of Science in Mechanical Engineering,  
Delft University Of Technology, The Netherlands  
born in Bangalore, India.

This dissertation has been approved by the promotors

Prof. dr. U. Staufer  
Dr. F. Alijani

Promotor  
Copromotor

Composition of the doctoral committee:

Rector Magnificus,  
Prof. dr. U. Staufer  
Dr. F. Alijani

chairperson  
Delft University of Technology  
Delft University of Technology

*Independent members:*

Prof. dr. A. Raman  
Prof. dr. R. Garcia  
Prof. dr. A. Metrikine  
Prof. dr. P. G. Steeneken  
Dr. P. Belardinelli  
Prof. dr. A. van Keulen

Purdue University, United States of America  
Spanish National Research Council (CSIC), Spain  
Delft University of Technology  
Delft University of Technology  
Polytechnic University of Marche, Italy  
Delft University of Technology, reserve member



*Keywords:* Atomic Force Microscopy, nanomechanical characterization, tip-sample interactions, nonlinear dynamics, machine learning, data driven analysis, nonlinear identification.

*Printed by:* proefschriftmaken, The Netherlands.

*Front & Back:* Artistic visualization of an AFM cantilever interacting with a soft sample.

Copyright © 2022 by A. Chandrashekar

ISBN 978-94-6384-366-9

An electronic version of this dissertation is available at  
<http://repository.tudelft.nl/>.

*To my beloved parents,*





# Contents

<b>Summary</b>	<b>ix</b>
<b>Samenvatting</b>	<b>xi</b>
<b>1 Introduction</b>	<b>3</b>
1.1 The physics and working principle behind AFM	4
1.2 Modes of operation in AFM	5
1.3 Tip-surface forces	6
1.4 Research objectives and scope of the thesis	8
1.5 Outline of the thesis	11
<b>2 Global dynamics of tapping mode atomic force microscopy</b>	<b>15</b>
2.1 Numerical Model	18
2.2 Numerical analysis	20
2.3 Dynamical integrity and robustness of attractors	28
2.4 Conclusions	38
<b>3 Mode coupling in Tapping mode atomic force microscopy</b>	<b>41</b>
3.1 Experimental results	43
3.2 Modeling and simulations	45
3.3 Conclusion	49
Appendix	51
3.A Theoretical model	51
3.B Numerical implementation and simulation parameters	53
3.C Phase synchronization at internal resonance	54
3.D Simulations with and without internal resonance condition	55
3.E Amplitude reduction and Set point ratio	55
3.F Influence of harmonics on phase space trajectories	57
3.G Additional experimental data sets	58
3.H Influence of excitation amplitude	60
<b>4 Sensitivity of viscoelastic characterization in multi-harmonic atomic force microscopy</b>	<b>63</b>

4.1	Introduction . . . . .	64
4.2	Experimental Results . . . . .	66
4.3	Modeling tip-sample interaction . . . . .	67
4.4	Linking viscoelasticity to intermodulation components . . . . .	68
4.5	Conclusions . . . . .	73
	Appendix . . . . .	74
4.A	Additional numerical data . . . . .	74
4.B	High volume gradient based optimization and initial point selection procedure . . . . .	79
<b>5</b>	<b>Data-Driven Force Reconstruction in Dynamic Atomic Force Microscopy</b>	<b>87</b>
5.1	Formulation . . . . .	88
5.2	Training . . . . .	90
5.3	Experiments . . . . .	93
5.4	Discussion . . . . .	97
	Appendix . . . . .	99
5.A	Experimental setup and measurement protocol . . . . .	99
5.B	Protocol for choosing hyper-parameters and constraints for the algorithm . . . . .	99
5.C	Identification of tip-sample interaction in LDPE sample . . . . .	101
5.D	Additional data: algorithm training . . . . .	101
<b>6</b>	<b>Outlook</b>	<b>111</b>
6.1	Tip monitoring through electrostatic forces . . . . .	112
6.2	Estimation of Hamaker constant using softening nonlinear response of AFM . . . . .	115
6.3	Machine learning based identification techniques for dynamic AFM . . . . .	118
<b>7</b>	<b>Conclusions and Recommendations</b>	<b>125</b>
	<b>Bibliography</b>	<b>131</b>
	<b>Acknowledgements</b>	<b>147</b>
	<b>Curriculum Vitæ</b>	<b>159</b>
	<b>List of Publications</b>	<b>161</b>

# SUMMARY

Most physical phenomena be it mechanical, chemical or biological are inherently nonlinear in nature. In fact, it is the linear phenomenon that is the exception rather than the rule. By harnessing these nonlinearities one can obtain far greater information about the underlying physics and develop more sensitive and efficient devices. This is especially true at the micro and nanoscale world where the forces tend to be highly nonlinear and the go-to tool for studying such forces is the atomic force microscopy (AFM).

Ever since its inception, AFM has revolutionized the world of nanotechnology through its ability to manipulate and characterize matter with atomic resolution. With the gradual development of novel characterization techniques, AFM has slowly transitioned from a traditional imaging technique to a powerful nanomechanical characterization tool capable of estimating material properties of wide variety of samples with ease. This transition is fueled by the greater interest in understanding the highly nonlinear tip-sample interaction forces that exist between an AFM probe and the sample of interest. However, in order to advance our understanding of nanoscale interactions, one must fully embrace the nonlinear nature of the system and develop parameter identification techniques based on nonlinear dynamics. In this regard, this thesis focusses on both fundamental and applied nonlinear dynamical studies to develop novel identification techniques for dynamic AFM applications.

In chapter 1, I briefly introduce AFM, its different modes of operation and the role of tip-sample interactions in obtaining compositional contrast of samples. I end this chapter by discussing the motivation behind developing identification techniques and its applications in the field of dynamic AFM.

Chapter 2 describes the global dynamics of tapping mode AFM. Here, I study the robustness and integrity of different oscillatory states of the AFM cantilever driven in Lennard-Jones potential. I make use of nonlinear dynamical tools such as frequency response curves, basins of attraction, and integrity measures to analyze the stability of cantilever oscillations under external perturbations. Moreover, I develop a global bifurcation chart to track the appearance of various cantilever oscillatory states as a function of excitation frequency and amplitude. The chart provides insight into choosing and optimizing the various parameters required for stable scanning operation. Furthermore, this work demonstrates that by studying the global dynamics of the system, unwanted scenarios such as jumps between dynamical states of the cantilever and chaotic motion can be avoided.

In chapter 3, I discuss the role of mode coupling in enhancing the sensitivity of higher harmonics in dynamic AFM. I begin by introducing a methodology for obtaining nonlinear frequency response curves in the experimental setting and use that to determine a frequency range in the spectral neighborhood of resonance that hosts strong modal interactions. I label this frequency range in the thesis as the "sweet spot". I find that in the sweet spot not only the signal to noise ratio (SNR) of higher harmonics increase by

several folds but also cantilever exhibits reduced indentation in the sample. By performing experiments on different cantilevers and samples I also show that the occurrence of sweet spot is independent from probe-sample configuration. I corroborate these findings by simulating a multiple degree of freedom model with a non-smooth tip-sample potential. I expect this work to be useful for developing multi-parameter identification techniques based on higher harmonics, bi-modal AFM, and multi-frequency AFM without the need for specialized cantilevers.

Chapter 4 sheds light on the influence of experimental observables on viscoelastic characterization in Multi-frequency AFM. By making use of Intermodulation AFM technique, I explore the dependency of bulk and surface viscoelastic response of a polymer blend to the instrument's observables. I highlight the sensitivity issues that can be faced when fitting a large number of observables, and touch upon non-convexity of the fitting problem that can also lead to inconsistent viscoelastic parameter estimations. I verify these findings by performing extensive simulations that employ both local and global optimization techniques. I believe this work to be useful for validating viscoelastic models and optimization routines that enable fast and accurate quantification of viscoelasticity in novel polymers and biological specimens.

In chapter 5, I leverage the strengths of data science and machine learning in distilling the governing equations of a dynamic AFM using the cantilever's deflection signal. The data driven algorithm obtains physically interpretable models from experiments and estimates the time resolved tip-sample interaction force with a sub-microsecond resolution. I train and test the algorithm on several well-established AFM models and create a library of functions that can approximate the underlying physics in various experimental scenarios. The data driven algorithm is then used to estimate the tip-sample interaction force from experimental data obtained on a co-block polymer blend. The method provides insight into the peak loading forces and energy dissipation during contact without prior knowledge of the interaction mechanisms. I expect this work to be used for exploring the transient dynamics behind chemical and biological processes and developing novel feedback architectures based on real time tip-sample force as well as obtain high-resolution dynamical force volume measurements.

Chapter 6 provides an outlook into future research directions based on preliminary investigations in this thesis. In particular, I discuss a methodology to exploit the electrostatic response of the cantilever to determine the tip radius, and experimentally show how Hamaker constant can be estimated from van der Waals forces. At the end of this chapter, I also discuss applications of machine learning in estimating sample viscoelasticity as well as its potential in developing data driven nonlinear model predictive feedback architectures, and show how neural networks can be used for predicting mode coupling from AFM time-domain data. In chapter 7, I conclude the thesis by providing a summary of the findings.

# SAMENVATTING

De meeste fysische fenomenen, zij het mechanisch, chemisch dan wel biologisch, zijn van nature inherent niet-lineair. In feite zijn het juist de lineaire fenomenen die eerder de uitzondering dan de regel zijn. Door deze niet-lineairiteiten te benutten kan men amper informatie vergaren over de onderliggende fysica, en gevoeliger en efficiëntere apparaten ontwikkelen. Dit geldt vooral op de schaal van de micro- en nanoscopische wereld waarin krachten doorgaans hoogst niet-lineair zijn, en de atoomkrachtmicroscop (AFM) het voorkeurswerktuig is voor het onderzoek naar zulke krachten.

Al sinds zijn ontdekking heeft de AFM de wereld van de nanotechnologie gerevolutioneerd dankzij de mogelijkheid om materie op de schaal van atomen te manipuleren en te karakteriseren. Met de geleidelijke ontwikkeling van moderne karakteriseringstechnieken is de AFM gaandeweg verandert van een traditioneel beeldvormingstechniek in een veelzijdige nanomechanische karakteriseringstechniek waarmee eenvoudig de materiaaleigenschappen kunnen worden ingeschat van een wijde variëteit samples. Deze transitie wordt versneld door de grote interesse in het begrijpen van de hoogst niet-lineaire interactiekracht die bestaat tussen een AFM sonde en het specimen. Om onze kennis van nanoschaal interacties te vergroten, moet men de niet-lineaire natuur van het systeem volledig omarmen, en parameter identificatie technieken ontwikkelen gebaseerd op niet-lineaire systemen. Vanuit dit oogpunt focust dit proefschrift op zowel fundamentele als toegepaste niet-lineaire dynamische studies voor de ontwikkeling van moderne identificatietechnieken voor dynamische AFM toepassingen.

In hoofdstuk 1 introduceer ik kort de AFM, zijn verschillende werkwijzen en de rol van tip-specimen interacties bij het verkrijgen van een samenstellingscontrast van een specimen. Ik sluit dit hoofdstuk af met een discussie over de motivatie voor de ontwikkeling van identificatie technieken en hun toepassingen in het veld van de dynamische AFM.

Hoofdstuk 2 beschrijft de globale dynamiek van tapmodus AFM. Ik bestudeer hoe robuust en betrouwbaar de verschillende oscillatietoestanden van de AFM cantilever zijn binnen een Lennard-Jones-potentiaal. Ik maak gebruik van technieken binnen de niet-lineaire dynamica, zoals frequentieresponscurves, aantrekkingsbassins en integriteitsparameters om de stabiliteit van oscillaties van een cantilever onder externe verstoringen te analyseren. Bovendien ontwikkel ik een globale bifurcatiediagram om het ontstaan van verschillende oscillatietoestanden van de cantilever te volgen als een functie van de excitatiefrequentie en amplitude. Het geeft inzicht in het kiezen en optimaliseren van de verschillende parameters die nodig zijn voor een stabiele scanwerking. Bovendien toont dit werk aan dat door de globale dynamiek van het systeem te bestuderen, ongewenste scenario's zoals sprongen tussen dynamische toestanden van de cantilever en chaotische beweging kunnen worden vermeden.

In hoofdstuk 3 bespreek ik de rol van koppeling tussen eigentrillingen bij het verbeteren van de gevoeligheid van hogere harmonischen in dynamische AFM. Ik begin

met de introductie van een methodologie voor het verkrijgen van niet-lineaire frequentieresponscurves in de experimentele omgeving en gebruik die om een frequentiebereik te bepalen die spectraal in de buurt ligt van de resonantie die sterke modale interacties herbergt. Ik noem dit frequentiebereik in het proefschrift de "sweet spot". Ik merk op dat in de sweet spot niet alleen de signaal-ruisverhouding (SNR) van hogere harmonischen enkele malen toeneemt, maar ook de AFM cantilever een verminderde indrukking van het specimen teweegbrengt. Door experimenten uit te voeren met verschillende sondes en samples, laat ik ook zien dat het optreden van een sweet spot onafhankelijk is van de sonde-sample configuratie. Ik bevestig deze bevindingen door een model met meerdere vrijheidsgraden te simuleren met een niet-gladde tip-sample-potentiaal. Ik verwacht dat dit werk nuttig zal zijn voor het ontwikkelen van multi-parameter identificatietechnieken op basis van hogere harmonischen, bimodale AFM en multi-frequentie AFM zonder de noodzaak van gespecialiseerde sondes.

Hoofdstuk 4 werpt licht op de invloed van experimentele waarnemingen op viscoelastische karakterisering bij multi-frequentie AFM. Door gebruik te maken van intermodulatie AFM techniek, verken ik de afhankelijkheid van bulk en oppervlak viscoelastische respons van een polymeermengsel op de waarneembare kenmerken van het instrument. Ik benadruk de gevoeligheidsproblemen waarmee men te maken kan krijgen bij het passen van een groot aantal waarneembare objecten, en bespreek de niet-convexiteit van het aanpasprobleem dat ook kan leiden tot inconsistente schattingen van viscoelastische parameters. Ik verifieer deze bevindingen door uitgebreide simulaties uit te voeren die zowel lokale als globale optimalisatietechnieken gebruiken. Ik geloof dat dit werk nuttig is voor het valideren van viscoelastische modellen en optimalisatieroutines die snelle en nauwkeurige kwantificering van viscoelasticiteit in nieuwe polymeren en biologische specimens mogelijk maken.

In hoofdstuk 5 maak ik gebruik van de sterke punten van datawetenschap en machine learning bij het distilleren van de beschrijvende vergelijkingen van een dynamische AFM met behulp van het deflectiesignaal van de cantilever. Het datagestuurde algoritme verkrijgt fysiek interpreteerbare modellen uit experimenten en schat de tijdsafhankelijke tip-sample-interactiekracht met een resolutie van minder dan een microseconde. Ik train en test het algoritme op verschillende gevestigde AFM-modellen en creëer een bibliotheek met functies die de onderliggende fysica kunnen benaderen in verschillende experimentele scenario's. Het datagestuurde algoritme wordt vervolgens gebruikt om de interactiekracht tussen AFM-naald en monster te schatten op basis van experimentele gegevens die zijn verkregen op een co-blokpolymeermengsel. De methode geeft inzicht in de krachten bij piekbelasting en energie-dissipatie tijdens contact zonder voorkennis van de interactiemechanismen. Ik verwacht dat dit werk zal worden gebruikt voor het onderzoeken van de overgangsdynamiek achter chemische en biologische processen en het ontwikkelen van nieuwe feedbackarchitecturen op basis van real-time tip-sample interactiekracht en het verkrijgen van dynamische krachtvolumentingen met hoge resolutie.

Hoofdstuk 6 biedt een vooruitblik op toekomstige onderzoeksrichtingen op basis van vooronderzoeken in dit proefschrift. In het bijzonder bespreek ik een methodologie om de elektrostatische respons van de cantilever te benutten om de tipstraal te bepalen, en laat ik experimenteel zien hoe de Hamaker-constante kan worden geschat aan de hand



van van der Waals-krachten. Aan het einde van dit hoofdstuk bespreek ik ook toepassingen van machine learning bij het schatten van de viscoelasticiteit van een monster, evenals het potentieel ervan bij het ontwikkelen van datagestuurde niet-lineaire model voorspellende feedbackarchitecturen. Ik laat zien hoe neurale netwerken kunnen worden gebruikt voor het voorspellen van eigentrilling koppeling op basis van AFM tijddomein gegevens. In hoofdstuk 7 sluit ik het proefschrift af met een samenvatting van de bevindingen.



1



# 1

## INTRODUCTION

*In the recent years, nanotechnology has made giant strides in improving the quality of human life. These improvements can be seen in every day life in the form of faster and cheaper computers, more compact smart phones, medical implants that can provide real-time information about one's health and in recent times even development of nanorobots that can make repair at cellular levels. These innovations are made possible due to the significant progress made by the scientific community in understanding the interactions between matter at nanoscale. The interactions at nanoscale are different from the macroscopic scale and thus understanding these differences can often be challenging without proper tools and techniques. In this aspect, the invention of Atomic Force Microscopy (AFM) played a key role in disentangling the subtle physics behind several nanoscale processes. Currently, AFM has transcended its function as an imaging tool with atomic resolution to a research tool capable of providing high resolution maps of mechanical, chemical and biological properties of sample at nanoscale. With further improvements in AFM characterization techniques, the field of nanotechnology can be better equipped to provide novel solutions for the betterment of the society.*

## 1.1. THE PHYSICS AND WORKING PRINCIPLE BEHIND AFM

The fundamental concept behind the working principle of an AFM is fairly simple to understand. An AFM utilizes an atomically sharp tip at the end of a micro-cantilever to interrogate and measure the surface of the sample [1]. It does this by bringing the tip in close proximity of the sample surface and measures the interaction between the atoms of the surface and the tip. Based on this interaction force, one can obtain information of the sample like the topography, stiffness, adhesion and other material properties at nanoscale. Although the physics behind the AFM seem relatively straight forward, it must be noted that the tip-sample interaction is highly nonlinear and is generally a convolution of different types of nanoscale forces [2]. Furthermore, the microcantilever exhibits complex and often non-smooth dynamics due to these different forces; thus making the nanomechanical characterization process even more complicated.

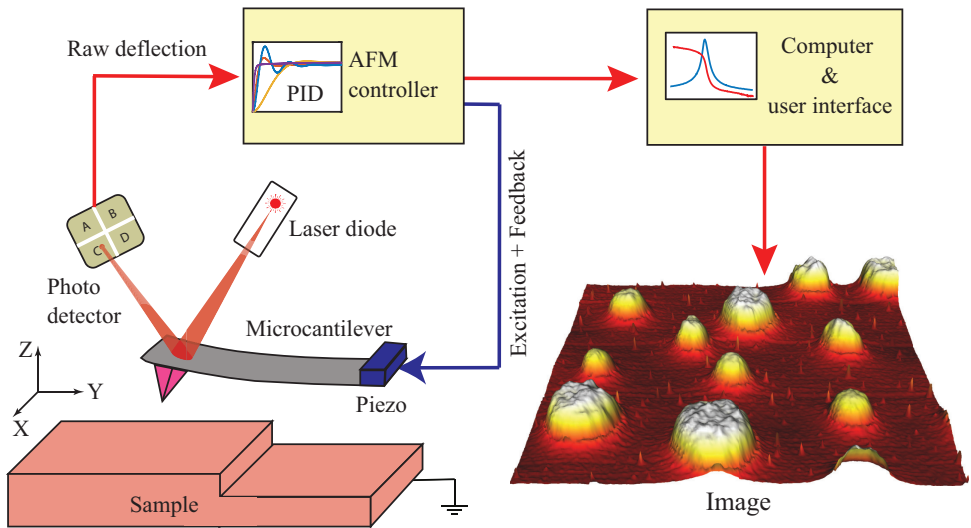


Figure 1.1: Schematic of an AFM. The probe is a microcantilever with a sharp tip at its free end that mechanically interacts with the sample surface. The deflection induced due to the tip-sample forces is measured using a laser beam and a photodetector. This deflection is further processed within the controller and displayed as a topographical image on the computer.

On the other hand, since the inception of AFM in 1986 [1], the technology behind an AFM system starting from the acquisition electronics, data processing algorithms as well as the mathematical and computational models utilized for nanomechanical characterization have made tremendous leaps in terms of sophistication and accuracy. Thanks to these advancements, AFM has become one of the most prominent nanoscale characterization tools in modern science with applications ranging from probing soft matter, understanding molecular metrology [3–8] to imaging live cells, bacteria and other transient biological processes with atomic resolution [9–13].

Figure 1.1 shows the schematic of an AFM system. At the heart of the AFM is a microcantilever which acts as a mechanical force transducer by periodically interacting with the sample and converting the forces between the cantilever tip and the sample into



measurable deflection. These forces are generally referred to as the tip-sample interaction forces. An AFM's main purpose is to maintain this tip-sample forces constant over time and is done by attaching either the cantilever or the substrate to a z-piezo actuator that allows for fine control of the vertical position. The deflections of the cantilever are monitored by a laser beam that reflects from the back-side of the cantilever onto a four quadrant photodiode. The output voltage from the photodiode is used to monitor changes in the cantilever position. Furthermore, in order to scan the sample in the x-y directions as shown in Fig.1.1, there exists an x-y piezo scanner that works in tandem with z-piezo actuator to position the cantilever from one pixel to another. The entire operation is carefully controlled via an AFM controller in order to maintain a constant tip-sample force and avoid any imaging artefacts.

## 1.2. MODES OF OPERATION IN AFM

The essence of an AFM technique is to probe the surface of a given sample. This is achieved in several different ways depending on the methodology employed to measure the tip-sample forces and each method is classified as an "operating mode". In this aspect, static or contact mode AFM was the first mode developed for topographical measurements, where the static deflection of the cantilever is monitored under the influence of tip-sample forces [1]. Although static AFM is a simple and robust method, it suffers from disadvantages such as sample damage and limited observables to study the complex nature of tip-sample interaction. This led to the development of dynamic AFM [14, 15] in which the microcantilever tip interacts intermittently with the sample while being driven close to or at its resonance frequency. Since these microcantilevers often possess a high quality factor they are sensitive to perturbations near the resonance and can react to minute changes in tip-sample forces. However, several developments in feedback control architectures have made imaging in liquids with low quality factors a possibility; thus extending the library of materials that can be probed using dynamic AFM technique. To date several studies have exploited the sensitivity of dynamic AFM to visualize individual atoms and molecular configurations in samples [16–20]. Furthermore, the intermittent contact of the tip with the sample helps in reducing sample damage due to reduced lateral forces.

Today, dynamic AFM has become one of the most popular operating modes and is further bifurcated into several sub-categories depending on the modulation techniques, observables of interest and controller methodologies. Among them, frequency modulation AFM (FM-AFM) [14], Amplitude modulation AFM (AM-AFM) [21], Intermodulation AFM (IM-AFM) [22], Bimodal AFM [23] are some of the prominent modes. Besides the static and dynamic modes of operation, researchers have also developed quasi-static or off-resonance modes such as peak force tapping [24, 25] and force volume imaging modes [26, 27], where the AFM instrument approaches the probe to contact the surface, and then pulls the probe away, periodically from one pixel to another. This method of measuring interactions provide individual force curves at each and every single pixel of the image. However, they are quite slow when compared to other modes of operation and often involves large amount of data processing.

In this thesis, we focus mainly on AM-AFM also known as tapping mode AFM (TM-AFM). In TM-AFM there are two observable channels at each image pixel: the amplitude

and phase of the cantilever response. The feedback loop monitors the change in amplitude of the cantilever under the influence of the tip-sample forces and corrects the error signal to maintain a constant amplitude throughout the scan operation. The feedback is further translated into other useful information channels such as change in amplitude to topography and change in phase to dissipation and many other important sample properties [28]. TM-AFM is the most regularly used technique since it can be easily used in ambient and liquid environments. Furthermore, the versatility of the technique in achieving atomic resolution and possessing the capability to scan large areas with stark change in topography makes TM-AFM the most popular imaging technique within the scientific community.

### 1.3. TIP-SURFACE FORCES

In order to make effective use of an AFM for nanomechanical characterization it is of utmost importance to understand the intricacies of tip-sample interaction forces. In general the interaction forces in AFM are of electromagnetic in nature as shown in Fig. 1.2(a) and can be broadly classified as non-contact forces (blue) and contact forces (red) depending on tip-sample separation distance as shown in Fig. 1.2(b). Non-contact forces refer to the long range forces influencing the cantilever dynamics when the tip is not in contact with the sample; whereas the contact forces are those which are activated when the tip comes into contact with the sample. Furthermore, these tip-sample forces are often distance dependent and can have conservative or non-conservative origins. To add another layer of complexity, some of these forces are attractive in nature and some repulsive, and depending on the surrounding medium the attractive or repulsive character of the forces can be changed for example by modifying the ionic strength of an electrolyte [2, 28, 29]. Thus, the variety of tip-sample forces combined with their different character and the difficulty of isolating the forces to a particular interaction type are some of the factors that make estimation of nanoscale material properties using an AFM a challenging task.

The non-contact forces that dominate the tip-sample interaction mechanics is the Van der Waals (VdW) force [29–31]. The VdW force between the atoms and/or molecules have their origin in electric dipole interactions. The dipoles could be of permanent or induced by thermal fluctuations and consists of three main interaction types: dipole-dipole, dipole-induced dipole and induced dipole-induced dipole. The VdW forces are found to be effective from large distances such as hundreds of nanometres to interatomic distances [32]. Below the interatomic distance, the contact repulsive forces between atoms and molecules arising from Pauli and ionic repulsion start dominating the interaction mechanics [29]. The surface of two bodies deform when brought into mechanical contact and depending on the contact area several hundreds or thousands of atoms can exert an effective repulsive force. The description of such a repulsive force is modelled using contact mechanics [33–36]. These models rely on continuum elasticity theories to describe the contact and adhesion between the probe tip and the sample under an external load. Some of the popular models that describe the contact mechanics are the Hertz [37], Johnson, Kendall, and Roberts (JKR) [33, 34] and Derjaguin, Muller, and Toporov (DMT) [35] models.

Although there exists numerous models that describe the indentation or contact un-

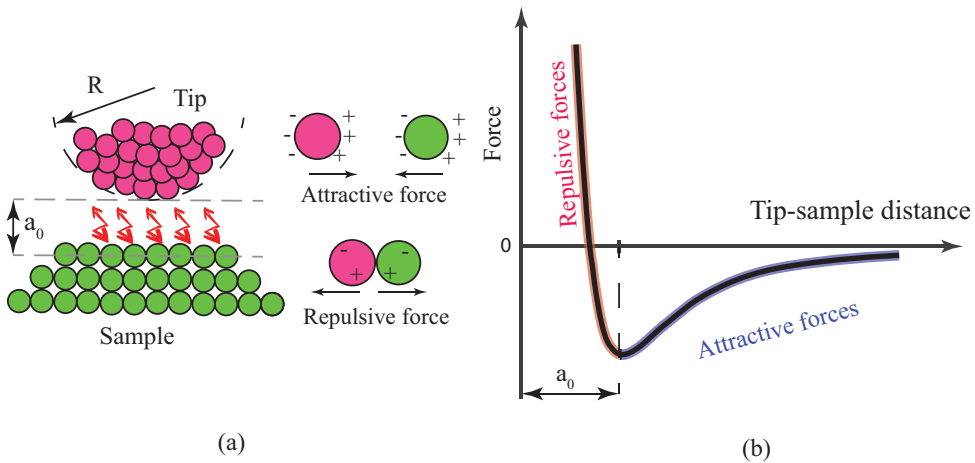


Figure 1.2: Schematic of tip-sample interaction in AFM. (a) When the tip (pink) and the sample (green) is separated by distance larger than inter-atomic distance value ( $a_0$ ) the long range forces (non-contact forces) dominate the interaction. Below the  $a_0$  value the repulsive forces (contact forces) dominate the interaction behaviour. (b) The variation in tip-sample force as a function of tip-sample separation distance.

der an AFM tip, these models have an underlying assumption regarding the nature of probe geometry and the sample under investigation. In general the geometry of the tip is not well defined and as a consequence the models are not universal and must be chosen with care. In addition to this, the use of continuum models to describe nanoscale processes is still an open question and has inherent limitations [38–40]. Nevertheless, continuum models have provided good description for experimental results [41, 42] and are currently employed in most of the newer AFM systems to perform sample characterizations.

Figure.1.2(b) shows the variation of tip-sample force with separation distance. It highlights the overall effect of the various forces influencing the cantilever oscillations as it approaches the sample. From the figure we observe that the cantilever experiences attractive force until the intermolecular distance and then repulsive force from then onwards. Additionally, close to the intermolecular distance there exists a region where both attractive and repulsive regions co-exist. The combined attractive and repulsive potentials bends the nonlinear resonance and leads to a hysteretic amplitude response. In fact, the first experimental evidence for the existence of bi-stability in TM-AFM was the observation of this hysteretic response under the influence of varying tip-sample distance [43–45].

In addition to the above forces, the cantilever can experience additional forces depending on the surrounding media and environmental conditions. For example, the tip or the surface can be electrostatically charged depending on the material properties. There could be capillary forces due to thin layer of water adhering to the sample at ambient experimental conditions and in special cases there could be additional local surface effects such as chemical bonds, localized charges and viscoelastic forces which could influence the dynamics of the system. Thus it is imperative to understand the nature of

interaction forces in a given experiment and choose an appropriate model for determining the nanomechanical properties of the sample using dynamic AFM methods.

#### 1.4. RESEARCH OBJECTIVES AND SCOPE OF THE THESIS

The primary goal of this thesis is to develop nonlinear identification techniques to estimate nanomechanical properties of samples. For this, we focus on nonlinear dynamics of the AFM cantilever, influence of operating parameters on nonlinear frequency response curves, sensitivity of instrument's observables on model parameters and subsequent estimation of material properties. Finally, we leverage machine learning and data science techniques for reconstructing tip-sample interaction forces in dynamic AFM.

- *To study the global dynamics and robustness of attractors in TM-AFM.*

Majority of the existing dynamic models in the literature tend to focus on governing the local dynamics of the system by tuning the operating parameters while leaving the impact on global dynamics largely unexplored. But, in order to control and predict the nonlinear dynamical events such as jump between attractors, chaos and feedback instabilities as well as preserve the stability of the scanning operation in TM-AFM, the understanding of the system response from a global perspective is necessary. In this regard, a vast number of previous studies have been dedicated to the study of microcantilever dynamics by using simplified single degree of freedom point mass models [43, 46–48]. These models utilize static analysis to determine the cantilever stiffness and then an equivalent mass is calculated by combining information from thermal calibration [49].

However, such a lumped parameter model does not accurately explain the experimental behaviour of the system, where certain nonlinear effects such as parametric resonance occurring due to base excitation<sup>1</sup> cannot be captured. These nonlinear effects often result in image artefacts and induce feedback instabilities hampering the proper functioning of the AFM. In order to understand the physics behind these artefacts, it is important to study the influence of operating parameters such as AFM tip radius, drive amplitude and frequencies on the stability of the scanning operation. By quantifying the influence of these parameters on the dynamical state of the system we can define robust guidelines for smooth functioning of the system.

- *To improve the signal to noise ratio of higher harmonics and thus enhance the sensitivity of TM-AFM.*

Accurate reconstruction of tip-sample interaction force has remained an important but often a difficult goal for the AFM community. The reconstruction of tip-sample force has wide range of implications such as the measurement of the height profile, development of novel feedback strategies and estimation of nanomechanical properties of the system. A major limitation in extracting the instantaneous tip-sample interaction force in dynamic AFM stems from the fact that conventional AFM is essentially driven with a single frequency and thus results in

<sup>1</sup>The base of the cantilever is given a prescribed harmonic motion causing the cantilever to oscillate.

at most two observable channels: the amplitude and the phase of the response. These two observables are insufficient to completely characterize mechanical properties of the sample. To remedy this limitation several multi-harmonic AFM techniques were established [7, 22, 50–52]. These techniques either utilize the higher harmonics or higher order modes as additional channels of observable and provide complementary information on the sample properties.

However, a majority of these multi-harmonic AFM techniques rely on high SNR of higher harmonics and eigenmodes to reconstruct information about the tip-sample interaction. This enhancement of SNR typically comes from physical modification of the cantilever by either changing the geometric shapes [53–55], creating notches and holes [56] or by adding concentrated mass at specific locations [57]. The use of these cantilever require extensive knowledge on the AFM dynamics thus making them less viable for normal AFM operations. In this thesis we show that the tip-sample interactions mediates an inherent mode coupling between several different modes of the cantilever. This mode coupling phenomena can in turn be exploited to enhance the SNR of several higher harmonics without any physical modification of the probes. In addition to improved SNR of higher harmonics, we show that the mode coupling phenomena leads to a decreased sample indentation thus making it suitable for normal AFM imaging operation.

- *To investigate the sensitivity of viscoelastic characterization in TM-AFM.*

Dynamic AFM has transitioned from being an imaging technique to a more versatile instrument that can perform nanomechanical characterization of wide variety of materials [5–7, 58, 59]. Amongst them, viscoelastic characterization of soft matter is currently an important topic in the AFM community due to its varied applications such as understanding cell functioning [60], mechanobiology [6, 61, 62], and novel polymers [59, 63–65]. To date, the most straightforward way to obtain the nanomechanical properties and in particular the viscoelastic properties of the sample from the experimental observables is by setting up an optimization problem that will tune the various model parameters within a specific range and obtain the best fit for the experimental data.

However, due to the highly nonlinear nature of the tip-sample interaction in dynamic AFM, these optimization techniques are prone to pitfalls such as vanishing gradient due to insensitivity of a particular model parameter to the experimental data, a barren flat topological landscape of the objective function, presence of multiple local minima and numerical non-convexity. Till date, there are no studies detailing on how to recognize and tackle the above issues for experimental characterization of samples.

In this thesis, we perform a systematic study on the sensitivity of viscoelastic characterization in Intermodulation AFM (IM-AFM). In particular, we use a model that has six distinct parameters and can model both the bulk and the surface viscoelastic responses of the sample; whereas, the IM-AFM experiment provides with 32 distinct harmonic observables that arise due to the tip-sample interactions. To understand the sensitivity of the model parameters on the physical observables, we

perform several local and global optimization routines and underline the aforementioned pitfalls in a physically intuitive fashion. Furthermore, we remedy the limitations of our model by reducing the initial six parameter model to a simpler three parameter model and analyse the experimental data. The analysis shows consistent results that are comparable with values previously reported in the literature. This further demonstrates the disadvantages of treating the fitting procedure in dynamic AFM application as a black box.

- *Reconstructing the tip-sample force from temporal data using machine learning in TM-AFM.*

One of the most important aspect of dynamic AFM is to understand the tip-sample interaction mechanism since the tip-sample interaction force is a unique fingerprint of every material; it is the basis for every nanomechanical characterization technique. In the previous section we discussed SNR of higher harmonics as one of the limiting factors for accurate reconstruction of tip-sample interaction. The other limiting factor is the lack of generalized universal approach for reconstructing the tip-sample interaction force. Dynamic AFM in contrast to its name does not measure the interaction forces directly but is often reconstructed from the limited number of experimental observables. For example by capturing the frequency or amplitude and phase information from the oscillating cantilever while changing the separation distance of the cantilever from the sample [54, 66–69].

Although, there are several analytical and experimental techniques available for force reconstruction, each come with its own set of limitations. For example, the analytical techniques such as the integral equations [66, 68], Fourier expansion methods [70] provide time averaged values of interaction forces and thus neglect crucial information of how the interaction force changes during the time period of the cantilever's oscillation. Whereas, experimental techniques suffer from disadvantages such as requiring special cantilever designs for obtaining large number of harmonics in the deflection signal for accurate force estimation [54, 56], having a priori knowledge on the transfer function and/or spatial mode shapes of the cantilever [70, 71].

In this thesis we overcome these limitations by combining the experimental observables with machine learning and data science techniques. Data driven models have revolutionized the analysis and understanding of complex data, recognizing patterns, and developing classifications based on multimodal datasets in various situations that are normally beyond the grasp of humans. Recently, data driven methodologies have made giant strides in their predictive capabilities to identify and extract the governing dynamics of a system beyond the attractor where they are sampled and constructed [72–74]. By utilizing these data driven techniques we eliminate the inherent assumptions on the mathematical models or the nature of interaction and focus on extracting the tip-sample interaction directly from the experimental data.



## 1.5. OUTLINE OF THE THESIS

This thesis is a collection of articles either published or submitted in peer reviewed journals. Hence, the reader might find some similarities in the introduction and methodology section of different chapters. The thesis outline is as follows:

Chapter 2 presents the global dynamics and robustness of different oscillatory states in TM-AFM. We begin by modelling the system using continuous beam theory that can provide precise and deep insights into the physics behind several nonlinear phenomena such as amplitude jumps, period-doubling cascades and grazing bifurcations. Additionally, we study the influence of several operating parameters such as AFM tip radius, excitation amplitude and drive frequencies on the cantilever dynamics through nonlinear frequency response curves and basins of attraction.

Furthermore, we study the robustness of attractors in TM-AFM by making use of systematic bifurcation diagrams to highlight the various possible steady state solutions and discuss their stability to external perturbations. We show that in addition to the well known bi-stable potential encompassing the standard attractive and repulsive oscillatory states, there exists a second co-existing potential well close to the sample surface which we refer to as "in-contact" attractor in this thesis. Finally, we conclude the chapter by quantifying the robustness of all the possible solutions present in TM-AFM using integrity measures.

Chapter 3 studies the enhancement of signal to noise ratio in higher harmonics by exploiting mode coupling. In particular, we determine a range of drive frequencies using the nonlinear frequency response curve with which the cantilever can be excited to enhance the SNR of higher harmonics. Furthermore, we show that by sweeping the frequency around this spectral neighbourhood we observe a decreased sample indentation. To simulate the experimental behaviour, a Multiple Degrees of Freedom (MDOF) is developed using reduced order modelling based on a non-smooth interaction force. The results from the simulations further reinforce the aforementioned mode coupling as the physical phenomena responsible for the enhancement of SNR of higher harmonics. The study also reveals the potential of phase space trajectories as tools for visualizing mode coupling phenomena and further highlights the potential of the technique to be used in a wide variety of multi-frequency AFM applications.

Chapter 4 discusses the importance of having experimental observables that have an appreciable influence on the nanomechanical property being estimated. The study involves characterizing the viscoelastic properties of the sample using multi-harmonic AFM together with a numerical model that can characterize both the bulk and the surface properties. The study offers insight into the various pitfalls of setting up an optimization problem and how to identify them. Furthermore, the analysis on experimental data obtained on a polymer blend shows that the multi-harmonic observables although large in number is incapable of characterizing the surface viscoelastic response in multi-harmonic AFM setting. We reinforce this analysis by doing numerous local and global optimization simulations. Finally, we show that by reducing the model parameters, the optimization problem produces meaningful results which suggests that novel viscoelastic models which can truly capture the surface response is crucial for accurate quantification of surface properties using dynamic AFM.

Chapter 5 focusses on using machine learning and data science to distil physically in-

interpretable models directly from experimental data. The identified models can be used to estimate the tip-sample interaction force with sub-microsecond resolution. Moreover, it provides insights on peak loading forces and energy dissipation during contact without prior knowledge of the interacting samples. We achieve this, by using the sparse identification technique to train and test on a large number of well established AFM models. These models are capable of representing different tip-sample interaction physics and thus help to build a library of linear and nonlinear functions capable of replicating the said interaction in experimental data. we showcase the capability of the technique by characterizing a co-block polymer and extract the interaction force as a function of tip-sample separation distance. In addition to this, we show that data driven analysis can be used for probing the geometry and the stiffness of the sample.

In Chapter 6, I discuss the future research outlook and possible research directions. The discussion is further supplemented with preliminary results that can bridge several areas of research such as extracting tip-radius using electrostatic forces, exploiting the softening dynamical response of the cantilever to quantify VdW forces, data driven based nonlinear control techniques, extending the data driven identification in dynamic AFM to characterize viscoelastic samples and finally, employing neural networks to identify specific signatures within temporal data that suggest inter-modal coupling.

In Chapter 7, the conclusions of this research are outlined and further discussion on the advantages and improvements of the employed techniques are provided.

2

2

# 2

## GLOBAL DYNAMICS OF TAPPING MODE ATOMIC FORCE MICROSCOPY

*In this chapter, we perform a comprehensive analysis of the robustness of attractors in tapping mode atomic force microscopy. We achieve this by developing a numerical model based on cantilever dynamics driven in the Lennard-Jones interaction potential. Pseudo arc-length continuation and basins of attraction are utilized to obtain the frequency response and dynamical integrity of the attractors. The global bifurcation and response scenario maps for the system are developed by incorporating several local bifurcation loci in the excitation parameter space. Moreover, the map delineates various escape thresholds for different attractors present in the system. Our work unveils the properties of the cantilever oscillation in proximity to the sample surface, which is governed by the so called in-contact attractor. The robustness of this attractor against operating parameters is quantified by means of integrity profiles. Our work provides a unique view into global dynamics in tapping mode atomic force microscopy and helps establishing an extended topological view of the system.*

This chapter is published as an article in Nonlinear dynamics journal [75]. The published article is adapted to fit into the context of the thesis.

Atomic Force Microscopy (AFM) has become one of the most prominent characterization tools in modern science. It is ubiquitously used to characterize and manipulate surface properties of materials down to atomic resolution in both air and liquid environments [4–6, 9–13, 76]. Among the various AFM operational modes, Tapping Mode AFM (TM-AFM) [21] also known as Amplitude Modulation AFM (AM-AFM) [28] is one of the most extensively used techniques to obtain high-resolution images of wide variety of samples. Owing to reduced lateral forces and high-phase sensitivity, TM-AFM is widely popular in soft matter [5], biological samples [6] and polymer [7, 77] applications.

TM-AFM is based on the near-resonant excitation of a microcantilever with a sharp tip at its free end that is vibrating in the vicinity of the sample. The vibrations in the cantilever are influenced by the tip-sample interaction forces, which modifies the beam dynamics. In general, the tip-sample interaction is nonlinear and comprises of long-range attractive Van der Waals forces, short-range quantum mechanical repulsive forces, adhesive and contact forces. The nonlinear response due to tip-sample interaction is even more involved in the presence of electrostatic and capillary forces [78]. In the existence of such complex nonlinearities, a comprehensive understanding of the multi-stable response is crucial, since these nonlinearities can be efficiently utilized for extracting several nanomechanical properties of the sample [6, 28, 79, 80]. Furthermore, the accuracy of imaging and nanomechanical characterization of sample surfaces from measured data depends crucially on the deconvolution of data with appropriate models.

In recent years, the underlying dynamics of AFM cantilever and its exploitation have been investigated by many authors [43, 46–48, 81]. The vast majority of these studies have been dedicated to study the microcantilever dynamics by utilizing a simplified single-degree-of-freedom point mass model [82–84]. In this approach, first a static analysis is performed to determine the cantilever stiffness and then the equivalent mass is calculated based on the experimentally evaluated fundamental resonance frequency. Furthermore, the excitation is modelled as an external force acting on the point mass. Such a lumped parameter model does not represent the conditions encountered in reality, where the microcantilever is subjected to base excitation at the clamped end by means of a piezoelectric actuator. The base excitation induces linear and nonlinear parametric excitations that are typically not captured by the lumped parameter model thus failing to accurately describe the dynamics of the microcantilever [81, 83].

Continuous beam models on the contrary, have proven to predict the nonlinear aspects of AFM cantilever dynamics accurately [46–48, 81]. These models are able to provide precise and deeper insights into the physics behind the nonlinear phenomena such as amplitude jumps, period-doubling, and grazing bifurcations [81, 85]. Therefore, in spite of the complexities involved in modelling of the AFM cantilever as a continuous beam, it allows for capturing the overall nonlinear aspects of the AFM dynamics [86].

In practical operation, the dynamics of AFM cantilever is influenced by several operating parameters such as tip radius, excitation amplitude, excitation frequency, and feedback values etc. The real-time variation of these parameters during an AFM operation can lead to unwanted dynamical phenomena such as bifurcations, unstable and aperiodic motions, which can decrease the reliability of results and strictly limit the operating ranges of the AFM. The dynamic models as well as the feedback strategies implemented in standard AFM systems tend to focus on governing the local dynamics of

the system, leaving the impact on the global dynamics largely unknown. Therefore, in order to predict and control these dynamical events as well as preserving the stability of operation in TM-AFM, it is important to study and understand the nonlinear responses from a global perspective.

Currently, there are no detailed works on global dynamics of TM-AFM, which i) evaluate the escape boundaries, ii) estimate dynamical integrity, and iii) perform detailed analysis of bifurcations. Existing literature have focussed on the dynamical integrity and bifurcation scenarios of non-contact AFM [85, 87]. But basins of attraction and erosion process of basin portraits in TM-AFM are lacking in the literature. The erosion of uncorrupted basins of attraction surrounding each main solution as a function of AFM operation parameters is of paramount importance from both theoretical and experimental perspective.

In this chapter, we elucidate the global dynamics and robustness of attractors in TM-AFM. Differently from existing works, which are based on limited analysis on the local dynamical behaviour, this work makes systematic use of bifurcation diagrams to highlight the appearance and disappearance of steady-state solutions. The latter offers an overall interpretation of the dynamic response with respect to operational parameters, namely, excitation frequency and forcing amplitude. Additionally, we show that, by changing the operation parameters, a microcantilever initially in the primary resonant branch, can escape from its local potential well and get captured by a second co-existing local potential well close to the sample surface. This regime of oscillation close to the sample surface, referred in this chapter as, 'in-contact' attractor is unexplored in the literature. In this work, we examine its evolution and robustness properties with frequency response curves and basins of attraction. Furthermore, the envelopes of local bifurcation boundaries are built to understand the escape scenarios of the solutions. Finally, integrity analysis is performed to quantify the steady-state solutions associated with all the attractors present in TM-AFM.

Based on these motivations, the chapter is organized as follows: the modelling of the system is discussed briefly in Sec.2.1. This is followed by a detailed analysis of frequency response of the system, bifurcation charts and response scenarios including escape of solutions in an excitation parameter space in Sec.2.2. Particular attention is paid to the frequency response analysis of the in-contact attractor around its primary and parametric resonance. The results of this section are then utilized to build basins of attraction and dynamical integrity curves for the main attractors present in the system in Sec.2.3.

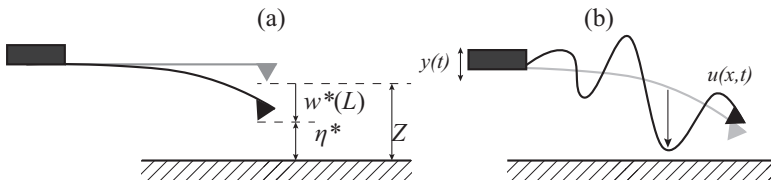


Figure 2.1: Schematic of the AFM cantilever in (a) static deflection configuration and (b) configuration at which AFM cantilever exhibits oscillations around the nonlinear static equilibrium. The sample is at  $\bar{\eta}_1 = 1$ .

## 2.1. NUMERICAL MODEL

The classical beam theory, based on the Euler-Bernoulli assumptions, is used to obtain the continuous model for the AFM microcantilever shown in Fig 2.1. The nomenclature used to describe the equations in this chapter is identical to the one described by Ruetzel et al [47]. The deflection of the cantilever towards the sample is treated as positive and the rest position of the cantilever is taken as reference. The considered microcantilever has a length  $L$ , mass density  $\rho$ , Young's modulus  $E$ , area moment of inertia  $I$ , and cross-section area  $A$ . The beam is clamped at  $x = 0$  and free at  $x = L$ . The tip-sample separation distance in the reference configuration is denoted by  $Z$  and the total deflection of the microcantilever  $w(x, t)$ , can be expressed as  $w(x, t) = u(x, t) + w^*(x) + y(t)$ , where  $u(x, t)$  is the deflection of the microcantilever relative to a non-inertial reference frame attached to the base and  $w^*(x)$  is the static deflection towards the sample due to tip-sample interaction. The base excitation is generated by a dither piezo and is assumed to be harmonic, i.e.  $y(t) = Y \sin(\Omega t)$ , where  $Y$  and  $\Omega$  are the amplitude and frequency of excitation, respectively.

### 2.1.1. TIP-SAMPLE INTERACTION

In TM-AFM, the microcantilever oscillates in close proximity to the sample surface. In our work, we use the Lennard-Jones (LJ) potential to describe the tip-sample interactions [29]. Although the model doesn't take into account the real contact mechanics encountered in TM-AFM, it represents a generic tip-surface interaction potential which mimics qualitatively, the more detailed and computationally expensive models [48]. The LJ potential models the non-retarded dispersive Van der Waals forces as well as the short-range repulsive exchange interactions between two molecules. Assuming a spherical tip apex with radius  $R$  and a flat sample surface, the interaction potential and the force are:

$$U_{LJ} = \frac{A_1 R}{1260 z^7} - \frac{A_2 R}{6z}, \quad (2.1a)$$

$$P_{LJ} = -\frac{\partial U}{\partial z} = \frac{A_1 R}{180 z^8} - \frac{A_2 R}{6z^2}, \quad (2.1b)$$

where  $z$  is the instantaneous tip-sample separation gap.  $A_1$  and  $A_2$  are the Hamaker constants for the repulsive and attractive potentials, respectively. A positive interaction force implies repulsion. The Hamaker constants are  $A_1 = \pi^2 \rho_1 \rho_2 c_1$  and  $A_2 = \pi^2 \rho_1 \rho_2 c_2$ , where  $\rho_1$  and  $\rho_2$  are the number densities of molecules in the interacting media and  $c_1$  and  $c_2$  are the interaction coefficients of intermolecular pair potential [29].

### 2.1.2. EQUATION OF MOTION

The nonlinear static deflection of the microcantilever in the absence of base excitation is computed by solving for the equilibrium gap between the tip and the sample shown in Fig. 2.1. The static equilibrium gap  $\eta^*$  at the free end is calculated as a function of the approach distance  $Z$  through static balancing of the cantilever restoring force and the tip-sample interaction forces.

The dynamic equation of motion of the tip deflection  $u(x, t)$  about its nonlinear equilibrium subjected to base harmonic motion is then derived through a single mode



discretization of the Euler-Bernoulli beam equation. The interaction forces given by Eq. (2.1)(b) are assumed to be acting on the free end of the cantilever and is mathematically achieved through the use of Kronecker delta ( $\delta$ ) function. Writing the equation of motion of the vibrating cantilever with respect to a non-inertial frame of reference leads to the following governing equation,

$$\rho A \ddot{u}(x, t) + EI(u''''(x, t) + w^{*''''}(x)) = F_i(Z - w(L, t))\delta(x - L) + \rho A \Omega^2 Y \sin(\Omega t), \quad (2.2)$$

where,

$$F_i(Z - w(L, t)) = -\frac{A_1 R}{180(Z - w(L, t))^8} + \frac{A_2 R}{6(Z - w(L, t))^2} \quad \text{and} \quad (2.3)$$

$$w(L, t) = w^*(L) - u(L, t) - Y \sin(\Omega T).$$

Equation (2.2) is a non-autonomous and nonlinear equation. The equation is discretized by projecting the dynamics onto the system's linear modes of vibration. The natural modes and frequencies are obtained using the Galerkin approach [47, 88]. The frequency range of the analyses in this paper spans around the neighbourhood of the fundamental resonance, where the contribution of higher modes is substantially negligible. Based on this assumption, a single-degree-of-freedom model is used. Assuming  $u(x, t) = \phi_1(x)q_1(t)$  (where  $\phi_1$  is the first approximate eigenfunction around the static deflected configuration) and using the Galerkin approach, the following nonlinear equation can be derived [47]:

The non-dimensional parameters and the corresponding coefficients of Eq. (2.4) are described below. For further details the reader is suggested to read the article [47].

$$\ddot{\bar{\eta}}_1 = -d_1 \dot{\bar{\eta}}_1 - \bar{\eta}_1 + B_1 + \frac{C_{11}}{(1 - \bar{\eta}_1 - \bar{y} \sin(\bar{\Omega} t))^8} + \frac{C_{12}}{(1 - \bar{\eta}_1 - \bar{y} \sin(\bar{\Omega} t))^2} + \bar{y} \bar{\Omega}^2 E_1 \sin(\bar{\Omega} t).$$

$$\bar{\eta}_1 = \frac{x_1(\tau)}{\eta^*}, \quad x_1(\tau) = \phi_1(L)q_1(\tau), \quad \eta^* = Z - w^*(L), \quad \tau = \omega_1 t, \quad \bar{\Omega} = \frac{\Omega}{\omega_1}, \quad d_1 = \frac{c_1}{\omega_1 \rho A \int_0^L \phi_1^2 dx},$$

$$B_1 = (1 - \frac{Z}{\eta^*})\Gamma_1, \quad C_{11} = -\frac{A_1 R}{180k(\eta^*)^9}\Gamma_1, \quad C_{12} = -\frac{A_2 R}{6k(\eta^*)^3}\Gamma_1, \quad \omega_1^2 = \frac{EI \int_0^L \phi_1 \phi_1'''' dx}{\rho A \int_0^L \phi_1^2 dx},$$

$$\Gamma_1 = \frac{k\phi_1^2(L)}{\omega_1 \rho A \int_0^L \phi_1^2 dx}, \quad k = \frac{3EI}{L^3}, \quad \bar{y} = \frac{Y}{\eta^*}, \quad E_1 = \frac{\phi(L) \int_0^L \phi_1 dx}{\int_0^L \phi_1^2 dx}. \quad (2.4)$$

The microcantilever tip deflection towards the sample is denoted by  $\bar{\eta}_1$ . In addition, the equation is made dimensionless with respect to equilibrium gap width ( $\eta^*$ ) and the fundamental frequency of the free microcantilever ( $\omega_1$ ) in the absence of tip-sample interaction forces. The amplitude of the dither piezoelectric actuator is denoted by  $\bar{y}$ . The

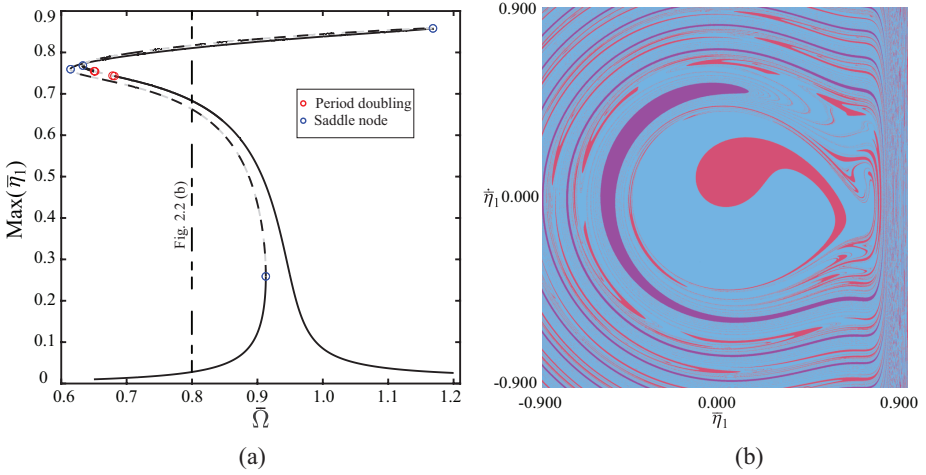


Figure 2.2: Frequency response curve and basin portrait of the system for fixed parameters  $\bar{y} = 0.006$  and  $R = 150$  nm. The parameters are obtained from the monostable region of nonlinear elastostatic equilibrium curve. (a) Frequency response shows softening and hardening behaviour corresponding to the attractive and repulsive tip-sample forces. Continuous and dotted lines indicate stable and unstable branches of the solution. Red and blue circles indicate period-doubling and saddle-node bifurcation points respectively. The natural frequency of the system is  $\bar{\Omega}_0 = 0.94$ . (b) Basins of attraction taken at section  $\bar{\Omega} = 0.8$ . The positive displacement implies movement of the tip closer to the sample. The details on basin color and the corresponding attractor/solution description is given in Table. 2.4.

dotted quantities represent derivatives with respect to rescaled time  $\tau$  ( $\tau = \omega_1 t$ ). Finally, the modal damping  $d_1$  is explicitly introduced in Eq. (2.4) and is related to the quality factor  $Q$  of the cantilever by the relation  $Q = 1/d_1$ .

## 2.2. NUMERICAL ANALYSIS

In order to investigate the dynamical behaviour of the TM-AFM, the simulations of the model given by Eq. (2.4) are performed in this section. The entire analysis is carried out for the interaction of a soft monocrystalline silicon microcantilever with the (111) face of flat silicon sample. The cantilever and interaction properties are listed in Table 2.1. Furthermore, the analysis is performed for tip-sample gap ( $\eta^*$ ) in the bi-stable region of nonlinear elastostatic equilibrium curve. Thus a value of  $\eta^* = 6.542$  nm<sup>1</sup> is chosen for the rest of the analysis in this work. However, a similar analysis can be carried out for any other tip-sample gap values.

Numerical simulations are performed by using a pseudo arc-length continuation technique [89]. We also make use of basins of attraction (phase space) in order to illustrate the presence of various attractors (steady state solutions). A basins of attraction is a set of possible initial conditions about an equilibrium point in phase space that assures a specific response from the cantilever. In other words, any chosen initial condition within the phase space will be 'attracted' to a particular steady state motion of the cantilever.

<sup>1</sup>This value allows for comparison of results with the reference paper of Ruetzel et al [47]. However, qualitatively the same results are obtained for  $\eta^* = 6.5$  nm.

Table 2.1: Properties and dimensions of the cantilever [47].

Description	Dimensions
Length ( $L$ )	449 $\mu\text{m}$
Width ( $b$ )	46 $\mu\text{m}$
Thickness ( $h$ )	1.7 $\mu\text{m}$
Tip radius ( $R$ )	150 nm
Density ( $\rho$ )	2330 $\text{kg m}^{-3}$
Static stiffness ( $k$ )	0.11 $\text{Nm}^{-1}$
Elastic modulus ( $E$ )	176 GPa
Fundamental resonance frequency ( $f_1$ )	11.804 kHz
Quality factor ( $Q$ )	100
Hamaker constant-repulsive ( $A_1$ )	$1.35961 \times 10^{-70} \text{Jm}^6$
Hamaker constant-attractive ( $A_2$ )	$1.8651 \times 10^{-19} \text{J}$

Unless specified, the basins are evaluated in a phase space grid of  $\bar{\eta}_1 = [-0.9, 0.9]$  and  $\dot{\bar{\eta}}_1 = [-0.9, 0.9]$  as it contains all the main attractors involved in the system potential well.

### 2.2.1. FREQUENCY RESPONSE AND BIFURCATION SCENARIOS

The interaction between tip and sample gives rise to different nonlinear frequency responses depending on the tip-sample separation distance. The response displayed in Fig. 2.2(a) shows an initial softening behaviour when the tip is far away from the sample. This region is dominated by attractive Van der Waals forces. However, when the tip-sample separation reaches the order of the interatomic distance, the response exhibits hardening behaviour and this region is dominated by repulsive forces (see Fig. 2.2(a)). Figure 2.2(b) shows the corresponding basin portrait associated with the frequency response at  $\bar{\Omega} = 0.8$ . The blue and crimson basins together form the attractive region, while the purple basin belongs to the repulsive region.

The nonlinear frequency response shown in Fig. 2.2(a) is well-known and studied extensively by many authors [47, 80, 90]. However, there exists another overlooked steady-state response when the cantilever escapes the local potential well and gets trapped by a subsequent attractor very close to the sample. Figure 2.3(a) shows the frequency response for the model given by Eq. (2.4) and Fig. 2.3(b) shows the position of the in-contact attractor in the basin portrait. Note that Fig. 2.3(a) is made up of two different solutions belonging to the attractive (lower frequency response curve) and the in-contact attractor (upper frequency response curve). The two solutions can be obtained by using different initial conditions in the numerical integration. In the next section, the detailed analysis of the in-contact attractor's frequency response and corresponding bifurcation scenarios are presented parametrically.

### 2.2.2. FREQUENCY RESPONSE CURVES

Local dynamic analysis is performed using frequency response curves together with the bifurcation charts. The analysis offers a complete overview into the bifurcations and escape scenarios of the system. Furthermore, the unstable solution branches shown in

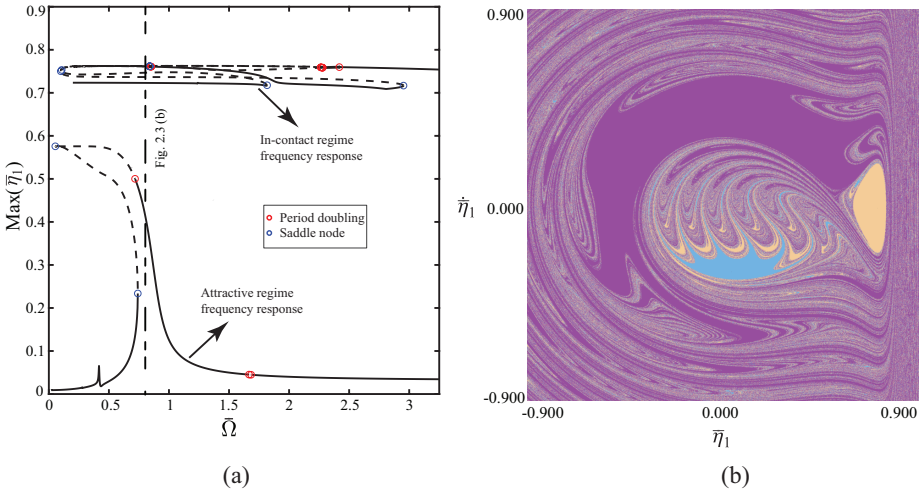


Figure 2.3: Frequency response curve and basin portrait of the system for fixed parameter  $\bar{y} = 0.020$  and  $R = 150$  nm. The parameters are obtained from the bi-stable region of nonlinear elastostatic equilibrium curve. (a) Frequency response of the system showing both attractive (lower curve) and in-contact (upper curve) main solutions. Continuous and dotted lines indicate stable and unstable branches of the solution. Red and blue circles indicate period-doubling and saddle-node bifurcation points, respectively. (b) Basins of attraction of the system is obtained at section  $\bar{\Omega} = 0.8$ . The details on basin color and the corresponding attractor/solution description is given in Table 2.4.

frequency response curves are not discussed in detail but are reported for the sake of completeness.

Figure 2.4 and 2.5 show the evolution of frequency response of the in-contact attractor as a function of the excitation amplitude,  $\bar{y} = 0.005$  and  $0.020$ , respectively. In both figures, red and blue circles indicate period-doubling and saddle-node bifurcation points, respectively. Although the dimensionless natural frequency of the system oscillating in attractive regime is found to be  $\bar{\Omega}_0 = 0.83$  ( $\bar{\Omega}_0$  is the natural frequency affected by the system potential well), it can be observed in Fig. 2.4 that, the first natural frequency of the system oscillating in the in-contact regime is  $\bar{\Omega}_0 = 3.72$  with corresponding parametric resonance at  $2\bar{\Omega}_0 = 7.44$ . This shift in resonance frequency is due to the presence of strong repulsive forces which act as a hard spring connecting the cantilever to the sample. This can be visualized as a change in the boundary conditions of the cantilever similar to that of a clamped-clamped beam. Interestingly, the system also exhibits softening nonlinearity in spite of the presence of repulsive forces. This is due to the fact that the cantilever is oscillating in the potential well with a duration of oscillation longer in the attractive regime. In addition, multi-stability can be observed with different solutions overlapping in several discrete ranges of frequencies (see Fig. 2.4(a)). At lower values of forcing frequency  $\bar{\Omega} \leq 1.85$ , the system has only one non-resonant low-amplitude solution ( $LP_1$ ). The corresponding basin associated with  $LP_1$  solution at  $\bar{\Omega} = 0.5$  is shown in light brown color in Fig. 2.4(b). The figure illustrates the low-amplitude attractor being the dominant solution in the in-contact regime at low-frequency values. The  $LP_1$  solution eventually gives rise to a superharmonic branch ( $Su_1HP_1$ ) at  $\bar{\Omega} = 1.85$  via saddle-

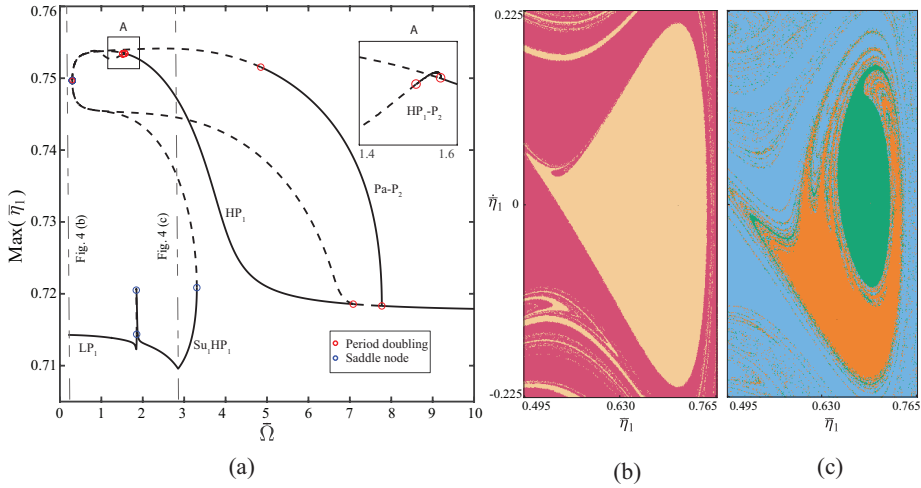


Figure 2.4: Frequency response curve and basins of attraction for the in-contact attractor. (a) Frequency response of in-contact attractor for fixed parameter  $\bar{\gamma} = 0.005$  and  $R = 150$  nm. Continuous and dotted lines indicate stable and unstable branches of solution. Red and blue circles indicate period-doubling and saddle-node bifurcation points, respectively. (b)-(c) Basins of attraction of in-contact attractor obtained at sections,  $\bar{\Omega} = 0.5$  and  $\bar{\Omega} = 2.96$ , respectively in the frequency response curve. The details on basin color and the corresponding attractor/solution description is given in Table. 2.4.

node bifurcation, and later a resonant high amplitude solution ( $HP_1$ ) at  $\bar{\Omega} = 3.3$ . Figure 2.4(c) reports the orange basin belonging to  $HP_1$  solution arising from the boundaries of  $Su_1HP_1$  solution (green basin) in the in-contact regime.

Furthermore, the  $HP_1$  branch in Fig. 2.4(a) destabilizes with the inception of a pair of period-2 branches via flip/period-doubling bifurcations. One of the period-doubling bifurcation occurs close to the low-frequency saddle-node bifurcation at  $\bar{\Omega} = 0.3$ , while the other period-doubling bifurcation occurs at  $\bar{\Omega} = 1.56$  (zoomed part of Fig. 2.4(a)). This behaviour is similar to the nonlinear cantilever response seen in attractive regime as illustrated earlier in Fig. 2.3(a). Moreover, in Fig. 2.4(a) the period-2 branch continuation shows stable motion over a short frequency range before undergoing further period-doubling bifurcation cascade. The subharmonic response associated with the period-doubling bifurcation can be observed around the principal parametric resonance frequency of  $2\bar{\Omega}_0 = 7.44$ . The stable large amplitude period-2 solution (referred to as Pa-P<sub>2</sub> in Fig. 2.4(a)), arising from one of the period-doubling points is found to be stable over a wide range of excitation frequency ( $\bar{\Omega} \in \{4.8, 7.7\}$ ). In addition to the above analysis, referring to Fig. 2.5, at larger excitation amplitudes ( $\bar{\gamma} \geq 0.0118$ ), the softening behaviour in the nonlinear response of the system increases along with a larger field of existence of the superharmonic response ( $Su_1HP_1$ ).

Furthermore, a second superharmonic branch ( $Su_2HP_1$ ) bifurcates through a saddle-node at  $\bar{\Omega} = 1.79$ . Here, four forced period-1 solutions co-exist out of which only two are stable ( $Su_2HP_1$  and  $Su_1HP_1$ ) and two are unstable. The superharmonic branch for larger excitations, eventually joins the main branch of the in-contact response via the saddle-node at  $\bar{\Omega} = 2.83$ . In addition, the  $Su_1HP_1$  branch is destabilized over narrow frequency

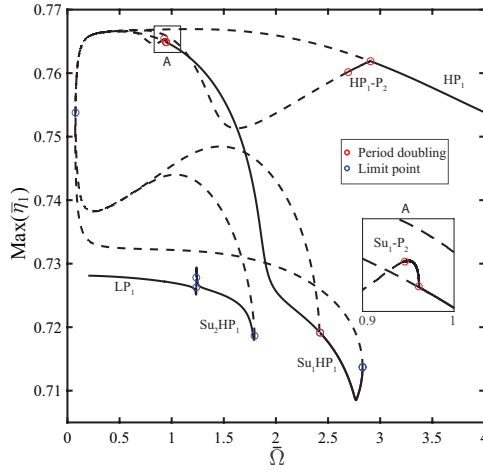


Figure 2.5: Frequency response curve of the in-contact attractor for fixed parameter values  $\bar{\gamma} = 0.020$  and  $R = 150$  nm. Continuous and dotted lines indicate stable and unstable branches of the solution, respectively. Red and blue circles indicate period-doubling and saddle-node bifurcation points, respectively.

ranges,  $\bar{\Omega} \in \{0.92, 0.95\}$  and  $\bar{\Omega} \in \{2.41, 2.42\}$ , by the occurrence of period-doubling bifurcations.

It is observed in Fig. 2.5 that, the low-frequency period-doubling point ( $\bar{\Omega} = 0.94$ ) has a stable period-2 solution over a short frequency range (see zoomed part of the figure) and the high-frequency period-doubling ( $\bar{\Omega} = 2.42$ ) presents mostly an unstable bifurcated period-2 solution except for few initial continuation points that are stable. These few stable points are not shown in the frequency response curves but are described in the bifurcation maps. In an analogous way, a period-doubling bifurcation at  $\bar{\Omega} = 2.90$  is observed on the  $HP_1$  branch having a stable period-2 solution limited in frequency range  $\bar{\Omega} \in \{2.7, 2.9\}$ . Moreover, period-doubling cascades are present in both stable period-2 solutions arising from  $Su_1HP_1$  and  $HP_1$  branches. This period-doubling cascade can lead to chaos in a similar fashion as encountered in standard TM-AFM systems [91].

### 2.2.3. BIFURCATION CHART, RESPONSE SCENARIOS AND ESCAPE THRESHOLD

Figures 2.6 and 2.7 provide an overview of the various bifurcation scenarios and escape thresholds occurring for a wide range of excitation amplitudes and frequencies. In these figures, local bifurcation envelope (loci) are constructed by following the variation of the bifurcation point (saddle-node or period-doubling) with respect to operating parameters, namely  $\bar{\Omega}$  and  $\bar{\gamma}$ . Furthermore, by assembling all the local bifurcation envelopes together, the global response and behaviour map of the entire system in the excitation amplitude and frequency control space is obtained. The bifurcation map has been obtained numerically for the in-contact attractor over a wide range of frequencies which includes the fundamental ( $\bar{\Omega}_0$ ) and principal parametric resonances ( $2\bar{\Omega}_0$ ). Thus, it is convenient to analyse the global dynamics by dividing the bifurcation map into two

Table 2.2: Bifurcation envelope data

Envelope name	Envelope color	Description
$USN_1/LSN_1$	Blue	Upper/lower saddle-node bifurcation loci belonging to the main solution branch.
$Su_1-USN_1/Su_1-LSN_1$	Blue	Upper/lower saddle-node bifurcation loci belonging to the first superharmonic solution branch.
$Su_2-USN_1/Su_2-LSN_1$	Blue	Upper/lower saddle-node bifurcation loci belonging to the second superharmonic solution branch.
$SN_2$	Blue	Saddle-node bifurcation loci belonging to the period-2 solution of the principal parametric resonance.
$Pa-SBF/Pa-SPF$	Red	Subcritical/supercritical flip bifurcation loci emerging from the principal parametric resonance.
$Su_1-SBF/Su_1-SPF$	Red	Subcritical/supercritical flip bifurcation loci emerging from the first superharmonic solution branch.
$Pa-SPF_2$	Green	Supercritical flip bifurcation loci emerging from the period-2 response of the principal parametric resonance.
$Su_1-SPF_2$	Green	Supercritical flip bifurcation loci emerging from the first superharmonic branch with period-2 response.

separate regions: the first region focuses around the fundamental resonance frequency  $\bar{\Omega}_0 = 3.72$  illustrated in Fig. 2.6, whereas the second region analyses the principal parametric resonance frequency  $\bar{\Omega}_0 = 7.44$  as shown in Fig. 2.7. In addition, Table 2.2 outlines the data concerning the various bifurcation envelopes of Fig. 2.6 and 2.7. Furthermore, Table 2.3 summarizes the various dynamic regions formed by these envelopes and the corresponding solutions involved. From an experimental perspective the response scenario map provides qualitative information on the form of cantilever response expected for the chosen set of excitation amplitude and excitation frequency.

#### ANALYSIS OF THE BIFURCATION MAP AROUND THE FUNDAMENTAL RESONANCE

Around the fundamental resonance frequency of the in-contact attractor, the dynamics is more involved than in the case of the attractive region [85]. The period-doubling/flip bifurcations appear not only on the main branch of the solution ( $HP_1$  branch in Fig. 2.5), but also on the first superharmonic branch ( $Su_1HP_1$  branch in Fig. 2.5). This drastically increases the possibility of global escape through crisis and also chaotic behaviour through period-doubling cascade. In an analogous way the saddle-node bifurcations that arise from the superharmonic branch increase the complexity of the response.

Figure 2.6 reports all the possible regions of motions for the cantilever in the range of

Table 2.3: Correlation data between the dynamic regions and corresponding solutions.

Dynamic region	Solution	Description
R1	$LP_1$	Low-amplitude non-resonant period-1 response from the main solution branch.
R2	$Su_1HP_1 + HP_1$	High-amplitude period-1 solution arising from the first superharmonic branch and High-amplitude resonant period-1 response arising from main solution branch.
R3	$HP_1-P_2$	Period-2 response arising from the resonant high-amplitude solution.
R4	$Su_1-P_2 + Su_1HP_1$	Period-2 solution together with high-amplitude period-1 solution arising from the first superharmonic branch.
R5	$LP_1 + Su_1HP_1$	Low-amplitude period-1 response belonging to the main solution branch together with high-amplitude period-1 solution arising from the first superharmonic branch.
R6	$Su_1HP_1$	High-amplitude period-1 solution arising from the first superharmonic branch.
R7	$LP_1 + Su_1HP_1 + Su_2HP_1$	Low-amplitude period-1 response together with high-amplitude period-1 solution arising from the first and second superharmonic branches, respectively.
R8	$Su_1-P_2$	Period-2 solution arising from the first superharmonic branch.
R9	$HP_1$	High-amplitude resonant period-1 response arising from main solution branch.
R10	$Su_1HP_1 + HP_1 + Pa-P_2$	High-amplitude period-1 solution arising from the first superharmonic branch, High-amplitude resonant period-1 solution and period-2 response from the principal parametric resonance solution.
R11	Escape region	period-doubling cascades and existence of strange attractors
R12	$HP_1 + Pa-P_2$	High-amplitude resonant period-1 solution and period-2 response from the principal parametric resonance solution.
R13	$Pa-P_2$	Period-2 response from the principal parametric resonance solution.
R14	$HP_1$	High-amplitude resonant period-1 response arising from main solution branch.



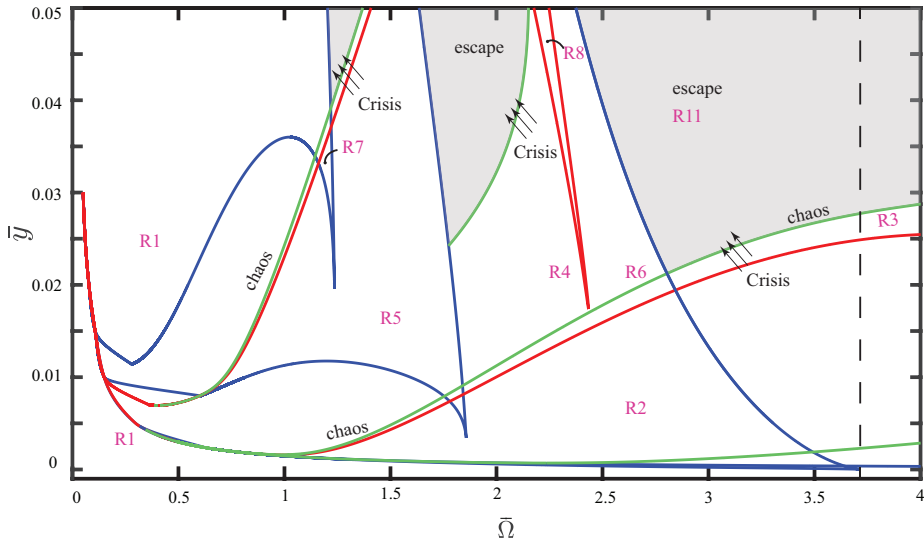









Figure 2.6: In-contact attractor bifurcation and response chart focussing on the region below the primary resonance frequency ( $\bar{\Omega}_0 = 3.721$  indicated by the vertical dashed line). Blue lines are the saddle-node bifurcation loci on period-1 solution branches, red lines are the period-doubling/flip bifurcation loci on period-1 solution branches, green lines are the period-doubling/flip bifurcation loci on period-2 solution branches. The details on individual bifurcation envelope description and the corresponding solution regions are summarized in Table 2.2 and Table 2.3, respectively.

Table 2.4: Correlation data between the basin colors and corresponding attractors.

Basin color	Attractor/Solution branch	Basin color	Attractor/Solution branch
	A-LP <sub>1</sub>		A-HP <sub>1</sub>
	Repulsive solution		LP <sub>1</sub>
	Su <sub>1</sub> -HP <sub>1</sub>		HP <sub>1</sub>
	A-Pa-P <sub>2</sub> and Pa-P <sub>2</sub>		

frequencies surrounding the fundamental resonance. The different regions are named with pink labels and accordingly numbered. For both low-amplitude excitations and frequencies up to  $\bar{y} = 0.004$  and  $\bar{\Omega} < 1.85$ , there exists only the LP<sub>1</sub> motion indicated by region R1 in Fig. 2.6. Hereafter, with increase in  $\bar{\Omega} \geq 1.85$ , the response consists of both the HP<sub>1</sub> and superharmonic high-amplitude (Su<sub>1</sub>HP<sub>1</sub>) solutions bound by loci HP<sub>1</sub>-SPF as shown in the region R2 of Fig. 2.6. Moving to even larger values of excitation frequency, the solution HP<sub>1</sub> governs the behaviour of the system (R9). Similarly, in addition to the discussion of aforementioned regions, the presence of other response scenarios

and dynamic regions data is tabulated in Table 2.3. Moreover, in contrast to the various stable responses seen in Fig. 2.6, the bifurcation analysis of in-contact attractor shows the presence of multiple strange attractors leading to crisis scenarios and global escape. The operating parameters leading to escape are depicted by grey regions (R11) in Fig. 2.6. The crisis scenario also highlights appearance of several rare attractors (period-5 and above) along with period-doubling cascades, which lead the solution to escape from the local potential well.

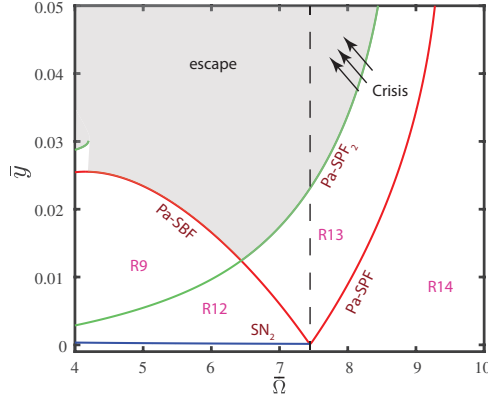


Figure 2.7: In-contact attractor bifurcation and response map focussing on the region near the neighbourhood of parametric resonance frequency ( $2\bar{\Omega}_0 = 7.44$  indicated by the vertical dashed line). The details on individual bifurcation envelope description and the corresponding solution regions are summarized in Table 2.2 and Table 2.3, respectively.

#### ANALYSIS OF THE BIFURCATION MAP AROUND THE PRINCIPAL PARAMETRIC RESONANCE

Figure 2.7 shows that, below the parametric resonance frequency,  $\bar{\Omega} < 7.44$ , only  $HP_1$  solution exists (R9) until the  $Pa-P_2$  solution from the parametric resonance ( $2\bar{\Omega}_0=7.44$ ) overlaps with the region R9 resulting in two co-existing period-1 ( $HP_1$ ) and period-2 ( $Pa-P_2$ ) responses as shown in region R12. In between the classic parametric instability tongue (V-shaped region near  $\bar{\Omega} = 7.44$ ) formed by the parametric subcritical (Pa-SBF) and supercritical (Pa-SPF) bifurcations, the  $HP_1$  solution becomes unstable and there exists only period-2 ( $Pa-P_2$ ) solution (R13). As expected in any of the archetypal parametric oscillators, the system requires a minimum excitation threshold to achieve parametric resonance. This is indicated by the lifting of the instability tongue (V-shaped region) along the  $\bar{y}$  axis and in our system the critical threshold is at  $\bar{y} = 0.00014$ . Finally, for excitation frequency  $\bar{\Omega} > 7.44$ , only  $HP_1$  solution is present as shown in region R14.

### 2.3. DYNAMICAL INTEGRITY AND ROBUSTNESS OF ATTRACTORS

In the previous section, we provided insight into diverse solutions and bifurcation scenarios including escape thresholds. However, the analysis did not furnish details on the various instability paths and eventual escape of the steady state solutions. The informa-

tion on the instability path (escape from local potential well, cross-well chaos) taken by the cantilever response is of utmost importance in practical applications of AFM. This helps to disentangle image artefacts from factual data.

From an experimental perspective, if the system perturbations can be quantized then basins of attraction provide insight into the evolution of various steady state responses (system attractors) and instabilities (erosion profiles) occurring in the system. Furthermore, measures of the basin portraits, the dynamical integrity of the system, are able to quantify the robustness of different attractors. This can be realized through various scalar integrity measures [92]. These integrity measures provide information on the strength of such quantized perturbations required to destabilize the corresponding system response. Therefore, basin portraits together with integrity measures provide a means to track the basin erosion process with respect to changes in operating parameters. Hence, in order to advance the dynamical analysis of the AFM cantilever in the in-contact regime of oscillation, this section focuses on the global topology analysis by means of basins of attraction [93, 94].

There have been multiple integrity measures introduced in the literature [95] and this section makes use of two integrity indicators to measure the evolution of phase-space topology, namely Local Integrity Measures (LIM) [92] and Integrity Factor [96] (IF). The LIM is defined as the normalized radius of the largest hypersphere (circle in 2D), centered on the safe attractor and entirely belonging to the safe basin. It is used to analyse the robustness of the attractor of interest against perturbations. On the other hand, the IF is defined as the normalized radius of the largest circle entirely belonging to the compact part of safe basin. The IF is suitable to study the dynamical integrity of the attractors subject to perturbation around its initial equilibrium condition. The reason to choose these measures with respect to others such as Global Integrity Measures (GIM) relies on the fact that, IF and LIM can disentangle the fractality of basin since they focus only on its compact part [92]. In our case this is a serious advantage since, the homoclinic tangling of the saddle results in fractalization of the low-amplitude attractive regime basin.

### 2.3.1. BASIN PORTRAITS AND EVOLUTION AS A FUNCTION OF TIP RADIUS

One of the common causes for image artefacts during AFM scanning operation is the degradation of tip radius  $R$  due to repetitive impacts with the sample surface [97]. Furthermore, the correct and reliable operation of the AFM is dependent on the status of the probe tip, since it is responsible for resolving the topography of the sample [80]. The change in radius value during the aforementioned scanning operation thus causes a sensible variation in the system response and corresponding global integrity values. Therefore, in this section, we make an effort to elucidate the variation of system integrity via basin portraits by considering the AFM tip radius ( $R$ ) as the corresponding varying parameter.

Figure 2.8 outlines the variation of dynamical integrity of system attractors as a function of AFM cantilever tip radius  $R$ . The numerical simulations are performed for tip radius ranging from 105 nm to 225 nm in steps of 3 nm, with excitation frequency  $\bar{\Omega} = 0.85$  being close to resonance, and excitation amplitude  $\bar{y} = 0.005$ . Figure 2.8(a)-(c) report the integrity variation trend as a function of tip radius and Fig. 2.8(d)-(f) reveal the snapshot of basin portrait at several crucial radius values, namely 114 nm, 117 nm, and 197 nm,

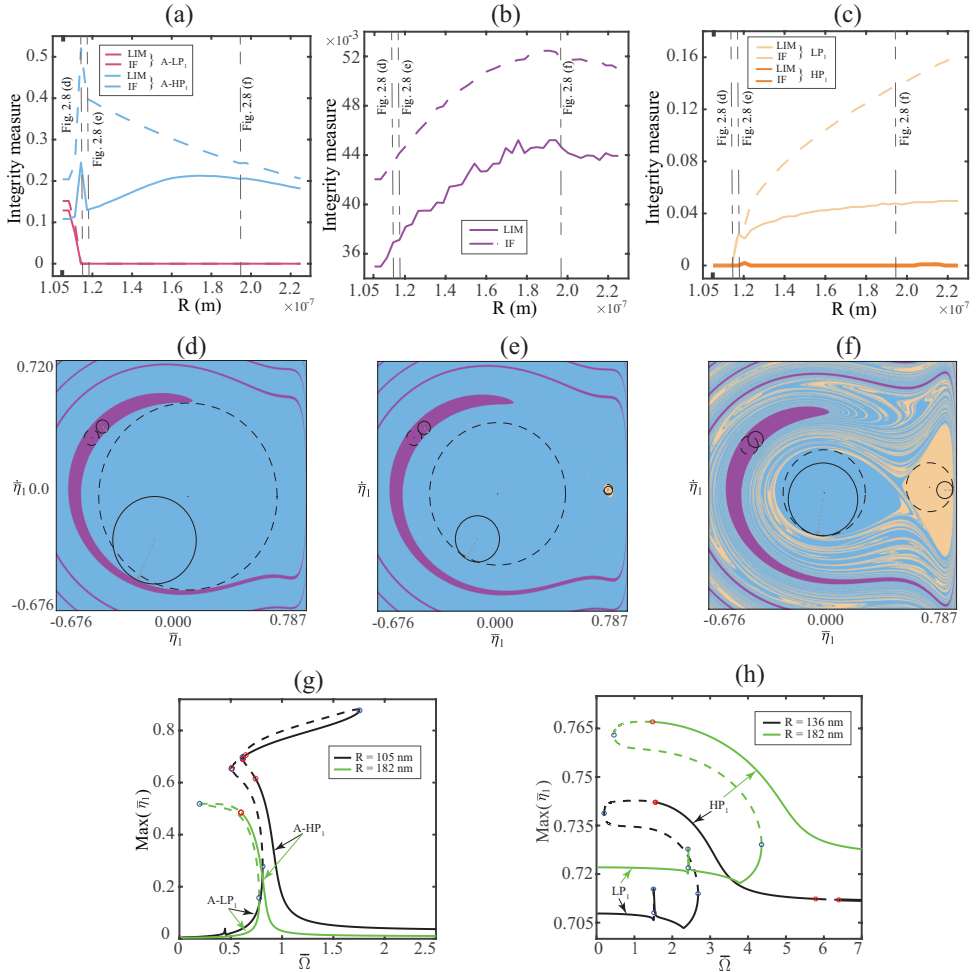


Figure 2.8: Variation of integrity measures (LIM, IF), basin portraits and frequency response curves as a function of tip radius ( $R$ ), for fixed parameter values of  $\bar{\gamma} = 0.005$  and  $\bar{\Omega} = 0.85$ . (a) Integrity profiles of the attractive region containing non-resonant low-amplitude (crimson) and resonant high-amplitude solution (blue) attractors. (b) Integrity profiles of repulsive region attractor. (c) Integrity profiles of the in-contact region consisting of non-resonant low-amplitude (light brown) and resonant high-amplitude solution (orange) attractors. The continuous and dotted lines indicate the LIM, IF integrity measures respectively. (d)-(f) show the basin portraits at specific radius values of 114 nm, 117 nm, and 197 nm, respectively. The details on basin color and the corresponding attractor/solution description is given in Table 2.4. (g) Frequency response of microcantilever with radius  $R = 105$  nm and  $R = 182$  nm oscillating with initial condition in attractive region. (h) Frequency response of microcantilever with radius  $R = 136$  nm and  $R = 182$  nm oscillating with initial condition in the in-contact region.

respectively. The continuous and dotted lines in Fig.2.8(a)-(c) belong to LIM and IF measures, respectively.

It is observed in Fig. 2.8(a) that in the attractive regime around the radius value  $R = 114$  nm, there is a sharp increase in the high-amplitude resonant solution (shown in

Fig. 2.8(g) as A-HP<sub>1</sub>) and the integrity of low-amplitude non-resonant solution (shown in Fig. 2.8(g) as A-LP<sub>1</sub>) rapidly decreases to zero, indicating the complete erosion of its basin from the system. This phenomenon is observed in the basin portrait of Fig. 2.8(d), where the blue basin representing A-HP<sub>1</sub> solution completely dominates the attractive region. Physically, the disappearance of A-LP<sub>1</sub> solution marks the transition from a bi-stable to a monostable cantilever response in the attractive regime. Interestingly, in Fig. 2.8(a), by considering an even blunter tip, with radius in the range of  $R \in \{114, 117\}$ nm, the robustness of A-HP<sub>1</sub> suddenly drops, due to the appearance of a novel competing attractor in the system. The new attractor is indicated by the light brown basin in Fig. 2.8(e). This novel attractor, which is the in-contact attractor, has a smaller growth rate at lower radius values and does not affect the erosion of the A-HP<sub>1</sub> solution rapidly. This is observed in Fig. 2.8(a) by a steady increase in the integrity measure of A-HP<sub>1</sub> solution between radius values  $R \in \{117, 185\}$ nm. With further increase in the blunting of the tip, the A-HP<sub>1</sub> basin is eroded along its boundaries smoothly by the in-contact attractor as seen in Fig. 2.8(f). The robustness characteristics shown by LIM and IF measures for attractive regime follow similar trend. However, the IF safe basin measure is larger in magnitude compared to LIM which is due to the smooth erosion of the basin without in-well fractality at low excitation amplitudes ( $\bar{\gamma} < 0.015$ ).

The repulsive attractor unlike attractive, shows a steady growth in basin size for increasing radius values as shown in Fig. 2.8(b). This trend of increasing basin size is due to the fact that, an increase in radius value will increase the area over which repulsive forces are perceived by the system. However, it is worth to observe in Fig. 2.8(d)-(f) that, the size of the purple basin (Strength of integrity measure) associated with repulsive attractor is very small compared to the attractive and the in-contact regimes. Thus, at low  $\bar{\gamma}$ , the repulsive attractor although resilient to changes in radius, has a smaller influence on the basin erosion process as compared to other two attractors. Moreover at low radius values, a perturbation inside the attractive regime (blue basin) can lead the system towards the repulsive attractor leading to hardening behaviour as illustrated in Fig. 2.8(g). In this case, for a cantilever oscillating initially in the attractive region, the system frequency response shows both softening due to attractive forces and hardening due to repulsive forces as shown in Fig. 2.8(g) (black frequency response curve). However with a further increase in radius values, the attractive and repulsive basins are separated and the system oscillates purely in attractive regime showing only softening nonlinearity (green frequency response curve in Fig. 2.8(g)).

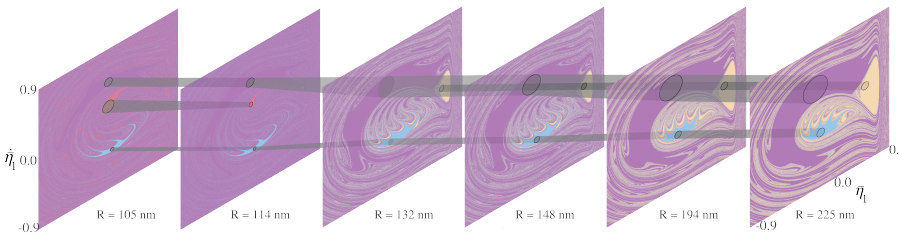


Figure 2.9: Phase-space topology evolution with respect to tip radius ( $R$ ) from 105 nm to 225 nm, at fixed excitation amplitude and frequency of  $\bar{\gamma} = 0.020$ ,  $\bar{\Omega} = 0.8$ , respectively.

The robustness characteristics displayed by the in-contact attractor in Fig. 2.8(c) are unique and present features not observed in the other two attractors. For low radius values, e.g.  $R < 117$  nm, the in-contact attractor does not exist as seen in Fig. 2.8(c) and further illustrated by the absence of light brown basin in Fig. 2.8(d). This highlights the existence of a critical radius value for the manifestation of the in-contact attractor. This critical radius value for our system is at  $R = 117$  nm. Around this radius value, there is a sudden appearance of the in-contact attractor (shown in Fig. 2.8(e) as light brown basin) and it grows steadily with the increase in the value of  $R$ . Interestingly, the critical radius value remains the same for higher excitation amplitudes and excitation frequencies. Furthermore, from Fig. 2.8(c) it is observed that, the growth rate of low-amplitude solution ( $LP_1$ ) is not as steep as the attractive and repulsive attractors, but at large radii, the in-contact attractor eventually becomes dominant with no in-well fractality or boundary erosion.

Figure 2.9 illustrates the evolution of the basin portrait with respect to the tip radius. The LIM integrity measure is utilized to characterize the robustness of the attractors and track the changes in the basin portraits as the tip deteriorates. The basin portraits are analysed for constant parameters  $\bar{y} = 0.020$  and  $\bar{\Omega} = 0.8$ . The figure reinforces the previous discussion pictorially. It depicts the disappearance of A- $LP_1$  basin, fractalization of the attractive regime triggering the erosion process and finally, the requirement of critical radius for manifestation of the in-contact attractor.

### 2.3.2. BASIN EROSION AS A FUNCTION OF EXCITATION FREQUENCY AND EXCITATION AMPLITUDE

In section 2.3.1, the evolution of phase space topology as a function of radius was showcased. Accordingly, in this section the dynamical integrity analysis aims at quantifying the extent and evolution of the basins along with their erosion process as a function of the excitation amplitude ( $\bar{y}$ ) and excitation frequency ( $\bar{\Omega}$ ). This is established in Fig. 2.10 for excitation amplitudes  $\bar{y} = 0.005$ ,  $\bar{y} = 0.010$  and  $\bar{y} = 0.020$ , respectively. Whereas, Fig. 2.11 and Fig. 2.12 report the snapshots of basin portraits at crucial excitation frequencies ( $\bar{\Omega}$ ) near the neighbourhood of fundamental and principal parametric resonance frequencies, respectively.

All simulations are performed at a constant radius value of  $R = 150$  nm and finally, LIM and IF measures are calculated for the aforementioned data. However, we observed that the strength of LIM and IF measure as a function of  $\bar{\Omega}$  remain approximately the same. Thus, we can argue that the excitation frequency in the selected interval, does not modify the global shape of the portrait and we do not experience a significant subdivision of the basin. Therefore, in order to simplify the analysis, only LIM is used to quantify the robustness of dominant attractors present in the system.

#### ANALYSIS OF BASIN EROSION PROFILES AROUND THE FUNDAMENTAL RESONANCE FREQUENCY

The fundamental ideology of TM-AFM is based on the near resonant excitation of the microcantilever. Therefore, it is of significant interest to study the system topology with regard to basin erosion profiles since, these profiles are indicative of solution instabilities. In this respect, the following section utilizes the integrity measures shown in Fig.

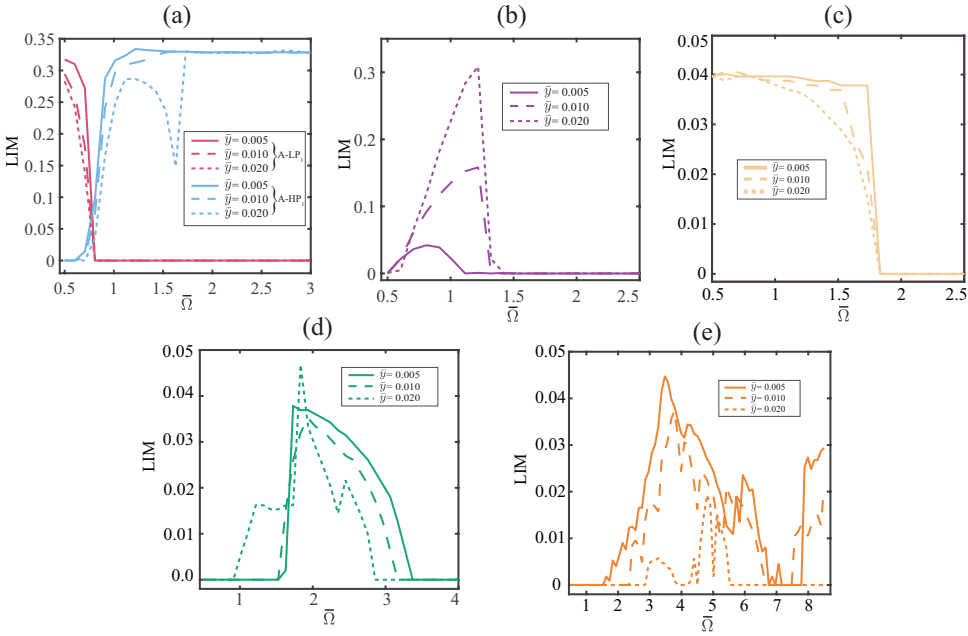


Figure 2.10: Variation of LIM as a function of excitation frequency ( $\bar{\Omega}$ ) for fixed parameter values of  $\bar{y} = 0.005$ ,  $\bar{y} = 0.010$ ,  $\bar{y} = 0.020$  and  $R = 150$  nm. (a) Integrity profiles for the attractive region consisting of non-resonant low-amplitude (crimson) and resonant high-amplitude branch attractors (blue). (b) Integrity profiles for repulsive region attractor (purple). (c) Integrity profiles for the non-resonant low-amplitude (light brown) attractor in the in-contact region. (d) Integrity profiles for the first superharmonic branch attractor in the in-contact region. (e) Integrity profiles for the resonant high-amplitude branch (orange) attractor in the in-contact region.

2.10 to discuss the various system attractors in the neighbourhood of their respective resonance frequencies. In addition, to further delineate the behaviours observed in the integrity profiles, the basin portraits are reported in Fig. 2.11 at specific frequencies.

The integrity profiles of attractive regime attractors are illustrated in Fig. 2.10(a) and, similar to section 2.3.1, the crimson and blue colors belong to the low-amplitude non-resonant solution (A-LP<sub>1</sub>) and the high-amplitude resonant solution (A-HP<sub>1</sub>), respectively. Figure 2.10(a) shows that, the attractive regime is dominated by A-LP<sub>1</sub> non-resonant solution at low excitation frequencies  $\bar{\Omega} < 0.77$ . This is illustrated through the basin portrait of Fig. 2.11(a) in which the crimson basin corresponding to A-LP<sub>1</sub> is the dominant solution. By further increasing the excitation frequency value above  $\bar{\Omega} > 0.77$ , the A-LP<sub>1</sub> solution exhibits a sharp decrease in its integrity value (illustrated in Fig. 2.10(a)). The sharp decline is attributed to the sudden appearance of the A-HP<sub>1</sub> resonant attractor from inside the local potential well via saddle-node bifurcation. The appearance of saddle-node triggers the erosion process of the A-LP<sub>1</sub> basin from outside its boundaries. The appearance of A-HP<sub>1</sub> (blue basin) inside the A-LP<sub>1</sub> local potential well (crimson basin) is shown in Fig. 2.11(b). Any further increment in excitation frequency causes the complete erosion of the low-amplitude attractive (A-LP<sub>1</sub>) solution as seen in Fig. 2.11(c), leaving large amplitude oscillations of A-HP<sub>1</sub> as the dominant solu-



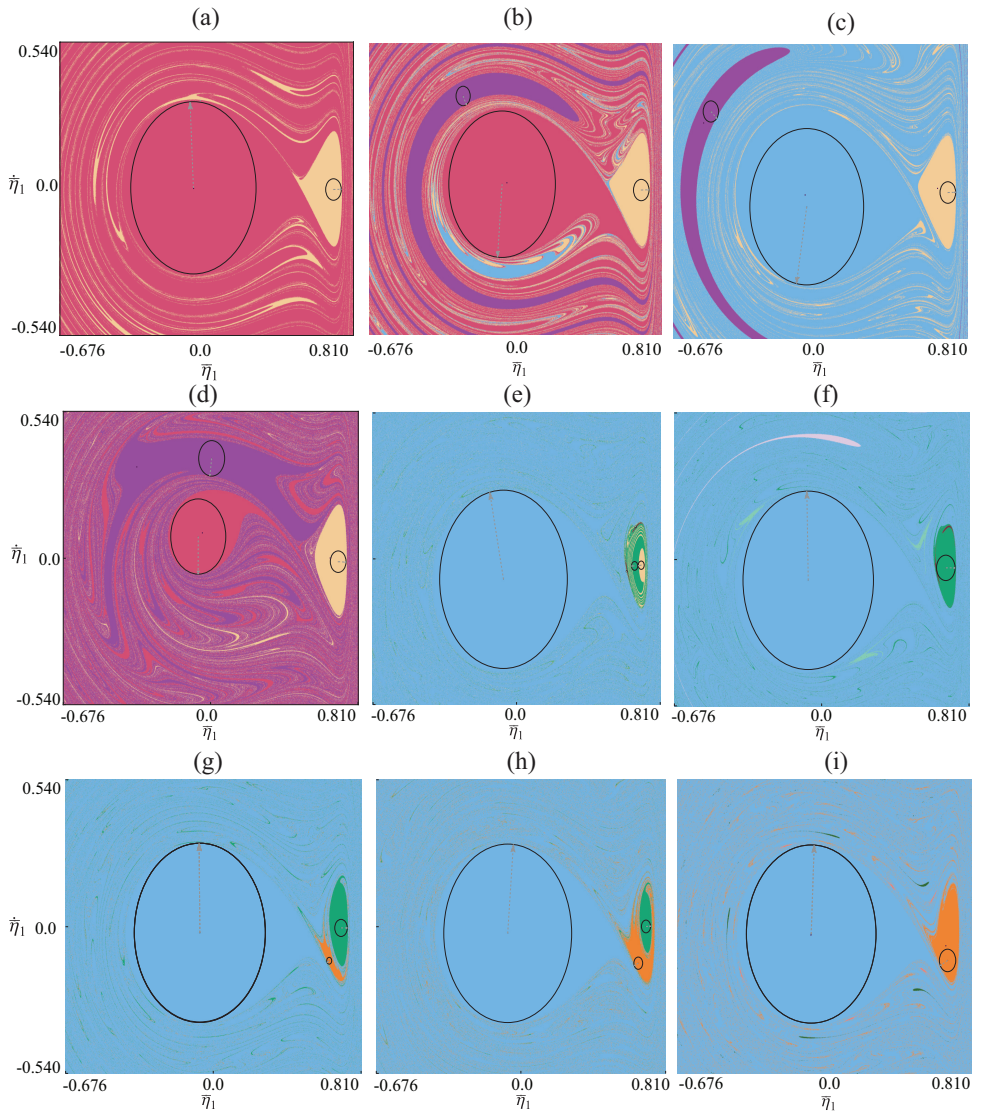


Figure 2.11: Variation of basin portraits as a function of excitation frequency ( $\bar{\Omega}$ ) for fixed parameter values of  $\bar{y} = 0.005$ ,  $\bar{y} = 0.020$ , and  $R = 150$  nm. The analysis is focussed around the fundamental resonance frequencies of respective system attractors. The circle inside the basin portrait indicates the LIM. (a)-(c) basins portraits at  $\bar{y} = 0.005$  and specific  $\bar{\Omega}$  values of 0.6, 0.8, 0.9, respectively. (d)-(f) basins portraits at  $\bar{y} = 0.020$  and specific  $\bar{\Omega}$  values of 0.7, 1.8, 1.9, respectively. (g)-(i) basins portraits at  $\bar{y} = 0.005$  and specific  $\bar{\Omega}$  values of 2.5, 2.9, 3.4, respectively. The details on basin color and the corresponding attractor/solution description is given in Table 2.4.

tion in the attractive potential well. Hereafter, the A-HP<sub>1</sub> solution remains largely stable as illustrated in Fig. 2.10(a) and its robustness is mainly affected when the excitation



frequency reaches the in-contact fundamental resonance or when the system is driven with an excitation amplitude above the parametric threshold of the system. This trend of solution instabilities observed around the fundamental resonance frequency remains unaffected irrespective of excitation amplitudes.

Contrary to the above discussion on attractive regime, where steady state solutions exist over a large range of frequencies; the repulsive basin (purple) exists in a narrow frequency range around the fundamental resonance frequency and shows sharp increase/decrease as we move closer/farther away from resonance. This is illustrated in Fig. 2.10(b) for  $\bar{y} = 0.005$ ,  $\bar{y} = 0.010$  and  $\bar{y} = 0.020$ , respectively. Moreover, the repulsive basin size is small compared to other two attractors in case of  $\bar{y} = 0.005$  as shown in Fig. 2.11(c). But displays a sharp increase in size for higher values of  $\bar{y}$  as seen in Fig. 2.11(d) for  $\bar{y} = 0.020$ . This is due to the fact that, the harder the cantilever is driven, the deeper the oscillations penetrate into the repulsive regime, and the time period of oscillations spent in repulsive regime increases. Therefore, contrary to the observation in section 2.3.1, the repulsive basin at higher excitation amplitudes significantly constricts the attractive regime basin in the neighbourhood of the fundamental resonance frequency.

On the other hand, the in-contact regime solution displays rich nonlinear behaviour absent in the case of the attractive and repulsive regimes. Figure. 2.10(c)-(e) illustrates the integrity profiles of various solution branches namely  $LP_1$ ,  $Su_1HP_1$ , and  $HP_1$  that are observed in the in-contact regime. Similar to section 2.3.1 and summarized in Table 2.4, the light brown color corresponds to non-resonant  $LP_1$  solution branch, the green color belongs to  $Su_1HP_1$  solution branch and orange color belongs to  $HP_1$  resonant solution branch. The appearance and disappearance of several rare attractors, together with period-2 responses appearing not only on  $HP_1$  solution branch but also on  $Su_1HP_1$  superharmonic solution causes the robustness of in-contact attractor to vary rapidly. This behaviour can be observed in the integrity profiles of Fig. 2.10(d) and (e) in the form of sharp peaks and valleys as the excitation amplitude is increased.

At low excitation frequencies  $\bar{\Omega} < 1.5$ , the in-contact basin is dominated by  $LP_1$  solution as shown in Fig. 2.10(c). This is further demonstrated in the basin portrait of Fig. 2.11(a) where only the light brown basin dominates the in-contact region. Further increasing  $\bar{\Omega} > 1.5$ , we observe the drop in integrity of  $LP_1$  solution due to the appearance of  $Su_1HP_1$  attractor. This is visualized by comparing the Figs. 2.10(c) and (d) between frequency ranges  $\bar{\Omega} \in \{1, 2\}$ . The drop in integrity is sharp for small values of  $\bar{y}$  and slowly smoothens with increasing  $\bar{y}$  amplitudes. This effect is due to the increased softening effect of the in-contact response which causes the  $Su_1HP_1$  branch to overlap with  $LP_1$  branch over larger  $\bar{\Omega}$  values. Along with the increased overlapping effect, at higher amplitudes of excitation  $\bar{y} > 0.00118$ , the  $Su_1HP_1$  solution grows more robust. The appearance of  $Su_1HP_1$  attractor (green basin) from within the  $LP_1$  basin for  $\bar{y} = 0.020$  is shown in Fig. 2.11(e) and (f).

Furthermore, with  $\bar{\Omega}$  growing closer to resonance (i.e.  $\bar{\Omega} = 3.72$ ), the high-amplitude resonant solution ( $HP_1$ ) appears via saddle-node bifurcation and grows in dominance as depicted in Fig. 2.10(e). In a similar fashion to the attractive regime, the saddle-node triggers the erosion of the previously dominant  $Su_1HP_1$  solution from outside the boundary. This is observed in basin portraits from Fig. 2.11(g)-(i) where, the orange basin belonging to  $HP_1$  solution is growing along the periphery of green basin. Interest-

ingly, at low-amplitudes of excitation,  $\bar{y} < 0.010$  the erosion of  $Su_1HP_1$  basin is smooth with no influence of rare attractors on its robustness. After the complete erosion of  $Su_1HP_1$  basin (see Fig. 2.11(i)), the in-contact response is completely dominated by  $HP_1$  solution until  $\bar{\Omega}$  reaches close to parametric resonance frequency. This is illustrated by the gradual drop in robustness measure in Fig. 2.10(e) for values of  $\bar{\Omega} > 3.7$ . The increase in  $\bar{y}$  has a peculiar effect on the  $HP_1$  solution since the robustness decreases in contrast to the expected increasing trend. This is due to the large number of rare attractors which tend to appear at higher excitation amplitudes. This peculiarity makes the experimental investigation of the in-contact attractor a challenging task.

#### ANALYSIS OF BASIN EROSION PROFILES AROUND THE PRINCIPAL PARAMETRIC RESONANCE FREQUENCY

The aforementioned discussion was focussed on the robustness and erosion profiles of system attractors for excitation amplitudes below the parametric threshold and excitation frequencies around the fundamental resonance. However, the system excited parametrically exhibits different dynamics that are not observed through direct excitation. In addition, the theoretical analysis of parametrically driven AFM has shown the added benefits such as high quality factor, lower imaging forces and reduced cantilever transients [98]. These advantages, if harnessed, can be of significant interest in areas such as soft polymers and biological specimens. Therefore, the current section focuses on the basin erosion profiles of system attractors in the neighbourhood of respective principal parametric resonance frequencies. Similar to the previous section, the analysis utilizes integrity measures illustrated in Fig. 2.10 to discuss the evolution of system responses. Whereas, Fig. 2.12 is used to understand the metamorphoses of basin erosion graphically.

Considering the attractive force regime, an excitation amplitude of  $\bar{y} = 0.020$  is utilized to study the robustness of attractors oscillating near the parametric resonance frequency. The chosen excitation amplitude is above the required threshold amplitude of  $\bar{y} = 0.01515$  needed to excite the system parametrically. The solution belonging to  $\bar{y} = 0.020$  case are drawn by dotted lines in Fig. 2.10(a). From Fig. 2.10(a) there is a sudden decline in the A- $HP_1$  attractor's integrity value around the parametric resonance frequency of  $\bar{\Omega} \in \{1.4, 1.75\}$ . This sudden decrease in robustness is promoted by the appearance of period-2 attractor (A-Pa- $P_2$ ) within the compact part of A- $HP_1$  basin. This is illustrated in the basin portraits of Fig. 2.12(a)-(c), where the A-Pa- $P_2$  attractors shown by dark red basin are surrounding the A- $HP_1$  blue basin. The rate of erosion of A- $HP_1$  basin is directly proportional to the nearness of  $\bar{\Omega}$  to the principal parametric resonance frequency. For values of  $\bar{\Omega}$  away from the parametric resonance the A- $HP_1$  integrity shows a steady increase back to its original value. Hereafter, the A- $HP_1$  solution remains almost independent of  $\bar{\Omega}$  until the in-contact resonance frequency is reached.

In case of the in-contact regime, the parametric threshold amplitude is found to be as low as  $\bar{y} = 0.00014$ . The low threshold amplitude also suggests the potential application of stochastic resonance of cantilever oscillating in the in-contact regime. However, in order to facilitate the study, an excitation amplitude of  $\bar{y} = 0.005$  is utilized. The corresponding integrity profile is illustrated in Fig. 2.10(e) by the continuous line and relative basin portraits are shown in Fig. 2.12(d)-(e). By considering Fig. 2.10(e), the integrity

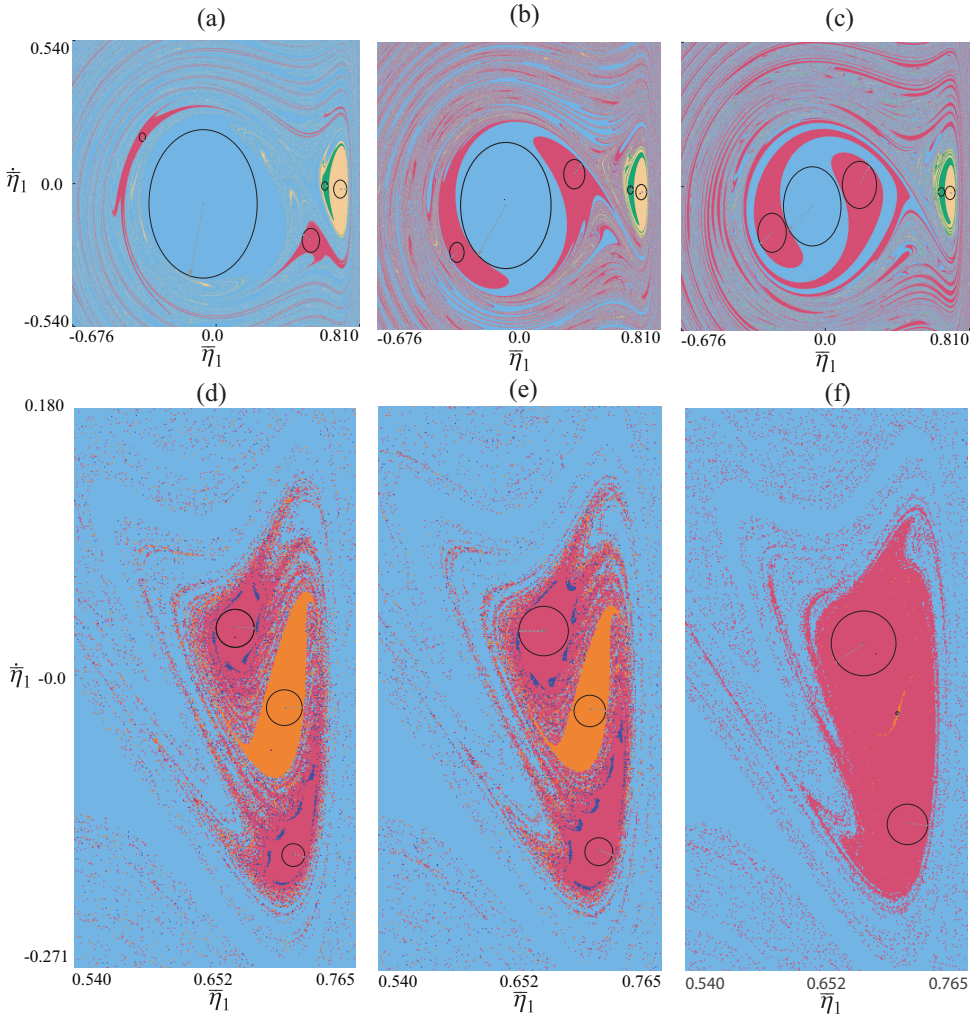


Figure 2.12: Variation of basin portraits as a function of excitation frequency ( $\bar{\Omega}$ ) for fixed parameter values of  $\bar{y} = 0.005$ ,  $\bar{y} = 0.020$ , and  $R = 150$  nm. The analysis is focussed around the principal parametric resonance frequencies of respective system attractors. The circle inside the basin portrait indicates the LIM. (a)-(c) basins portraits at  $\bar{y} = 0.020$  and specific  $\bar{\Omega}$  values of 1.4, 1.6, 1.7, respectively. (d)-(f) basins portraits at  $\bar{y} = 0.005$  and specific  $\bar{\Omega}$  values of 6.6, 6.7, 7.1, respectively. The details on basin color and the corresponding attractor/solution description is given in Table. 2.4.

measure of  $HP_1$  solution displays a steady decline as  $\bar{\Omega}$  is brought close to principal parametric resonance frequency ( $\Omega = 7.44$ ). Finally, around  $\bar{\Omega} = 7.1$  the  $HP_1$  basin completely disappears indicating that the system is in the parametric instability region. The appearance of parametric period-2 attractors ( $Pa-P_2$ ) in the basin portrait is indicated by the dark red basin in Fig. 2.12(d)-(e). The figures illustrates the appearance of period-2 attractors (dark red) from the compact part of  $HP_1$  basin (orange) along with period-6

rare attractors (dark blue). Finally, the erosion process of  $HP_1$  solution is non-smooth with the interacting basins featuring severe fractality.

## 2.4. CONCLUSIONS

The global dynamics of TM-AFM has been investigated with the aim of evaluating the robustness and dynamical integrity of co-existing attractors of the system. Extensive numerical analyses have been carried out to show the existence and the properties of the in-contact attractor. The frequency response curves and basin portraits are obtained showing that, the in-contact attractor is highly sensitive to the main driven parameters with large amplitude superharmonic branches appearing for small excitation amplitudes.

In order to unveil the entire bifurcation scenario of the in-contact attractor around the primary and parametric resonance, several local bifurcation envelopes are combined together to build global bifurcation maps. Utilizing the bifurcation maps, the escape thresholds along with various response scenarios in the excitation parameter space are analysed in detail around the direct and parametric resonance frequency. The outcome of the analysis shows new routes to crisis, escape scenarios via appearance of strange attractors and multiple period-doubling cascades.

Furthermore, the robustness of attractors has been analysed by making use of basins of attraction and integrity measures such as Local Integrity Measure (LIM) and Integrity Factor (IF). The analysis is focussed on the basin erosion with respect to variation in excitation frequency, excitation amplitude and the AFM probe tip radius. The results highlight the appearance of in-contact attractor for a critical radius value. Next, the parametric resonance and its effect on basin erosion via fractalization is discussed for both attractive and in-contact attractors. It is seen that the period-2 attractors arising from parametric resonance decrease the robustness of attractive regime in a smooth fashion. Whereas, in case of in-contact attractor the period-2 solution together with higher-order strange attractors, erodes the basin through fractalization. In conclusion, our analysis of basins of attraction, global bifurcation charts and integrity profiles provides a method to study the complex dynamics involved in TM-AFM.

3

3

# 3

## MODE COUPLING IN TAPPING MODE ATOMIC FORCE MICROSCOPY

*Enhancing the signal-to-noise ratio in dynamic AFM plays a key role in nanomechanical mapping of materials with atomic resolution. In this chapter, we develop an experimental procedure for boosting the sensitivity of higher harmonics of an AFM cantilever without modifying the cantilever geometry but instead by utilizing dynamical mode coupling between its flexural modes of vibration. We perform experiments on different cantilevers and samples and observe that via nonlinear resonance frequency tuning, we can obtain a frequency range where strong modal interactions lead up to 7 and 16 folds increase in the sensitivity of the 6<sup>th</sup> and 17<sup>th</sup> harmonic while reducing sample indentation. We derive a numerical model that captures the observed physics and confirms that nonlinear mode coupling can be held accountable for increasing the amplitude of higher harmonics during tip-sample interactions.*

Dynamic Atomic Force Microscopy (AFM) has emerged as a powerful tool for nanoscale imaging of matter in many technical and scientific application areas [58]. In dynamic AFM, an oscillating microcantilever tip interacts intermittently with the sample while being driven close to or at a resonance frequency. Dynamic AFM is routinely used to characterize the topography of samples with nanometer or even atomic resolution. Irrespective of the outstanding capabilities offered by this AFM mode, the understanding of nanoscale processes and quantification of material properties using AFM is yet far from being well-established. One curbing reason for this is that in the conventional dynamic AFM experiments a single drive frequency is used to scan the sample and the feedback system maintains either the amplitude or the phase of oscillations constant. As a result, the number of observable channels that are required to quantify the mechanical properties of the sample are not sufficient. To overcome this limitation, multi-frequency AFM techniques are being adopted [50]. These methods mainly use higher harmonics of the cantilever deflection signal [51, 52] or the output signals of two or three resonant modes [5, 100] to obtain complementary information of the interacting sample. Other modes of multi-frequency AFM are also available that use torsional harmonics [54] or intermodulation products [22] to probe sample properties.

To date, many studies have incorporated the aforementioned multi-frequency AFM techniques to map nanomechanical properties of samples, ranging from polymeric [59, 101] to biological substances [6, 102]. However, only a handful of these works have looked into the possibilities for enhancing the sensitivity of the higher order spectral components [53, 55–57, 103]. Among them, a majority have exploited a phenomenon known as internal resonance [104]. This condition occurs when the ratio between two or more resonance frequencies of the cantilever is a rational number, and results in strong coupling between the interacting modes of vibration [105]. The significance of intermodal coupling arises from its correlation with the effective spring constant of the resonant modes that can be tuned either by modifying the geometry of the cantilever [54, 55], or creating notches/ holes [56], or by adding concentrated mass at specific locations on the cantilever [57].

Here, in contrast to previous works, we propose a technique to boost the signal-to-noise ratio (SNR) of higher harmonics and higher order flexural mode of an AFM cantilever without the need to modify its geometry. By sweeping the drive frequency in the spectral neighborhood of a resonance, we find a frequency range where strong interactions between the first three flexural modes of the cantilever significantly increases the amplitude of higher harmonics. Using this technique, we are able to enhance the amplitude of the 6<sup>th</sup> and the 17<sup>th</sup> harmonic up to 7 and 16 folds, respectively. Interestingly, driving the cantilever in this frequency range also results in a decreased sample indentation due to the phase synchronization of the eigenmodes. These phenomena are showcased at drive amplitudes comparable to set point ratios used in conventional scanning operation, thereby highlighting the utility of the technique in dynamic AFM. To understand the physics behind our observations, we develop a theoretical model comprising Multiple-Degrees of Freedom (MDOF) and non-smooth nonlinear interactions between the tip and the sample. Our simulations qualitatively conform with the observed physics, and confirms that mode coupling is responsible for the increase in the SNR of higher harmonics. Our study also reveals the use of real-time temporal data for identifying dy-



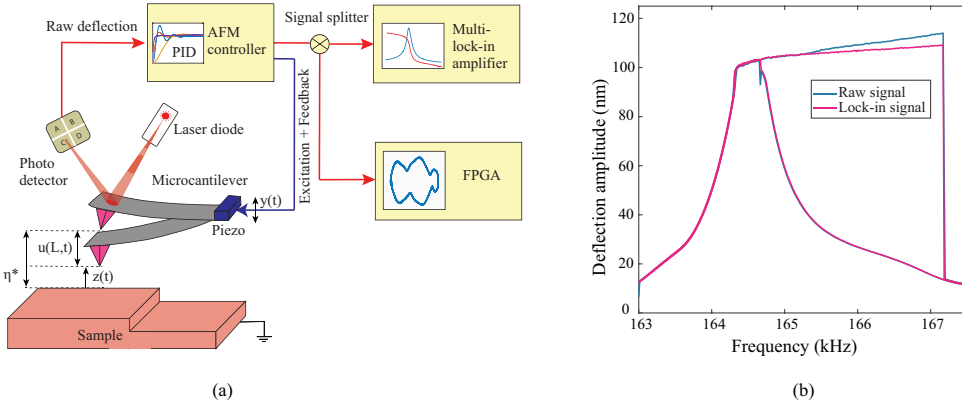


Figure 3.1: Schematic of the experimental setup and the acquired experimental nonlinear dynamic response. The response is obtained with a commercial rectangular cantilever (NCLR) on a Silicon sample with an excitation amplitude of 0.013 V. (a) The schematic of the setup employing two different data acquisition electronics, namely the multi-lock-in amplifier and an FPGA device. The schematic details the initial static cantilever configuration  $\eta^*$  and the dynamic configuration with the cantilever vibrating about the elastostatic equilibrium  $u$  at the free end  $L$  of the cantilever. (b) The blue and the pink curves indicate the nonlinear dynamic response obtained using the raw deflection signal and the lock-in signal. The forward and reverse sweeps are combined into one curve.

namical coupling in AFM applications. Because of its simplicity and ease of use, the proposed technique has the potential to be utilised in a variety of multi-frequency AFM techniques.

### 3.1. EXPERIMENTAL RESULTS

Our experiments are performed by using a commercial AFM (JPK Nanowizard) and two separate acquisition electronics, namely a multi-lock-in amplifier from Intermodulation products and a Field Programmable Gated Array (FPGA) from National Instruments, to collect and analyze the cantilever deflection data. We used a commercially available rectangular Silicon cantilever (NCLR, NanoWorld AG) and a flat Silicon sample to perform the experiments. For each experiment, the spring constant of the cantilever ( $k = 22.68 \text{ N m}^{-1}$ ), its resonance frequency ( $f_0 = 164.52 \text{ kHz}$ ), and quality factor ( $Q = 428$ ) are determined using the thermal calibration method [49]. A schematic of the setup is shown in Fig. 3.1(a).

In order to obtain the nonlinear resonance response of the AFM cantilever while interacting with the sample, we have implemented a procedure where a standard force-distance curve is first used to statically approach the sample surface with a small set point of 2 nm. Next, the end condition of the force-distance curve is preserved to hold the cantilever at the precise fixed distance of  $\eta^* = 100 \text{ nm}$  from the sample surface. The latter operation is feasible using the feedback loop on the z-piezo of the AFM, which stays active for a specific period of time. While maintaining the static position ( $\eta^*$ ), the drive frequency ( $f_d$ ) of the dither piezo is swept around the resonance frequency from 163 kHz to 170 kHz ( $f_0 = 164.52 \text{ kHz}$ ). The resulting change in vibrational amplitude is

recorded using the multi-lock-in amplifier and the FPGA, simultaneously. Additionally, during the entire sweep duration a specific excitation  $y(t)$  is applied such that the reduction in vibrational amplitude due to tip-sample interaction is maintained at 84%. This reduction is comparable with that of the amplitude set-point ratios used during normal scanning operation in dynamic AFM (See Fig. 3.E.1 in Appendix 3.E). The outcome of this procedure is shown in Fig. 3.1(b). It can be seen that, when the deflection amplitude is increased, the resonance curve first slightly bends to the left (spring softening) [80] and as the tip further approaches the sample, the curve bends towards the right side of the resonance (spring hardening). We note that the presence of nonlinear attractive and repulsive forces between the tip and the sample lie at the root of our observation [75].

In Fig. 3.1(b) we also observe that the nonlinear resonance curve obtained by using the lock-in amplifier (pink curve) is different from the one obtained by analyzing the raw deflection signal using the FPGA (blue curve). Interestingly, we observe a mismatch in the amplitudes of the two signals that exacerbates at higher  $f_d$ . The observed discrepancy hints at the presence of higher-order spectral components that are essentially eliminated when the lock-in amplifier is used. This is because, the lock-in amplifier allows detection of a single frequency component when sweeping  $f_d$  around resonance and effectively approximates the cantilever dynamics as a Single-Degree of Freedom (SDOF) system. However, the FPGA stores the real-time deflection signal and thus can efficiently capture modal interactions that may exist around the resonance.

To further investigate the cantilever's nonlinear dynamic response, we obtain the maximum and minimum of the deflection in an oscillatory cycle using the FPGA (see Fig. 3.2(a)). We note that the cantilever deflection signal reaches a maximum far away from the sample, whereas the minimum shows that the tip is interacting with the sample. This segregation reveals a broken symmetry in the response due to the non-smooth nature of the contact between the tip and the sample when  $f_d$  is detuned from  $f_0$ . To study the physical origin of this symmetry breaking response, we trace the phase space trajectories of the cantilever in real-time when moving from  $f_d = 164.5$  kHz to  $f_d = 167$  kHz (see Fig. 3.2(b) and (c)). The phase space trajectories are highly sensitive to the presence of higher order modes and can be used to identify modal interactions [75]. In Fig. 3.2(b) we observe simple harmonic oscillations of the cantilever close to the free air resonance ( $f_d = 164.5$  kHz); however, at large detuning ( $f_d \geq 166.4$  kHz), the phase space warps and ripples appear on the periphery of the trajectory (Fig. 3.2(c)). To understand the origin of this phase space distortion, we perform Fast Fourier Transform (FFT) of the temporal data (See Fig. 3.2(d) and (e)), and observe that the frequency content of the signal at  $f_d=164.5$  kHz involves only  $f_0$  and few of its higher harmonics. But, when applying FFT on the time signal taken at  $f_d=167$  kHz, an additional resonance peak appears at  $f_2 = 1020$  kHz (see Fig. 3.2(e)), suggesting the activation of the second eigenmode of the cantilever. In essence, this shows that the phase space distortions are a direct result of activation of higher order vibration modes and that the presence of higher harmonics has trivial effect on these trajectories (see Fig. 3.E.1 of Appendix 3.F for details).

To elaborate on our observation, we note that for the cantilever used in the experiments, the frequency ratio  $f_2/f_0 \approx 6.2$  is close to the factor 6. Therefore, by tuning the nonlinear resonance frequency (via sweeping  $f_d$ ), we can reach a 6:1 internal resonance in the frequency range  $f_d \in [165, 166]$  kHz, where the contribution of the second mode

becomes apparent. The resulting mode coupling enhances the SNR of specific harmonics that are close to the interacting eigenmode. In particular, we observe a 7 fold increase in the SNR of the 6<sup>th</sup> harmonic compared to its amplitude near the free air resonance (refer to Fig. 3.2(d) and (e)).

Interestingly, this modal interaction is not only characterized by an increase in the strength of harmonics, but it is also accompanied by a reduced sample indentation when compared to normal scanning operations with similar amplitude set-point ratios at  $f_d = f_0$ . As we sweep  $f_d$  around resonance we observe a decrease in the minimum amplitudes in the frequency range between  $165 < f_d < 166$  kHz which is associated with a decrease in the sample indentation. Such properties make the frequency range over which mode coupling occurs, an ideal range of excitation for the mapping of nanomechanical properties. Therefore, we label this region as the "sweet spot". This lower sample indentation is highlighted in the inset of Fig. 3.2(a), and can be formally described as a gradual curving of the nonlinear dynamic curve in its deflection minima forming a convex shape. It may be intuitively thought that the increased coupling should increase the interaction force and, as a consequence, increase the sample indentation. However, in the sweet spot, the phases of the interacting modes synchronize in such a way that there is a reduced sample indentation (See Fig. 3.C.1 in Appendix 3.C). This dynamic feature is similar to what has been previously reported in dynamically tuned trapezoidal cantilevers [55].

To investigate the repeatability of the observed phenomena, we performed additional set of experiments using a TAP190Al-G rectangular cantilever on a Highly Oriented Pyrolytic Graphite (HOPG) sample, a TAP300Al-G rectangular cantilever on a nanocrystalline diamond island and finally a TAP150AL-G rectangular cantilever on a Polystyrene island. We found that the "sweet spot" is not a unique feature that belongs to a particular sample-cantilever configuration (see Appendix 3.G for details). These interesting observations highlight the role of higher eigenmodes and mode coupling in AFM applications.

### 3.2. MODELING AND SIMULATIONS

In order to underpin the physics behind our experimental observation and to further understand the nature of the mode coupling, we develop a theoretical model based on a non-smooth two-degree of freedom system. The derivation of the model can be found in Appendix 3.A. The model utilizes the long range nonlinear Van der Waals (VdW) and Derjaguin–Muller–Toporov (DMT) contact forces to describe the tip-sample interactions  $F_{ts}(z)$  as follows [48, 83]

$$F_{ts}z = \begin{cases} F_{\text{vdW}} = -\frac{HR}{6z^2} & \text{for } z > a_0 \\ F_{\text{DMT}} = -\frac{HR}{6a_0^2} + \frac{4}{3}E^*\sqrt{R}a_0 - z^{3/2} & \text{for } z \leq a_0. \end{cases} \quad (3.1)$$

Here,  $H$  stands for the Hamaker constant,  $R$  the tip radius,  $a_0$  the intermolecular distance, and  $E^*$  the effective Young's modulus. The tip-surface interaction is purely attractive ( $F_{\text{VdW}}$ ) when the separation distance  $z$  is larger than the intermolecular distance  $a_0$ . If  $z$  is smaller than  $a_0$  the interaction is governed by contact mechanics ( $F_{\text{DMT}}$ ). This

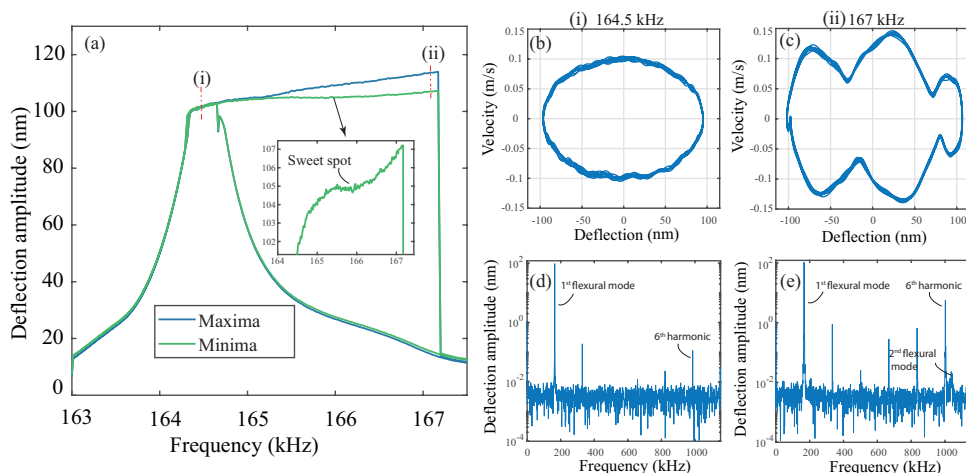


Figure 3.2: Experimental nonlinear dynamic response, phase space trajectories and the associated frequency spectra obtained from the raw deflection signal of the cantilever. (a) Experimental frequency response curve; the blue and green curves represent the maximum and minimum position of the tip, respectively. The forward and reverse sweeps are combined into one curve. The inset highlights the gradual curving of the nonlinear dynamic response in a specific range of drive frequency. The sweet spot frequency range is highlighted using dashed lines. (b)-(c) Phase space trajectories at 164.5 kHz and 167 kHz of drive frequency showing the influence of the second eigenmode in the cantilever oscillations. (d)-(e) Frequency spectra of raw deflection signal at 164.5 kHz and 167 kHz showing the presence of higher harmonics and the second eigenmode.

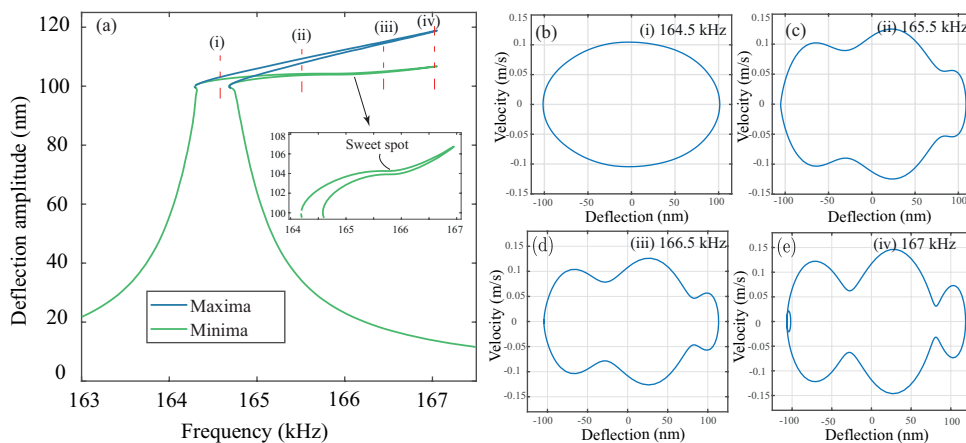


Figure 3.3: Simulated nonlinear dynamic response and phase space trajectories obtained using the two mode model. (a) Numerical frequency response curve; the blue and green curves represent the maximum and minimum position of the tip, respectively. The nonlinear dynamic response is simulated considering 6:1 internal resonance condition between the first two flexural modes. The inset highlights the gradual curving of the nonlinear dynamic response in a specific range of drive frequency. The sweet spot frequency range is highlighted using dashed lines. (b)-(e) Phase space trajectories at 164.5 kHz, 165.5 kHz, 166.5 kHz, and 167 kHz of drive frequency, respectively.

non-smoothness in the interaction force mediates an energy channel between different modes of the cantilever and acts as the root cause of our observation.

To obtain the equations of motion, we model the AFM cantilever as a continuous dynamical system using the Euler-Bernoulli beam theory. We discretize the model by projecting the cantilever deflection onto its linear eigenmodes (computed near free air resonance) and employ the Galerkin approach to obtain a system of ordinary differential equations as follows [75]

$$\ddot{\tilde{q}}_i + D_i \dot{\tilde{z}} \dot{\tilde{q}}_i + K_i \tilde{q}_i = -C_i - F_{ts,i} \tilde{z} + B_i \tilde{\Omega}^2 \tilde{y} \sin \tilde{\Omega} \tau. \quad (3.2)$$

The cantilever deflection, splitted across the generalized coordinates  $\tilde{q}_i$  ( $i = 1, 2, \dots, N$ , with  $N$  being the number of generalized coordinates), is written in Eq. (3.2) on a reference system attached to the cantilever (See Fig. 3.1(a)). The coupling between the generalized coordinates occurs through the relation,  $\tilde{z} = 1 - \sum_{i=1}^n \tilde{q}_i - \tilde{y} \sin \tilde{\Omega} \tau$ . In addition, Eq. (3.2) is made dimensionless with respect to the equilibrium gap width ( $\eta^*$ ) and the fundamental frequency of the cantilever ( $\omega_0 = 2\pi f_0$ ) in the absence of the tip-sample interaction. The amplitude of the dither piezo is given by  $\tilde{y}$  and the dotted quantities represent derivatives with respect to the rescaled time  $\tau$  ( $\tau = \omega_0 t$ ). Additionally, modal damping  $D_i(\tilde{z})$  has been explicitly added to Eq. (3.2). In particular, we consider a piecewise model [48] that accounts for the dissipation mechanism when the tip is in air ( $\tilde{D}_i^{\text{att}}$ ) or when it is in contact with the sample ( $\tilde{D}_i^{\text{rep}}$ ). Finally, the coefficients  $K_i$ ,  $C_i$ , and  $B_i$  represent the modal stiffness, static deflection, and mode participation factor, respectively. The final discretized equation is then simulated using pseudo arc-length continuation technique to fit the experimental data [106].

The simulations performed using the two-mode VdW-DMT model qualitatively describe our experimental observations. In Fig. 3.3(a) the blue and green nonlinear dynamic response curves represent the maximum and minimum deflection of the cantilever similar to what is observed in experiments. Referring to Fig. 3.3(a), the gradual curving of the minimum response (green curve) occurs when the simulation parameters of the coupled oscillator system are tuned to produce a 6:1 internal resonance condition, confirming the presence of this unconventional internal resonance at a few kHz of detuning (see Appendix 3.D for details). Adding to this, the theoretical nonlinear dynamic curves highlight the influence of the higher order modes in the distortion of the phase space trajectory. Similar to the experimental results, the periodic orbit exhibits simple harmonic motion close to free air resonance (Fig. 3.3(b)), which becomes distorted by detuning  $f_d$  to higher frequencies. The distortion gradually increases in depth, in accordance with the contribution given by the second mode of vibration (Figs. 3.3(c)-(e)).

Although the two-mode model accurately predicts the dominance of the second mode at large detuning and explains the physics behind the curving of the nonlinear dynamic response in the sweet spot, it masks the effect of any further couplings that may exist among higher modes of vibration. In particular as depicted in Fig. 3.4, at  $f_d = 165.5$  kHz we observe an increase in the number of ripples on the periphery of the phase space (blue curve). We note that this additional distortion of the phase space is accompanied with 16 folds increase in the amplitude of the 17<sup>th</sup> harmonic that is closely located to the third flexural mode of the cantilever ( $f_3 \approx 17.5 f_0$ ). To prove our hypoth-

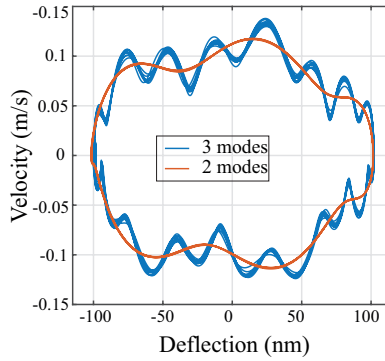


Figure 3.4: Phase space trajectories obtained from experimental deflection at  $f_d = 165.5$  kHz. The experimental deflection signal is low pass filtered with different cut off frequencies to identify the contribution from the second (orange curve) and the third flexural mode (blue curve), respectively.

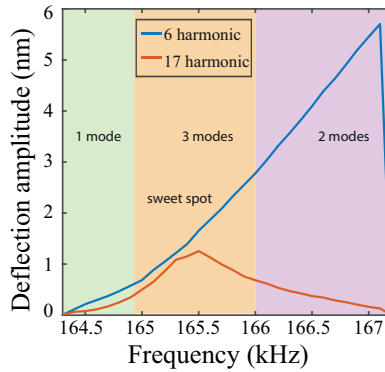


Figure 3.5: Variation of the 6<sup>th</sup> and the 17<sup>th</sup> harmonic amplitude as a function of the driving frequency  $f_d$ . The amplitude of the 6<sup>th</sup> and the 17<sup>th</sup> harmonic increase in a specific frequency range highlighted by the orange section due to intermodal coupling. Thereafter, only the 6<sup>th</sup> harmonic amplitude increases due to increased tip-sample interaction and dominance of the second mode of vibration.

esis about the influence of the third flexural mode, we low-pass filter the experimental data up to the 16<sup>th</sup> harmonic and observe that the resulting phase space (orange curve) closely matches with that of the simulated trajectory obtained using the two mode approximation model shown in Fig. 3.3(c). Although including an additional mode in the numerical model (with consequent increase of the complexity in the simulations) could capture completely the dynamics observed in experiments, it would not add physical insights for the observations stated in this work.

Finally, as an extensive outlook on the various stages of influence of higher-order modes as  $f_d$  is detuned from  $f_0$ , we report in Fig. 3.5 the variation of the 6<sup>th</sup> and 17<sup>th</sup> harmonic as a function of  $f_d$ . At first, when  $f_d$  is close to  $f_0$ , the amplitude of the harmonics generated due to tip-sample forces is relatively low and comparable with the strength of the signals observed during normal tapping mode scanning operation. In the low

frequency range (green region of Fig. 3.5) the entire cantilever dynamics can be well approximated as a SDOF system. With increased detuning, when  $f_d$  lies in the sweet spot (orange region), there is sharp increase in the contribution of the second and third eigenmode in the cantilever motion and the dynamics is governed by the three flexural modes of the cantilever. In this region the amplitude of the 6<sup>th</sup> and 17<sup>th</sup> harmonic increase by 7 and 16 folds respectively as a consequence of an enhanced mode coupling both with the second and the third eigenmode. Upon further detuning, we observe the continuous increase of SNR of the 6<sup>th</sup> harmonic but at the expense of an increased sample indentation. At the same time, the large resonance frequency tuning brings the amplitude of the 17<sup>th</sup> harmonic to drop gradually, until the third mode contribution completely disappears. In the violet region of Fig. 3.5, the dynamics is fully governed by the first and the second mode only. Additionally, by increasing the amplitude of the excitation, the sweet spot widens by few kHz while the physics remains unaltered. However, this increase in the sweet spot range comes at the expense of larger set point ratio (see Fig. 3.H.1 of Appendix 3.H for details).

Currently, the methodology provides significant improvement in SNR of higher harmonics for single point measurements and could be implemented in techniques that extract the nanomechanical properties of samples at several pre-determined pixels. However, in order to integrate the technique with conventional scanning operation there are a few limitations that still need to be addressed. In particular, as a first step, the algorithm routine used to capture the raw deflection signal and tune nonlinear resonance frequency has to be integrated into the AFM's controller in order to handle the data processing at imaging speeds. Such integration also helps tackling the issue of choosing the right drive frequency within the sweet spot for samples comprising multiple materials. Secondly, since the sweet spot is driven beyond the bifurcation point into a bi-stable region, a thorough study has to be performed to understand the influence of noise and feedback settings on the robustness of sweet spot during imaging [107]. In this aspect, our technique can be incorporated together with latest feedback architectures such as modulated time delay control [108] that have already been successfully used to control the cantilever oscillations in the bi-stable regime and reduce perturbation-induced jumps during the scanning operation. Finally, it is important to consider the influence of the geometric and modal characteristics of the cantilever used for performing the measurements. The technique reported in this work has been showcased with standard rectangular cantilevers and is applicable to cantilevers with the second and the third bending modes close to  $6f_0$  and  $17f_0$ , respectively.

### 3.3. CONCLUSION

In summary, we propose a technique to actively tune the nonlinear resonance frequency of AFM cantilevers to achieve high SNR of harmonics at low sample indentation compared to conventional dynamic AFM operations. We discuss the influence of higher order modes on the phase space trajectories of the cantilever as a function of the detuned frequency and highlight the presence of a sweet spot in a specific frequency range around resonance where there is a significant increase in the amplitude of higher harmonics, due to strong modal interactions. We use a two mode nonlinear non-smooth model to qualitatively describe our experiments and explain the observed physics. The

model reinforces the idea of mode coupling as the phenomenon behind the increase in the amplitude of higher harmonics and the lower sample indentation. Finally, given the ease of use and utility, we anticipate that this experimental technique can be used together with various multi-frequency AFM techniques to study nanomechanical properties of organic and inorganic samples without the need for specialized cantilevers. Our technique can also be easily employed in multi-frequency scanning operations to obtain images of the higher harmonics with increased sensitivity, which is an essential requirement in dynamic AFM applications.



## APPENDIX

## 3.A. THEORETICAL MODEL

Here, we obtain the dynamical equation for the AFM initially resting in a static equilibrium at a distance  $\eta^*$  from the sample (see Fig. 3.A.1). The mathematical framework to

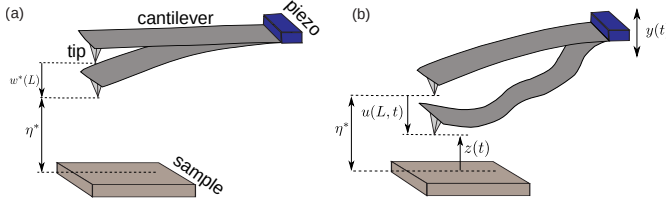


Figure 3.A.1: A schematic of the AFM. (a) Initially statically deflected configuration. (b) Dynamic configuration with the cantilever vibrating about its elastostatic equilibrium.

develop the continuous model for the AFM cantilever is within the Euler-Bernoulli beam theory assumptions. The AFM cantilever has length  $L$ , mass density  $\rho$ , Young's modulus  $E$ , area moment of inertia  $I$ , and cross-section area  $A$ . The beam is clamped at  $x = 0$  and free at  $x = L$ . The cantilever deflection is expressed in a non-inertial reference frame attached to the base, and excited with harmonic motion  $y(t) = Y \sin \Omega t$  via a dither piezo, where  $Y$  and  $\Omega$  are the amplitude and frequency of excitation, respectively. The static deflection due to tip-sample forces at  $\eta^*$  is given by  $w^*(x)$  (see Fig. 3.A.1(a)). Finally, the instantaneous tip-sample distance is  $z(t) = \eta^* - u(L, t) - y(t)$  where  $u(x, t)$  is the dynamic deflection of the cantilever as shown in Fig. 3.A.1(b). The vibrations about the elastostatic equilibrium are governed by the equation [48]:

$$\rho A \ddot{u}(x, t) + EI(u''''(x, t) + w^{*''''}(x)) = F_{ts}(z(t))\delta(x - L) + \rho A \Omega^2 Y \sin(\Omega t). \quad (3.3)$$

We discretize Eq. (3.3) by projecting it onto linear mode shapes  $\phi_i(x)$  computed around the cantilever static configuration. For this, we approximate the response as

$$u(x, t) = \sum_{i=1}^n \phi_i(x) q_i(t) \quad (3.4)$$

with  $q_i(t)$  being the generalized time dependent coordinate for the  $i$ -th mode of vibration. We then substitute Eq. (3.4) in Eq. (2.2) and by utilizing the Galerkin procedure we take the inner products with the same shape functions employed in the discretization. The final discretized dimensionless set of nonlinear ordinary differential equations are:

$$\ddot{\tilde{q}}_i + D_i \tilde{z} \dot{\tilde{q}}_i + K_i \tilde{q}_i = -C_i - F_{ts,i} \tilde{z} + B_i \bar{\Omega}^2 \tilde{y} \sin \bar{\Omega} \tau. \quad (3.5)$$

where  $\tilde{z}$  is the dimensionless tip-sample separation distance given by

$$\tilde{z} = 1 - \sum_{i=1}^n \tilde{q}_i - \tilde{y} \sin \bar{\Omega} \tau. \quad (3.6)$$

Replacing Eq. (3.6) in the tip-sample interaction force (Eq. (3.1)) obtains

$$F_{ts,i}\bar{z} = \begin{cases} C_i/\bar{z}^2, & \text{for } \bar{z} > \bar{a}_0 \\ C_i/\bar{a}_0^2 + G_i\bar{a}_0 - \bar{z}^{3/2}, & \text{for } \bar{z} \leq \bar{a}_0. \end{cases} \quad (3.7)$$

where the coefficients arising in Eqs. (3.5),(3.7) are defined as

$$K_i = \frac{\omega_i^2}{\omega_0^2}, \quad C_i = -\frac{HR\phi_i^2 L}{6\rho A\eta^{*3}\omega_0^2 \int_0^L \phi_i^2 x dx}, \quad (3.8)$$

$$B_i = \frac{\phi_i L \int_0^L \phi_i x dx}{\int_0^L \phi_i^2 x dx}, \quad G_i = \frac{4E^* \sqrt{R\eta^*} \phi_i^2 L}{3\rho A\omega_0^2 \int_0^L \phi_i^2 x dx}.$$

In the presented formulation the generalized coordinates  $\tilde{q}_i$  are normalized with respect to the value of the mode shape at the free end of the cantilever ( $\tilde{q}_i = \phi_i L q_i$ ). The overdot in Eq. (3.5) means differentiation with respect to the dimensionless time, namely  $\tau = \omega_0 t$  where  $\omega_0$  is the fundamental frequency of the cantilever. The amplitude and frequency of the excitation,  $Y$  and  $\Omega$  are related to their dimensionless counterparts through  $\bar{y} = Y/\eta^*$  and  $\bar{\Omega} = \Omega/\omega_0$ , respectively. Finally,  $\bar{a}_0 = a_0/\eta^*$  is the dimensionless conjugate of the intermolecular distance  $a_0$ . Note that the modal damping  $D_i\dot{\bar{z}}$  has been considered in Eq. (3.5). Similar to Ref. [48], we consider a piecewise model that accounts for the dissipation mechanisms while the tip is in air ( $\tilde{D}_i^{\text{att}}$ ) or in contact with the sample ( $\tilde{D}_i^{\text{rep}}$ ):

$$D_i\bar{z} = \begin{cases} D_i^{\text{att}} = \frac{\tilde{D}_i^{\text{att}}}{\omega_0 \rho A \int_0^L \phi_i^2 x dx}, & \text{for } \bar{z} > \bar{a}_0 \\ D_i^{\text{rep}} = \frac{\tilde{D}_i^{\text{rep}}}{\omega_0 \rho A \int_0^L \phi_i^2 x dx}, & \text{for } \bar{z} \leq \bar{a}_0. \end{cases} \quad (3.9)$$

In our simulations we restrict ourselves to a two-degree-of-freedom model, that means we limit Eq. (3.5) to  $i = 2$ . In this case the coupled set of nonlinear differential equations become:

$$\left\{ \begin{array}{l} \ddot{\tilde{q}}_1 + D_1^{\text{att}} \dot{\tilde{q}}_1 + K_1 \tilde{q}_1 = -C_1 - \frac{C_1}{(1 - \tilde{q}_1 - \tilde{q}_2 - \bar{y} \sin \bar{\Omega} \tau)^2} \\ \quad + B_1 \bar{\Omega}^2 \bar{y} \sin \bar{\Omega} \tau \\ \ddot{\tilde{q}}_2 + D_2^{\text{att}} \dot{\tilde{q}}_2 + K_2 \tilde{q}_2 = -C_2 - \frac{C_2}{(1 - \tilde{q}_1 - \tilde{q}_2 - \bar{y} \sin \bar{\Omega} \tau)^2} \\ \quad + B_2 \bar{\Omega}^2 \bar{y} \sin \bar{\Omega} \tau \end{array} \right. \quad (3.10)$$

$$\left\{ \begin{array}{l} \ddot{\tilde{q}}_1 + D_1^{\text{rep}} \dot{\tilde{q}}_1 + K_1 \tilde{q}_1 = -C_1 - C_1/\tilde{a}_0^2 \\ -G_1 (\tilde{a}_0 - (1 - \tilde{q}_1 - \tilde{q}_2 - \bar{y} \sin \bar{\Omega} \tau))^{3/2} + B_1 \bar{\Omega}^2 \bar{y} \sin(\bar{\Omega} \tau) \\ \ddot{\tilde{q}}_2 + D_2^{\text{rep}} \dot{\tilde{q}}_2 + K_2 \tilde{q}_2 = -C_2 - C_2/\tilde{a}_0^2 \\ -G_2 (\tilde{a}_0 - (1 - \tilde{q}_1 - \tilde{q}_2 - \bar{y} \sin \bar{\Omega} \tau))^{3/2} + B_2 \bar{\Omega}^2 \bar{y} \sin(\bar{\Omega} \tau) \end{array} \right. \quad (3.11)$$

where Eq. (3.10) and (3.11) shall be integrated with conditions  $(1 - \tilde{q}_1 - \tilde{q}_2 - \bar{y} \sin \bar{\Omega} \tau) \leq \tilde{a}_0$  and  $(1 - \tilde{q}_1 - \tilde{q}_2 - \bar{y} \sin \bar{\Omega} \tau) > \tilde{a}_0$ , respectively.

The simulation parameters used in Eq.(3.10) and (3.11) to obtain the results presented in Fig. 3.3 are provided in Appendix 3.B.

### 3.B. NUMERICAL IMPLEMENTATION AND SIMULATION PARAMETERS

Equations (3.10) and (3.11) are integrated in the Computational Continuation Core toolbox (COCO) for a parametric analysis of the AFM dynamics [106]. The toolbox allows building frequency response curves by performing pseudo-arclength continuation of periodic solutions [106]. The tool is ideally suited for hybrid dynamical systems, such as Eq. (3.5) that is characterized by discontinuities in both force (Eq. (3.7)) and damping (Eq. (3.9)). In addition, the tool permits continuation of both unstable and stable periodic solutions.

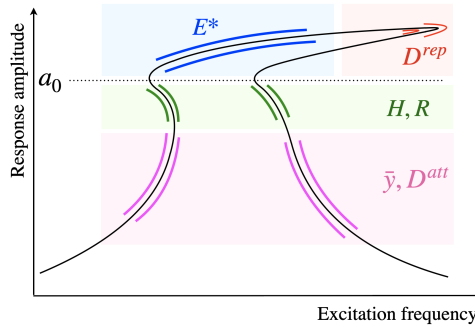


Figure 3.B.1: Schematic frequency response function with the major areas of influence for the different parameters of Eqs. (3.10) -(3.11).

The fitting procedure consists of isolating branches of the nonlinear dynamic curve where a parameter influence is predominant and then making a reasonable guess for the specific parameter. Figure 3.B.1 summarises the major areas of influence for the different parameters of Eqs. (3.10) -(3.11). The fit of the response far from the tip-sample interaction gives hints on the damping in the non-contact region ( $D^{\text{att}}$ ) and the amplitude of the excitation ( $\bar{y}$ ). The attractive forces leading to softening response are taken into account for the estimation of the  $C_1$  coefficient that depends on the Hamaker constant  $H$  and the tip radius  $R$ .

The saturation of the response in the contact region mainly depends on the effective Young's modulus  $E^*$ . Finally, the dissipation in the amplitude-saturated region, is closely related to the parameter  $D^{\text{rep}}$ , that changes the position of the bifurcation point associated with jump-down in the forward frequency sweep. This fitting process requires multiple iterations before the parameters are converged. The parameters reported in Table 3.B.1 are the set of parameters obtained via this fitting procedure that reconstruct the dynamics observed in the experiments.

Table 3.B.1: The parameters used for simulating Fig. 3.3 in the main chapter.

Coefficient	value	Coefficient	value
$\bar{\Omega}$	[0.990149, 1.1327]	$\bar{y}$	$2.649109 \times 10^{-3}$
$a_0$	0.2	$K_1$	1
$B_1$	1.565980	$G_1$	10.5
$D_1^{\text{att}}$	$2.9 \times 10^{-3}$	$D_1^{\text{rep}}$	$5.7 \times 10^{-3}$
$K_2$	36	$B_2$	-0.867872
$G_2$	13.5	$D_2^{\text{att}}$	$5 \times 10^{-4}$
$D_2^{\text{rep}}$	$8 \times 10^{-3}$		

### 3.C. PHASE SYNCHRONIZATION AT INTERNAL RESONANCE

We reported a reduction in sample indentation in Fig. 3.2(a) when  $f_d$  is detuned to coincide with the sweet spot. In this appendix, we utilize the simulations from our two mode VdW-DMT model described in Eq. (3.11) and show that the phase synchronization between the eigenmodes is responsible for the aforementioned reduction in sample indentation. Figure 3.C.1 shows the time signals of the first (blue) and second (orange) flexural modes extracted from the same simulations reported in Fig. 3.3. The signals are extracted at different excitation frequencies from the nonlinear frequency response curve to track the variation of phase difference between the two modes. At resonance  $f_d = f_0$  (see Fig. 3.C.1(a)) the phase difference between the two modes is  $\approx 90^\circ$ . However, when  $f_d$  is detuned to enter the sweet spot (see Figs. 3.C.1(b)-(c)), the phase difference changes drastically such that the two modes interact almost in out-of-phase motion. The phase difference between the two modes is found to be  $152.11^\circ$  to  $163.38^\circ$  as  $f_d$  is swept from 165.5 kHz to 166 kHz, respectively. This out-of-phase motion between the two eigenmodes interfere destructively, resulting in a reduced sample indentation. Finally, when  $f_d$  is out of the sweet spot range the phase difference gradually shrinks to  $32.4^\circ$  at 167 kHz (see Fig. 3.C.1(d)). This reduction in phase difference causes the two modes to interfere constructively and therefore results in larger indentation at higher excitation frequencies.

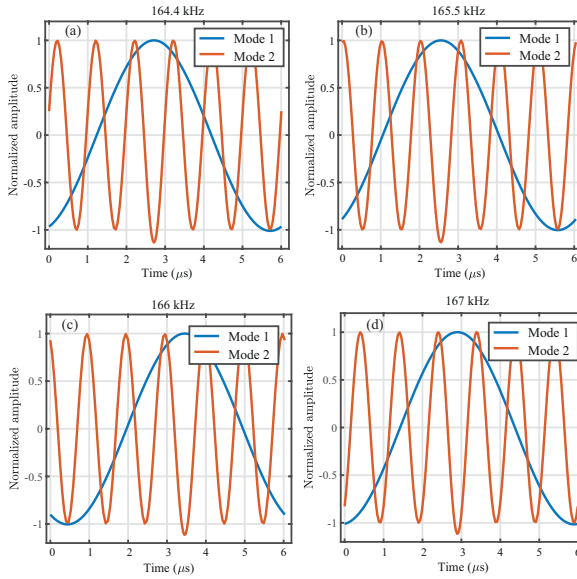


Figure 3.C.1: Simulations depicting Auto phase synchronization between first (blue) and second (orange) flexural modes in the sweet spot. To aid with the visualization, the amplitudes of the time signals are normalized with respect to their corresponding maximum value in a given time period. (a) At resonance, the first and second flexural mode oscillations start with a phase difference of  $90^\circ$ . (b)-(c) The phase difference between the two eigenmodes in the sweet spot at 165.5 kHz and 166 kHz, respectively. (d) The phase difference between the two modes out of the sweet spot at 167 kHz.

### 3.D. SIMULATIONS WITH AND WITHOUT INTERNAL RESONANCE CONDITION

In this section, we highlight the necessity of incorporating a 6:1 internal resonance condition to qualitatively capture our experimental observations. This is shown in Fig. 3.D.1 where two different simulations are performed with and without 6:1 internal resonance. It can be clearly seen from Fig. 3.D.1(a) that in order to mimic the presence of sweet spot at a particular range of excitation frequency, an internal resonance is needed.

The global effect of internal resonance can be also well-captured in time domain by investigating the phase space diagrams of the two cases with and without internal resonance. Fig. 3.D.1(b) shows the phase space trajectories obtained for 6:1 internal resonance (green) and without (blue) internal resonance. The trajectories are compared at a fixed excitation frequency of 166.5 kHz. By comparing Fig. 3.D.1(b) with Fig. 3.2(c), we clearly observe that only the trajectory obtained with a 6:1 internal resonance condition mimics the observed response in the experiments.

### 3.E. AMPLITUDE REDUCTION AND SET POINT RATIO

In order to obtain the nonlinear dynamic curves presented in Fig 3.2(a), we maintained a specific excitation amplitude of 0.013V for the dither piezo. To estimate the set point ratio during nonlinear resonance frequency tuning, we fit the experimental frequency

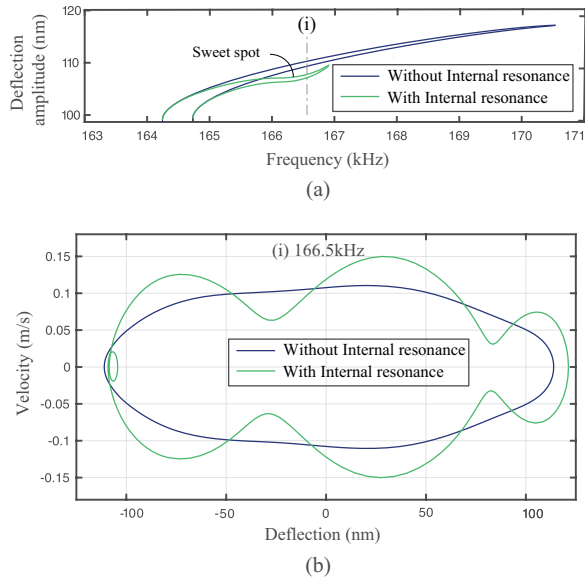


Figure 3.D.1: Simulations depicting the frequency response and the phase space trajectories of a cantilever undergoing 6:1 internal resonance (a) Frequency response curve highlighting the importance of internal resonance condition in obtaining the sweet spot. (b) Phase space trajectories obtained at a fixed excitation frequency of 166.5kHz. The trajectory obtained with a 6:1 internal resonance condition matches qualitatively the phase space observed in Fig. 3.2(c) of the main chapter.

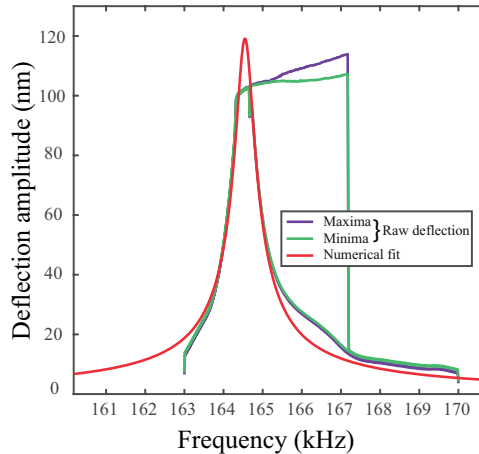


Figure 3.E.1: Estimating the set point ratio for the experimental frequency response curve presented in Fig. 3.2(a). The blue and green curves are the experimental maximum and minimum position of the tip, respectively. The forward and reverse sweeps are combined into one curve. The red curve is the Lorentzian fit obtained with a numerical model based on simple harmonic oscillator with base excitation.

response curve with a simple harmonic oscillator with known spring constant  $k$  and quality factor  $Q$ . The fit is given in Fig. 3.E.1 and shows the reduction of the amplitude caused by the tip-sample interaction forces. The maximum amplitude of the Lorentzian fit is 119 nm, whereas the maximum reduction in amplitude is 100 nm resulting in a set point ratio of 84%.

### 3.F. INFLUENCE OF HARMONICS ON PHASE SPACE TRAJECTORIES

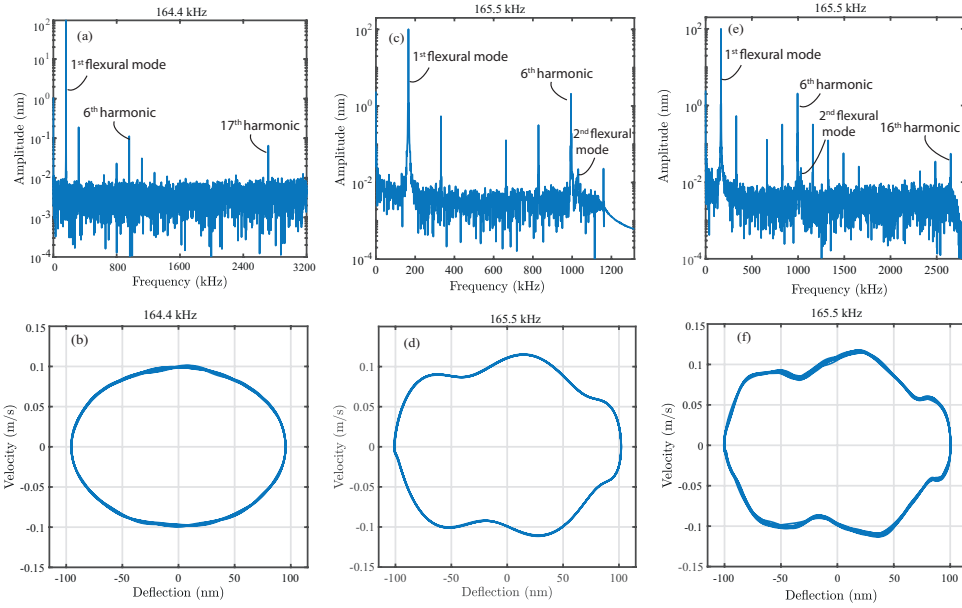


Figure 3.F.1: Influence of harmonics and higher order eigenmodes on phase space trajectories. (a)-(b) Discrete frequency spectra and the associated phase space trajectory at  $f_d = 164.4$  kHz. (c)-(d) Discrete frequency spectra and the associated phase space trajectory at  $f_d = 165.5$  kHz. The time data is low pass filtered to include the first 7 harmonics of the cantilever. (e)-(f) Discrete frequency spectra and the associated phase space trajectory at  $f_d = 165.5$  kHz. The time data is low pass filtered to include the first 16 harmonics of the cantilever.

In this section, we study the influence of harmonics and higher order modes on the phase space trajectories and present additional results to corroborate our findings. In particular, we focus on the warping of the phase space trajectories and its insensitivity towards higher harmonics. Figure 3.F.1 shows the experimental phase space trajectories and the associated frequency spectra at several distinct excitation frequencies. The data is extracted from the nonlinear frequency response curve Fig. 3.2(a). The time data is digitally low pass filtered at different stages with different cut off frequencies to understand the influence of higher order spectral components. At first, we choose a frequency point close to the resonance at  $f_d = 164.4$  kHz and obtain the phase space and the corresponding frequency spectra as shown in Fig. 3.F.1(a) and (b). The data is digitally low pass filtered with a cut off frequency of 3.5 MHz. Looking at Fig. 3.F.1(a), the frequency spectra

clearly shows the presence of several higher harmonics and in particular the 6<sup>th</sup> and the 17<sup>th</sup> harmonics are of special interest since they are closer to the second and third flexural modes of the cantilever and thus show more contrast in AFM imaging operations. Referring to these figures, even when the higher harmonics are present in the cantilever deflection, the phase space trajectories remain approximately circular and show no signs of warping (see Fig. 3.F1(b)).

In the next step of the analysis, we choose the frequency point  $f_d = 165.5$  kHz reported in Fig. 3.4 but low pass filter the time data with two different cut off frequencies namely 1.1 MHz (upto the 7<sup>th</sup> harmonic) (Fig. 3.F1(c)-(d)) and 2.65 MHz (upto the 16<sup>th</sup> harmonic) (Fig.3.F1(e)-(f)), respectively. From the frequency spectra of Fig. 3.F1(c), we see that by including spectral components only until the second mode, we see a gradual warping of the phase space with characteristic ripples appearing on its periphery (see Fig. 3.F1(d)). Furthermore, by including the spectral components up to the 16<sup>th</sup> harmonic (see Fig. 3.F1(e)), we see that the shape of the phase space trajectory is unaltered (see Fig. 3.F1(f)). However, if the time data at this particular frequency point was not low pass filtered then it would have resembled the phase space shown in Fig. 3.4. This analysis shows the insensitivity of the phase space trajectories to higher harmonics and further highlights the utility of phase space orbits as tools for probing the presence of higher order eigenmodes and modal interactions in dynamic AFM applications.

### 3.G. ADDITIONAL EXPERIMENTAL DATA SETS

Table 3.G.1: The geometric and modal properties of cantilevers used for measurements. Here, L,W,T stands for length, width and thickness of the cantilever and their values are obtained from the manufacturer. Whereas,  $f_0$  and k stands for resonance frequency and force constant of the cantilever whose values are measured via thermal calibration method.

Cantilever name	Sample	L ( $\mu\text{m}$ )	W ( $\mu\text{m}$ )	T ( $\mu\text{m}$ )	$f_0$ (kHz)	k ( $\text{Nm}^{-1}$ )
TAP190AL-G	HOPG	225	38	7	161.1	26.632
TAP300AL-G	Nanocrystalline diamond	125	30	4	249.23	28.37
TAP150AL-G	Polystyrene	125	25	4	125.5	5.6

In this section we show that the sweet spot is not a unique feature that belongs to a particular sample-cantilever configuration, and can be observed for different experimental layouts. In Table I we summarize these additional experiments. We report in Fig. 3.G.1(a) a second experimental set of data collected with a commercially available rectangular silicon cantilever (TAP190AL-G, budget sensors) and freshly cleaved Highly Oriented Pyrolytic Graphite (HOPG). The experiments are performed at different excitation amplitudes and with a different dither piezo as compared to the data set reported in the main chapter. In Fig. 3.G.1(b)-(e) we show the variation of phase space trajectories and the associated influence of higher order eigenmodes as  $f_d$  is detuned from resonance. The figure corroborates the findings reported in the main chapter.

In addition to the above, we report in Fig. 3.G.2 a third and a fourth data set obtained using commercial rectangular tapping mode cantilevers. In particular, Fig. 3.G.2 (a) shows nonlinear dynamic response of a TAP300AL cantilever interacting with nano-



crystalline diamond, whereas, Fig. 3.G.2 (b) shows the response of a soft tapping mode TAP150AL cantilever in contact with Polystyrene island distributed on a Polybutadiene substrate. In all the curves, the sweet spot region is apparent when the excitation frequency is detuned from the resonance frequency.

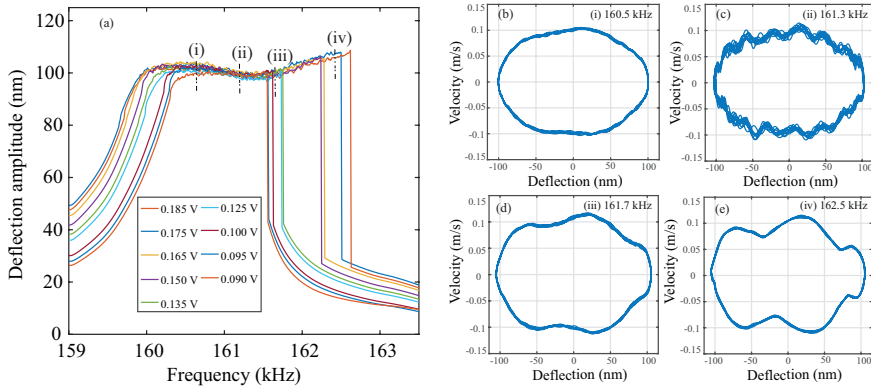


Figure 3.G.1: Experimental nonlinear dynamic response curves obtained with the minima of raw deflection signal for a second set of data with TAP190AL-G cantilever and Highly oriented pyrolytic graphite (HOPG) sample. The experiment is repeated for different excitation amplitudes from 0.90 V to 0.185V. Phase space variations showing the influence of higher order modes obtained from a second experimental data set ((TAP190AL-G cantilever interacting with HOPG). The amplitude of excitation is 0.175V. (a) The phase space trajectory obtained at 160.5 kHz close to resonance shows a simple harmonic motion with no influence from higher order modes. (b) The phase space trajectory at 161.3 kHz is in the sweet spot range and thus shows the influence of second and third eigenmode. (c) - (d) The phase space trajectories obtained far away from the sweet spot at 161.7 kHz and 162.5 kHz clearly show that the influence of the second mode is dominant at higher excitation frequencies.

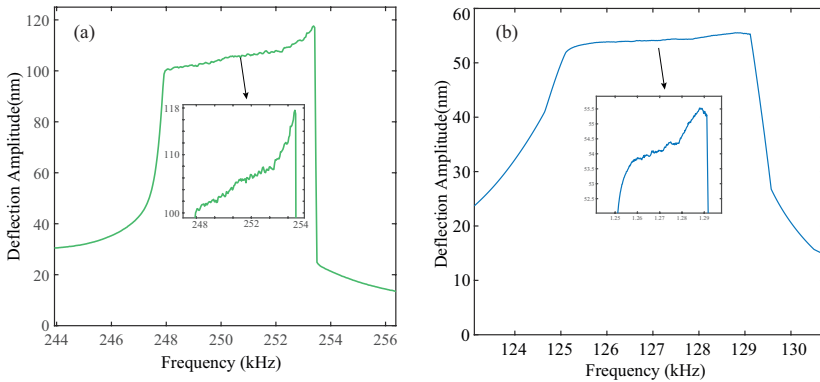


Figure 3.G.2: Additional data sets showcasing the presence of sweet spot in different cantilever-sample configurations. The experimental frequency response curves are obtained using the minima of raw deflection signal. (a) TAP300AL cantilever with a resonance frequency of 249.23 kHz and stiffness of  $28.37 \text{ N m}^{-1}$  to characterize a nano-crystalline diamond island deposited on a silicon substrate. (b) TAP150AL cantilever with a resonance frequency of 125.5 kHz and stiffness of  $5.6 \text{ N m}^{-1}$  to characterize a Polystyrene island distributed on a Polybutadiene matrix.

### 3.H. INFLUENCE OF EXCITATION AMPLITUDE

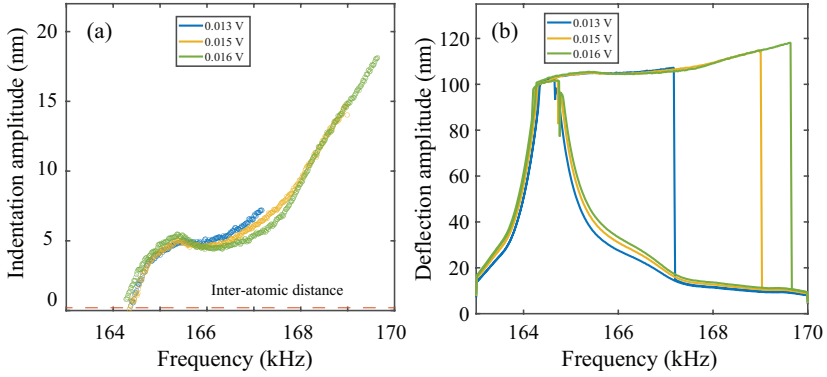


Figure 3.H.1: Indentation amplitude and nonlinear dynamic response curves for different excitation amplitudes using NCLR cantilever on a silicon sample (a) Amplitude of cantilever indentation into the sample. The indentation depths are calculated by subtracting the static distance  $\eta^*$  from the cantilever deflection minima. The plots are obtained for 0.013 V (blue), 0.015 V (yellow) and 0.016 V (green) drive amplitudes. (b) Experimental nonlinear dynamic response obtained at different driving amplitudes for the silicon sample data set. Only the minima of the signals are shown in an oscillatory cycle.

Figure 3.H.1 shows the influence of excitation amplitude on the dynamic response of the cantilever. The experimental data set reported in this figure are the same as the one reported in the main chapter. The experiments are performed by using a commercial NCLR rectangular cantilever on a flat silicon sample. The cantilever is excited with three different excitation amplitudes of 0.013V, 0.015V and 0.016V, respectively. From Figure 3.H.1, we see that increasing the excitation voltage does not alter the dynamic features described in the main chapter but serves to enhance them further. For example, by increasing the excitation voltage, the frequency range of sweet spot is increased; additionally, we also observe an increased sample indentation at higher frequencies. It must be noted that, although the sweet spot range increases with the increase in excitation amplitude, this comes at the cost of larger set-point ratio.

4

4

# 4

## **SENSITIVITY OF VISCOELASTIC CHARACTERIZATION IN MULTI-HARMONIC ATOMIC FORCE MICROSCOPY**

*Quantifying the nanomechanical properties of soft-matter using multi-frequency atomic force microscopy (AFM) is crucial for studying the performance of polymers, ultra-thin coatings, and biological systems. Such characterization processes often make use of cantilever's spectral components to discern nanomechanical properties within a multi-parameter optimization problem. This could inadvertently lead to an over-determined parameter estimation with no clear relation between the identified parameters and their influence on the experimental data. In this work, we explore the sensitivity of viscoelastic characterization in polymeric samples to the experimental observables of multi-frequency intermodulation AFM. By performing simulations and experiments we show that surface viscoelasticity has negligible effect on the experimental data and can lead to inconsistent and often non-physical identified parameters. Our analysis reveals that this lack of influence of the surface parameters relates to a vanishing gradient and non-convexity while minimizing the objective function. By removing the surface dependency from the model, we show that the characterization of bulk properties can be achieved with ease and without any ambiguity. Our work sheds light on the sensitivity issues that can be faced when optimizing for a large number of parameters and observables in AFM operation, and calls for the development of new viscoelastic models at the nanoscale and improved computational methodologies for nanoscale mapping of viscoelasticity using AFM.*

A major part of this chapter is submitted as an article to Soft Matter journal for review[109]. The submitted article is adapted to fit into the context of the thesis.

## 4.1. INTRODUCTION

Viscoelastic characterization of soft-matter at the nanoscale is important for understanding cell membrane functioning [6, 60–62], developing innovative materials in polymer science [110–112], and for advancing nanolithography [113, 114]. In this regard, dynamic atomic force microscopy (AFM) has emerged as an indispensable tool for characterizing nanomechanical properties of soft matter, offering diverse operating conditions under which a wide variety of samples can be probed with gentle forces [115, 116].

Dynamic AFM imaging offers multiple observable channels in the form of higher harmonics, modal amplitude, and phase contrast signals to map nanomechanical properties. Among multi-harmonic AFM techniques, the emergence of bi-modal and intermodulation AFM (IM-AFM) has led to a drastic increase in the number of experimental observables and a consequent advancement in our understanding of material properties at the nanoscale. In particular, IM-AFM extends the concept of multi-frequency observables by providing a fast and convenient method to measure a set of frequency components in a narrow frequency band centered around the fundamental resonance of the AFM cantilever [22, 117]. These frequency components directly benefit from the mechanical resonance gain of the first mode and can be easily converted to tip-sample force quadratures, which are in turn linked to the conservative and dissipative interactions with a sample [67, 117].

Despite the advancements in AFM instrumentation and the abundance of viscoelastic models at hand [63, 64, 101, 118–120], a consistent and robust estimation of viscoelasticity using AFM has remained a challenge [62]. This is mainly due to the fact that the compositional contrast of AFM images depend on several nanomechanical properties including elasticity, surface relaxation, and adhesion. Untangling these effects from one another requires setting up an optimization problem, where a large parameter space has to be searched to minimize the error between the simulations from a model and experimental data. But, similar to any optimization problem, the insensitivity of the model parameters with respect to the measurement data on one side, and the non-convexity of the objective function on the other side, can lead to non-unique and often non-physical estimation of parameters. Therefore, knowledge about the sensitivity of the model parameters to AFM observable channels is of paramount importance to extract consistent and reliable viscoelastic properties in dynamic AFM applications.

In this chapter we discuss the sensitivity issues that can arise when characterizing viscoelasticity using multi-frequency IM-AFM. We perform measurements on a polymer blend made of stiff Polystyrene (PS) and soft Low-Density-Polyethylene (LDPE), and use a moving surface model [101, 121] to extract the bulk and the surface viscoelasticity. The estimation of viscoelastic properties is achieved by matching the experimental spectral components of tip-sample force to the ones predicted by a computational model via an optimization procedure. To ascertain the sensitivity of the model parameters on the physical observables, we perform a comprehensive comparison involving both local and global optimization techniques, and reveal a lack of sensitivity of surface motion to the experimental data obtained from IM-AFM. We show that the issue of insensitivity manifests itself during the optimization of the objective function by means of a vanishing gradient with respect to the surface parameters. To overcome this problem, we introduce a simple model, neglecting surface motion, which leads to statistically consistent and

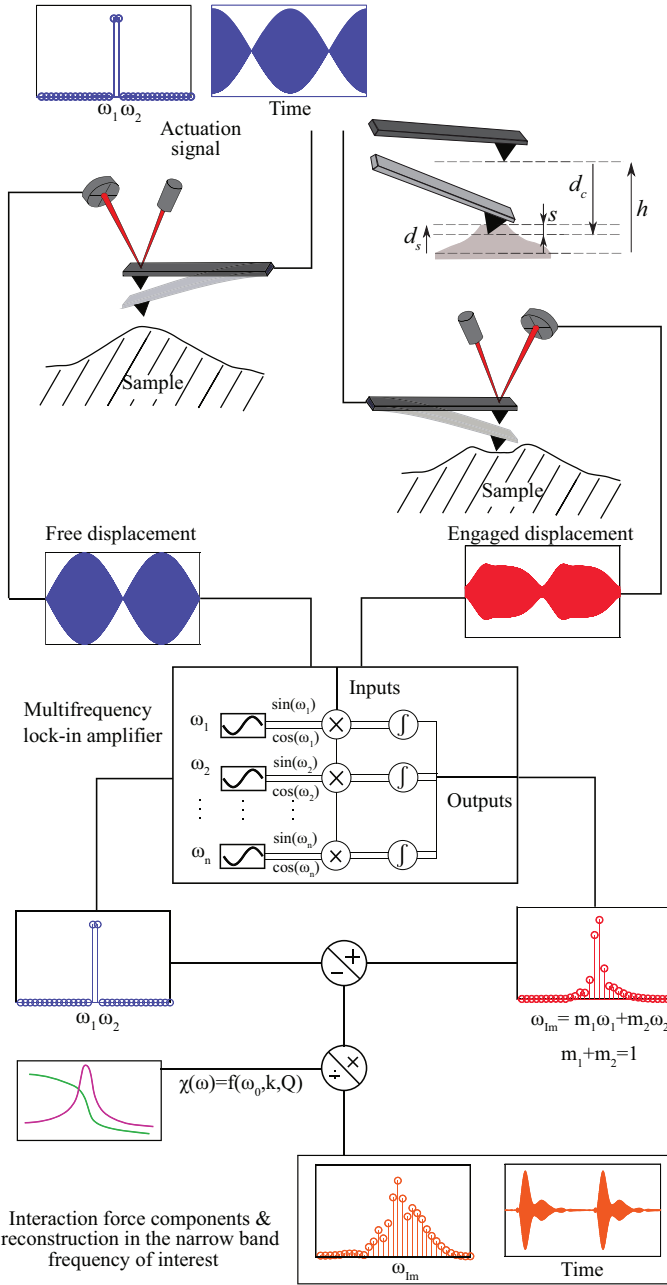


Figure 1: Schematic of the working principle of the IM-AFM. The cantilever is driven with a signal comprising two close frequencies  $\omega_1$  and  $\omega_2$ , centered around its first resonance frequency. The intermodulation distortion caused by the nonlinear tip-sample interaction creates frequency comb at commensurate frequencies  $\omega_{IM} = m_1\omega_1 + m_2\omega_2$ , with  $m_1, m_2 \in \mathbb{Z}$ . The linear transfer function of the cantilever  $\chi(\omega)$  is measured via thermal calibration, and the amplitudes and phases of these intermodulation products are captured using a multi-lock-in amplifier. Here,  $d_c$  and  $d_s$  denote the tip cantilever and surface vertical displacements and  $h$  corresponds to the unperturbed probe height. Finally,  $s = h + d_c - d_s$  represents the tip-sample distance.

robust identification of bulk viscoelastic parameters. This work thus provides a general framework that can be used for investigating the reliability of similar viscoelastic models used for nanomechanical characterization in multi-frequency AFM applications.

## 4.2. EXPERIMENTAL RESULTS

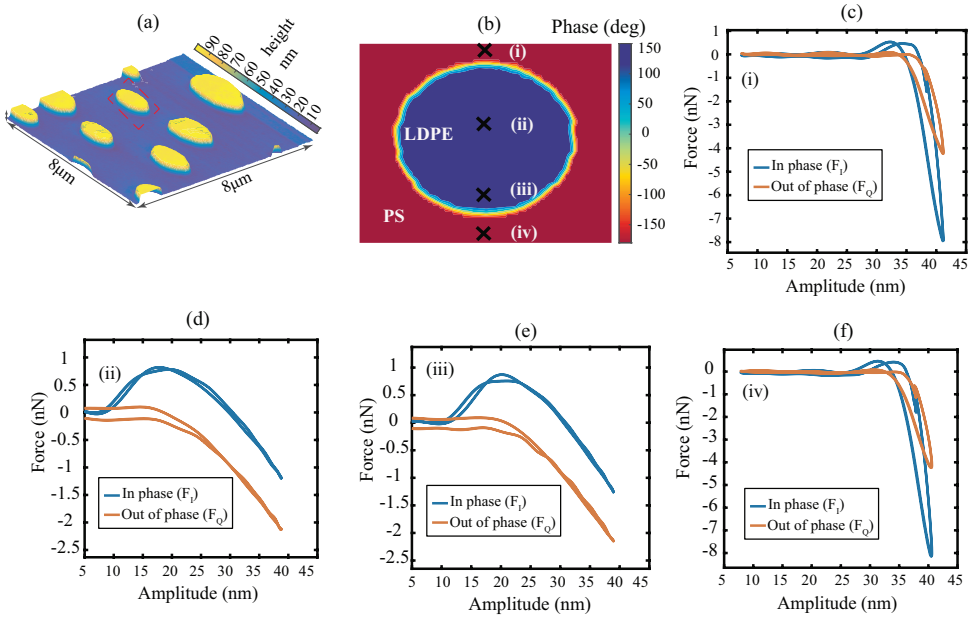


Figure 2: Experimental measurements performed on the PS-LDPE polymer blend. (a) Amplitude image at the second drive frequency ( $\omega_2$ ), which is part of the 32 different image pairs captured during the scanning operation. (b) Phase image at the second drive frequency. The image shows an island of LDPE within the PS matrix (red dashed box in Fig. 2(a)). The points of measurements are indicated with black crosses. (c-f) Experimental force quadratures obtained at the pixels marked by black crosses in the phase image. The quadratures in subfigures (c)-(f) are obtained on PS material, whereas the quadratures in sub figures (d)-(e) are obtained on LDPE material.

We perform our experiments with a commercial AFM (JPK nanowizard 4) and use a multi-lock-in amplifier (Intermodulation products AB) to measure and analyse the frequency components resulting from the tip-sample interaction. A rectangular Silicon cantilever (Tap190Al-G, BudgetSensors) probes the viscoelastic response of a polymer blend made up of PS-LDPE materials. The stiffness of the cantilever ( $k = 26.70 \text{ N/m}$ ), its resonance frequency ( $f_0 = 153.9 \text{ kHz}$ ) and the quality factor ( $Q = 596$ ) are determined using the thermal calibration method [122]. A schematic of the intermodulation AFM setup is shown in Fig. 1. The cantilever is excited with two frequencies centered around its fundamental mode of vibration. The interaction of the cantilever with the sample, under the influence of nonlinear surface forces, generates frequency combs that are measured using the lock-in amplifier. In particular, the amplitude and phase of the combs are used



as experimental inputs for the viscoelastic identification procedure. Details of IM-AFM operation, processing of the experimental data can be found in [22, 117, 121, 123]. Additionally, we summarize the essential operations in Section 4.A of the appendix.

The experiments performed on the PS-LDPE polymer blend are reported in Fig. 2. Figures 2(a)-(b) depict the amplitude and phase images at the second drive frequency  $\omega_2$ . The phase image is presented for one specific LDPE island surrounded by PS matrix. In total 32 amplitude and phase intermodulation components are used to reconstruct the tip-sample interaction in the narrow frequency band around the fundamental resonance. Furthermore, the frequency components are used to calculate the tip-sample force quadratures, which represent the time averaged interaction force that the cantilever experiences in one oscillation cycle (see Figs. 2(c)-(f) for both PS and LDPE). The force quadratures are a local measure of material properties since they are calculated for every pixel of the AFM image; they provide information about the conservative and dissipative contributions of the interaction force between the tip and the sample. For instance, the in-phase quadratures provide information about the amount of adhesive (positive part) and repulsive (negative part) forces at the measured pixels [67, 121].

### 4.3. MODELING TIP-SAMPLE INTERACTION

In order to probe the viscoelastic response of the sample and interpret the in-phase and out-of-phase quadrature information quantitatively, we begin by describing the dynamics of the AFM cantilever using the following simple model [48, 75]:

$$\frac{1}{\omega_0^2} \ddot{d}_c + \frac{1}{Q\omega_0} \dot{d}_c + d_c = \frac{1}{k} (F_d(t) + F_{ts}(s, \dot{s})), \quad (4.1)$$

where  $d_c$  describes the total deflection of the cantilever from its equilibrium,  $\omega_0=2\pi f_0$  denotes its resonance frequency,  $k$  represents the stiffness of the cantilever,  $t$  denotes the time and  $F_d$  is the excitation force. The above equation couples to the sample through the nonlinear tip-surface force

$$F_{ts}(s, \dot{s}) = \begin{cases} -F_{ad} - k_v s - \eta_v \dot{s}, & \text{if } s \leq 0, \\ 0 & \text{if } s > 0. \end{cases} \quad (4.2)$$

Here, the piecewise linear (PWL) model assumes  $F_{ts}$  to be function of the indentation ( $s$ ) and the rate of indentation ( $\dot{s}$ ). In Eq. (4.2), the tip-sample interaction comprises of an adhesion force represented by  $F_{ad}$ , a repulsive force due to surface indentation governed by the bulk sample stiffness  $k_v$ , and finally, a viscous force due to material flow upon indentation governed by the coefficient  $\eta_v$ . It must be noted that the PWL model preserves an essential feature of the interaction that is well-known in AFM, which is the presence of large force gradient localized near the point of contact, *i.e* at  $s = 0$ . This rapid change of force is responsible for the jump-to-contact and pull-off hysteresis seen in nearly all quasi-static force curves in AFM. However, in dynamic AFM, the oscillation amplitude is typically much larger than the range of this localized interaction. Hence, we approximate this region of large interaction gradient as an adhesion force that instantly turns on and off when crossing the point of contact, whose magnitude is counterbalanced by the contribution of the velocity-dependent term  $\eta_v \dot{s}$ .

We then couple the cantilever dynamics with a moving surface model [101, 121] to account for the motion of the sample interacting with the tip

$$\eta_s \dot{d}_s + k_s d_s = -F_{ts}(s, \dot{s}). \quad (4.3)$$

Here, the stiffness and viscosity of the sample surface are  $k_s$  and  $\eta_s$ , respectively. The instantaneous surface motion is related to the cantilever oscillation through the relation  $s = h + d_c - d_s$ , where  $h$  is the unperturbed cantilever height as shown in Fig. 1.

The tip-sample interaction process as described by Eqs. (4.1)-(4.3) introduces a large set of unknown parameters that shall be extracted from the intermodulation components. However, few of them, namely  $\omega_0$ ,  $Q$ , and  $k$  are obtained directly from thermal calibration [49]. This reduces the unknown set of parameters that needs to be identified to  $\mathbf{P} = \{F_{ad}, k_v, \eta_v, k_s, \eta_s, h\}$ . At this stage, the optimization problem is written as:

$$\text{find } \min_{\mathbf{P} \in \mathbb{R}^6} f(\mathbf{P}) \quad (4.4)$$

with  $f(\mathbf{P})$  the objective function defined as [67, 124, 125]:

$$f(\mathbf{P}) = \sqrt{\sum_{\omega=\omega_{IM}} |\tilde{F}_{ts,\text{exp}}(\omega) - \tilde{F}_{ts,\text{sim}}(\omega, \mathbf{P})|^2} \quad (4.5)$$

where  $\tilde{F}_{ts,\text{sim}}$  and  $\tilde{F}_{ts,\text{exp}}$  denote the complex spectral components of the simulated and experimental interaction force at the intermodulation frequencies  $\omega_{IM}$ , respectively.

#### 4.4. LINKING VISCOELASTICITY TO INTERMODULATION COMPONENTS

We start the identification by analyzing the two pixels denoted by (i) and (iii) in Fig. 2(b). These pixels belong to the PS and the LDPE material, respectively. The optimization of the model parameters is carried out using the Levenberg-Marquardt algorithm since it has strong convergence properties and robustness against numerical inconsistencies [126]. We note that the minima obtained by the optimizer are largely dependent on the initial points (IP) chosen for the unknown parameter set  $\mathbf{P}$ . Thus, several initial starting configurations are tested for the identification procedure; these are selected based on values previously reported in the literature [65, 127–129] (see Section 4.B.2 in appendix for additional details).

Table 1 summarises the identified model parameters and the corresponding errors between the simulation and the experimental counterparts for several different IPs on pixels (i) and (iii). Here, we note that the surface stiffness ( $k_s$ ) and damping ( $\eta_s$ ) of LDPE is much higher than PS matrix. This qualitative and counter-intuitive result (PS being the stiffer material), can be explained by a larger penetration depth which results in a larger contact area and thus a larger estimated  $k_s$  for the softer material. In addition to this, we observe from Fig. 3(a)-(b) that the reconstructed cantilever motion (green) and the surface motion (pink) look identical, even though they represent different set of identified values (See table 1). Moreover, in Fig. 3(c)-(d) the surface motion in case of LDPE is strongly dependent on the choice of IPs and consequently leads to different

	Pixel (i) - PS			Pixel (iii) - LDPE		
Initial point	IP 1	IP 55	IP 99	IP 1	IP 22	IP 87
$F_{ad}$ (nN)	30.5	31.6	41.6	7.08	7.12	7.13
$k_v$ (N/m)	94.9	43.2	89.5	0.848	0.854	0.860
$\eta_v$ (mg/s)	15.5	7.33	6.60	0.520	0.521	0.521
$k_s$ (N/m)	18.8	16.8	11.8	123.8	239.3	28.4
$\eta_s$ (mg/s)	0.0552	0.00884	0.993	57.2	0.0594	62.0
$h$ (nm)	26.35	24.69	24.11	14.43	14.69	14.67
Final $E$ (nN)	0.511	0.537	0.579	0.193	0.194	0.194
$R^2$	0.961	0.957	0.950	0.979	0.979	0.979

Table 1: Extracted results from a large set of local minimization routines using Levenberg-Marquardt algorithm. The model including surface motion and the grid initial points (IPs) defined in table 4.B.2 of appendix. The initial points are ranked according to the best results, defined here as the lowest errors / highest  $R^2$ .

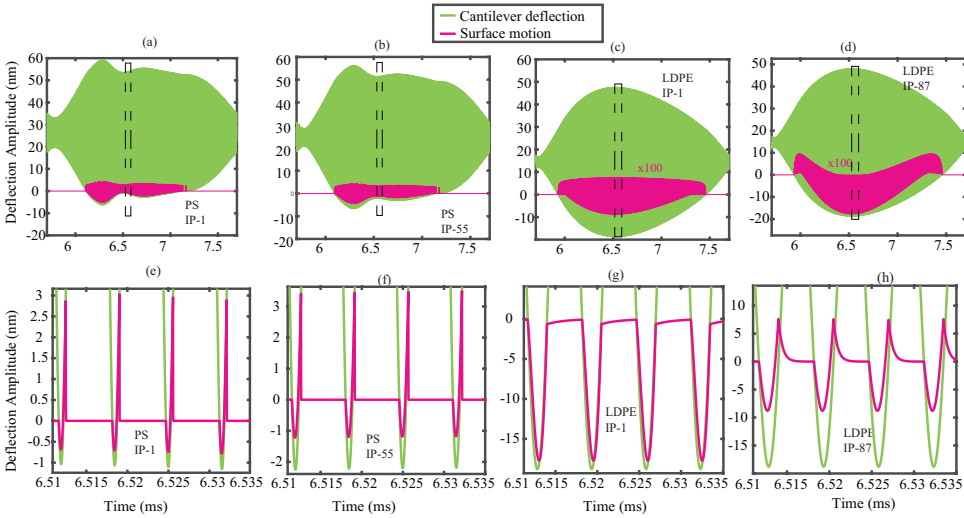


Figure 3: Simulations of the cantilever (green) and sample (pink) surface dynamics based on the results provided in table 1. (a)-(b) Simulated results for PS material with parameter values taken from initial point 1 and 55, respectively. (c)-(d) Simulated results for LDPE material with parameter values taken from initial point 1 and 87. (e)-(f)-(g)-(h) A close up visualization of the surface dynamics is reported in (a)-(b)-(c)-(d).

parameter value estimations. Contrary to the popular notion, the amplitude of surface motion in case of soft LDPE is also much smaller when compared to the stiff PS material.

We relate the above discrepancies to possible insensitivity of the objective function towards certain model parameters and the presence of multiple local minima, which indicates that the objective function is non-convex. To elaborate on these issues, we analyze the topological landscape of the objective function on a larger parameter range. We note that the objective function includes 6 parameters, out of which  $F_{ad}$  and  $h$  show consistent convergence. Hence, we limit our analysis to the bulk and surface viscoelastic

parameters governed by  $k_v$ ,  $\eta_v$ ,  $k_s$ , and  $\eta_s$ . This is showcased in Fig. 4, where topological landscapes of the objective function are obtained by sweeping across the viscoelastic parameters for both PS and LDPE material at pixels (i) and (iii), respectively. In each sub-figure, the four non-varied parameters are chosen as those of IP 1 in table 1. Interestingly, we note that Figs. 4(a)-(b) exhibit a valley in which a single optimum solution is found. This is further highlighted in the 2D cross sections shown as Figs. 4(c)-(d), confirming the strong dependency of parameters  $k_v$  and  $\eta_v$  on the experimental observables. Contrary to this, the objective landscape of Figs. 4(e)-(f) highlight multiple local minima (in the case of pixel (i) in Fig. 4(e)) or a flat insensitive gradient (for pixel (iii), in Fig. 4(f)). A flat landscape of the objective function in case of softer LDPE is counter-intuitive since one would expect a softer material to show pronounced surface dynamics compared to PS. This behaviour is also reflected in the large spread of values reported in table 1.

4

In order to verify that the discrepancy does not stem from the optimizer used, we also employ a heuristic global optimization technique in pursuit of a global solution in the parameter space. We create synthetic data sets with known optima to analyse how the global optimizer performs (for details see Section 4.A.2 in appendix). Once again the optimizer fails to overcome the aforementioned discrepancies. Since a wide range of non-physical parameter values reconstructs the cantilever motion while surface viscoelastic parameters do not affect the objective function. Upon closer inspection of results, we noticed a trend for synthetic data sets with good solution convergence, where the bulk parameters of the model, namely  $k_v$ ,  $\eta_v$ , tends to the original optimum (for details see table 4.A.2 in appendix). This is in accordance with our hypothesis regarding the insensitivity of surface viscoelastic parameters on the experimental observables. Therefore, fine-tuning of the global optimization parameter space is effective in determining bulk viscoelastic parameters. Nevertheless, isolation of non-physical solutions as outliers is computationally expensive when aiming for fast parameter estimation. For this reason we explore an alternative local optimization route paired with an initial point selection procedure in the following section.

### ESTIMATING BULK VISCOELASTICITY IN THE ABSENCE OF SURFACE MOTION

In order to overcome the aforementioned limitations as well as to improve the computational efficiency for the parameter estimation procedure, we neglect the surface dynamics of the sample and reduce the unknown parameter set to  $\vec{P} = \{F_{ad}, k_v, \eta_v, h\}$ . It must be noted that this reduced set is still descriptive of the nanomechanical mapping of polymer blends and coherent with several well-established formulations, *e.g.*, Derjaguin-Muller-Toporov (DMT)-Kelvin-Voigt [127], 3D Kelvin-Voigt [130], and DMT-Garcia [4].

We begin by repeating the quantitative analysis at pixels (i) and (iii) of Fig. 2, once again applying the Levenberg-Marquardt algorithm. In this procedure we use a grid of  $3^4$  IPs, by defining three values for the four free parameters of the model. This choice of three values is motivated by a compromise between a wide range of parameter exploration and a reasonable simulation duration. These parameter values include in particular at least one order of magnitude for the viscoelastic properties (for details see Section 4.B.2 in appendix). Furthermore, the three values of the probe height  $h$  can be framed from the force quadrature profiles and from onsets of repulsive forces (for de-

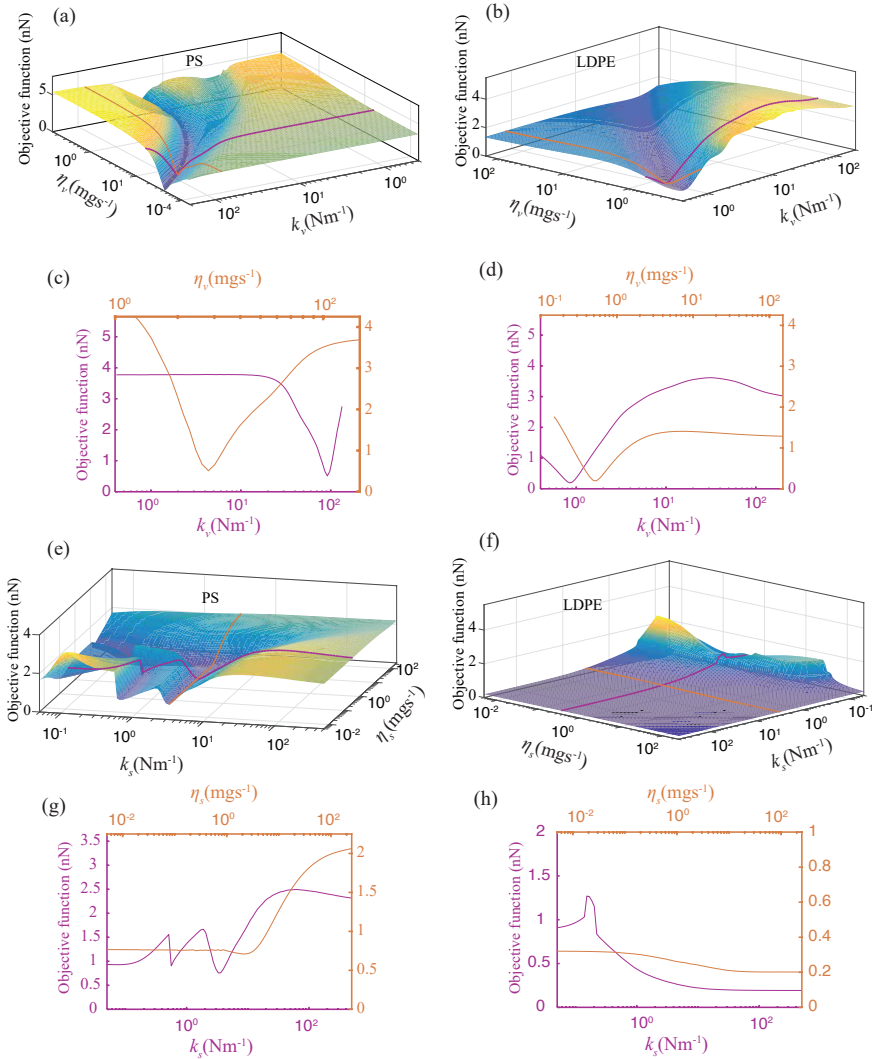


Figure 4: Variation of the objective function in a 2-dimensional parameter space comprising  $((k_s, \eta_s)$  or  $(k_v, \eta_v))$ , with the other parameters fixed in accordance with the best results found from the local minimization routine. (a)-(d) Visualizing the landscape of the minimization objective as a function of  $k_v$  and  $\eta_v$  for PS and LDPE material obtained at pixel (i) and (iii) of Fig. 2(b). The Pink and orange lines indicate a 2D cross-sectional view of the objective function. (a)-(d) Visualizing the landscape of the minimization objective as a function of  $k_s$  and  $\eta_s$  for PS and LDPE material obtained at pixel (i) and (iii) of Fig. 2(b). Pink and orange lines indicate 2D cross-sectional views of the objective function.

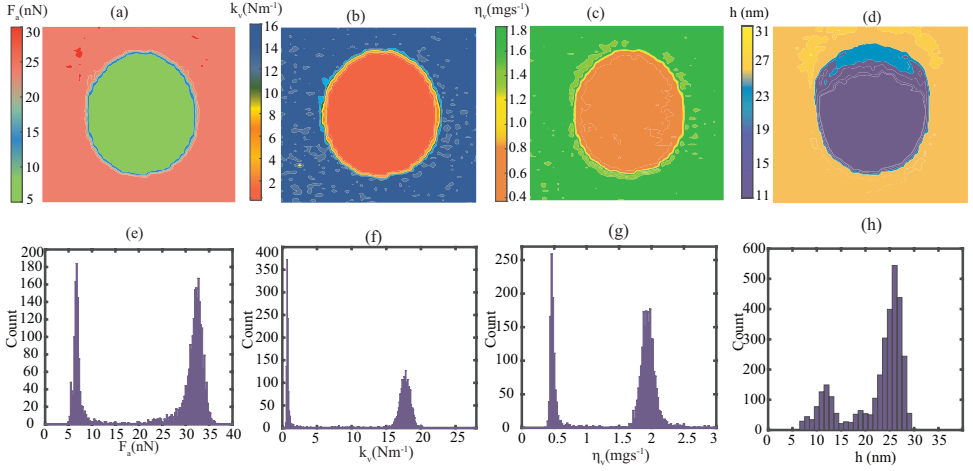


Figure 5: Estimated properties of the PS-LDPE sample obtained using the model without surface motion and the initial points selection procedure described in this work. The maps are of dimensions  $2.5 \mu\text{m} \times 2.5 \mu\text{m}$ . Left: parameter maps of (a) adhesion force, (b) contact force stiffness, (c) contact force viscosity, (d) Probe height. Right: histogram distribution of the respective parameters (e-f-g-h).

tails see Section 4.A.3 in appendix). We then perform a gradient-based optimization for each combination of parameters in the parameter space and conduct statistical analysis by obtaining the Gaussian distribution profiles of the identified parameters (for more details see Section 4.B.2 in appendix). Interestingly, for most of the IPs the optimizer converges towards an admissible physical solution.

Based on this statistical analysis we extract a set of three initial points for performing the parameter identification at all pixels of the entire AFM scan. The first two sets of IPs are derived from the mean values of the Gaussian distribution for both the PS and LDPE material. Indeed, these mean values lead to the lowest errors at pixels (i) and (iii). As for the third set, an IP is chosen which can lead to a set of identified parameter within a specific confidence interval for both the PS and LDPE material. The reasoning for choosing such an IP is rooted in our optimization procedure where, we assume that pixels belonging to the same material have similar objective function topology. This assumption may not hold true at the junctions where the two materials blend. Hence, having a third IP that could identify the parameters of both PS and LDPE material within a certain confidence interval is crucial to avoid non-physical parameter estimation (for details see Section 4.B.2 of appendix). Finally, among the three optimization run at each pixel, we retain the parameters of the best fit (*i.e.* the lowest error) as the identified model parameters.

Figure 5 shows the identified parameter values for the PS-LDPE polymer blend. It highlights a clear distinction between the identified bulk parameters  $F_{ad}$ ,  $k_v$ , and  $\eta_v$  between the island of LDPE and the surrounding PS matrix. This can be seen in the observed compositional contrast in the colored figures. Additionally, the histogram displayed on the right side of the figure highlights clear separated Gaussian profiles for each of the parameters. The estimated values lie within a 95% confidence interval for the

entire image, as table. 2 shows. Moreover, we remark that our identified values are in line with those previously reported in the literature [65, 127–129] and align with the expected physical behaviour of the two polymers, i.e ( $F_{a,PS} > F_{a,LDPE}$ ,  $k_{v,PS} > k_{v,LDPE}$  and  $\eta_{v,PS} > \eta_{v,LDPE}$ ). Our analysis suggests that intermodulation frequency components have a direct correlation with the bulk properties of the sample and the interaction force function can be robustly characterized.

	PS	LDPE
$F_{ad}$ [nN]	$31.49 \pm 0.12$	$6.960 \pm 0.076$
$k_v$ [N/m]	$17.31 \pm 0.09$	$0.819 \pm 0.020$
$\eta_v$ [mg/s]	$1.951 \pm 0.007$	$0.492 \pm 0.005$
$h$ [nm]	$26.71 \pm 0.02$	$12.86 \pm 0.021$

Table 2: Identified parameters resulting from the Gaussian fits, made from the material properties estimated at all pixels plotted in Fig. 5. The uncertainties are estimated with a 95% confidence interval.

## 4.5. CONCLUSIONS

In summary, we studied the dependency of viscoelastic response of polymeric samples to multi-frequency IM-AFM. We discussed the sensitivity issues that can be faced when minimizing the error between IM-AFM spectral components and a tip-sample force model with surface dynamics, and confirmed that insensitivity of surface viscoelasticity to experimental observables could lead to non-physical parameter estimations. We attribute this finding to the non-convexity and flat topological landscape of the objective function with respect to the sample's surface viscoelastic parameters. This was further reinforced with numerical simulations that used both gradient-based and heuristic global optimization techniques.

Next, we remedy this issue with a simplified model that only accounts for the bulk viscoelastic parameters and by implementing an initial point selection procedure that searches a large parameter space to estimate model unknowns with ease. This new framework results in consistent identification of viscoelastic parameters that are in good agreement with previously reported values. However, in order to take full advantage of the vast amount of multi-frequency observables, a more accurate and sensitive viscoelastic tip-surface model is needed [64, 65, 118], and computational developments to speed up the optimization process are required. Finally, given the growing interest in developing multi-parametric techniques in multi-frequency AFM, we believe that the techniques showcased in this work can be useful in providing guidance to future investigations that are aimed at studying soft, adhesive and viscoelastic surfaces of samples.

## APPENDIX

### 4.A. ADDITIONAL NUMERICAL DATA

#### 4.A.1. SIMULATIONS

The driving force signal  $F_d(t)$  used in the simulations is defined specifically for the experimental data considered in the study. In particular it is estimated for the set of frequency, stiffness and quality factor of the first resonance of the cantilever  $f_0, k$  and  $Q$  obtained from the thermal calibration. The excitation signal is obtained from the free motion frequency components as :

$$F_d(t) = \sum_{\omega \in \omega_{1M}} 2|\tilde{F}_d(\omega)| \cos(\omega t + \arg(\tilde{F}_d(\omega))) \quad (4.6)$$

with

$$\tilde{F}_d(\omega) = k \left[ -\frac{\omega^2}{\omega_0^2} + j \frac{\omega}{Q\omega_0} + 1 \right] \tilde{d}_{\text{free}}(\omega) \quad (4.7)$$

where the  $\omega_{1M}$  denotes the pulsation of intermodulation [117].

The time signals were simulated using the following dimensionless values:

$$\bar{d}_c = \frac{d_c}{A}, \quad \bar{d}_s = \frac{d_s}{A}, \quad \bar{F}_d = \frac{F_d}{kA}, \quad \bar{F}_{ts} = \frac{F_{ts}}{kA}, \quad \bar{t} = \omega_0 t, \quad \bar{h} = \frac{h}{A}, \quad \bar{s} = \frac{s}{A}. \quad (4.8)$$

in which the displacement of reference is the amplitude of the engaged motion at the second drive frequency  $A = |d_c|_{\omega=\omega_2}$ . The following dimensionless design parameters are considered in the numerical procedure:

$$\bar{F}_{ad} = \frac{F_{ad}}{kA}, \quad \bar{k}_v = \frac{k_v}{k}, \quad \bar{k}_s = \frac{k_s}{k}, \quad \bar{\eta}_v = \frac{\eta_v \omega_0}{k}, \quad \bar{\eta}_s = \frac{\eta_s \omega_0}{k}. \quad (4.9)$$

Thus the equation of motion is

$$\ddot{d}_c + \frac{\dot{d}_c}{Q} + d_c = F_d(t) + F_{ts}(s, \dot{s}) \quad (4.10)$$

in which the overbars are dropped for a sake of clarity. The time signals are computed by simulating Eq. (4.10) using Runge-Kutta schemes, which are at hand in standard functions of Matlab. At low sample relaxation times  $\bar{\tau}_s = \bar{\eta}_s / \bar{k}_s < 10^{-3}$ , a scheme designed for stiff systems is employed (the *ode23s* function of Matlab is used, instead of the classical *ode45* time integration solver). The signals for  $d_c$ ,  $d_s$  and  $F_{ts}$  are simulated on 8 ms, which corresponds to four intermodulation beatings since  $\Delta f = \frac{\omega_2 - \omega_1}{2\pi} = 500$  Hz is applied in experiments. A zero initial condition for displacements and velocities is applied, the tolerance is set at  $10^{-7}$ , and the nonsmooth event ( $s = 0$ ) is processed using a conditional rule.

#### OPTIMIZATION

The objective function used for estimating the viscoelastic parameters is defined by [117, 125]:

$$f(\mathbf{P}) = \sqrt{\sum_{\omega=\omega_{1m}} |\tilde{F}_{ts,\text{exp}}(\omega) - \tilde{F}_{ts,\text{sim}}(\omega, \mathbf{P})|^2}. \quad (4.11)$$



Next, in order to minimize Eq. (4.11) we use Levenberg-Marquardt algorithm [131] and combine it with non-linear least squares (*lsqnonlin* function) in Matlab. A least-square minimization is performed with an iterative procedure which involves the computation of the partial derivatives (gradient) at each iteration and it is based on a finite difference scheme.

A parallel implementation on a small cluster was used to perform multiple minimization routines: approximately 10 nodes and 36 hours in total were needed to obtain the results shown in Fig. 5. We show in table 4.A.1 the lower and upper limit of parameter values defined for the optimization. These parameter ranges are deliberately wide because we assume that we have no prior knowledge of the material properties, except in the case of the probe height for which a first approximation can be extracted from the force quadrature curves.

Parameter	$F_{ad}$ [nN]	$k_v$ [N.m <sup>-1</sup> ]	$\eta_v$ [mg.s <sup>-1</sup> ]	$k_s$ [N.m <sup>-1</sup> ]	$\eta_s$ [mg.s <sup>-1</sup> ]	$h$ [nm]
Min value	0.05	$\approx 0$	$\approx 0$	$\approx 0$	$\approx 0$	5
Max value	100	$10k$	$10k/\omega_0$	$20k$	$20k/\omega_0$	45

Table 4.A.1: Parameter ranges used for the optimization routine. Here,  $k$  represents the cantilever stiffness in N/m and  $\omega_0$  represents the first resonance frequency in rad/s

#### 4.A.2. RESULTS OF GLOBAL OPTIMIZATION TESTS ON SYNTHETIC DATA

In this section we discuss the use of a global optimization procedure for parameter estimation and further elaborate on the limitations of the procedure. In general global optimization techniques such as Particle swarm optimization does not rely on gradient descent method used by local optimization techniques like the Levenberg-Marquardt method, and hence don't require a differentiable objective function. Such a characteristic helps to determine if the lack of sensitivity of surface motion can be attributed to the chosen optimization algorithm or it is linked to model parameters. Additionally a global optimization method has the advantage that a large parameter space can be searched from different initial starting points without having prior knowledge on the optimum solution. However, in order to obtain a physically interpretable solution and to reduce the computational time, it is necessary to restrict the search range. We achieve this by assigning values for each of the model parameter from previous experimental characterizations and then extending their ranges by an order of magnitude [101, 121, 132].

In particular, we choose the sample parameters suitable for PS-LDPE material and generate synthetic data sets based on the interaction with a Silicon cantilever. The sample properties used for the simulations is provided in table 4.A.2 together with the following cantilever properties:  $f_0 = 163$  kHz,  $Q = 491$ ,  $k = 23.95$  N m<sup>-1</sup>, the effective driving force  $F_d = 1.39$  nN and the unperturbed height  $h = 22.6$  nm. Next, we use random sampling to select different starting parameter sets. A total of 15 different parameter sets are created and simulated with the moving surface model to generate the amplitude and phase frequency components which are then used as inputs for the Particle swarm based global optimization. For all the 15 data sets, the optimization procedure is performed starting from the same initial "swarm".

Table 4.A.2 shows the optimization results for 4 randomly chosen parameter sets out

No.	Designation	$F_{ad}$ [nN]	$k_\nu$ [ $\text{N}\cdot\text{m}^{-1}$ ]	$\eta_\nu$ [ $\text{mg}\cdot\text{s}^{-1}$ ]	$k_s$ [ $\text{N}\cdot\text{m}^{-1}$ ]	$\eta_s$ [ $\text{mg}\cdot\text{s}^{-1}$ ]	$E$ (pN)
$P_1$	Optimum	2.98	2.60	0.199	8.31	0.0371	3.80
	PSO	2.49	2.04	0.181	81.0	2.14	
	Error	16.4 %	21.3 %	9.17 %	875 %	5670 %	
$P_2$	Optimum	0.161	0.0101	0.141	0.220	1.51	0.254
	PSO	0.165	0.0100	0.135	16.8	0.00155	
	Error	3.00 %	0.547 %	4.05 %	7.53e3 %	99.9 %	
$P_3$	Optimum	4.49	6.81	0.0221	0.108	0.582	21.1
	PSO	8.18	0.97	0.378	0.938	0.00105	
	Error	39.6 %	25.7 %	20.0 %	680 %	99.0%	
$P_4$	Optimum	0.473	0.349	0.469	65.5	0.0105	0.812
	PSO	0.277	0.283	0.802	1.20	0.0360	
	Error	41.5 %	19.0 %	71.1 %	98.2 %	245 %	

Table 4.A.2: Parameter Convergence for data sets  $P_1$ ,  $P_2$ ,  $P_3$  and  $P_4$ . Cantilever properties used:  $f_0 = 163$  kHz,  $Q = 491$ ,  $k = 23.95$  N/m. Scanning properties:  $F_d = 1.39$  nN,  $h = 22.6$  nm, and 41 amplitude and phase intermodulation products.

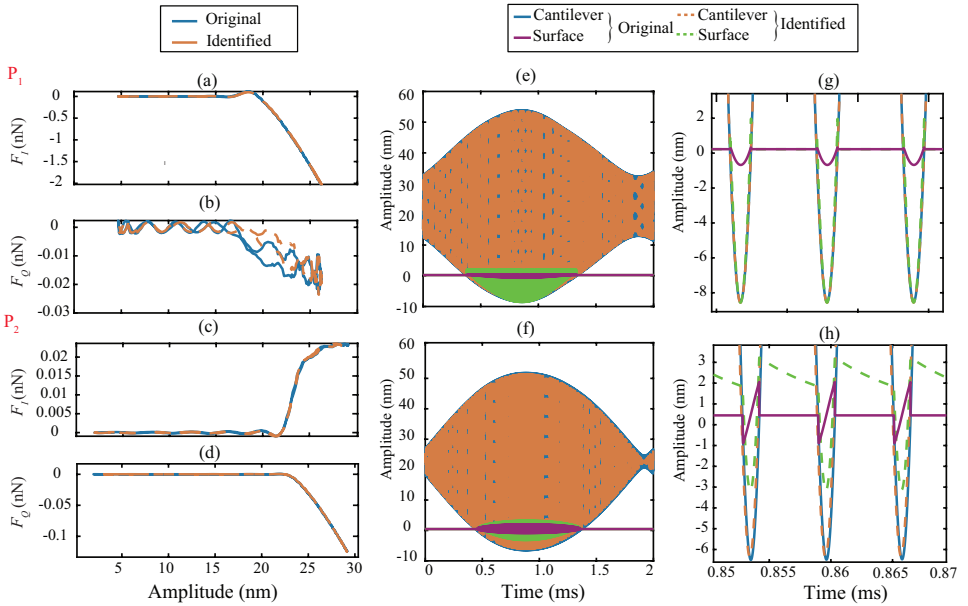


Figure 4.A.1: Global optimization results for parameter sets 1 and 2. Cantilever properties:  $f_0 = 163$  kHz,  $Q = 491$ ,  $k = 23.95$  N/m. Scanning properties:  $F_d = 1.39$  nN,  $h = 22.6$  nm, and 41 amplitude and phase intermodulation products. (a)-(d) Force quadratures showing the conservative and dissipative tip-sample interactions. The blue color represents the original quadratures obtained from model simulations and the orange color represents the identified quadratures based on optimization. (e)-(f) Time data depicting the motion of the cantilever and the corresponding surface motion due to tip-sample interaction. right: (g)-(h) Zoomed surface motion indicating discrepancies between the original and the identified surface dynamics. The blue and purple color represents the original cantilever and surface dynamics obtained from model simulations; whereas, the orange and green color the original cantilever and surface dynamics based on optimization.

of 15 simulated data sets. The results show that tip-sample dynamics is well approximated with low error values  $E$ , but the identified parameter values are far from their true values. This deviation is far more significant for surface parameters in comparison with bulk parameters. Once again, we attribute this issue to non-convexity and lack of sensitivity of surface parameters as discussed in the main chapter. Additionally, Figs. 4.A.1 and 4.A.2 show the temporal data of the cantilever and the associated surface motion together with the force quadratures for both the original dynamics coming from the model simulations and the identified dynamics resulting from optimization. In both the figures, while we observe a good agreement for the force quadratures, the identified motion of the sample surface does not match with the simulated motion (See Figs 4.A.1(g)-(h) and 4.A.2(g)-(h)). This further confirms the trivial contribution of the surface motion on amplitude and phase of intermodulation components.

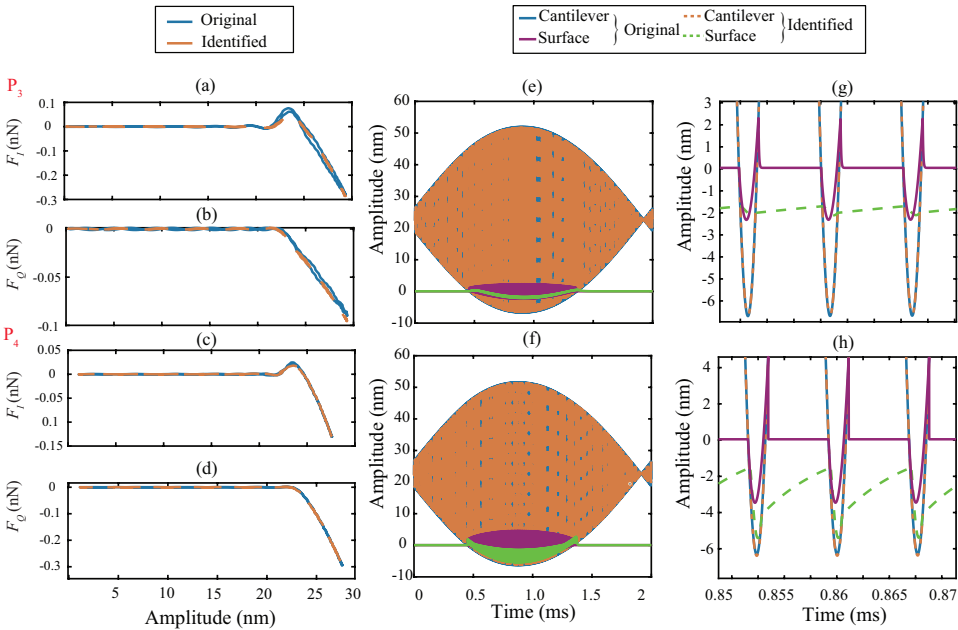


Figure 4.A.2: Global optimization results for parameter sets 3 and 4. Cantilever properties:  $f_0 = 163$  kHz,  $Q = 491$ ,  $k = 23.95$  N/m. Scanning properties:  $F_d = 1.39$  nN,  $h = 22.6$  nm, and 41 amplitude and phase intermodulation products. (a)-(d) Force quadratures showing the conservative and dissipative tip-sample interactions. The blue color represents the original quadratures obtained from model simulations and the orange color represents the identified quadratures based on optimization. (e)-(f) Time data depicting the motion of the cantilever and the corresponding surface motion due to tip-sample interaction. right: (g)-(h) Zoomed surface motion indicating discrepancies between the original and the identified surface dynamics. The blue and purple color represents the original cantilever and surface dynamics obtained from model simulations; whereas, the orange and green color the original cantilever and surface dynamics based on optimization.

### 4.A.3. CRITERION FOR PROBE HEIGHT IDENTIFICATION FROM FORCE QUADRATURES

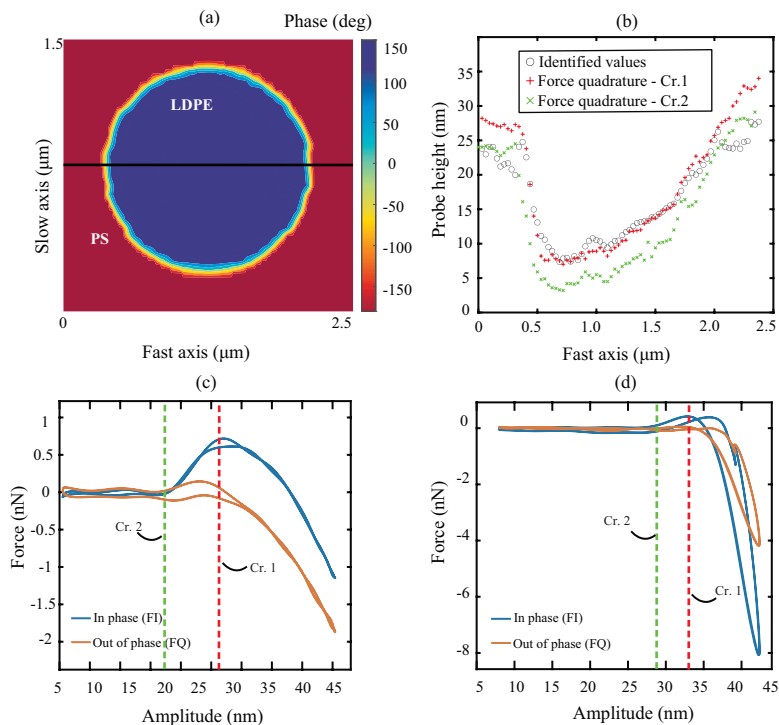


Figure 4.A.3: Portion of the extracted line for the analysis in the AFM image (top left). Identified  $h$  and reported values directly read from the force quadratures (top right). Illustration of the two criteria (dashed lines) for estimating the probe height on the quadratures on one pixel made of PS (bottom left) and of LDPE (bottom right).

The probe height  $h$  is included in the set of unknown parameters (see main chapter modelling section). In general  $h$  varies with the working height of the cantilever which in turn depends on how much the feedback control moves the z-piezo during the scanning operation. By taking advantage of the conservative quadrature, in phase with the cantilever motion, it is possible to estimate an approximate value for  $h$  based on the onset of repulsive forces.

We suggest two criteria for extracting  $h$  from force quadratures as illustrated in Fig. 4.A.3. We assume the maximum of the in-phase force component (related to adhesion) is achieved closely after the tip starts to penetrate the sample. Thus, the first criterion (denoted by red crosses in Fig. 4.A.3 (b)) is taken at the middle of the increasing part of  $F_I$ , whereas the second one corresponds to the amplitude where the in-phase component starts to increase. We browse and apply these two criterion on all pixels of the black line displayed in Fig. 4.A.3(a). The comparison shown in Fig. 4.A.3(b) highlights a better match between the heights corresponding to LDPE pixels using the first criteria, when the second criteria seems more suited for the pixels related to PS material. That

can be explained by the different material properties, for instance the larger stiffness for PS causes a faster increase of  $F_I$ , whereas in case of the softer material the short-range adhesive force is more significantly involved before the tip starts to indent the sample. The analysis of these force quadrature curves could be further developed using a more accurate tip-sample force model such as Attard's model [40, 63–65, 119], in order to describe first the transition between the non-contact and adhesive regime, and secondly the transition between the adhesive and repulsive regime.

## 4.B. HIGH VOLUME GRADIENT BASED OPTIMIZATION AND INITIAL POINT SELECTION PROCEDURE

In this section, we discuss the results obtained using the Levenberg-Marquardt algorithm from multiple initial points for both models with and without sample's surface motion. This is done to analyze the sensitivity of the model on initial starting points for the optimization. We begin by creating a numerical range for each parameter based on previous literature studies. Then, a grid of initial starting points is chosen and for each initial point we perform the optimization routine. The distribution of the identified parameters is analysed with histograms and by fitting Gaussian function to extract statistics. The distribution are discussed for each model separately in the following sections.

### 4.B.1. PIECEWISE LINEAR MODEL WITH SURFACE MOTION

Using the moving surface model, we run multiple gradient-based optimizations for pixel (i) and pixel (iii) of Fig. 2 with the grid of initial parameters defined in table 4.B.1. The grid includes 3 different values per parameters, chosen in such a way that the parameter exploration recovers a large parameter space (including notably at least one order of magnitude in the case of the viscoelastic properties), and that all routines are performed within a reasonable computational time. In total,  $3^6 = 729$  optimizations were performed, starting from all the combinations of the grid.

In this section we present the histograms used to extract the values reported in table 1.

$F_{ad}$ [nN]	$k_v$ [N.m <sup>-1</sup> ]	$\eta_v$ [mg.s <sup>-1</sup> ]	$k_s$ [N.m <sup>-1</sup> ]	$\eta_s$ [mg.s <sup>-1</sup> ]	$h$ [nm]
[5 25 45]	[0.02 1 40]	[0.2 1 5]	[0.02 1 40]	[0.2 1 5]	[15 25 35]

Table 4.B.1: Grid of initial points for the local optimization procedure using the moving surface model.

Figures 4.B.1 and 4.B.2 highlight the distribution of the identified parameters with respect to the objective function for pixels (i) and (iii), respectively. We see a clear correlation between a large distribution and low errors only for some parameters such as  $F_a$ ,  $k_v$ ,  $\eta_v$ ,  $h$  for pixel (iii) in Fig. 4.B.1. If model parameters have strong correlation with the objective function then the maximum of the histogram counts (rows 1 and 3) coincides with the minima of the scatter plots (rows 2 and 4). For example, in case of Figs. 4.B.1(a) and (d), we look at the influence of adhesion force  $F_a$  on the objective function and we observe that the location of the maximum along the x-axis in Fig. 4.B.1(a) coincides with the minima along the same x-axis in Fig. 4.B.1(d). A similar behaviour is observed in Figs. 4.B.1 (b)&(e), (c)&(f), and (i)&(l). On the contrary, Figs. 4.B.1 (g)&(j) and (h)&(k) lack

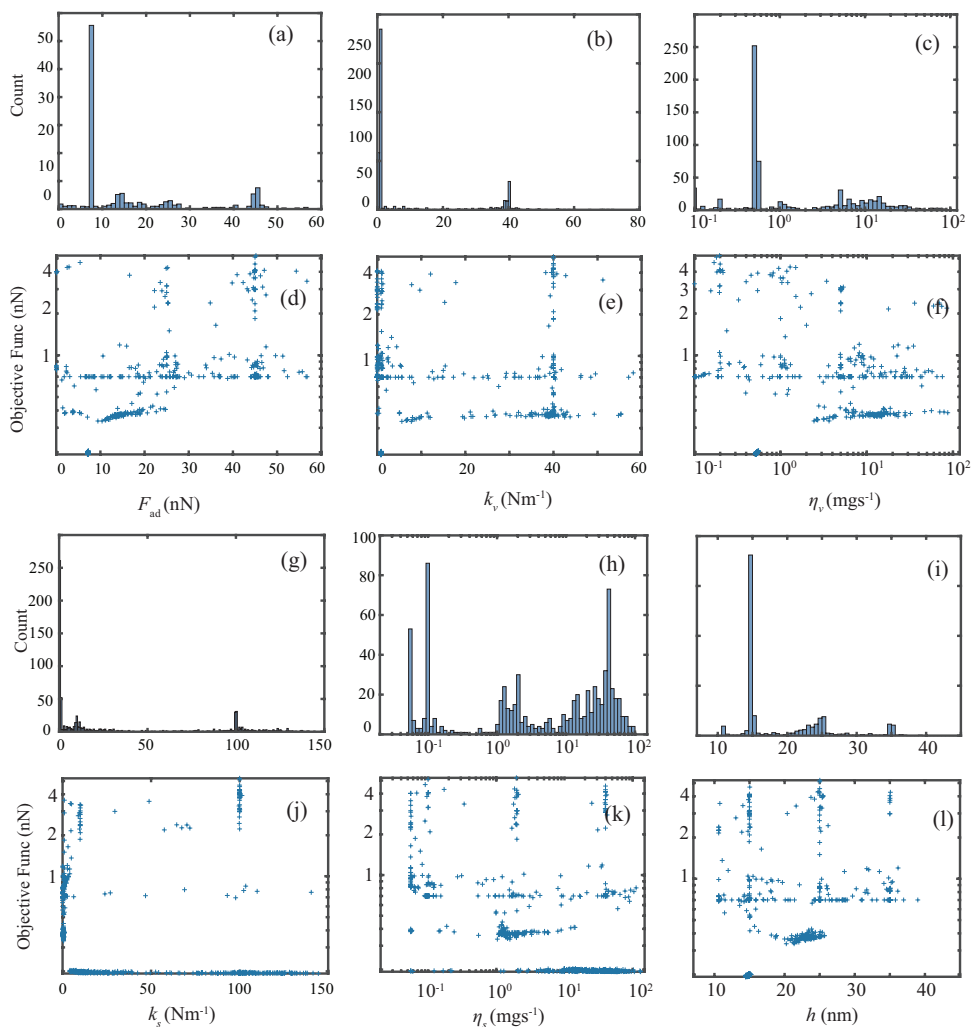


Figure 4.B.1: Identified parameters of the PWL model with sample motion, obtained on LDPE material at pixel (iii) of Fig. 2(b) with the initial positions defined in table 4.B.1. Parameter distributions and errors are respectively plotted in (a)&(d) for  $F_{ad}$ , (b)&(e) for  $k_v$ , (c)&(f) for  $\eta_v$ , (g)&(j) for  $k_s$ , (h)&(k) for  $\eta_v$  and (i)&(l) for  $h$ .

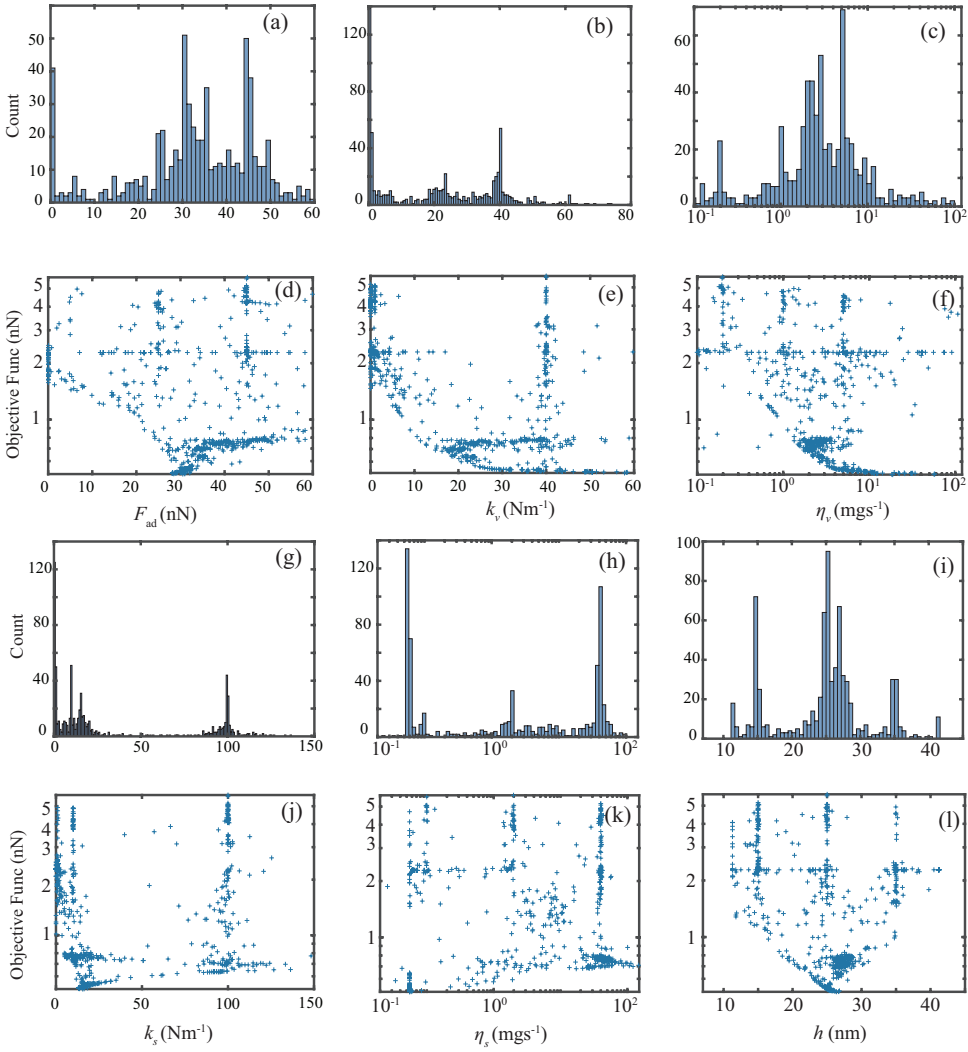


Figure 4.B.2: Identified parameters of the PWL model with sample motion, obtained on PS material at pixel (i) of Fig. 2(b) with the initial positions defined in table 4.B.1. Parameter distributions and errors are respectively plotted in (a)&(d) for  $F_{ad}$ , (b)&(e) for  $k_v$ , (c)&(f) for  $\eta_v$ , (g)&(j) for  $k_s$ , (h)&(k) for  $\eta_v$  and (i)&(l) for  $h$ .

such property and instead exhibit random and spread distributions. This behavior is due to the insensitivity of the objective function to the sample parameters. A similar observation holds for the PS material (Fig. 4.B.2) with an even more complex distribution. It is here attributed to the combined effect of non-convexity and insensitive regions in which the optimizer encounters a stopping condition.

#### 4.B.2. PIECEWISE LINEAR MODEL WITHOUT SURFACE MOTION

Here, we report the results and histograms obtained from the large set of optimizations carried out using the piecewise linear model without surface motion. We begin with a set of  $3^4$  initial parameters defined by the grid presented in table 4.B.2, and analyze the parameter distributions in the same way as outlined in the previous section.

4

$F_{ad}$ [nN]	$k_v$ [N.m <sup>-1</sup> ]	$\eta_v$ [mg.s <sup>-1</sup> ]	$h$ [nm]
[5 25 45]	[0.02 1 40]	[0.2 1 5]	[15 25 35]

Table 4.B.2: Grid of initial points for the local optimization procedure using PWL model without sample motion.

With the 4 parameters model, statistics for the identified parameters depicts well defined Gaussian distributions that are specific for each type of material. Additionally, the mean of the Gaussian distributions correspond to the lowest values of the objective function. This is shown in Figs. 4.B.1 and 4.B.2 for PS and LDPE material sampled at pixel locations (i) and (iii) of Fig. 2. The parameter values from the optimization procedure are reported in table 4.B.3.

From this statistical analysis, we extract a reduced set of starting parameters. The parameters summarised in table 4.B.4 have been used to obtain the results showcased in Fig. 5. The two first initial points in Table 4.B.4 were selected by identifying the mean values (also corresponding with the lowest error) among the final results displayed in Figs. 4.B.3 and 4.B.4. In addition, we add a third initial point leading to identified parameters within the confidence intervals for all parameters and both the pixels. We detail the final parameters and errors obtained on pixels (i) and (iii) with these three initial points in table 4.B.5.

	Pixel (i)	Pixel (iii)
$F_{ad}$ [nN]	$32.7 \pm 0.45$	$7.13 \pm 0.008$
$k_v$ [N/m]	$17.52 \pm 0.52$	$0.854 \pm 0.002$
$\eta_v$ [mg/s]	$1.975 \pm 0.006$	$0.519 \pm 0.001$
$h$ [nm]	$26.7 \pm 0.18$	$14.7 \pm 0.03$

Table 4.B.3: Identified parameters resulting from the Gaussian fits. We extracted the results with errors smaller than 0.71 nN for pixel (i) (cf Fig. 4.B.4) and 0.25 nN for pixel (iii) (cf Fig. 4.B.3). The uncertainties are estimated with a 95% confidence interval.



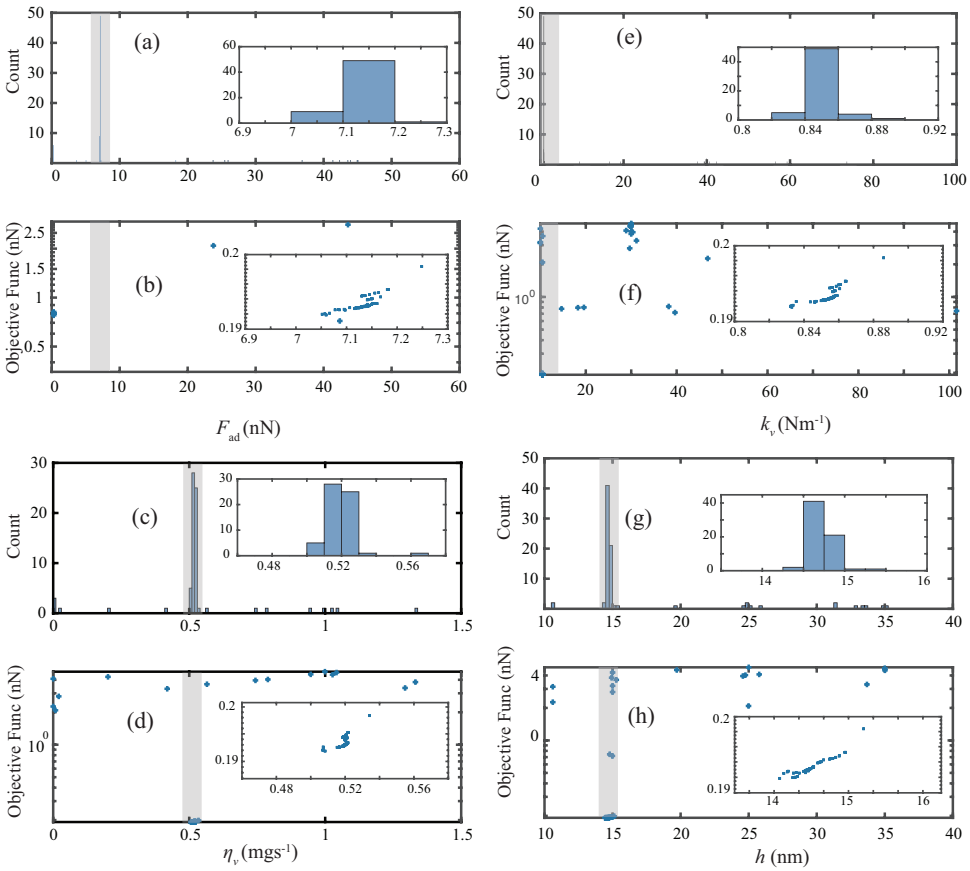


Figure 4.B.3: Identified parameters of the PWL model without sample motion, obtained on pixel (iii) Fig. 2(b) (LDPE) from the initial positions defined in table 4.B.2. Parameter distributions and errors are respectively plotted in (a)&(b) for  $F_{ad}$ , (e)&(f) for  $k_v$ , (c)&(d) for  $\eta_v$  and (g)&(h) for  $h$ . The shadowed areas highlight the Gaussian distributions.

$F_{ad}$ [nN]	$k_v$ [N.m <sup>-1</sup> ]	$\eta_v$ [mg.s <sup>-1</sup> ]	$h$ [nm]
[45 5 5]	[0.02 1 1]	[0.2 1 1]	[35 35 15]

Table 4.B.4: Initial starting parameters used as inputs for the optimization performed on the AFM scan shown in Fig. 5.

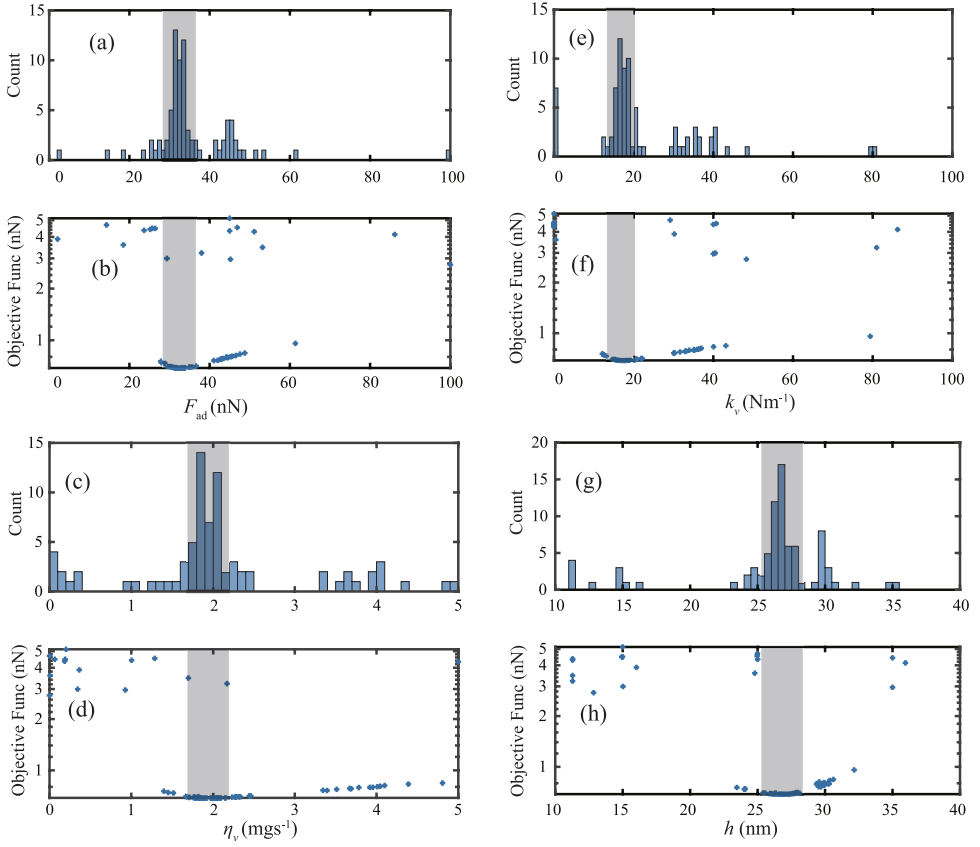


Figure 4.B.4: Identified parameters of the PWL model without sample motion, obtained on pixel (i) of Fig. 2 (PS), starting from the initial positions defined in table 4.B.2. Parameter distributions and errors are respectively plotted in (a)&(b) for  $F_{ad}$ , (e)&(f) for  $k_v$ , (c)&(d) for  $\eta_v$  and (g)&(h) for  $h$ . The shadowed areas highlight the Gaussian distributions.

Pixel (i)					Pixel (iii)				
Final parameters				Final Error	Final parameters				Final Error
$F_{ad}$	$k_v$	$\eta_v$	$h$	$E$	$F_{ad}$	$k_v$	$\eta_v$	$h$	$E$
[nN]	[N/m]	[mg/s]	[nm]	[nN]	[nN]	[N/m]	[mg/s]	[nm]	[nN]
32.9	17.74	1.99	26.9	0.68	0.3	9.33	21.1	31.5	0.78
33.8	18.6	2.08	27.0	0.69	7.06	0.833	0.508	14.4	0.192
32.0	16.7	1.89	26.6	0.69	7.12	0.852	0.519	14.6	0.193

Table 4.B.5: Identified parameters and final errors obtained at pixels (i) and (iii) from the three selected initial points defined in table 4.B.4.

5

5

# 5

## DATA-DRIVEN FORCE RECONSTRUCTION IN DYNAMIC ATOMIC FORCE MICROSCOPY

*Dynamic AFM is a key platform that enables topological and nanomechanical characterization of novel materials. This is achieved by linking the nanoscale forces that exist between the AFM tip and the sample to specific mathematical functions through modeling. However, the main challenge in dynamic AFM is to quantify these nanoscale forces without the use of complex models that are routinely used to explain the physics of tip-sample interaction. Here, we make use of machine learning and data science to characterize tip-sample forces purely from experimental data with sub-microsecond resolution. Our machine learning approach is first trained on standard AFM models and then showcased experimentally on a polymer blend of Polystyrene (PS) and Low Density Polyethylene (LDPE) sample. Using this algorithm we probe the complex physics of tip-sample contact in polymers, estimate elasticity, and provide insight into energy dissipation during contact. Our study opens a new route in dynamic AFM characterization where machine learning can be combined with experimental methodologies to probe transient processes involved in phase transformation as well as complex chemical and biological phenomena in real-time.*

This chapter is published as an article in *Nanoscale Advances* [133]. The published article is adapted to fit into the context of the thesis.

Dynamic atomic force microscopy (AFM) has transitioned from a high resolution imaging technique to a versatile tool that provides spatially resolved maps of mechanical [4, 5], chemical [19, 134], and biological properties [6, 7] of samples. This transition is primarily fueled by the interest of the scientific community in precise quantification of materials at the nanoscale, which can be achieved by probing the tip-sample interaction force [5, 6]. However, dynamic AFM, in contrast to its name, does not directly measure the interaction force while imaging in any of its modalities. Instead, it uses different information channels like frequency, amplitude, and phase of the oscillating probe to reconstruct the interaction force indirectly [54, 66–71].

Tip-sample reconstruction in dynamic AFM is essentially an inverse problem [135–137], where the measured deflection data is used to infer the underlying interaction physics and thus estimate parameters that are not directly observed. The reconstruction techniques in dynamic AFM are broadly categorized into two classes: analytical methods that rely on slow variations of amplitude and phase of the cantilever [66–69], and experimental techniques that depend on the spectral components generated due to the nonlinear nature of the tip-sample contact [54, 70, 71]. Although versatile in discerning the tip-sample force, analytical methods cannot trace the variations in interaction force at the fast time scale; a scenario that is of importance when probing biological and chemical processes [9, 12, 13]. On the other hand, experimental techniques often follow a multi-step procedure to invert cantilever oscillations for obtaining the interaction force. These procedures either require measurement of the experimental transfer function [71] or make use of special harmonic probes that are tailor-made to resolve the interaction force with high-resolution [54]. Thus, despite the success of dynamic AFM in topography mapping and nanoscale imaging in its diverse modes of operation [50], a generic approach that allows direct access to the time-resolved surface forces, irrespective of the chosen probe-sample configuration is still missing.

Here, we develop a novel method for reconstructing the tip-sample interaction forces of dynamic AFM by making use of the recent advances in data science [73] and machine learning [138–140] that are well-suited for tackling inverse problems. In particular, we make use of sparse identification of nonlinear dynamical systems [73, 139–142] to distill the governing equations of dynamic AFM. We train the algorithm on numerically generated data from several standard AFM models, and use that to discover physically interpretable models in experiments. The discovered models are able to predict the time-resolved interaction forces in dynamic AFM with sub-microsecond resolution. Unlike existing methods, our approach has no inherent assumptions on the type of interactions, and instead, relies solely on the extracted temporal data from AFM measurements. Using this method we are able to extract the variation in contact duration and peak loading forces in stiff and compliant materials as well as highlight the ability of the technique in probing transient surface forces and hysteresis phenomenon during tip-sample interactions.

## 5.1. FORMULATION

In order to obtain the tip-sample interaction force, we begin by finding the governing equations of AFM using an unified sparse identification framework known as sparse relaxed regularized regression [138, 139, 141]. This approach aims at finding the equations

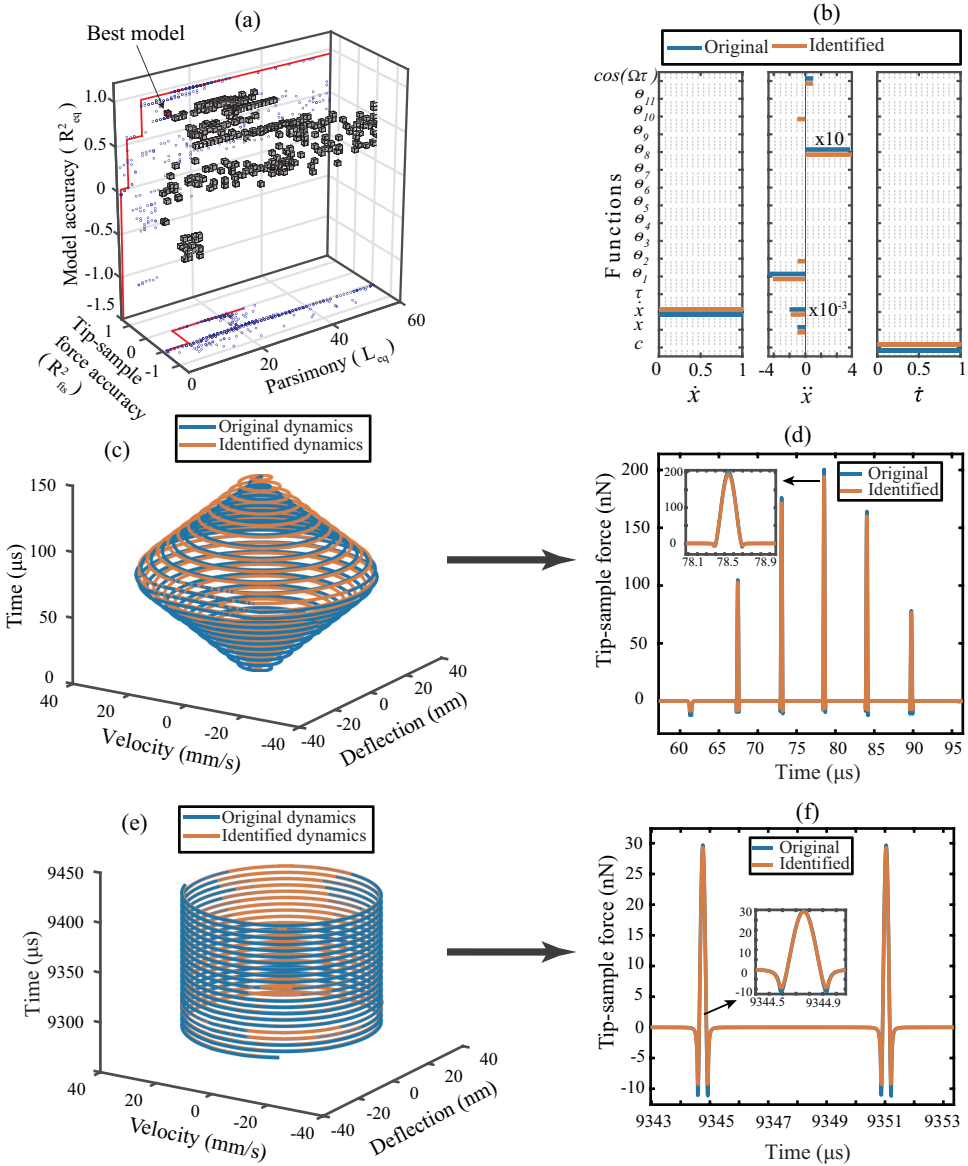


Figure 1: Training the algorithm on synthetic data obtained for a cantilever with DMT force model described in Appendix 5.D.1 [48, 99]. (a) 3D pareto frontier with parsimony, accuracy of the predicted model, and the tip-sample force as the selection parameters. The blue dots indicate the projection of the 3D cubes onto 2D planes. In the  $(x,z)$  plane the red line indicates the pareto optimal line between parsimony and the model accuracy; whereas, in the  $(x,y)$  plane it is the optimal line between the parsimony and the tip-sample force accuracy. The best model in this 3D space is highlighted by a red cube. (b) Coefficient matrix showing the influence of each library function on the governing equations. The blue color indicates the original value of the coefficients and the orange color indicates the coefficients as determined by the data-driven algorithm. The description of the functions are given in table. 1. (c)-(d) Transient dynamics prediction: Comparison of the state vectors and the tip sample force between the DMT simulation (blue) and the data-driven model (orange). (e)-(f) Steady-state response prediction: Comparison of the state vectors and the tip sample force between the DMT simulation (blue) and the data-driven model (orange). Additional details on selection of hyper-parameters and constraints on the optimization are provided in the methods section.

Table 1: Description of the nonlinear functions used in the coefficient matrix of Fig. 1(b). We represent the instantaneous tip-sample distance by  $z$ , the indentation depth by  $\delta$ , the intermolecular distance by  $a_0$  and the normalized time vector as  $\tau$ . It should be noted that both  $z$  and  $\delta$  are functions of  $x$ .

Function ID	$\theta_1$	$\theta_2$	$\theta_3$	$\theta_4$	$\theta_5$	$\theta_6$	$\theta_7$	$\theta_8$	$\theta_9$	$\theta_{10}$	$\theta_{11}$
Function definition	$z^{-2}$	$z^{-3}$	$\delta^{0.5} \delta$	$\delta \delta^2$	$z^{0.5} z$	$z z^2$	$\delta^2$	$\delta^{2.5}$	$\delta^{1.5}$	$z^{-2} \forall z \leq a_0$	$\sin(\Omega\tau)$

of nonlinear dynamical systems of the form

$$\dot{\mathbf{x}}(t) = \mathbf{f}(\mathbf{x}(t)), \quad (5.1)$$

subjected to initial condition  $\mathbf{x}(0) = \mathbf{x}_0$ , where  $\mathbf{x}(t) \in \mathcal{R}^n$  is the state of the dynamical system at time  $t$  in the experimental time frame. Here,  $\mathbf{f}$  is a nonlinear function that maps the dynamical state vectors to that of the experimental observables. In order to retrieve a minimal set of  $\mathbf{f}$ , a library of linear and nonlinear candidate functions  $\Theta(\mathbf{X}) = [\theta_1(\mathbf{X}) \theta_2(\mathbf{X}) \dots \theta_n(\mathbf{X})]$  is introduced such that

$$\mathbf{f}(\mathbf{x}(t)) = \Theta(\mathbf{X})\Xi,$$

where  $\Xi = [\xi_1 \xi_2 \dots \xi_n]$  is the unknown coefficient vector containing weights for each of the candidate functions that shall be determined. In addition,  $\mathbf{X} = [\mathbf{x}(t_1) \mathbf{x}(t_2) \dots \mathbf{x}(t_n)]^T$  are snapshots of the time histories used as the inputs. Here, for example  $\mathbf{x}(t_1) = [\mathbf{x}_1(t_1) \mathbf{x}_2(t_1) \dots \mathbf{x}_n(t_1)]$  is a vector containing the measurements of all  $n$  state vectors at a specific time interval  $t_1$ . Moreover, the time series may include trajectories from multiple initial conditions concatenated together. We note that, the derivative  $\dot{\mathbf{X}}$  is not an experimental observable but can be numerically evaluated from  $\mathbf{X}$ . Finally, the unknown vector  $\Xi$  is found by solving the following optimization problem via sparse regression

$$\begin{aligned} \min_{\mathbf{W}, \Xi} \frac{1}{2} \|\dot{\mathbf{X}} - \Theta(\mathbf{X})\Xi\|^2 + \lambda R(\mathbf{W}) + \frac{1}{2\nu} \|\Xi - \mathbf{W}\|^2 \\ \text{s.t } \mathbf{C}\Xi =: \mathbf{d}. \end{aligned} \quad (5.2)$$

In Eq. (5.2),  $R(\cdot)$  is the regularization function that promotes sparsity and minimizes over-fitting. In our study, we choose  $R(\cdot)$  as the  $l_0$  norm of the auxiliary variable  $\mathbf{W}$ . This variable is introduced here to enable relaxation and partial minimization in order to improve the conditioning of the problem and tackle the non-convexity of the optimization [139]. In addition,  $\lambda$  and  $\nu$  are hyper-parameters that control the strength of regularization and relaxation, respectively. Finally, in order to find physics-inspired models, we incorporate constraints derived from experiments through matrices  $\mathbf{C}$  and  $\mathbf{d}$  (See Appendix 5.B). In particular, these constraints make sure that during model discovery the stiffness  $k$ , quality factor  $Q$ , and external force  $F_c$  exerted on the cantilever match those from experiments.

## 5.2. TRAINING

We begin by training the algorithm over numerically generated data sets from several standard AFM models. For the sake of clarity, we explain the training methodology on



the data obtained from a Derjaguin-Muller-Toporov (DMT) model here [35]. The training data includes both the transient and steady-state interactions typically observed during scanning operation in dynamic AFM as shown in Fig. 1.

In our study, the library  $\Theta(\mathbf{X})$  consists of constants, polynomials, and trigonometric terms of  $\mathbf{X}$ . To predict the true physics of interaction, we also incorporate nonlinear functions in  $\Theta(\mathbf{X})$  that are derived from consolidated AFM models (e.g., DMT [35], Johnson, Kendall and Roberts (JKR) [34] and Lennard-Jones (LJ) [29] as discussed in Appendix 5.D).

In addition to the functions describing the tip-sample interactions, the library also includes bridging functions that mediate a smooth switch between the attractive and repulsive forces experienced by the tip's trajectory at the intermolecular distance ( $a_0$ ). Overall, we used 500 functions  $\theta_i$  in the training phase of the analysis. To mimic experimental conditions, we also corrupted the numerically generated state vectors  $\mathbf{X}$  with 1% Gaussian noise with zero mean. This signal is then differentiated by using Savitzky-Golay algorithm [143] to obtain the velocity, and acceleration vectors.

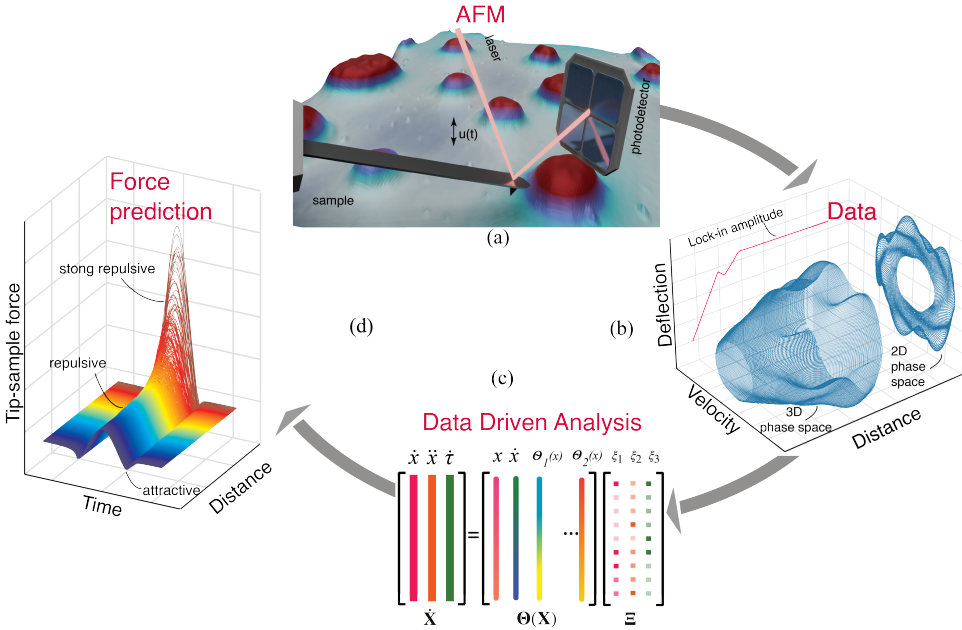


Figure 2: Schematic of the identification process. (a) Experimental data is obtained directly from the photodetector of the AFM. (b) The data is captured using an FPGA device and post-processed to create state vector channels. (c) The state vectors are used as inputs in the sparse identification algorithm to discover the governing model of the system. (d) The data-driven model is used to estimate the tip-sample interaction force.

Before proceeding with the sparse identification, elimination of non-candidate functions from the library  $\Theta(\mathbf{X})$  is necessary to improve the interpretability of the predicted models and avoid ill-conditioned matrices or large computational times [140]. In order to achieve this, we augment the optimization problem defined in Eq. (5.2) with constraints derived from experiments [99], the details of which are provided in the Ap-

pendix 5.B.

Finally, the noisy state measurements and the constraints are fed into the data-driven algorithm as part of a final routine in which the hyper parameters  $\lambda$  and  $\nu$  are swept in a 2D space to obtain an approximate model capable of predicting the dynamics of the system. For each configuration of hyper-parameters, we perform 10 instance of rolling cross-validation with each instance running 250 iterations of an optimization routine to determine the optimum value of the coefficients. The optimization objective is defined such that the identification routine will find the best parsimonious model by penalizing the goodness of fit value based on the number of terms present in that particular model. In other words, the lengthier the equation of motion the more penalty the model is awarded. This not only promotes parsimony but also improves the general interpretability of the predicted model.

### 5.2.1. NUMERICAL RESULTS

In order to identify the best model that can approximate the dynamics of the system, we build a three dimensional (3D) pareto diagram as shown in Fig. 1(a). The 3D Pareto frontier is calculated by plotting parsimony (the length of the identified equation of motion  $L_{eq}$ ) on the x-axis, the accuracy of state vector prediction on the z-axis ( $R_{eq}$ ) and the accuracy of the tip-sample force on the y-axis ( $R_{fts}$ ). The best model is readily identifiable by following the marked red line at the sharp drop in prediction accuracy (marked by the red cube). In table 1 we list the candidate functions that represent the best model, and in Fig. 1(b) we compare the coefficients of this identified model (orange line) against the original DMT model (blue line) based on which the numerical data were generated. It can be seen that the identified coefficients are within 1% of their true values. We also note that the data-driven approach has led to two additional functions, namely  $\theta_2$  and  $\theta_{10}$  that were not present in the original model. This can be understood by comparing the total number of blue lines vs orange lines. Among the two,  $\theta_2$  appears in the identified model purely due to the noise added to the state vectors. Whereas,  $\theta_{10}$  acts as a bridging function to connect the non-smooth interaction forces namely, the non-contact Van der Waals and the contact repulsive forces. We highlight that the DMT model inherently contains a bridging function in the form of adhesion force given by  $f_{adh} = C_3/a_0^2$  (see Appendix 5.D.1).

To clarify this observation further, we compare the transient and steady-state response of the predicted model with the true dynamics in Figs. 1(c) and (e). We observe that the motion of the cantilever is well-replicated with an accuracy of 95% in a 3D phase space. The resulting 5% estimation error is due to the deviation of the identified coefficients from the true values which causes a small shift in the phase value between the original and the identified trajectories (For details, see Appendix 5.D.3).

Irrespective of this slight discrepancy, the ability of the selected model to unravel the corresponding tip-sample interaction force stands out in Figs. 1(d) and (f). Figure 1(d) shows the development of transient tip-sample interaction force when the cantilever encounters a step like feature during the scanning; whereas, Fig. 1(f) shows the steady-state tip-sample interaction force when the cantilever is imaging a uniform surface. In both cases, the blue and the orange colors represent the original and the identified force

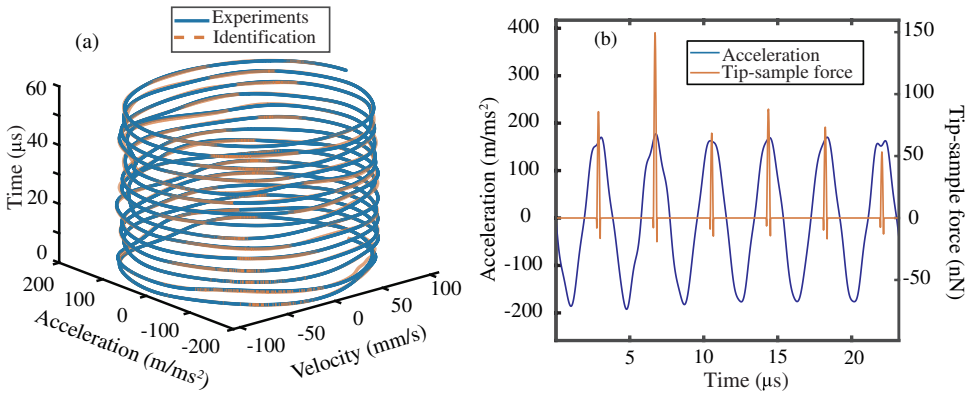


Figure 3: Data-driven identification for a Silicon cantilever interacting with PS sample. The experimental deflection is obtained at a fixed tip-sample distance of 66 nm (a) Identification of velocity and acceleration state vectors. The blue and orange curves represent the experimental and identified state space trajectories, respectively. (b) Estimation of the tip-sample force from data-driven model (orange) superimposed on the experimental acceleration signal (blue).

signals and the negative and positive force values indicate attractive and repulsive forces, respectively. The inset in both figures highlights the ability of the data-driven algorithm to identify specific features of interaction with sub-microsecond precision.

Finally, we remark that the algorithm has an accuracy of 99% in predicting the repulsive or contact interaction and 94% accuracy in predicting the attractive or non-contact interaction. These numbers drop down to approximately 82% near the interatomic distance where both contact and non-contact interactions co-exist. This is primarily due to the non-smooth nature of the contact and the lack of resolution in data points to approximate the behaviour of the system near the minima of the potential well.

### 5.3. EXPERIMENTS

Based on the insights gained from the training data-sets, we extend the formulation to experimental data and follow the methodology presented in Fig. 2. We begin by acquiring the raw deflection signal of an AFM cantilever directly from the photodetector using a Field Programmable Gated Array (FPGA) (see Appendix 5.A). We estimate the tip-sample force for two sets of experiments using a silicon cantilever tapping on a two component polymer blend made of PS and LDPE. In the first experiment, we read-out the motion of the cantilever at a fixed distance from the sample, and in the second, we move the cantilever from a distance with zero-interaction to a point with maximum repulsive force similar to conventional dynamic spectroscopy measurements (see Fig. 2(b)). In both experiments, the acquired time signal is processed as described in the training procedure. Furthermore, we reduce the library of the candidate functions to a smaller subset of 40 functions. Next, we regress the AFM dynamics onto this library (see Fig. 2(c)) and estimate the instantaneous tip-sample force (see Fig. 2(d)).

Figure 3 shows the identification of the cantilever motion and the estimation of the interaction force when the probe is engaged with the PS polymer matrix at a fixed dis-

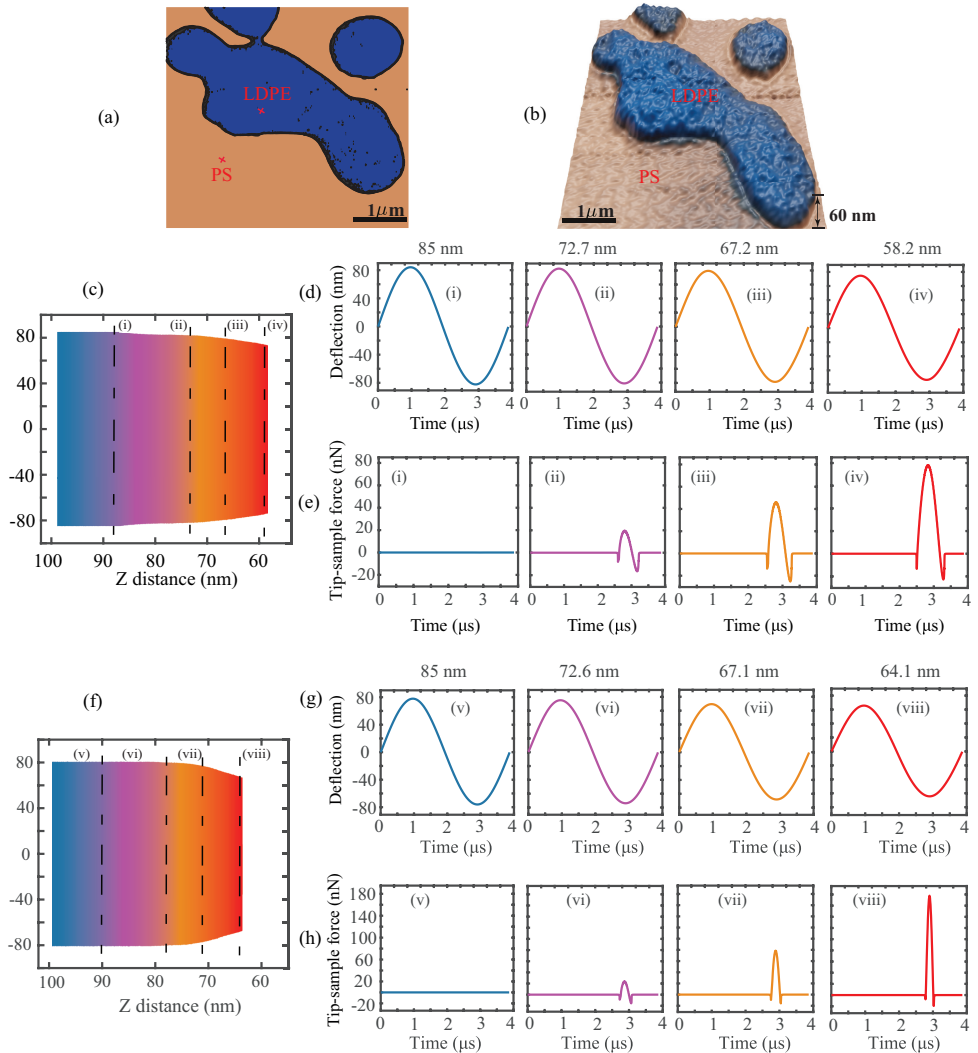


Figure 4: Data-driven identification of tip sample interaction as a function of tip-sample separation on PS-LDPE sample. (a)-(b) Phase and topography images of PS-LDPE blend sample, respectively. The blue contour indicates the LDPE islands and the orange contour the PS matrix. (c) Experimental dynamic spectroscopy signal obtained with 80% set-point ratio on LDPE material. The dashed lines indicate specific tip-sample distances at which data-driven identification is performed. The distances as read from left to right are at 85 nm, 72.7 nm, 67.2 nm, 58.2 nm, respectively. (d) Experimental deflection signal obtained from averaging 15 periods at different tip-sample sample distances. (e) Identification of tip-sample force based on the data-driven model at different tip-sample distances. (f) Experimental dynamic spectroscopy signal obtained with 80% set-point ratio on PS material. The dashed lines indicate specific tip-sample distances at which data-driven identification is performed. The distances as read from left to right are at 85 nm, 72.6 nm, 67.1 nm, 64.1 nm, respectively. (g) Experimental deflection signal obtained from averaging 15 periods at different tip-sample distances. (h) Identification of the tip-sample force based on data-driven model at different tip-sample sample distances.

tance of 66 nm from the sample. It can be observed from the 3D phase space shown in Fig. 3(a) that our data-driven approach successfully captures the cantilever dynamics, and that the identified model follows the true experimental trajectory with an accuracy of 90%.

In Fig. 3(b) we also show the estimated tip-sample force for several consecutive periods in the same experiment. It is interesting to note that the data-driven algorithm is capable to reconstruct the time-sample interaction from fast cantilever oscillations. A similar trend in behaviour for LDPE sample is also observed and showcased in Appendix 5.C. Here, it is noted that the variation in the estimated force per period, is associated with the slight changes in the acceleration vector from one oscillatory period to another which may have multiple origins. These may include, perturbations that cantilever experiences during the tapping cycle or may stem from numerical differentiation of the deflection signal. We highlight that by further suppression of noise in the experimental signal [144–146], the accuracy of the identification process can be further improved.

To further investigate the applicability of the data-driven approach in dynamic AFM measurements, in our second experiment we capture the deflection signal of the cantilever while varying the tip-sample distance. The measurements are once again performed on the PS-LDPE blend which shows a large contrast in the material properties and thus allows probing of different interaction mechanics.

Figures 4(a)-(b) depict the phase and topography data of the this sample. The points of time measurements are marked on each material with a red cross for reference. Figure 4(c) corresponds to the spectroscopic time data obtained on LDPE sample by varying the tip-sample separation. Here, the color gradient indicates the increase in strength of interaction as the probe is brought closer to the sample. The evolution of this interaction is showcased in Figs. 4(d)-(e) by slicing the time data at specific tip-sample separations.

It can be observed that at 85 nm the cantilever is initially in a state of no-interaction far away from the sample (Fig. 4(d)-(i)) and thus the corresponding tip-sample force is zero as indicated by the blue curve. As the cantilever is brought closer to the sample, the amplitude of the deflection signal drops (Figs. 4(d) (ii)-(iv)) owing to the presence of tip-sample forces and thus the interaction force gradually increases as shown in Figs. 4(e) (ii)-(iv). A similar trend is observed for the PS sample in Figs. 4(f)-(h).

### 5.3.1. TIP-SAMPLE CONTACT ANALYSIS

In the experimental results shown in Fig. 4(e) and (h) the tip-sample force appears as a clipped sine wave whose magnitude depends on the contact duration, i.e. pulse width. The contact span in turn depends on the effective stiffness of the cantilever-sample configuration. For compliant samples such as LDPE, we expect a larger contact duration and thus a broadly distributed tip-sample force [147]. In contrast, we expect a faster increase in tip-sample force on stiffer PS sample since larger forces are required to produce a given depth of indentation in these samples [103, 147]. This results in a shorter duration of contact and thus a narrower tip-sample force waveform [71]. It is interesting to note that our data-driven analysis captures these underlying features accurately in both samples without any prior assumption on the nature of the interaction.

Furthermore, by analyzing the interaction exponent of functions that describe the indentation of the tip into the sample, we show that the interaction geometry follows a cone indenting a flat geometry as opposed to the commonly used sphere-half-plane model. The tip-sample interaction in dynamic AFM is mathematically described by power-law relations [29]. In particular, several studies in contact mechanics have shown that the indentation force and the indentation depth are linked by a nonlinear function that depends not only on the material properties but also on the geometry of the AFM tip and the sample being investigated. This prompted the force reconstruction techniques in dynamic AFM to seek the instantaneous force profiles as a function of tip-sample distance in the form [29, 67, 147]

$$F_{ind} = \gamma \delta^\rho, \quad (5.3)$$

where  $F_{ind}$  is the indentation force,  $\gamma$  the effective stiffness,  $\delta$  the indentation depth and  $\rho$  the interaction exponent. The value of exponent  $\rho$  is assumed to be 1.5 in several traditional AFM models, e.g. Derjaguin-Muller-Toporov (DMT) [35] or the Johnson, Kendall and Roberts (JKR) force model [34]. This value stems from the assumption of a sphere (tip apex) interacting with a planar surface (sample). However, due to fabrication processes, the AFM tip shape resembles more a pyramidal cone rather than a sphere. An exponent equal to  $\rho = 2.0$  in Eq. (5.3) provides in this case a better representation of the interaction [33]. Nevertheless, a generalization of the exponent value is not trivial. Each probe can be assumed unique in its own geometry, wear, and contamination status. If the interaction ensemble does not change then the exponent  $\rho$  will be constant across various experiments with minor changes. On the contrary, the interaction with a different sample causes the  $\gamma$  coefficient to vary due to the change in the material properties.

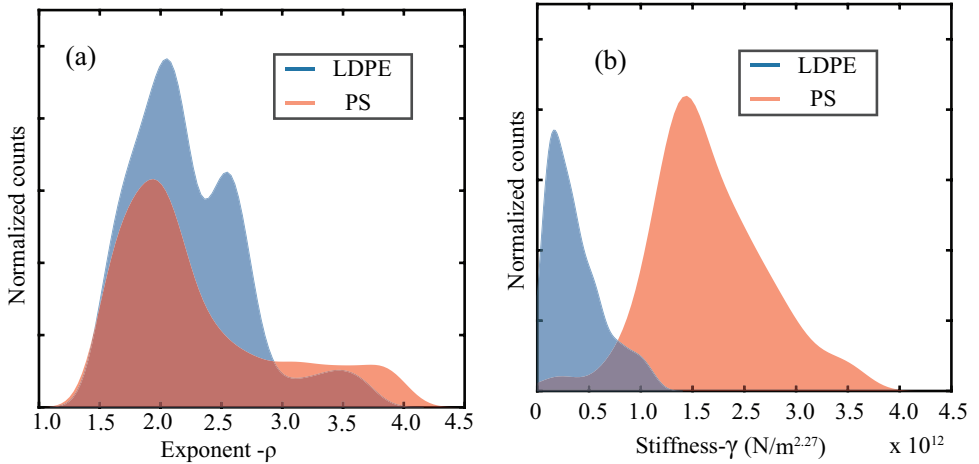


Figure 5: Histograms of conservative tip-sample interaction measurements on PS-LDPE sample. (a) Histograms of the interaction geometry for the PS (red) and LDPE (blue) domains of the sample. (b) Histograms of the stiffness factor for the PS (red) and LDPE (blue) domains of the sample assuming the mean interaction geometry factor of 2.27. The histograms confirm that the PS sample is stiffer than LDPE sample.

Using our machine learning approach we retrieve  $\rho$  from a library containing a col-

lection of functions with varying exponents. Depending on the nature of interaction, our optimization procedure automatically converges to the best value. This is further highlighted in Fig. 5 (a), where we plot the histogram of the exponents of the indentation functions chosen directly by the machine learning process. The analysis shows a mean value of  $\rho = 2.27 \pm 0.4$  which is in excellent agreement with the values previously reported in different studies [67, 147]. Adding to this, we extract the effective stiffness value by assuming an interaction exponent of 2.27 and plot the histograms for both PS and LDPE material. The analysis shows a clear distinction in the stiffness value, where the PS material is approximately twelve times stiffer than the LDPE material. This is in agreement with previous measurements and in-line with the expected bulk modulus values of PS and LDPE [66, 67, 148].

Finally, in addition to providing insight into elastic behaviour of the sample, our machine learning approach also predicts the hysteresis in the interaction force due to energy dissipation as an asymmetry in the clipped sine wave (see Figs. 4(e) and (h)). The hysteresis is obtained in both PS and LDPE samples, but similar to previous observations [71, 147, 149], the dissipation in case of the compliant sample (LDPE) is found to be much larger than PS. Within our function library, the dissipation is linked to  $\delta^l \dot{\delta}^p$ -type functions where  $\delta$  and  $\dot{\delta}$  are the indentation depth and rate of indentation, respectively and the coefficients  $l$  and  $p$  are material-related interaction exponents. This suggests that the viscoelastic nature of the polymer could be a major contributor to the energy dissipation [2, 4, 5, 8, 150]. Our analysis shows the potential of machine learning approaches to overcome some of the inherent short comings of prior methods where complex or *ad hoc* models are often used to estimate elastic/viscoelastic properties [4, 101, 121] and thus are limited in their ability to accurately represent tip contact with softer, more adhesive and viscoelastic surfaces. In contrast to this, machine learning algorithm can autonomously pick the best functions to represent the experimental data and distil a physically interpretable model that governs the tip-sample dynamics.

## 5.4. DISCUSSION

In summary, we proposed an approach based on sparse identification of nonlinear dynamical systems to reconstruct the tip-sample interaction in dynamic AFM measurements. We discussed the training methodology and supervision of the algorithm based on standard AFM models, and explained the model selection criterion in the pareto space via tuning hyper-parameters. We showed that our data-driven algorithm captures the governing equations and the tip-sample interaction force on numerically generated data with an accuracy of more than 90%. To highlight the utility of our approach, we also performed several experiments on soft and stiff polymeric samples and estimated their tip-sample force with high resolution.

The results from our data-driven analysis were inline with the findings previously reported from AFM measurements of polymers. This further illustrates the potential of data-driven methodologies to uncover the true physics of the tip-sample interaction in materials at the nanoscale without any prior assumption on the mathematical models to estimate surface forces. The results further highlight the inherent sub-microsecond temporal resolution and nN peak loading forces expected in dynamic AFM and facil-

itate high resolution mapping of nanomechanical properties. In addition to estimating the sample properties, by taking advantage of future generations of high-frequency force sensors, acquisition electronics and data processing algorithms, we envision that data science combined with machine learning techniques will uncover the true potential of dynamic AFM in understanding the physics behind transient biological processes, developing novel feedback architectures and high-resolution dynamical force–volume measurements at video rate.



## APPENDIX

### 5.A. EXPERIMENTAL SETUP AND MEASUREMENT PROTOCOL

The experiments are performed using a commercial AFM (JPK Nanowizard) and a multi-lock-in amplifier from Intermodulation products [22, 99] that can function as a Field Programmable Gated Array (FPGA). The FPGA is used to collect and analyze the cantilever deflection data. We used a commercially available rectangular Silicon cantilever (TAP300AL-G, Budgetsensors) and a two-component polymer blend made up of Polystyrene (PS) and Low Density Polyethylene (LDPE) (from Bruker) to perform the experiments. For each experiment, the spring constant of the cantilever ( $k = 20.68 \text{ N/m}$ ), its resonance frequency ( $f_0 = 259.9 \text{ kHz}$ ), and quality factor ( $Q = 443$ ) are determined using the thermal calibration method [49].

The time signal of the cantilever interacting with the polymer sample is captured by implementing a procedure which uses standard modalities available in commercial AFM. As a first step, we perform standard dynamic spectroscopy operation at a specific set point ratio comparable with the ratios used in normal scanning operation in dynamic AFM. The AFM is then synchronized with the FPGA using a trigger signal to ensure a one-to-one-correlation between the time axis and the tip-sample distance measurements. Next, the resulting change in vibrational amplitude is recorded using the built in lock-in amplifier within the AFM and using the FPGA at 50 MHz, simultaneously. In this way, we capture the lock-in amplitude and phase data as well as the real-time motion of the cantilever as a function of the varying tip-sample distance.

In the next step, the experimental data obtained by the FPGA is post-processed to align the deflection versus time signal with that of the lock-in amplitude versus tip-sample distance signal extracted from the AFM. This step correlates to access chunks of time data corresponding to specific tip-sample separations. Finally, the deflection signal is de-noised and differentiated using Savitzky-Golay filter to obtain all three state vector channels, namely acceleration, velocity, and time.

### 5.B. PROTOCOL FOR CHOOSING HYPER-PARAMETERS AND CONSTRAINTS FOR THE ALGORITHM

The data-driven algorithm requires the specification of two parameters,  $\nu$  and  $\lambda$  that control the learning process. The parameter  $\nu$  controls the strength of relaxation for the coefficient matrix  $\mathbf{W}$  and how closely it matches  $\Xi$ . A larger value of  $\nu$  allows for larger relaxation and vice versa. Whereas, the parameter  $\lambda$  controls the strength of regularization. In our analysis we use a  $l_0$  regularization which is equivalent to hard-thresholding, making the optimization problem non-convex. The  $l_0$  norm will threshold coefficients below a value determined by both  $\nu$  and  $\lambda$ . For example, if the desired threshold value is called  $\eta$  then the value of  $\lambda$  is chosen via the relationship  $\lambda = \eta^2/2\nu$  [147].

We note that it is often difficult to know the desired threshold value a priori for every AFM experiment; hence we performed extensive simulations and experiments and based on the analysis we observed that for the best results in a dynamic AFM application, it is a good starting point to use  $\eta = 1/Q$ , where,  $Q$  is the quality factor of the cantilever. By normalizing the dynamical system with the correct length and time scales it is possible

to make  $Q$  the smallest identifiable coefficient in the equation of motion, thus making it the ideal candidate as a threshold parameter. Furthermore, we extend the parameter range by allowing a tolerance of 15% and utilize the hyper-opt python package to determine the best threshold coefficient that results in the smallest possible equation of motion via cross validation.

The physics informed constraints that must be imposed to determine the governing equations are obtained from experimental conditions. In particular, we obtain information on the stiffness ( $k$ ), quality factor ( $Q$ ) and the resonance frequency ( $f_0$ ) of the cantilever directly from the experiments by performing a thermal calibration procedure [147]. In addition to these information, a final constraint on the amplitude of excitation is required. This is crucial for performing accurate system identification since the amplitude of the forcing function  $F_c$  (dither piezo based excitation) remains constant while the cantilever approaches the sample and thus the reduction in the amplitude should be purely attributed to the tip-sample interaction force. Therefore, a constraint on the amplitude of base excitation will force the algorithm to select the right nonlinear functions that can accommodate this amplitude reduction.

We derive the constraint on  $F_c$  by performing an intermediate identification step on what we refer to as no-interaction data. The no-interaction data are obtained far from the sample and as the name suggests has no influence from the tip-sample forces. These data-sets are similar to free air vibration in an experimental scenario and the intermediate step to identify the final constraint can be considered similar to fitting the free air vibration data with a simple harmonic oscillator to estimate the excitation amplitude. Based on these information, we then introduce constraints into the data-driven algorithm by assuming the governing equation of the cantilever to be of the form:

$$\ddot{x} + D\dot{x} + Kx = -F_{ts}(z, \dot{z}) + B \cos(\Omega\tau),$$

the constraints that must be imposed are

$$D = Q^{-1} \tag{5.4}$$

$$K = k$$

$$B = F_c$$

The above constraints can be more intuitively understood by looking at the function library below. Here for example the coefficient of function 'X' which co-relates to the

$$\left[ 1 \quad \overbrace{X}^k \quad \overbrace{\dot{X}}^{Q^{-1}} \quad X^2 \quad X^3 \quad \dots \quad \overbrace{\cos(\Omega\tau)}^{F_c} \right]$$

deflection of the cantilever is given by stiffness ' $k$ ', the function describing the velocity of the cantilever ( $\dot{X}$ ) has its coefficient dictated by the inverse of the quality factor ( $Q$ ) and finally the function governing the amplitude of excitation ( $\cos(\Omega\tau)$ ) by ' $F_c$ '. Furthermore, during the model discovery, we allow a tolerance of 15% in the aforementioned coefficient values to account for the inconsistencies encountered in the determination of cantilever properties via thermal calibration procedure.

## 5.C. IDENTIFICATION OF TIP-SAMPLE INTERACTION IN LDPE SAMPLE

Figure 5.C.1 reports the data-driven identification for a silicon cantilever interacting with a LDPE sample. The presentation of the results is similar to that of Fig. 3. We acquire a total of 50 periods of time oscillations obtained at a fixed distance of 63.1 nm from the sample. We performed data driven analysis to identify the dynamics (Fig. 5.C.1(a)) and to capture the variation of the instantaneous tip-sample force period by period (Fig. 5.C.1(b)).

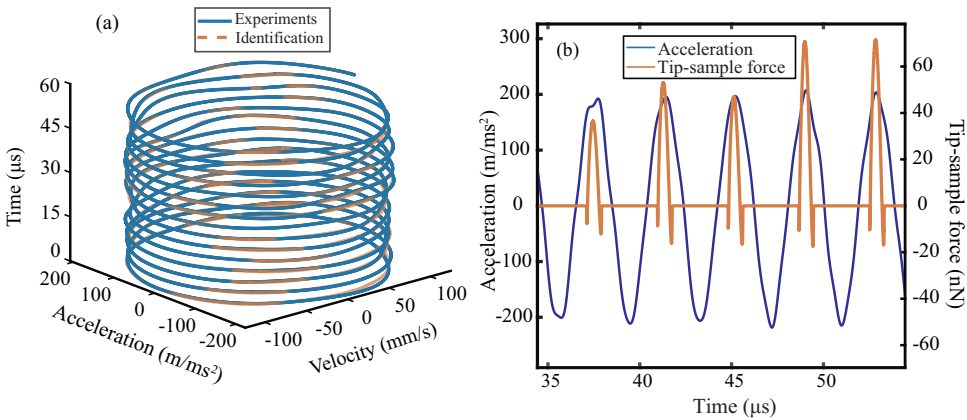


Figure 5.C.1: Data driven identification on Silicon cantilever interacting with LDPE sample. The experimental deflection is obtained at a fixed tip-sample distance of 63.1 nm. (a) Identification of velocity and acceleration state vectors from data driven model. The blue and orange curve represents the experimental and identified state space trajectories, respectively. (b) Estimation of tip sample force from data driven model (orange) superimposed on the experimental acceleration signal (blue).

## 5.D. ADDITIONAL DATA: ALGORITHM TRAINING

In this section we report additional results from training the data-driven algorithm. Training data is derived from various well established AFM models with different interaction physics. In particular, we utilized the following models for the training and validation of the algorithm:

- 5.D.1 Derjaguin-Muller-Toporov (DMT) model<sup>1</sup>. Training outcome is shown in Fig. 1 with description of the library functions in Tab. 1
- 5.D.2 Lennard-Jones model.
- 5.D.3 DMT model with viscoelastic damping.
- 5.D.4 DMT model with exponential damping.
- 5.D.5 JKR model.

<sup>1</sup>Model employed to train the sparse identification algorithm in the main chapter

### 5.D.1. DMT MODEL

The equation of motion governing the AFM dynamics with a DMT interaction model is given by Eq. (5.5). Here, the microcantilever tip deflection towards the sample is denoted by  $x$  and the instantaneous tip-sample distance and the indentation depth are indicated by  $z$  and  $\delta$ , respectively. It should be noted that both  $z$  and  $\delta$  are functions of  $x$ . The damping and stiffness coefficients are indicated by  $D$  and  $K$ , the amplitude of the dither piezoelectric actuator is denoted by  $B$ . The dotted quantities represent derivatives with respect to re-scaled time  $\tau$  ( $\tau = \omega_0 t$ ), where  $\omega_0$  is the natural frequency of the cantilever. In the DMT model, the tip-sample force  $F_{ts}$  consists of: i) long range Van der Waal's attractive force with coefficient  $C_1$  governed by a second order inverse power law; ii) repulsive component described by the Hertz contact force with effective stiffness governed by the coefficient  $C_2$ ; iii) adhesion force given by  $F_a = 4\pi R\gamma$  with  $R$  and  $\gamma$  representing the AFM tip radius and surface interaction energy, respectively. The adhesion force  $F_a$  can be reformulated as an attractive force such that it depends on the inter-molecular distance  $a_0$  and its strength governed by the coefficient  $C_3$ . The coefficients utilized for the simulations are that of reference article. [48, 99]. The results of this model are discussed in the main chapter.

$$\begin{aligned} \ddot{x} + D\dot{x} + Kx &= F_{ts}(z) + B \cos(\Omega\tau) \\ F_{ts}(z) &= \begin{cases} C_1/z^2, & \text{for } z > a_0 \\ C_2(\delta)^{3/2} - F_a, & \text{for } z \leq \bar{a}_0. \end{cases} \\ F_a &= 4\pi R\gamma = C_3/a_0^2. \end{aligned} \quad (5.5)$$

### 5.D.2. LENNARD-JONES MODEL

In the Lennard-Jones (LJ) force model the tip-sample interaction is described by the continuous and smooth functions of Eq. (5.6). The tip-sample force  $F_{ts}$  consists of Van der Waal's attractive force comprising a second and a eighth order inverse power law function of the instantaneous tip-sample separation  $z$  and proportional to the coefficients  $C_1$  and  $C_2$ , respectively. Additional parameters in Eq. (5.6) related to the cantilever dynamics are those of Eq. (5.5) and described in Sec. 5.D.1. The coefficients for the simulations are obtained from the reference article [47, 75].

$$\begin{aligned} \ddot{x} + D\dot{x} + Kx &= F_{ts}(z) + B \cos(\Omega\tau) \\ F_{ts}(z) &= C_1/z^2 + C_2/z^8. \end{aligned} \quad (5.6)$$

Figures. 5.D.1 (a) & (b) highlight the transient and steady state dynamics as determined by the data driven analysis. In addition to the state vectors, Figs. 5.D.1 (c) & (d) highlights the transient and steady state tip-sample force. In either of the cases the blue and orange colours indicate the original and identified system. Furthermore, Fig. 5.D.2 shows the coefficients obtained from the data driven algorithm in comparison with the values used for simulation; whereas table 5.D.1 provides an insight into the library functions used in the simulation. It must be noted that since the model is governed by a smooth and continuous tip-sample force with relatively simple functions, the LJ model shows the fastest convergence rate among all the tested models.

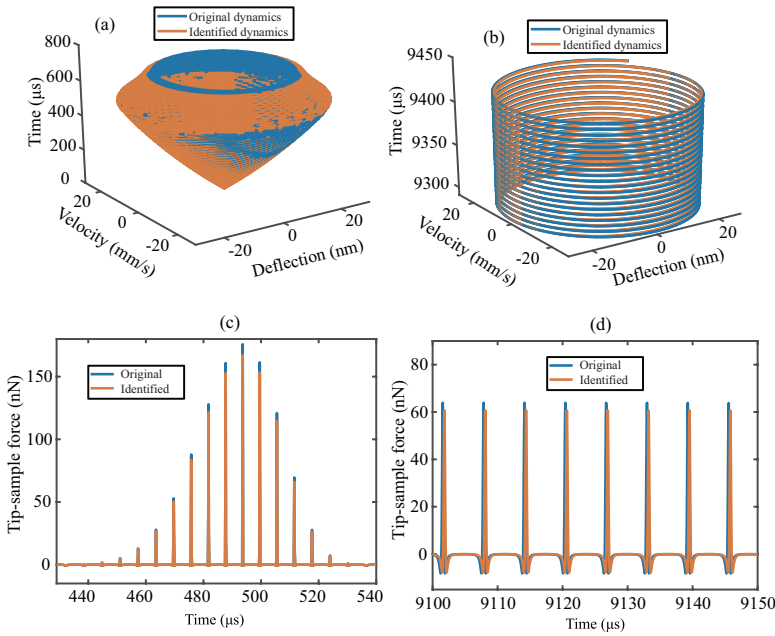


Figure 5.D.1: Simulations of a cantilever interacting with a sample based on LJ force model. The LJ model parameters are tuned to induce transient and steady state dynamics in order to replicate the experiments. (a) Transient dynamics prediction: The blue curve indicates the simulated transient phase space trajectory and the orange curve is the prediction from the data driven model. (b) Steady state dynamics prediction: The blue curve indicates the simulated steady state phase space trajectory and the orange curve shows prediction from the data driven model. (c)-(d) Comparison of the tip sample force between the LJ simulation (blue) and the data driven model (orange) for both the transient and steady state scenarios. The coefficients utilized for the simulations are that of Rutzel et al. [47, 75]

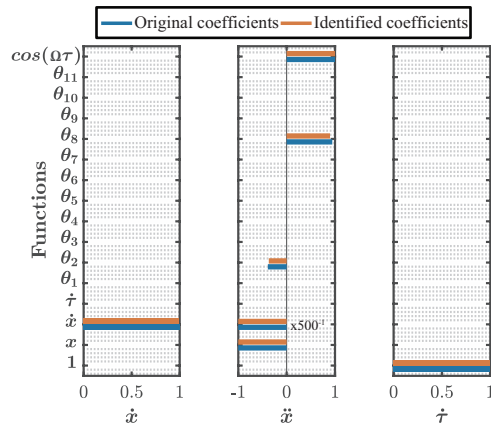


Figure 5.D.2: Coefficient matrix showing the influence of each library function on the governing equations of LJ force model. The blue color indicates the original value of the coefficients and the orange color indicates the coefficients as determined by the data driven model. The  $\theta_i$  functions are detailed in Tab. 5.D.1

Table 5.D.1: Description of the nonlinear functions used in the coefficient matrix of Fig. 5.D.2.

Function ID	$\theta_1 - \theta_8$	$\theta_9$	$\theta_{10}$	$\theta_{11}$
Function definition	$z^{-n}$ , $n=1$ to $8$	$z^{1.5}$	$z^2$	$\sin(\Omega\tau)$

### 5.D.3. DMT MODEL + VISCOELASTIC DAMPING

The third stage of the training is performed employing a standard DMT model with an additional viscoelastic term in the interaction mechanism. Viscoelasticity plays an important role in the energy dissipation mechanisms when dealing with soft samples, e.g. polymers and biological specimens [4, 5, 7]. Identification of these dissipation mechanisms is crucial to understand the hysteresis observed in experiments. Equation. 5.7 describes the DMT model accounting for the viscoelastic behaviour. The basic mathematical model is that of Eq. (5.5), adding a viscoelastic contribution controlled by the coefficient  $C_3$  and that depends on the rate of indentation ( $\dot{\delta}$ ). Similar to the LJ model, the amplitude of deflection is governed by  $x$ , the instantaneous tip-sample distance by  $z$  and the indentation depth by  $\delta$ . The coefficients utilized for the simulations are derived from the reference articles [4, 5, 7]. Contrary to the LJ model, the DMT model with viscoelastic terms contains both conservative and dissipative nature of interaction and represents a closer picture to what is encountered in an experimental scenario.

$$\ddot{x} + D\dot{x} + Kx = F_{ts}(z, \dot{z}) + B \cos(\Omega\tau)$$

$$F_{ts}(z, \dot{z}) = \begin{cases} C_1/z^2, & \text{for } z > a_0 \\ C_2(\delta)^{3/2} - C_3\sqrt{\delta}\dot{\delta} - F_a, & \text{for } z \leq \bar{a}_0. \end{cases} \quad (5.7)$$

$$F_a = 4\pi R\gamma = C_4/a_0^2$$

Figures. 5.D.3 (a) and (b) highlight the transient and steady state dynamics as determined by the data driven analysis. In addition, Figs. 5.D.3 (c) and (d) show the simulated and reconstructed tip-sample force for the transient and steady state case. The coefficients extracted from the data-driven approach are compared with those of the simulations in Fig. 5.D.4. The difference in the identified coefficients leads to a phase drift of the identified trajectory and visible in Fig. 5.D.3(d). The description of the library functions used in the simulation is reported in table 5.D.2. The algorithm identifies three additional functions with respect to those in Eq. (5.7): i)  $\theta_2 = z^{-3}$ , in combination with  $\theta_1$  is used by the algorithm for estimating long range attractive forces; ii)  $\theta_{11} = \sin(\tau)$ , function that is similar to the excitation function  $\cos(\tau)$  but with a 90 deg phase difference; iii)  $\theta_{10}$ , a bridging function similar to the constant term described by  $F_a$  in Eq. (5.7). These additional functions help to accommodate the perturbation in the dynamics due to the presence of noise.

Table 5.D.2: Description of the nonlinear functions used in the coefficient matrix of Fig. 5.D.4.

Function ID	$\theta_1$	$\theta_2$	$\theta_3$	$\theta_4$	$\theta_5$	$\theta_6$	$\theta_7$	$\theta_8$	$\theta_9$	$\theta_{10}$	$\theta_{11}$
Function definition	$z^{-2}$	$z^{-3}$	$\delta^{0.5}\dot{\delta}$	$\delta\dot{\delta}^2$	$z^{0.5}z$	$z\dot{z}^2$	$\delta^2$	$\delta^{2.5}$	$\delta^{1.5}$	$z^{-2} \forall z \leq a_0$	$\sin(\Omega\tau)$

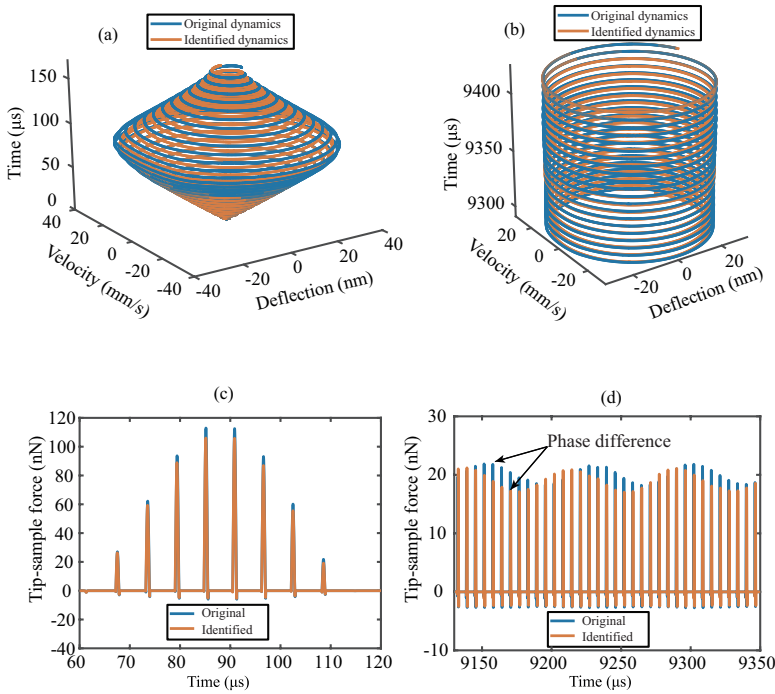


Figure 5.D.3: Simulations of a cantilever interacting with a sample based on DMT force model with additional viscoelastic interaction. The model parameters are tuned to induce transient and steady state dynamics in order to replicate the experiments. (a) Transient dynamics prediction: The blue curve indicates the simulated transient phase space trajectory and the orange curve is the prediction from the data driven model. (b) Steady state dynamics prediction: The blue curve indicates the simulated steady state phase space trajectory and the orange curve shows prediction from the data driven model. (c)-(d) Comparison of the tip sample force between the simulation (blue) and the data driven model (orange) for both the transient and steady state scenarios.

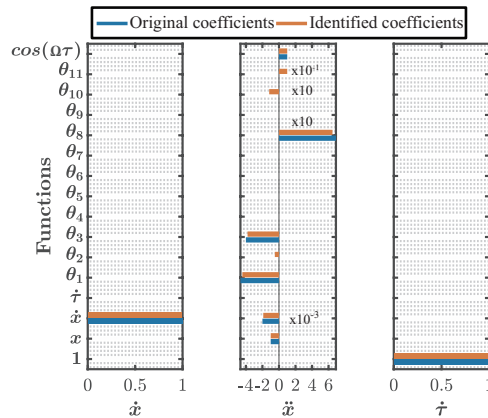


Figure 5.D.4: Coefficient matrix showing the influence of each library function on the governing equations of DMT force model with additional viscoelastic interactions. The blue color indicates the original value of the coefficients and the orange color indicates the coefficients as determined by the data driven model.

### 5.D.4. DMT + EXPONENTIAL DAMPING

This stage of the training sees the DMT model augmented with exponential damping term in the interaction mechanism (Eq. (5.8)). The exponential damping term captures the capillary forces, adhesion and other surface forces with certain decay length [67]. In turn they contribute to the hysteresis in the interaction. The exponential damping term in Eq. (5.8) is governed by the coefficient  $C_3$  and depends on the instantaneous tip-sample distance  $z$  and the instantaneous velocity  $\dot{z}$ , contributing to the non-dissipative nature of interaction. Furthermore, in a similar fashion to the aforementioned models, the amplitude of deflection is governed by  $x$ , the indentation depth by  $\delta$  and the decay length of the exponential damping by  $z_\beta$ . The coefficients utilized for the simulations are derived from the reference articles [67].

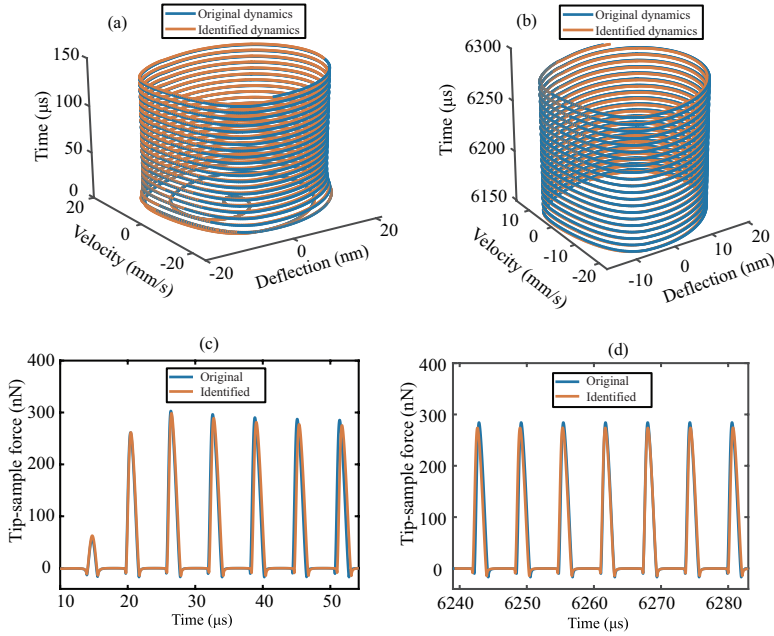


Figure 5.D.5: Simulations of a cantilever interacting with a sample based on DMT force model with additional exponential damping term. The model parameters are tuned to induce transient and steady state dynamics in order to replicate the behaviour found in experiments. (a) Transient dynamics prediction: The blue curve indicates the simulated transient phase space trajectory and the orange curve is the prediction from the data driven model. (b) Steady state dynamics prediction: The blue curve indicates the simulated steady state phase space trajectory and the orange curve shows prediction from the data driven model. (c)-(d) Comparison of the tip sample force between the simulation (blue) and the data driven model (orange) for both the transient and steady state scenarios.

$$\ddot{x} + D\dot{x} + Kx = F_{ts}(z, \dot{z}) + B \cos(\Omega\tau)$$

$$F_{ts}(z, \dot{z}) = \begin{cases} C_1/z^2 - C_3 \exp(z/z_\beta) \dot{z}, & \text{for } z > a_0 \\ C_2(\delta)^{3/2} - F_a - C_3 \exp(z/z_\beta) \dot{z}, & \text{for } z \leq \bar{a}_0. \end{cases} \quad (5.8)$$

$$F_a = 4\pi R\gamma = C_4/a_0^2$$



Figures 5.D.5 (a) and (b) illustrate the transient and steady state dynamics as determined by the data driven analysis. In addition to the state vectors, Figs. 5.D.5 (c) and (d) report the transient and steady state tip-sample force. The coefficients obtained from the data driven algorithm are listed in Fig. 5.D.6. The data-driven reconstruction with DMT model and exponential damping does not highlight the phase shift of Sec. 5.D.3. The library functions used in the simulation is in Tab. 5.D.3. Again we observe three additional functions in the identification. The functions  $\theta_2$  described by  $z^{-3}$  and  $\theta_9$  described by  $z\dot{z}$  arise due to the presence of noise. Whereas, the function  $\theta_{10}$  acts as a bridging function similar to the constant term described by  $F_a$  in Eq. (5.8).

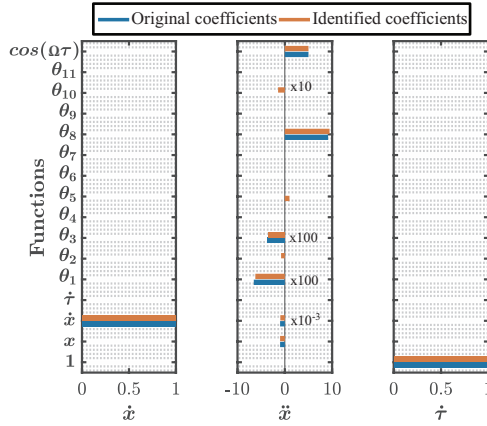


Figure 5.D.6: Coefficient matrix showing the influence of each library function on the governing equations of DMT force model with additional exponential damping. The blue color indicates the original value of the coefficients and the orange color indicates the coefficients as determined by the data driven model. The  $\theta_i$  functions are detailed in Tab. 5.D.3.

Table 5.D.3: Description of the nonlinear functions used in the coefficient matrix of Fig. 5.D.6.

Function ID	$\theta_1$	$\theta_2$	$\theta_3$	$\theta_4$	$\theta_5$	$\theta_6$	$\theta_7$	$\theta_8$	$\theta_9$	$\theta_{10}$	$\theta_{11}$
Function definition	$z^{-2}$	$z^{-3}$	$\exp(z/z_\beta)\dot{z}$	$\exp(z/z_\beta)^2\dot{z}^2$	$z\dot{z}$	$z\dot{z}^2$	$\delta^2$	$\delta^{2.5}$	$\delta^{1.5}$	$z^{-2} \forall z \leq a_0$	$\sin(\Omega\tau)$

### 5.D.5. JKR MODEL

The last stage of the training is performed with a Johnson, Kendall and Roberts (JKR) force model. The JKR model is particularly suited for AFM cantilever with large tip radius and large adhesion forces, which are regularly encountered in biological and soft polymers [28]. The equation describing the tip-sample interaction is shown in Eq. (5.9). Here, the tip-sample force  $F_{ts}$  consists of long range Van der Waal's attractive force with coefficient  $C_1$  governed by a second order inverse power law. The contact mechanics is described by the Hertz contact force with effective stiffness governed by the coefficient  $C_2$ , and the adhesion force given by  $F_a$  similar to the DMT model used in the main chapter. However, in case of JKR model the adhesion force given by  $F_a = 3\pi R\gamma$  is in general larger in amplitude due to larger tip radius and surface energy and thus leads to larger

dissipation and hysteresis during the pull off event. Once gain, here  $R$  and  $\gamma$  are the AFM tip radius and surface interaction energy respectively. Similar to Eq. (5.7), the adhesion force  $F_a$  translates into an attractive force that depends on the intermolecular distance  $a_0$  and its strength governed by the coefficient  $C_4$ .

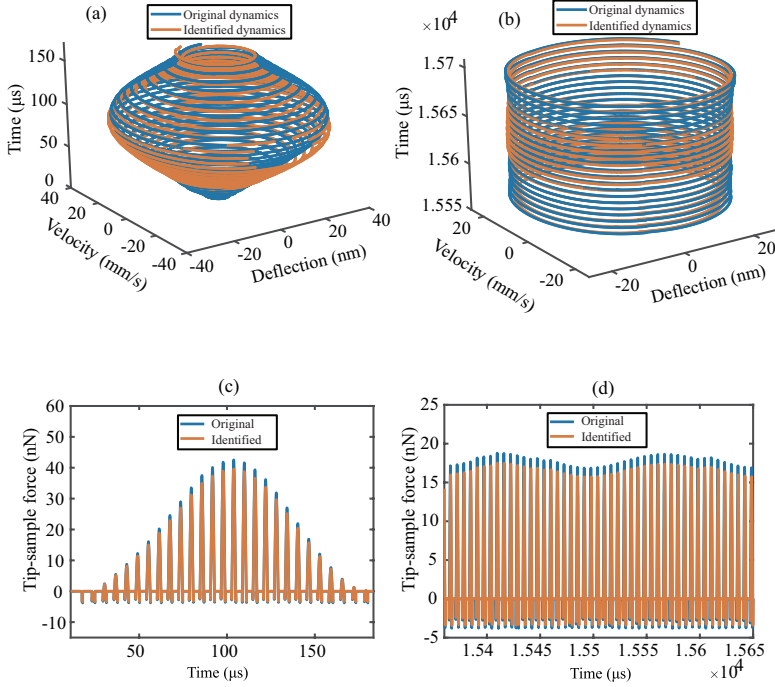


Figure 5.D.7: Simulations of a cantilever interacting with a sample based on JKR force model used in the training stage of the data driven model. The model parameters are tuned to induce transient and steady state dynamics in order to replicate the behaviour found in experiments. (a) Transient dynamics prediction: The blue curve indicates the simulated transient phase space trajectory and the orange curve is the prediction from the data driven model. (b) Steady state dynamics prediction: The blue curve indicates the simulated steady state phase space trajectory and the orange curve shows prediction from the data driven model. (c)-(d) Comparison of the tip sample force between the simulation (blue) and the data driven model (orange) for both the transient and steady state scenarios. The coefficients utilized for the simulations are derived from the reference article [8].

$$\ddot{x} + D\dot{x} + Kx = F_{ts}(z, \dot{z}) + B \cos(\Omega\tau)$$

$$F_{ts}(z, \dot{z}) = \begin{cases} C_1/z^2, & \text{for } z > a_0 \\ C_2(\delta)^{3/2} - F_a, & \text{for } z \leq \bar{a}_0. \end{cases} \quad (5.9)$$

$$F_a = 3\pi R\gamma = C_4/a_0^2$$

The dynamics of the system described by a JKR interaction force resembles that of the DMT model in the main chapter as observed in Figs. 5.D.5 (a) and (b). The data driven algorithm is able to accurately capture the governing dynamics with a small phase difference which occurs once again due to the presence of noise. The Reconstruction of

Table 5.D.4: Description of the nonlinear functions used in the coefficient matrix of Fig. 5.D.8.

Function ID	$\theta_1$	$\theta_2$	$\theta_3$	$\theta_4$	$\theta_5$	$\theta_6$	$\theta_7$	$\theta_8$	$\theta_9$	$\theta_{10}$	$\theta_{11}$
Function definition	$z^{-2}$	$z^{-3}$	$\delta^{0.5} \dot{\delta}$	$\delta \delta^2$	$z^{0.5} \dot{z}$	$z \dot{z}^2$	$\delta^2$	$\delta^{2.5}$	$\delta^{1.5}$	$z^{-2} \forall z \leq a_0$	$\sin(\Omega \tau)$

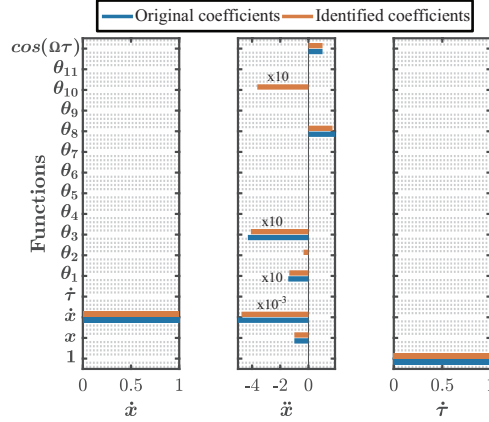


Figure 5.D.8: Coefficient matrix showing the influence of each library function on the governing equations of JKR force model. The blue color indicates the original value of the coefficients and the orange color indicates the coefficients as determined by the data driven model. The  $\theta_i$  functions are detailed in Tab. 5.D.4.

transient and steady state tip-sample force is reported in Figs. 5.D.5 (c) and (d). Here, in contrast to the DMT model, the presence of a larger adhesion force during the pull off of the cantilever results in larger hysteresis as observed in Figs. 5.D.5 (c) and (d). Furthermore, Fig. 5.D.8 shows the coefficients obtained from the data driven algorithm in comparison with the values used for simulation. Due to similar nature of the functions required to described both the JKR and DMT models, we utilize the same library used for the DMT model in main chapter (Tab. 1) to describe the JKR force interactions as well which highlights the interchangeability and universal nature of the technique.

6

# 6

## OUTLOOK

*In this chapter, I present some of the on-going research directions that are unpublished. I begin with an identification technique based on Kelvin probe microscopy to characterize the tip radius and then discuss how VdW forces can be used to probe Hamaker constant of materials. Next, I highlight the possibility of extending the data driven analysis for extracting viscoelastic response of soft matter and finally, discuss how neural networks can be used to identify mode coupling in dynamic AFM.*

## 6.1. TIP MONITORING THROUGH ELECTROSTATIC FORCES

Accurate quantification of the AFM probe geometry is crucial for characterizing the nano-mechanical properties of samples. However, identifying the probe radius and geometry from experimental observables is far from trivial. Previous studies in this direction have made use of methods where an scanning electron microscope (SEM) is used to take an image of the AFM tip or an AFM tip is used to scan a sample with specific features to estimate the tip radius [151–154]. However, these techniques are time consuming and often destructive, since the wear on the tip can increase during the scan or a carbon contamination in the SEM can skew the estimated tip radius value. On the other hand there are in situ nonlinear dynamic techniques which rely on the experimental observables to characterize the tip radius [80, 149]. However, they require good understanding of the cantilever nonlinear dynamics as these techniques rely on operating the AFM in the bistable regime and monitoring the change in strength of the attractive force caused by tip wear [149].

Here, we present an alternative in situ methodology based on Kelvin Probe Force Microscopy (KPFM) to probe tip shape geometry and wear during AFM operation. KPFM is a non-contact variant of conventional AFM that measures the contact potential difference (CPD) between the tip and the sample. The non-contact aspect of the method results in a non-destructive estimation of the tip radius.

### 6

#### 6.1.1. NUMERICAL MODELING

In order to probe the electrostatic interaction between the probe and the sample, we model the cantilever as a Single Degree of Freedom (SDOF) system under electrostatic excitation as follows

$$\frac{1}{\omega_0^2} \ddot{x} + \frac{1}{Q\omega_0} \dot{x} + x = \frac{1}{k} F_e(z, t). \quad (6.1)$$

Here,  $x$  represents the deflection of the cantilever,  $\omega_0 = 2\pi f_0$  is the resonance frequency of the fundamental mode,  $k$  denotes the stiffness of the cantilever,  $Q$  represents the quality factor and  $F_e$  corresponds to the excitation force. The major difference between Eq. (6.1) and that of models introduced in the previous studies is the absence of other nanomechanical forces such as repulsive or VdW forces which would make the analysis much more complicated. In contrast to this, here the only nonlinear force acting between the tip and the sample is modelled with the following expression

$$F_e(z, t) = -\frac{1}{2} \frac{dC}{dz} \left( (V_s - V_{DC})^2 + \frac{1}{2} V_{AC}^2 \right) + \frac{dC}{dz} (V_s - V_{DC}) V_{AC} \sin(\omega_e t) + \frac{1}{4} \frac{dC}{dz} V_{AC}^2 \cos(2\omega_e t), \quad (6.2)$$

where,  $V_s$ ,  $V_{AC}$  and  $V_{DC}$  are the sample voltage, AC voltage and DC voltage applied to the cantilever, respectively. Additionally,  $dC/dz$  is the capacitance gradient which is a function of geometry of the cantilever as well as the tip-sample distance ( $z$ ), and  $\omega_e$  is the electrical excitation frequency. From Eq.(6.2), we can divide the contribution of the electrostatic force into three categories at three different frequencies i.e at  $\omega = 0$ ,  $\omega_e$  and  $2\omega_e$ , respectively. Thus a lock-in amplifier can be used at either  $\omega_e$  or  $2\omega_e$  to monitor the change in amplitude and phase of the signal under the influence of electrostatic interactions; however, by exciting the cantilever electrically with a frequency close to its first

resonance frequency i.e  $\omega_e = \omega_0$ , we can exploit the resonance gain to enhance the SNR and therefore  $\omega_0$  is the ideal frequency at which the tip radius can be estimated.

Furthermore, to link the tip radius to the experimental lock-in amplitude channel, we solve Eq. (6.1) using the method of averaging technique to obtain an expression for the slow amplitude  $A_{\omega_e}$  as follows:

$$A_{\omega_e} = \frac{dC}{dz} \frac{V_{AC}}{k} Q(V_s - V_{DC}). \quad (6.3)$$

Although Eq. (6.3) doesn't appear to have a direct dependency on the tip radius, this dependency is embedded indirectly in the term  $dC/dz$  via the expression

$$\begin{aligned} \frac{dC}{dz} &= \frac{dC}{dz_{tip}} + \frac{dC}{dz_{cone}} + \frac{dC}{dz_{lever}} \\ \frac{dC}{dz} &= -2\pi\epsilon \frac{R^2}{z^2 + Rz} - \frac{8\pi\epsilon \left( \frac{2H_c \tan^2(\frac{\theta}{2})}{R} + \sin(\frac{\theta}{2}) \right)}{(\pi - \theta)^2} \\ &\quad - \frac{4\epsilon Lw \tan^2(\frac{\theta_t}{2})}{H_c \theta_t^2 (H_c + 2L \tan(\frac{\theta_t}{2}))}. \end{aligned} \quad (6.4)$$

Here, the overall capacitance gradient ( $dC/dz$ ) can be divided into three parts based on the tip-apex, tip-cone and the lever part of the cantilever. The detailed derivation of the expression for each of these parts can be obtained from [155]. In Eq. (6.4),  $\epsilon$  represents the absolute permittivity constant,  $z$  is the instantaneous tip-sample gap,  $R$  is the radius of the AFM probe,  $H_c$  is the height of the tip-cone,  $\theta$  is the cone angle,  $L$  and  $w$  are the length and width of the cantilever, and finally,  $\theta_t$  is the tilt angle of the cantilever. It must be noted that the values for the above constants can be easily obtained from the cantilever specification sheet provided by the manufacturer.

In this work, we make use of the entire expression shown in Eq. (6.4) for identification. However, the contributions from the cone and the lever remain almost constant at small  $z$  values [155] which leads to a simplified expression for the capacitance gradient as follows

$$\frac{dC}{dz} = -2\pi\epsilon \frac{R^2}{z^2 + Rz} + constant. \quad (6.5)$$

The above simplified expression can be combined with experiments at small tip-sample gaps to obtain a faster in-situ identification of tip radius. However, the experiments must be done with care, since the cantilever is electrically excited they have smaller amplitudes of oscillation and this could easily result in snap-into contact phenomena. Furthermore, at room temperature the SNR can be low due to the presence of humidity and the influence of water layer between the tip and the sample.

### 6.1.2. EXPERIMENTAL METHODS AND DISCUSSION

In order to estimate the tip radius, we have implemented a procedure where standard AFM modalities is used to extract the experimental observables. As a first step, the can-

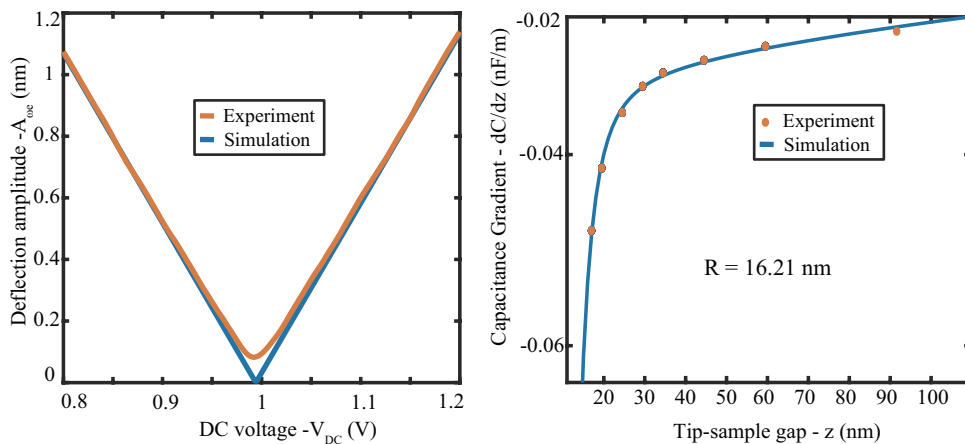


Figure 1: Identification of probe radius from electrostatic response of the cantilever. (a) The cantilever is electrically excited at resonance and modulated with DC voltage at a specific tip-sample gap ( $z$ ) of 28 nm. The resulting deflection amplitude  $A_{\omega_e}$  variation as a function of DC voltage  $V_{DC}$  (orange) is fitted (blue) with Eq. (6.3) to extract the value of  $V_{bias}$  and capacitance gradient  $dC/dz$ . (b) The experimental  $dC/dz$  values (orange) obtained at different tip-sample distances are fitted with Eq. (6.4) to extract the AFM tip radius.

6

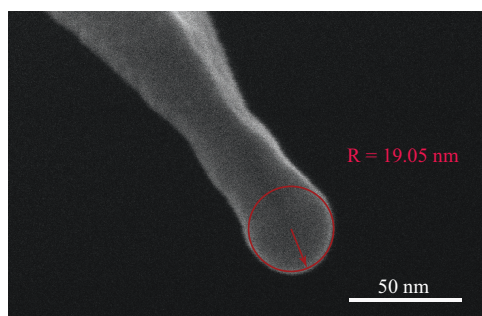


Figure 2: AFM tip radius estimation using SEM image. The image is obtained at a tilt of 30 degrees. The value extracted from the SEM is used as a benchmark to compare the value estimated from KPFM technique.



tiler and the sample are connected to ground to ensure the only difference in electrical potential comes from the CPD between the materials. Next, a force distance curve is used to statically approach the sample at a fixed distance "z" from the sample. Then, the cantilever is electrically excited at the first mechanical resonance frequency ( $\omega_0$ ) with a voltage of " $V_{AC}$ " and simultaneously the DC voltage " $V_{DC}$ " is modulated. The modulation causes the lock-in amplitude ( $A_{\omega_e}$ ) at frequency " $\omega_e = \omega_0$ " to reach a minimum and traces a V-shaped curve as shown in Fig. 1(a). The characteristic minimum in the V-shaped curve indicates the bias voltage required to nullify the electrostatic forces between the tip and the cantilever i.e  $V_{bias} = V_s - V_{DC}$ . Additionally, the slope of the resulting  $A_{\omega_e}$  versus  $V_{DC}$  curve provides information about the capacitance gradient which in turn holds information about the cantilever geometry including the tip radius (see Eq.(6.4)). The above procedure is repeated at different tip-sample gaps to average piezo drift and noise within the measurements as shown in Fig. 1(b). Finally, the tip radius is estimated from the experimental measurements by fitting Eq. (6.4) resulting in a value approximately equal to  $16.21 \pm 0.72$  nm.

Next, in order to verify this value, the probe is imaged using a high resolution SEM as shown in Fig. 2. From the SEM image a tip radius of  $19.05 \pm 0.285$  nm is estimated. The discrepancy between the SEM and the identified radius value can be attributed to trapped charges on the sample, presence of intermediate water layer in ambient conditions as well as the influence of other long range forces. However, some of these problems such as water layer can be mitigated to a certain extent by using a controlled environment chamber and using dry nitrogen; whereas, trapped local charges can be mitigated by performing multiple experiments at several different locations on the sample and average the data to minimize the impact. Additional details regarding the experiments, modelling and data analysis techniques can be found in [156].

## 6.2. ESTIMATION OF HAMAKER CONSTANT USING SOFTENING NONLINEAR RESPONSE OF AFM

In chapter 2 we discussed the improvement of SNR in higher harmonics by studying the nonlinear frequency response of the cantilever interacting with the sample. In this work, we exploit the dependency between the model coefficients and specific features in the nonlinear frequency response to identify the Hamaker constant of the sample. The Hamaker constant is a key parameter that measures the strength of VdW forces between two materials. Characterizing the VdW forces is key in understanding nanoscale phenomena such as surface adhesion [157, 158], wetting behaviour [159], colloidal and emulsion stability [160], stiction and friction [158].

Traditionally, the Hamaker constant is estimated by Lifshitz theory [30] but measuring the same experimentally is far from trivial. Although, some of the previous studies have employed quasi-static and quasi-dynamic methods to measure the Hamaker constant, they are more prone to instabilities such as snap-in contact and are thus difficult to control [161, 162]. Since, the VdW force is strongest at few tens of nanometers from the sample surface, additional surface effects such as capillary, magnetic and electrostatic forces often distort the results. Other techniques which rely on higher harmonics are almost impossible to employ in day to day studies since VdW forces barely excite any

higher harmonics above the noise floor [163]. Hence, in this work we use nonlinear frequency response of the cantilever together with an analytical model for characterizing the Hamaker constant.

### 6.2.1. NUMERICAL MODELING

In order to probe the VdW interaction between the tip and the sample, we model the cantilever probe as a Single Degree of Freedom (SDOF) system with base excitation as follows

$$\ddot{x} + \frac{1}{Q}\dot{x} + x = \frac{\Omega^2 Y}{k} \cos(\Omega\tau + \phi) + F_{vdw}. \quad (6.6)$$

Here,  $x$  represents the normalized deflection of the cantilever ( $x=x^*/\eta$ , where  $\eta$  is the static equilibrium gap width). In addition,  $\Omega=\omega/\omega_0$  is the normalized excitation frequency and  $\omega_0 = 2\pi f_0$  is the fundamental frequency of the free microcantilever in the absence of tip-sample interaction forces; whereas  $\omega$  is the excitation frequency.  $Q$  represents the quality factor and the amplitude of the dither piezoelectric actuator is denoted by  $Y$ . The dotted quantities represent derivatives with respect to rescaled time  $\tau$  ( $\tau = \omega_0 t$ ). Finally,  $F_{vdw}$  is the nonlinear tip-sample interaction force defined as

$$F_{vdw}(z, t) = -\frac{HR^3}{z^2(2R+z)^2}, \quad (6.7)$$

where,  $H$  is the Hamaker constant,  $R$  is the tip radius and  $z$  is the tip-sample gap. Similar to the previous section, Eq. (6.6) is solved using the method of averaging to obtain the slow varying expressions for both the amplitude ( $A$ ) and phase ( $\phi$ ) of the cantilever as a function of excitation frequency. These expressions are defined as follows

$$\Omega = 1 \pm \frac{1}{2} \sqrt{\left(\frac{Y\eta}{kzA}\right)^2 - \left(\frac{1}{A}\right)^2 - I(A, \eta, R, k)H}$$

where,

$$I(A, \eta, R, k) = \frac{1}{6kr^2z^3} \left[ \frac{(1 - (A/\eta)^2)\eta^4 + 8R^3z + 12R^2z^2 + (6 - (A/\eta)^2)Rz^3}{(4R^2 + 4Rz + (1 - (A/\eta)^2)\eta^2)^{(3/2)}} \right] + \frac{1}{6kr^2z^3} \left[ \frac{(A/\eta)^2(R + \eta) - \eta}{(1 - (A/\eta)^2)^{(3/2)}} \right]. \quad (6.8)$$

$$\Omega = 1 \pm \frac{1}{2Q \tan(\phi)} - G(R, k, \eta, Y, Q, \phi)H$$

where,

$$G(R, k, \eta, Y, Q, \phi) = \frac{k^2}{6F^2Q^2 \sin^2(\phi)} \left[ \frac{Y^2Q^2(R + \eta) \sin^2(\phi) - k^2\eta^3}{(k^2\eta^2 - Y^2Q^2 \sin^2(\phi))^{(3/2)}} \right] + \frac{k^2}{6F^2Q^2 \sin^2(\phi)} \left[ \frac{Y^2Q^2(R + \eta) \cos^2(\phi) - Y^2Q^2(R + \eta) + k^2(2R + \eta)^3}{(Y^2Q^2 \cos^2(\phi) - Y^2Q^2 + k^2(2R + \eta)^2)^{(3/2)}} \right]. \quad (6.9)$$

Here,  $I(A, \eta, R, k)$  and  $G(R, k, \eta, Y, Q, \phi)$  are nonlinear functions that capture the effect of VdW forces (detailed derivation can be found in [156]); whereas, the remaining expression within the equations capture the amplitude and phase coming from the dither piezo excitation. Finally, in order to extract the Hamaker constant of the sample, an optimization routine is developed using Eqs. (6.8) and (6.9) to fit the experimental data as described in the next section.

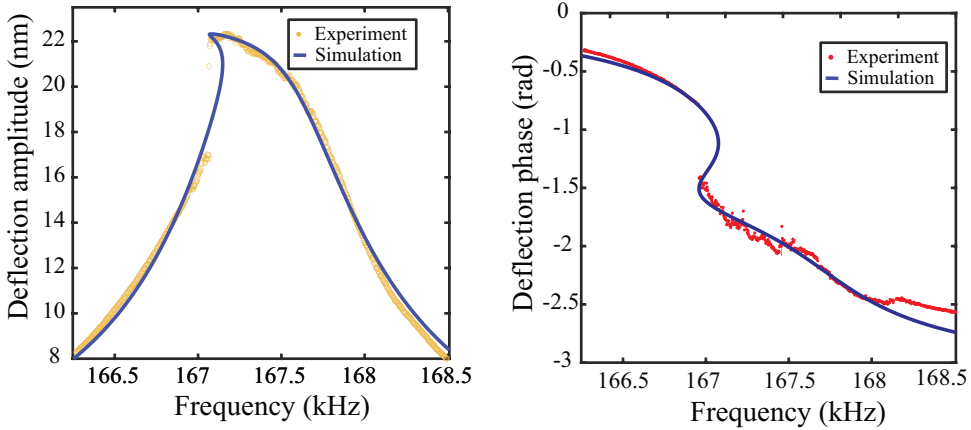


Figure 3: Identification of Hamaker constant from the softening response of the cantilever due to VdW forces. (a) Experimental frequency response of the cantilever (yellow) and the corresponding fit (blue) from Eq. (6.8). (b) Experimental phase response (red) as a function of frequency and the corresponding fit (blue) from Eq. (6.9).

### 6.2.2. EXPERIMENTAL RESULTS AND DISCUSSION

The experimental procedure to obtain the nonlinear frequency response is similar to the one described in section. 3.1 of chapter 3. Figure. 3 shows an experimental frequency response curve with amplitude (yellow) and phase data (red). Furthermore, the corresponding analytical fit from Eqs. (6.8) and (6.9) are highlighted in blue lines. The experiment is performed with a silicon cantilever with platinum conductive coating (TAP190ALG, budget sensors) on HOPG sample. Additionally, the AFM tip radius  $R=20 \pm 0.31$  nm is measured using SEM, and the stiffness  $k=4.5$  N/m,  $Q=300.98$ , and  $f_0=135.34$  kHz is measured using thermal calibration [49].

Since HOPG is susceptible to influence from electrostatic forces, the previously discussed methodology from section. 6.1 is employed to nullify the electric field between the tip and the sample before obtaining the frequency response curve. The extracted Hamaker constant value from the experimental data is  $30 \times 10^{-19}$  J which is order of magnitude different from the literature value is  $4 \times 10^{-19}$  J [29, 30]. We postulate several reasons to this observed discrepancy such as the drift from the piezo, the influence of water layer at ambient conditions, the influence of electrostatic and other long range forces coming from the cone and lever of the mechanical transducer as crosstalk signals, and finally, the optical lever sensitivity which has an inherent error depending on the length of the cantilever [122, 164]. Nevertheless, the technique shows potential for robust iden-

tification; however, the practical limitations of experiments have to be efficiently tackled to make the technique useful for AFM applications.

### 6.3. MACHINE LEARNING BASED IDENTIFICATION TECHNIQUES FOR DYNAMIC AFM

In chapter 5, we looked into a novel identification technique that combines data science and machine learning with experimental observables of dynamic AFM to obtain not only the governing equations of motion but also obtain the tip-sample interaction force. Similarly, here we discuss some of the possible applications of data driven algorithms in dynamic AFM.

#### 6.3.1. CHARACTERIZATION OF VISCOELASTIC RESPONSE OF SOFT MATTER USING DATA DRIVEN ANALYSIS

Chapter 4 highlighted the growing interest in the scientific community to understand nanoscale viscoelastic effects and the need for developing computational models that can exploit the vast number of experimental observables for accurate viscoelastic characterization. In this regard, data driven algorithms provide the necessary tools required to investigate and characterize nanoscale viscoelastic properties in dynamic AFM applications. For example, one of the limiting factors of using self-consistent viscoelastic models is that they require higher computational time (see chapter 4). This limitation is primarily due to the fact that these models need to know a-priori the tip's trajectory and its history. However, such a limitation can be easily overcome by using data driven analysis since it predicts the temporal motion of the cantilever in real time. Next, the data driven techniques can correlate the various functions within the library to their underlying physical mechanisms. This was highlighted in chapter 5, where we showed that certain functions such as indentation and rate of indentation have larger coefficients when probing softer polymeric samples and are the result of viscoelastic dissipative effects.

In addition to above, the sparse identification technique can be easily modified to incorporate parameterized library functions and forcing functions. This allows the functions to be not only dependent on the tip-sample gap but also on inter-atomic distance, surface relaxation times among others. This enhanced functional library has the potential to capture the actual physical phenomena behind the instrument's observables without any approximation or linearisation of the phenomena. This improved library combined with a robust optimization routine can provide the means to probe viscoelastic properties from real time interaction data in dynamic AFM.

#### 6.3.2. IDENTIFICATION OF INTER-MODAL COUPLING IN DYNAMIC AFM USING NEURAL NETWORKS

In chapter 3, we discussed the importance of mode-coupling for dynamic AFM and how internal resonance based cantilevers have demonstrated a strong SNR of higher harmonics for tip-sample force reconstruction. Outside of AFM, mode coupling finds applications in various micro and nanomechanical systems [165] from improving the accuracy of mass sensing devices [166–168], reducing phase noise in micromechanical

resonators [169–171] to encoding quantum information by confining light to a quantum state [172]. In each of these cases, the temporal data of the cantilever such as deflection and velocity possess specific features coded on to their trajectories that indicate inter-modal coupling. This was highlighted in chapter 3, where we proposed phase space trajectory as the method of choice to visualize the presence of mode-coupling in dynamic AFM.

However, mode-coupling in nanomechanical systems has numerous origins [105, 173–177] and is often difficult to attribute it to a specific physical mechanism via traditional modelling approach. In this regard, an effective strategy would be employing machine learning to solve the problem. Since data driven models have revolutionized the analysis and understanding of complex data, recognizing patterns, and developing classifications based on multimodal datasets [178–183], it is best suited for parsing large amounts of temporal data in order to identify mode-coupling phenomena and its underlying physics. In this work, we demonstrate the capability of one such data driven algorithm namely, quasi recurrent neural networks to identify the mode-coupling phenomena in dynamic AFM. We highlight some of our first results in the following section.

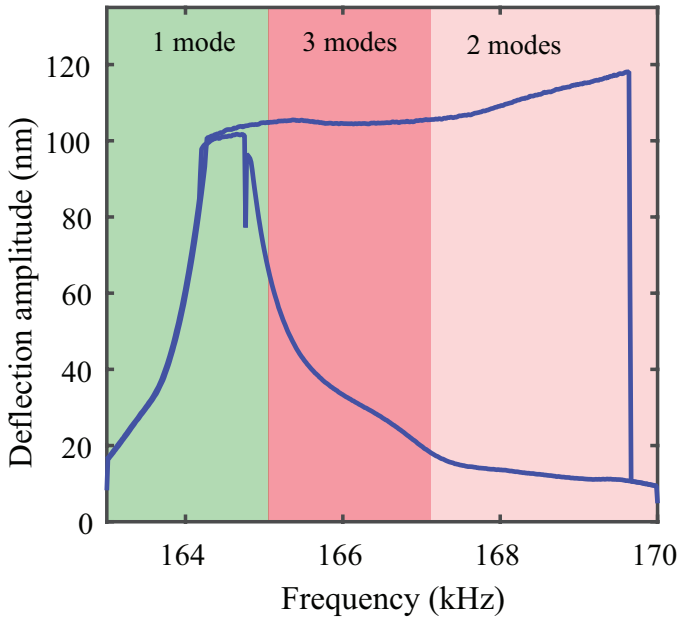


Figure 4: Experimental frequency response curve obtained with raw deflection signal of the cantilever on Mica sample. The frequency range is divided into three regions depending on the number of higher order eigenmodes contributing to the overall cantilever oscillations.

### 6.3.3. METHODS AND RESULTS

The quasi recurrent neural networks (QRNN) is a powerful tool for modelling sequential data and have been proven to be efficient in untangling complex dynamics behind structures by studying the time data [184, 185]. Furthermore, the hidden units of QRNN

provide interpretable information that can be distilled to understand the physics behind the data. This capability is well suited to identify the coupling mechanism between the fundamental mode and higher order modes of the cantilever in a dynamic AFM application. It must be noted that in this section we only highlight some of the preliminary results obtained through this technique; whereas, all the intricate details regarding the QRNN deployment and algorithm can be found in the works of Bradbury et al [186].

Figure 4 shows the experimental frequency response curve obtained with a standard tapping mode cantilever made of silicon (NCLR, Nanoworld) on Mica sample. The experimental data is obtained in a similar fashion to the data showcased in chapter 3 i.e by making use of nonlinear frequency sweeps. Through this method, the tip-sample distance at which the nonlinear frequency sweeps are obtained can be carefully controlled which in turn allows to obtain several data sets with varying degrees of tip-sample interaction. The multiple data sets facilitate an efficient training of the neural network; since, they capture different degrees of distortion within the time data due to mode coupling.

A second way to induce mode-coupling is by tuning the excitation frequency to the sweet spot frequency range as discussed in chapter 3 and this tuning is inherently present in frequency sweeps. This will further allow the trained network to track the change in coupling strength as a function of drive frequency. Furthermore, each frequency sweep is made up of 501 frequency points and is considered as a single data set. Additionally, each frequency point contains temporal data made up of 50000 data points obtained at 250MHz sampling rate. The first 20000 time steps are used for training the algorithm; whereas the rest are used to perform cross validation and model prediction. This step is then repeated for every frequency point and for multiple data sets which are obtained at different points on the sample and with different tip-sample distances. Thus the above approach covers a whole spectrum of possible tip-sample interactions with varying degrees of contribution from the higher order modes and is ideal for training the QRNN algorithm.

Figure 5 shows the identification of deflection time series (orange) and phase space orbits (red) by the trained network (blue) at different excitation frequencies. QRNN shows remarkably accurate representation of the underlying dynamics considering that no mathematical model nor prior knowledge of the underlying physics was used to teach the network. Additionally, it must be noted that, once the network is fully trained, only the input highlighted in black curve (approximately 1500 time steps) in Figs. 5(a), (c) and (e) which corresponds to just one period of oscillation is sufficient for the network to identify the underlying dynamics. This further highlights the utility of the technique to predict the dynamics of AFM in real time.

Furthermore, the network is capable of reconstructing the dynamics with varying degrees of tip-sample interaction strength as seen in Figs. 5(b), (d) and (f). For example, in Fig. 5(a) and (b) at excitation frequency of 164.175 kHz, the cantilever is essentially free from any repulsive tip-sample interaction and only experiences weak long range attractive forces and the phase space orbit is circular representing a simple harmonic motion. Whereas, in Fig. 5 (e) and (f), repulsive interactions kick in and the phase space is warped showing high degree of contributions from the higher order modes in the deflection signal. In both of these cases, the network can accurately identify the varying contributions from the higher order modes and reconstruct the cantilever dynamics efficiently.

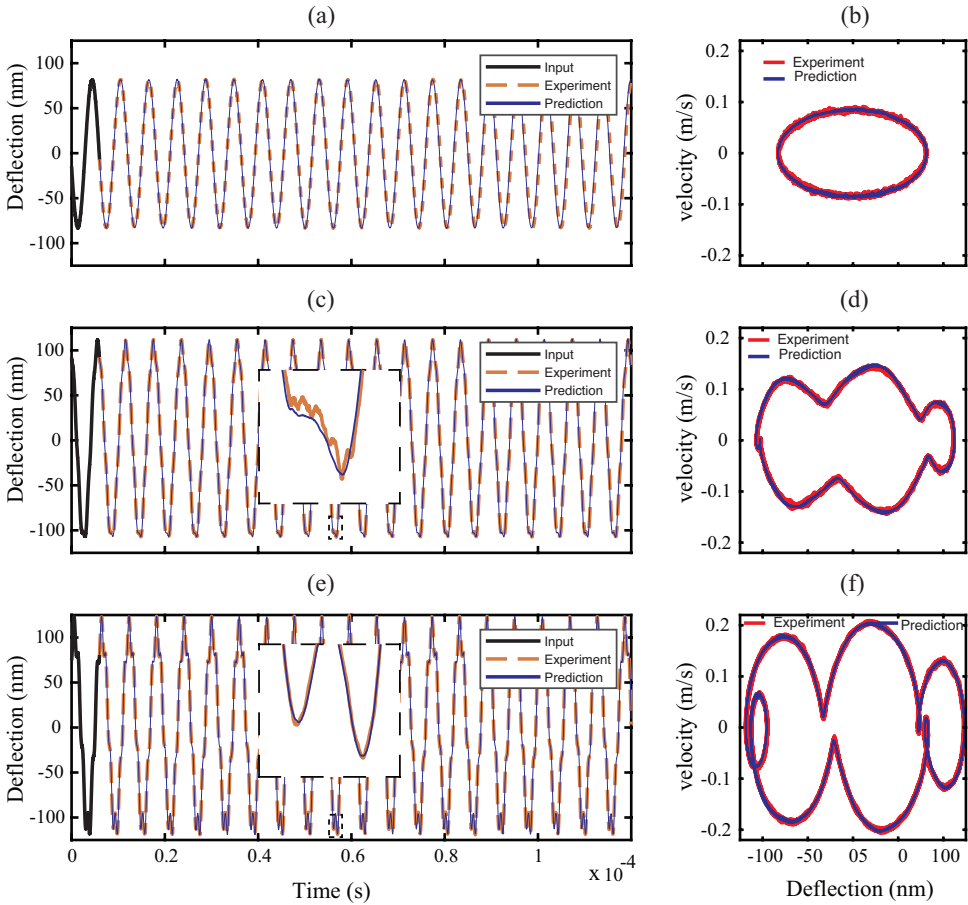


Figure 5: QRNN prediction of the AFM nonlinear oscillations and the evolution of the orbits as a function of excitation frequency. The experimental cantilever oscillations and the corresponding phase orbits are indicated by the orange and red curves, respectively. The fit from neural network is indicated by blue curves. Additionally, the single cycle input to the neural network is indicated by black curve. (a)-(b) The oscillations at a frequency of 164.175 kHz show a weak interaction force between the tip and the sample. This is highlighted by the circular experimental phase space orbit (red) and its corresponding prediction by neural network (blue). (c)-(d) The oscillations at a frequency of 166.976 kHz show a moderate interaction force between the tip and the sample. This is highlighted by the warping of the experimental phase space orbit (red) and its corresponding prediction by neural network (blue). The warping is caused by an increased contribution of the second mode to the overall cantilever oscillations. (e)-(f) The oscillations at a frequency of 169.356 kHz show high interaction force between the tip and the sample. This is highlighted by a highly warped experimental phase space orbit (red) and its corresponding prediction by neural network (blue).

In addition to reconstructing the dynamics of the cantilever under varying tip-sample strengths, the QRNN network can also distinguish the contribution of different modes in the cantilever oscillations. An example of this is shown in Fig. 6, where we show 3 out of 350 different hidden units that are activated at different frequency ranges. By comparing this activation with the original experimental frequency response curve in Fig. 4, we see that the contribution of hidden unit 36 and 135 slowly increases with increasing excitation frequency; whereas, the hidden unit 341 has a particular peak in a specific frequency range which we referred to as the sweet spot in chapter 3. This indicates that, the hidden unit 341 is following the activation of third mode of the cantilever and tracks its contribution to the overall cantilever oscillations; whereas, the units 36 and 135 are indicative of the second mode. This behaviour is in line with the results discussed in chapter 3.

Although, the data driven algorithm shows potential in identifying mode coupling in dynamic AFM; further experiments with different tip-sample configurations are necessary to fully explore its capability. Nevertheless, the approach has shown that the data driven analysis is capable of uncovering hidden dynamics of nanomechanical systems without any prior knowledge of the underlying physics which could prove instrumental in probing certain mode interactions in other complex NEMS and MEMS devices.

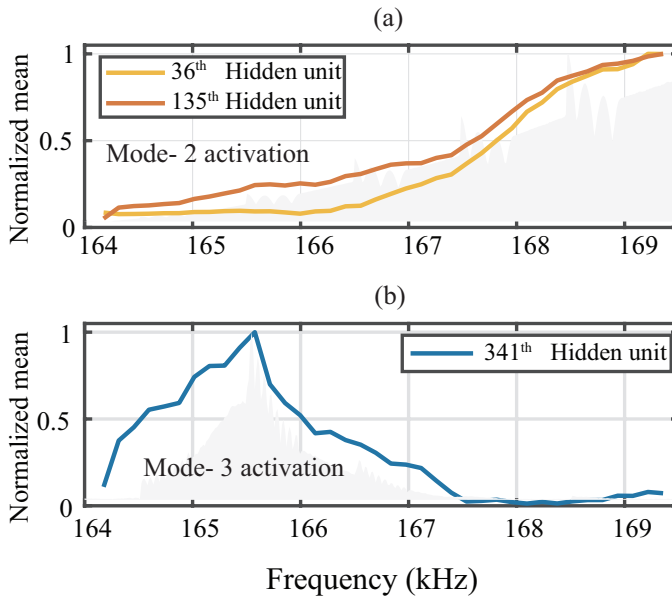


Figure 6: The neuron activation of individual hidden units due to mode coupling. (a) Activating of 36<sup>th</sup> and 135<sup>th</sup> hidden units indicating the increasing influence of second mode in the cantilever oscillations. (b) Activating of 341<sup>th</sup> hidden unit over specific frequency identified as the sweet spot in chapter 3 indicating the increasing influence of second mode in the cantilever oscillations.



7

7

# 7

## CONCLUSIONS AND RECOMMENDATIONS

*In this chapter, a brief summary and relevant conclusions derived from the performed research are presented. Furthermore, reflections on the limitations of the chosen approaches and recommendations for continuation on basis of this research are discussed.*

### 7.0.1. OVERVIEW AND CONCLUSIONS

The main goal of this research was to exploit the nonlinear dynamical behaviour of the cantilever in TM-AFM and develop novel identification techniques for material characterization. The techniques developed in this thesis have taken the AFM community a step closer in identifying the nanomechanical properties with an increased accuracy. In this section, I briefly summarize the main findings of each chapter and highlight the potential impact of the research on future applications in dynamic AFM.

Intuitively, we started by first investigating the global nonlinear dynamics of TM-AFM and the robustness of attractors in chapter 2. We showed that in addition to the well known bi-stable solutions of TM-AFM, there exists another possible state of motion close to the sample characterized by small amplitude of deflection. This previously unknown state of motion was referred to as "in-contact" attractor in this thesis. Interestingly, during the parametric study of in-contact attractor it was found that there exists a critical threshold value of AFM tip radius below which the in-contact attractor doesn't exist. We highlighted this using basins of attraction and tracking the evolution of in-contact attractor as a function of tip radius. Furthermore, we showed that by operating the cantilever close to the sample with a small amplitude of oscillation; one can obtain high resolution images, better stability as well as lower tip wear. Additionally, the feedback instabilities caused by switching between repulsive and attractive regimes can be avoided by operating the cantilever in the in-contact regime [187–189].

Next, we highlighted the utility of bifurcation diagrams and nonlinear frequency response curves to map the appearance and disappearance of several stable oscillatory motions in TM-AFM. Moreover, the robustness of these oscillatory motions and their corresponding attractors to external perturbations were studied using local integrity measures (LIM) and integrity factor (IF). We showed that these nonlinear dynamical tools not only help in identifying the dynamical scenario under which the system is rendered unfit for use, but can also provide details on new routes to crisis and escape scenarios which could lead to chaos and be detrimental to AFM operation [91, 107, 190, 191]. Hence, based on the aforementioned results we see that such fundamental studies are required to not only understand some of the underlying mechanisms affecting the performance of the AFM; but also to help identify which specific nonlinear dynamical tool can be used to understand and solve some of the practical issues such as feedback instabilities, chaotic motion or amplitude jumps that are regularly observed when operating an AFM.

The insights derived from studying the global dynamics of TM-AFM were exploited in chapter 3 to develop a novel methodology to boost the signal to noise ratio (SNR) of higher harmonics. In this chapter, we showed that by actively detuning the drive frequency of the cantilever to a specific excitation range, one can induce strong modal interactions between the eigenmodes of the cantilever. In particular, we made use of internal resonance phenomena between the first three eigenmodes of the cantilever and improved the SNR of the 6<sup>th</sup> and 17<sup>th</sup> harmonics by 7 and 16 folds, respectively. Traditionally, such improvements in SNR had stemmed from geometrical modification of the AFM probe [53–56]. In contrast to this, here we highlighted the importance of understanding the nonlinear dynamical behaviour of the AFM probe under the influence

of the tip-sample forces and how we can exploit these nonlinear phenomena for signal amplification. Moreover, mode coupling also has additional benefits such as lowered sample indentation due to phase synchronization between the interacting modes. This lowered indentation reduces the peak repulsive forces exerted by the cantilever on to the sample thus minimizing sample damage.

In addition to above, we showed that such a nonlinear dynamical study is not just limited to parameter identification but can also be used to construct tools for visual inspection. We illustrated this by highlighting how the phase-space orbit can be utilized for visualization of mode-coupling. Finally, we corroborated the experimental results using a computational model comprising of Multiple-Degrees of Freedom (MDOF) and non-smooth nonlinear interactions between the tip and the sample. The model reinforces the idea of mode coupling as the physics behind the observed increase in the amplitude of higher harmonics as well as the associated lower sample indentation. We believe that this work will enable efficient characterization of nanomechanical properties of organic and inorganic samples using multi-frequency AFM techniques.

In chapter 4, we studied the influence of experimental observables on the identified viscoelastic parameters. In particular, we looked into viscoelastic response of a soft PS-LDPE polymer blend sample using the moving surface model and IM-AFM technique. The detailed analysis revealed that the surface viscoelastic response obtained from the model is often non-physical and dominated by only those parameters which can be attributed to the bulk viscoelastic properties of the sample. We attributed this finding to the non-convexity and flat topological landscape of the objective function with respect to the sample's surface viscoelastic parameters. We further reinforced this hypothesis by performing a large number of simulations using both local gradient-based and heuristic based global optimization techniques.

To remedy this, we introduced a simplified model with only three bulk parameters that were deemed important from the previous statistical analysis. In addition to this, we introduced a numerical framework wherein an initial point selection criteria was introduced to ensure that the optimization routine leads to consistent results. The results obtained from this procedure were in excellent agreement with the values previously reported in the literature. This work highlights the importance of testing the dependency of instrument's observables on the model's viscoelastic response before attempting nanomechanical characterization. Additionally, the work also sheds light on the need to develop novel numerical models that can take advantage of the large number of experimental observables available in multi-frequency AFM to truly probe the surface dynamics of the sample.

Some of the aforementioned limitations is addressed in chapter 5 by moving away from traditional AFM models and brute force fitting techniques in favour of machine learning and data science based approaches for dynamic AFM applications. We showed that by using sparse identification technique [73, 138–142] combined with symbolic regression [72, 74] the nanoscale interaction forces in dynamic AFM measurements can be easily identified. The machine learning algorithm not only identifies the interaction force with a sub-microsecond resolution but also determines the underlying governing equation of motion of the AFM cantilever. This governing equation is often crucial for untangling the hidden physical mechanisms responsible for the observed tip-sample in-

teraction.

In addition to above, we also discussed in detail the training methodology and supervision of the algorithm based on standard AFM models, and explained the model selection criterion in the pareto space by tuning hyper-parameters. Finally, we showed the usefulness of the approach by performing experiments on polymer blend of PS-LDPE materials and estimating their nanoscale interaction forces.

The experimental results obtained in our study was inline with the values previously reported in the AFM measurements of polymers which further reinforced the capability of the proposed approach. Since, accurate measurement of tip-sample force is central to many AFM applications, we believe that data science combined with machine learning will ease the difficulty of reconstructing the tip-sample force in dynamic AFM. Furthermore, the use of machine learning algorithms to study the nano-scale interactions in dynamic AFM circumvents the problems previously reported in literature such as the requirements of high number of harmonics [54], measuring experimental transfer function [71] and inability to follow changes in tip-sample forces under fast time scales [66–69]. Thus the proposed approach is of importance when studying transient biological processes or chemical reactions as well as obtaining high resolution dynamical force volume measurements.

Finally, a detailed overview of possible research directions based on preliminary investigation carried out during the course of this thesis is presented in chapter 6. In particular, we discussed a methodology to monitor the AFM probe radius via electrostatic forces. We further discussed in detail the experimental procedure to obtain the dynamical response of the cantilever as a function of bias voltage and fitted the experimental data with a SDOF model. An SEM image was used to corroborate the results obtained from KPFM technique. Although the method was found promising, including a more accurate capacitance model and streamlining the experimental procedure can enhance the accuracy of the characterization.

Next, we proposed an identification technique to extract the Hamaker constant of the sample through the nonlinear frequency response curves. We showed through both experiments and simulations that the cantilever exhibits softening response under the influence of VdW forces and this softening response is directly proportional to the nonlinear forces existing between the tip and the sample. Furthermore, the proposed model based on method of averaging provides expressions for amplitude and phase of the cantilever response which can be combined with optimization algorithms to develop a automated and fast fitting procedure.

I finalized the research outlook by looking at possibilities of incorporating machine learning and data driven analysis to improve dynamic AFM capabilities. In particular, I discussed the opportunities in extracting the viscoelastic properties of the sample by combining self consistent models together with data driven analysis. Finally, I highlighted some results where neural networks can be trained on experimental data alone without any prior knowledge of the physics to determine the presence of mode coupling. This method can be easily extended to other nanomechanical systems to determine complex nonlinear phenomena such as internal resonance, quasi-periodic motion and chaotic behaviour.

In conclusion, I believe that the approaches and ideas discussed in this thesis will

offer insight and inspire the scientific community to develop novel concepts and identification techniques that can tackle the future challenges in nanoscale characterization.





# BIBLIOGRAPHY

- [1] G. Binnig, C. F. Quate, and Ch. Gerber. Atomic force microscope. *Phys Rev Lett*, 56:930–933, 1986.
- [2] Chia-Yun Lai, Tuza Olukan, Sergio Santos, Amal Al Ghaferi, and Matteo Chiesa. The power laws of nanoscale forces under ambient conditions. *Chemical Communications*, 51(99):17619–17622, 2015.
- [3] Amir F. Payam, Jorge R. Ramos, and Ricardo Garcia. Molecular and nanoscale compositional contrast of soft matter in liquid: Interplay between elastic and dissipative interactions. *ACS Nano*, 6(6):4663–4670, 2012.
- [4] R. Garcia, C. J. Gomez, N. F. Martinez, S. Patil, C. Dietz, and R. Magerle. Identification of nanoscale dissipation processes by dynamic atomic force microscopy. *Physical Review Letters*, 97(1):016103, 2006.
- [5] Elena T Herruzo, Alma P Perrino, and Ricardo Garcia. Fast nanomechanical spectroscopy of soft matter. *Nature communications*, 5(1):1–8, 2014.
- [6] A. Raman, S. Trigueros, A. Cartagena, A. P. Stevenson, M. Susilo, E. Nauman, and S. A. Contera. Mapping nanomechanical properties of live cells using multi-harmonic atomic force microscopy. *Nat Nanotechnol*, 6(12):809–14, 2011.
- [7] Simone Benaglia, Victor G. Gisbert, Alma P. Perrino, Carlos A. Amo, and Ricardo Garcia. Fast and high-resolution mapping of elastic properties of biomolecules and polymers with bimodal afm. *Nature Protocols*, 13(12):2890–2907, 2018.
- [8] Horacio V. Guzman, Alma P. Perrino, and Ricardo Garcia. Peak forces in high-resolution imaging of soft matter in liquid. *ACS Nano*, 7(4):3198–3204, April 2013.
- [9] Adrian P. Nievergelt, Niccolo Banterle, Santiago H. Andany, Pierre Gonczy, and Georg E. Fantner. High-speed photothermal off-resonance atomic force microscopy reveals assembly routes of centriolar scaffold protein sas-6. *Nature Nanotechnology*, 13(8):696–701, 2018.
- [10] David Alsteens, Heykel Trabelsi, Patrice Soumillion, and Yves F. Dufrene. Multi-parametric atomic force microscopy imaging of single bacteriophages extruding from living bacteria. *Nature Communications*, 4(1):2926, 2013.
- [11] Noriyuki Kodera, Daisuke Yamamoto, Ryoki Ishikawa, and Toshio Ando. Video imaging of walking myosin v by high-speed atomic force microscopy. *Nature*, 468(7320):72–76, 2010.

- [12] Mingdong Dong and Ozgur Sahin. A nanomechanical interface to rapid single-molecule interactions. *Nature Communications*, 2(1):247, 2011.
- [13] Mikihiro Shibata, Hayato Yamashita, Takayuki Uchihashi, Hideki Kandori, and Toshio Ando. High speed atomic force microscopy shows dynamic molecular processes in photoactivated bacteriorhodopsin. *Nature Nanotechnology*, 5(3):208–212, 2010.
- [14] T. R. Albrecht, P. Grutter, D. Horne, and D. Rugar. Frequency modulation detection using high-q cantilevers for enhanced force microscope sensitivity. *Journal of Applied Physics*, 69(2):668–673, 1991.
- [15] Y. Martin, C. C. Williams, and H. K. Wickramasinghe. Atomic force microscope force mapping and profiling on a sub 100 angstrom scale. *Journal of Applied Physics*, 61(10):4723–4729, 1987.
- [16] Leo Gross, Bruno Schuler, Fabian Mohn, Nikolaj Moll, Jascha Repp, and Gerhard Meyer. *Atomic Resolution on Molecules with Functionalized Tips*, pages 223–246. Springer International Publishing, Cham, 2015.
- [17] Y Gan. Atomic and subnanometer resolution in ambient conditions by atomic force microscopy. *Surface Science Reports*, 64(3):99–121, 2009.
- [18] Dmitry Klinov and Sergei Magonov. True molecular resolution in tapping-mode atomic force microscopy with high-resolution probes. *Applied Physics Letters*, 84(14):2697–2699, 2004.
- [19] Yoshiaki Sugimoto, Pablo Pou, Masayuki Abe, Pavel Jelinek, Ruben Perez, Seizo Morita, and Oscar Custance. Chemical identification of individual surface atoms by atomic force microscopy. *Nature*, 446(7131):64–67, 2007.
- [20] Yasuhiro Sugawara, Hitoshi Ueyama, Takayuki Uchihashi, Masahiro Ohta, Seizo Morita, Mineharu Suzuki, and Shuzo Mishima. True atomic resolution imaging with noncontact atomic force microscopy. *Applied Surface Science*, 113-114(Supplement C):364–370, 1997.
- [21] Q. Zhong, D. Inniss, K. Kjoller, and V. B. Elings. Fractured polymer/silica fiber surface studied by tapping mode atomic force microscopy. *Surface Science Letters*, 290(1):L688–L692, 1993.
- [22] Daniel Platz, Erik A Tholén, Devrim Pesen, and David B Haviland. Intermodulation atomic force microscopy. 92(15):153106.
- [23] Tomas R. Rodriguez and Ricardo Garcia. Compositional mapping of surfaces in atomic force microscopy by excitation of the second normal mode of the microcantilever. *Applied Physics Letters*, 84(3):449–451, 2004.
- [24] T J Young, M A Monclus, T L Burnett, W R Broughton, S L Ogin, and P A Smith. The use of the PeakForce quantitative nanomechanical mapping AFM-based method for high-resolution young's modulus measurement of polymers. *Measurement Science and Technology*, 22(12):125703, oct 2011.

- [25] P. J. de Pablo, J. Colchero, J. Gomez-Herrero, and A. M. Baro. Jumping mode scanning force microscopy. *Applied Physics Letters*, 73(22):3300–3302, 1998.
- [26] William F Heinz and Jan H Hoh. Spatially resolved force spectroscopy of biological surfaces using the atomic force microscope. *Trends in Biotechnology*, 17(4):143–150, 1999.
- [27] L. Chopinet, C. Formosa, M.P. Rols, R.E. Duval, and E. Dague. Imaging living cells surface and quantifying its properties at high resolution using afm in qi mode. *Micron*, 48:26–33, 2013.
- [28] Ricardo Garcia. *Theory of Amplitude Modulation AFM*. Wiley-VCH Verlag GmbH & Co. KGaA, 2010.
- [29] Jacob N Israelachvili. *Intermolecular and Surface Forces*. Academic Press, San Diego, 2011.
- [30] E.M. LIFSHITZ and M. Hamermesh. The theory of molecular attractive forces between solids. In L.P. PITAEVSKI, editor, *Perspectives in Theoretical Physics*, pages 329–349. Pergamon, Amsterdam, reprinted from soviet physics jetp 2, part 1, 73, 1956. edition, 1992.
- [31] K. Schram. On the macroscopic theory of retarded van der waals forces. *Physics Letters A*, 43(3):282–284, 1973.
- [32] Jeffrey L. Hutter and John Bechhoefer. Measurement and manipulation of van der waals forces in atomic-force microscopy. *Journal of Vacuum Science & Technology B: Microelectronics and Nanometer Structures Processing, Measurement, and Phenomena*, 12(3):2251–2253, 1994.
- [33] K. L. Johnson. *Contact Mechanics*. Cambridge University Press, 1985.
- [34] Kenneth Langstreth Johnson, Kevin Kendall, A. D. Roberts, and David Tabor. Surface energy and the contact of elastic solids. *Proceedings of the Royal Society of London. A. Mathematical and Physical Sciences*, 324(1558):301–313, 1971.
- [35] B.V Derjaguin, V.M Muller, and Yu.P Toporov. Effect of contact deformations on the adhesion of particles. *Journal of Colloid and Interface Science*, 53(2):314–326, 1975.
- [36] Daniel Maugis. Adhesion of spheres: The jkr-dmt transition using a dugdale model. *Journal of Colloid and Interface Science*, 150(1):243–269, 1992.
- [37] H. HERTZ. Translated and reprinted in english in "hertz's miscellaneous papers" (macmillan and co, london). *J. Reine Angew. Math.* 92 (1881) 156, 1896.
- [38] W. N. Unertl. Implications of contact mechanics models for mechanical properties measurements using scanning force microscopy. *Journal of Vacuum Science & Technology A*, 17(4):1779–1786, 1999.

- [39] B. Luan and M. O. Robbins. Contact of single asperities with varying adhesion: comparing continuum mechanics to atomistic simulations. *Physical Review E, Statistical, Nonlinear, and Soft Matter Physics*, 74(2 Pt 2):026111, 2006.
- [40] Phil Attard. Measurement and interpretation of elastic and viscoelastic properties with the atomic force microscope. *Journal of Physics: Condensed Matter*, 19(47):473201, nov 2007.
- [41] M. A. Lantz, S. J. O'Shea, M. E. Welland, and K. L. Johnson. Atomic-force-microscope study of contact area and friction on nbse<sub>2</sub>. *Phys Rev B*, 55:10776–10785, Apr 1997.
- [42] Robert W. Carpick and Miquel Salmeron. Scratching the surface: Fundamental investigations of tribology with atomic force microscopy. *Chemical Reviews*, 97(4):1163–1194, 1997. PMID: 11851446.
- [43] Ricardo Garcia and Alvaro San Paulo. Dynamics of a vibrating tip near or in intermittent contact with a surface. *Physical Review B*, 61(20):R13381–R13384, 2000.
- [44] L. Nony, R. Boisgard, and J. P. Aime. Nonlinear dynamical properties of an oscillating tip-cantilever system in the tapping mode. *The Journal of Chemical Physics*, 111(4):1615–1627, 1999.
- [45] Tomas R. Rodriguez and Ricardo Garcia. Tip motion in amplitude modulation (tapping-mode) atomic-force microscopy: Comparison between continuous and point-mass models. *Applied Physics Letters*, 80(9):1646–1648, 2002.
- [46] K. Wolf and O. Gottlieb. Nonlinear dynamics of a noncontacting atomic force microscope cantilever actuated by a piezoelectric layer. 91(7):4701–4709.
- [47] S Ruetzel and A Lee, Sand Raman. Nonlinear dynamics of atomic force microscope probes driven in lennard-jones potentials. 459(2036):1925–1948.
- [48] S. I. Lee, S. W. Howell, A. Raman, and R. Reifengerger. Nonlinear dynamic perspectives on dynamic force microscopy. 97(1-4):185–198.
- [49] John E. Sader, James W. M. Chon, and Paul Mulvaney. Calibration of rectangular atomic force microscope cantilevers. *Review of Scientific Instruments*, 70(10):3967–3969, 1999.
- [50] R. Garcia and E. T. Herruzo. The emergence of multifrequency force microscopy. *Nature Nanotechnology*, 7(4):217–26, 2012.
- [51] R. Hillenbrand, M. Stark, and R. Guckenberger. Higher-harmonics generation in tapping-mode atomic-force microscopy: Insights into the tip-sample interaction. *Applied Physics Letters*, 76(23):3478–3480, 2000.
- [52] Martin Stark, Robert W. Stark, Wolfgang M. Heckl, and Reinhard Guckenberger. Spectroscopy of the anharmonic cantilever oscillations in tapping-mode atomic-force microscopy. *Applied Physics Letters*, 77(20):3293–3295, 2000.

- [53] Randi Potekin, Sajith Dharmasena, D. Michael McFarland, Lawrence A. Bergman, Alexander F. Vakakis, and Hanna Cho. Cantilever dynamics in higher-harmonic atomic force microscopy for enhanced material characterization. *International Journal of Solids and Structures*, 110-111:332–339, 2017.
- [54] Ozgur Sahin, Sergei Magonov, Chanmin Su, Calvin F. Quate, and Olav Solgaard. An atomic force microscope tip designed to measure time-varying nanomechanical forces. *Nature Nanotechnology*, 2:507, 2007.
- [55] Aliasghar Keyvani, Hamed Sadeghian, Mehmet Selman Tamer, Johannes Frans Loodewijk Goosen, and Fred van Keulen. Minimizing tip-sample forces and enhancing sensitivity in atomic force microscopy with dynamically compliant cantilevers. *Journal of Applied Physics*, 121(24):244505, 2017.
- [56] O. Sahin, G. Yaralioglu, R. Grow, S. F. Zappe, A. Atalar, C. Quate, and O. Solgaard. High-resolution imaging of elastic properties using harmonic cantilevers. *Sensors and Actuators A: Physical*, 114(2-3):183–190, 2004.
- [57] Huiling Li, Yan Chen, and Lanhong Dai. Concentrated-mass cantilever enhances multiple harmonics in tapping-mode atomic force microscopy. *Applied Physics Letters*, 92(15):151903, 2008.
- [58] Yves F. Dufrene, Toshio Ando, Ricardo Garcia, David Alsteens, David Martinez-Martin, Andreas Engel, Christoph Gerber, and Daniel J. Muller. Imaging modes of atomic force microscopy for application in molecular and cell biology. *Nature Nanotechnology*, 12:295, 2017.
- [59] Ricardo Garcia and Roger Proksch. Nanomechanical mapping of soft matter by bimodal force microscopy. *European Polymer Journal*, 49(8):1897–1906, 2013.
- [60] Manuel R. Uhlig and Robert Magerle. Unraveling capillary interaction and viscoelastic response in atomic force microscopy of hydrated collagen fibrils. *Nanoscale*, 9(3):1244–1256, 2017.
- [61] Yuri M Efremov, Wen-Horng Wang, Shana D Hardy, Robert L Geahlen, and Arvind Raman. Measuring nanoscale viscoelastic parameters of cells directly from afm force-displacement curves. *Scientific reports*, 7(1):1–14, 2017.
- [62] Y.M. Efremov, T. Okajima, and A. Raman. Measuring viscoelasticity of soft biological samples using atomic force microscopy. *Soft matter*, 16(1):64–81, 2020.
- [63] Bahram Rajabifar, Jyoti M Jadhav, Daniel Kiracofe, Gregory F Meyers, and Arvind Raman. Dynamic afm on viscoelastic polymer samples with surface forces. *Macromolecules*, 51(23):9649–9661, 2018.
- [64] Bahram Rajabifar, Ryan Wagner, and Arvind Raman. A fast first-principles approach to model atomic force microscopy on soft, adhesive, and viscoelastic surfaces. *Materials Research Express*, 2021.

- [65] Bahram Rajabifar, Anil K Bajaj, Ronald G Reifenger, Roger Proksch, and Arvind Raman. Discrimination of adhesion and viscoelasticity from nanoscale maps of polymer surfaces using bimodal atomic force microscopy. *Nanoscale*, 2021.
- [66] Amir F Payam, Daniel Martin-Jimenez, and Ricardo Garcia. Force reconstruction from tapping mode force microscopy experiments. *Nanotechnology*, 26(18):185706, 2015.
- [67] Daniel Platz, Daniel Forchheimer, Erik A. Tholen, and David B. Haviland. Interaction imaging with amplitude-dependence force spectroscopy. *Nature Communications*, 4:1360, 2013.
- [68] Hu Shuiqing and Raman Arvind. Inverting amplitude and phase to reconstruct tip-sample interaction forces in tapping mode atomic force microscopy. *Nanotechnology*, 19(37):375704, 2008.
- [69] H. Holscher. Quantitative measurement of tip-sample interactions in amplitude modulation atomic force microscopy. *Applied Physics Letters*, 89(12):123109, 2006.
- [70] Karim Gadelrab, Sergio Santos, Josep Font, and Matteo Chiesa. Single cycle and transient force measurements in dynamic atomic force microscopy. *Nanoscale*, 5(22):10776–10793, 2013.
- [71] Martin Stark, Robert W. Stark, Wolfgang M. Heckl, and Reinhard Guckenberger. Inverting dynamic force microscopy: From signals to time-resolved interaction forces. *Proceedings of the National Academy of Sciences*, 99(13):8473–8478, 2002.
- [72] Michael Schmidt and Hod Lipson. Distilling free-form natural laws from experimental data. *Science*, 324(5923):81–85, 2009.
- [73] Steven L. Brunton, Joshua L. Proctor, and J. Nathan Kutz. Discovering governing equations from data by sparse identification of nonlinear dynamical systems. *Proceedings of the National Academy of Sciences*, 113(15):3932–3937, 2016.
- [74] Silviu-Marian Udrescu and Max Tegmark. Ai feynman: A physics-inspired method for symbolic regression. *Science Advances*, 6(16):eaay2631, 2020.
- [75] Abhilash Chandrashekar, Pierpaolo Belardinelli, Urs Staufer, and Farbod Alijani. Robustness of attractors in tapping mode atomic force microscopy. *Nonlinear Dynamics*, 97(2):1137–1158, 2019.
- [76] Leo Gross, Fabian Mohn, Nikolaj Moll, Peter Liljeroth, and Gerhard Meyer. The chemical structure of a molecule resolved by atomic force microscopy. *Science*, 325(5944):1110–1114, 2009.
- [77] A. Knoll, R. Magerle, and G. Krausch. Tapping mode atomic force microscopy on polymers: Where is the true sample surface? *Macromolecules*, 34(12):4159–4165, 2001.

- [78] Dror Sarid. *Scanning force microscopy with applications to electric, magnetic and atomic forces*, volume 14. Oxford University Press, 1991.
- [79] H. Hoelscher, W. Allers, U. D. Schwarz, A. Schwarz, and R. Wiesendanger. Determination of tip-sample interaction potentials by dynamic force spectroscopy. *Physical Review Letters*, 83(23):4780–4783, 1999.
- [80] E. Rull Trinidad, T. W. Gribnau, P. Belardinelli, U. Staufer, and F. Alijani. Nonlinear dynamics for estimating the tip radius in atomic force microscopy. *Applied Physics Letters*, 111(12):123105, 2017.
- [81] Arash Bahrami and Ali H. Nayfeh. On the dynamics of tapping mode atomic force microscope probes. *Nonlinear Dynamics*, 70(2):1605–1617, 2012.
- [82] A Bahrami and A. H. Nayfeh. Nonlinear dynamics of tapping mode atomic force microscopy in the bistable phase. *Communications in Nonlinear Science and Numerical Simulation*, 18(3):799–810, 2013.
- [83] Ricardo Garcia and Alvaro San Paulo. Attractive and repulsive tip-sample interaction regimes in tapping-mode atomic force microscopy. *Physical Review B*, 60(7):4961–4967, 1999.
- [84] Alvaro San Paulo and Ricardo Garcia. Tip-surface forces, amplitude, and energy dissipation in amplitude-modulation (tapping mode) force microscopy. *Physical Review B*, 64(19):193411, 2001.
- [85] Giuseppe Rega and Valeria Settimi. Bifurcation, response scenarios and dynamic integrity in a single-mode model of noncontact atomic force microscopy. *Nonlinear Dynamics*, 73(1):101–123, 2013.
- [86] S. Hornstein and O. Gottlieb. Nonlinear dynamics, stability and control of the scan process in noncontacting atomic force microscopy. *Nonlinear Dynamics*, 54(1-2):93–122, 2008.
- [87] Valeria Settimi and Giuseppe Rega. Global dynamics and integrity in noncontacting atomic force microscopy with feedback control. *Nonlinear Dynamics*, 86(4):2261–2277, 2016.
- [88] Arturas Ulcinas and Valentinas Snitka. Intermittent contact afm using the higher modes of weak cantilever. *Ultramicroscopy*, 86(1):217–222, 2001.
- [89] J. D Eusebius, R. C Alan, F F Thomas, A. K Yuri, S Bjoern, and W Xianjun. Auto-07p: Continuation and bifurcation software for ordinary differential equations, 1998.
- [90] Aliasghar Keyvani, Hamed Sadeghian, Hans Goosen, and Fred van Keulen. On the origin of amplitude reduction mechanism in tapping mode atomic force microscopy. *Applied Physics Letters*, 112(16):163104, 2018.
- [91] Aliasghar Keyvani, Farbod Alijani, Hamed Sadeghian, Klara Maturova, Hans Goosen, and Fred van Keulen. Chaos: The speed limiting phenomenon in dynamic atomic force microscopy. *Journal of Applied Physics*, 122(22):224306, 2017.

- [92] M. S. Soliman and J. M. T. Thompson. Integrity measures quantifying the erosion of smooth and fractal basins of attraction. *Journal of Sound and Vibration*, 135(3):453–475, 1989.
- [93] Pierpaolo Belardinelli and Stefano Lenci. An efficient parallel implementation of cell mapping methods for mdof systems. *Nonlinear Dynamics*, 86(4):2279–2290, 2016.
- [94] P. Belardinelli and S. Lenci. A first parallel programming approach in basins of attraction computation. *International Journal of Non-Linear Mechanics*, 80:76 – 81, 2016.
- [95] P. Belardinelli, S. Lenci, and G. Rega. Seamless variation of isometric and anisometric dynamical integrity measures in basins erosion. *Communications in Non-linear Science and Numerical Simulation*, 56:499 – 507, 2018.
- [96] Stefano Lenci and Giuseppe Rega. Optimal control of nonregular dynamics in a duffing oscillator. *Nonlinear Dynamics*, 33(1):71–86, 2003.
- [97] Vahid Vahdat and Robert W. Carpick. Practical method to limit tip sample contact stress and prevent wear in amplitude modulation atomic force microscopy. *ACS Nano*, 7(11):9836–9850, 2013.
- [98] G. Prakash, S. Hu, A. Raman, and R. Reifengerger. Theoretical basis of parametric-resonance-based atomic force microscopy. *Physical Review B*, 79(9):094304, 2009.
- [99] Abhilash Chandrashekar, Pierpaolo Belardinelli, Stefano Lenci, Urs Staufer, and Farbod Alijani. Mode coupling in dynamic atomic force microscopy. *Phys. Rev. Applied*, 15:024013, Feb 2021.
- [100] D. Martinez-Martin, E. T. Herruzo, C. Dietz, J. Gomez-Herrero, and R. Garcia. Noninvasive protein structural flexibility mapping by bimodal dynamic force microscopy. *Phys Rev Lett*, 106:198101, May 2011.
- [101] Per-Anders Thoren, Riccardo Borgani, Daniel Forchheimer, Illia Dobryden, Per M Claesson, Hailu G Kassa, Philippe Leclere, Yifan Wang, Heinrich M Jaeger, and David B Haviland. Modeling and measuring viscoelasticity with dynamic atomic force microscopy. *Physical Review Applied*, 10(2):024017, 2018.
- [102] Mingdong Dong, Sudhir Husale, and Ozgur Sahin. Determination of protein structural flexibility by microsecond force spectroscopy. *Nature nanotechnology*, 4(8):514–517, 2009.
- [103] Ozgur Sahin. Time-varying tip-sample force measurements and steady-state dynamics in tapping-mode atomic force microscopy. *Physical Review B*, 77(11):115405, 2008.
- [104] Ali H Nayfeh and Dean T Mook. *Nonlinear oscillations*. John Wiley & Sons, 2008.



- [105] Ata Keskekler, Oriël Shoshani, Martin Lee, Herre S. J. van der Zant, Peter G. Steeneken, and Farbod Alijani. Tuning nonlinear damping in graphene nanoresonators by parametric-direct internal resonance. *Nature Communications*, 12(1):1099, 2021.
- [106] H. Dankowicz and F. Schilder. *Recipes for Continuation*. Computational Science and Engineering. Society for Industrial and Applied Mathematics, 2013.
- [107] Robert W. Stark. Bistability, higher harmonics, and chaos in afm. *Materials Today*, 13(9):24–32, 2010.
- [108] Ilham Kirrou and Mohamed Belhaq. Control of bistability in non-contact mode atomic force microscopy using modulated time delay. *Nonlinear Dynamics*, 81(1):607–619, 2015.
- [109] Abhilash Chandrashekar, Arthur Givois, Pierpaolo Belardinelli, Casper L. Penning, Alejandro M. Aragon, Urs Staufer, and Farbod Alijani. Sensitivity of viscoelastic characterization in multi-harmonic atomic force microscopy. 2022.
- [110] John Chiefari, Y. K. (Bill) Chong, Frances Ercole, Julia Krstina, Justine Jeffery, Tam P. T. Le, Roshan T. A. Mayadunne, Gordon F. Meijs, Catherine L. Moad, Graeme Moad, Ezio Rizzardo, and San H. Thang. Living free-radical polymerization by reversible addition-fragmentation chain transfer: The raft process. *Macromolecules*, 31(16):5559–5562, Aug 1998.
- [111] Marius Chyasnachyus, Seth L. Young, and Vladimir V. Tsukruk. Probing of polymer surfaces in the viscoelastic regime. *Langmuir*, 30(35):10566–10582, 2014.
- [112] Roger Proksch, Marta Kocun, Donna Hurley, Mario Viani, Aleks Labuda, Waiman Meinhold, and Jason Bemis. Practical loss tangent imaging with amplitude-modulated atomic force microscopy. *Journal of Applied Physics*, 119(13):134901, 2016.
- [113] Ricardo Garcia, Armin W. Knoll, and Elisa Riedo. Advanced scanning probe lithography. *Nature Nanotechnology*, 9(8):577–587, 2014.
- [114] Dong Wang and Thomas P. Russell. Advances in atomic force microscopy for probing polymer structure and properties. *Macromolecules*, 51(1):3–24, 2018.
- [115] Ricardo Garcia. Nanomechanical mapping of soft materials with the atomic force microscope: methods, theory and applications. *Chemical Society Reviews*, 49(16):5850–5884, 2020.
- [116] David W Collinson, Richard J Sheridan, Marc J Palmeri, and L Catherine Brinson. Best practices and recommendations for accurate nanomechanical characterization of heterogeneous polymer systems with atomic force microscopy. *Progress in Polymer Science*, page 101420, 2021.

- [117] Daniel Platz, Daniel Forchheimer, Erik A Tholén, and David B Haviland. Interpreting motion and force for narrow-band intermodulation atomic force microscopy. *Beilstein journal of nanotechnology*, 4(1):45–56, 2013.
- [118] T. C. T. Ting. The Contact Stresses Between a Rigid Indenter and a Viscoelastic Half-Space. *Journal of Applied Mechanics*, 33(4):845–854, 12 1966.
- [119] Phil Attard. Interaction and deformation of viscoelastic particles. 2. adhesive particles. *Langmuir*, 17(14):4322–4328, 2001.
- [120] Santiago D Solares. Probing viscoelastic surfaces with bimodal tapping-mode atomic force microscopy: Underlying physics and observables for a standard linear solid model. *Beilstein journal of nanotechnology*, 5(1):1649–1663, 2014.
- [121] D. B. Haviland, C. A. van Eysden, D. Forchheimer, Daniel Platz, H. G. Kassa, and P. Leclère. Probing viscoelastic response of soft material surfaces at the nanoscale. *Soft Matter*, 12(2):619–624, 2015.
- [122] M. J. Higgins, R. Proksch, J. E. Sader, M. Polcik, S. Mc Endoo, J. P. Cleveland, and S. P. Jarvis. Noninvasive determination of optical lever sensitivity in atomic force microscopy. *Review of Scientific Instruments*, 77(1):013701, 2006.
- [123] Daniel Platz, Erik A Tholén, Carsten Hutter, Arndt C von Bieren, and David B Haviland. Phase imaging with intermodulation atomic force microscopy. *Ultramicroscopy*, 110(6):573–577, 2010.
- [124] Daniel Platz, Daniel Forchheimer, Erik A Tholén, and David B Haviland. The role of nonlinear dynamics in quantitative atomic force microscopy. *Nanotechnology*, 23(26):265705, 2012.
- [125] Daniel Forchheimer, Daniel Platz, Erik A Tholén, and David B Haviland. Model-based extraction of material properties in multifrequency atomic force microscopy. *Physical Review B*, 85(19):195449, 2012.
- [126] Ananth Ranganathan. The levenberg-marquardt algorithm. *Tutorial on LM algorithm*, 11(1):101–110, 2004.
- [127] Simone Benaglia, Carlos A Amo, and Ricardo Garcia. Fast, quantitative and high resolution mapping of viscoelastic properties with bimodal afm. *Nanoscale*, 11(32):15289–15297, 2019.
- [128] Nurul Huda Shaik, Ronald G Reifengerger, and Arvind Raman. Nanomechanical mapping in air or vacuum using multi-harmonic signals in tapping mode atomic force microscopy. *Nanotechnology*, 31(45):455502, 2020.
- [129] Amir Farokh Payam, Alessio Morelli, and Patrick Lemoine. Multiparametric analytical quantification of materials at nanoscale in tapping force microscopy. *Applied Surface Science*, 536:147698, 2021.

- [130] Pablo D. Garcia and Ricardo Garcia. Determination of the viscoelastic properties of a single cell cultured on a rigid support by force microscopy. *Nanoscale*, 10:19799–19809, 2018.
- [131] Kenneth Levenberg. A method for the solution of certain non-linear problems in least squares. *Quarterly of applied mathematics*, 2(2):164–168, 1944.
- [132] C. L. Penning. Modelling of viscoelasticity using multifrequency afm, 2020.
- [133] Abhilash Chandrashekar, Pierpaolo Belardinelli, Miguel A. Bessa, Urs Staufer, and Farbod Alijani. Quantifying nanoscale forces using machine learning in dynamic atomic force microscopy. *Nanoscale Adv.*, pages –, 2022.
- [134] Chia-Yun Lai, Saverio Perri, Sergio Santos, Ricardo Garcia, and Matteo Chiesa. Rapid quantitative chemical mapping of surfaces with sub-2 nm resolution. *Nanoscale*, 8(18):9688–9694, 2016.
- [135] Elsa Couderc. Inverse problem for photovoltaics. *Nature Energy*, 3(2):85–85, 2018.
- [136] L. Herve, D. C. A. Kraemer, O. Cioni, O. Mandula, M. Menneteau, S. Morales, and C. Allier. Alternation of inverse problem approach and deep learning for lens-free microscopy image reconstruction. *Scientific Reports*, 10(1):20207, 2020.
- [137] Shihao Yang, Samuel W. K. Wong, and S. C. Kou. Inference of dynamic systems from noisy and sparse data via manifold-constrained gaussian processes. *Proceedings of the National Academy of Sciences*, 118(15):e2020397118, 2021.
- [138] K. Champion, P. Zheng, A. Y. Aravkin, S. L. Brunton, and J. N. Kutz. A unified sparse optimization framework to learn parsimonious physics-informed models from data. *IEEE Access*, 8:169259–169271, 2020.
- [139] P. Zheng, T. Askham, S. L. Brunton, J. N. Kutz, and A. Y. Aravkin. A unified framework for sparse relaxed regularized regression: Sr3. *IEEE Access*, 7:1404–1423, 2019.
- [140] N. M. Mangan, S. L. Brunton, J. L. Proctor, and J. N. Kutz. Inferring biological networks by sparse identification of nonlinear dynamics. *IEEE Transactions on Molecular, Biological and Multi-Scale Communications*, 2(1):52–63, 2016.
- [141] Brian M. de Silva, Kathleen Champion, Markus Quade, Jean-Christophe Loiseau, J. Nathan Kutz, and Steven L. Brunton. Pysindy: A python package for the sparse identification of nonlinear dynamical systems from data. *Journal of Open Source Software*, 5(49):2104, 2020.
- [142] N. M. Mangan, T. Askham, S. L. Brunton, J. N. Kutz, and J. L. Proctor. Model selection for hybrid dynamical systems via sparse regression. *Proceedings of the Royal Society A: Mathematical, Physical and Engineering Sciences*, 475(2223):20180534, 2019.
- [143] Abraham. Savitzky and M. J. E. Golay. Smoothing and differentiation of data by simplified least squares procedures. *Anal. Chem.*, 36(8):1627–1639, July 1964.

- [144] E. Solak, Roderick Murray-Smith, William E. Leithead, Douglas J. Leith, and Carl E. Rasmussen. Derivative observations in gaussian process models of dynamic systems. In *NIPS*, 2002.
- [145] Maziar Raissi, Paris Perdikaris, and George Em Karniadakis. Inferring solutions of differential equations using noisy multi-fidelity data. *Journal of Computational Physics*, 335:736–746, 2017.
- [146] Leonid I. Rudin, Stanley Osher, and Emad Fatemi. Nonlinear total variation based noise removal algorithms. *Physica D: Nonlinear Phenomena*, 60(1):259–268, 1992.
- [147] Ozgur Sahin, Calvin F. Quate, Olav Solgaard, and Franz J. Giessibl. *Higher Harmonics and Time-Varying Forces in Dynamic Force Microscopy*, pages 711–729. Springer Berlin Heidelberg, Berlin, Heidelberg, 2010.
- [148] Ozgur Sahin and Natalia Erina. High-resolution and large dynamic range nanomechanical mapping in tapping-mode atomic force microscopy. 19(44):445717, oct 2008.
- [149] Sergio Santos, Li Guang, Tewfik Souier, Karim Gadelrab, Matteo Chiesa, and Neil H. Thomson. A method to provide rapid in situ determination of tip radius in dynamic atomic force microscopy. *Review of Scientific Instruments*, 83(4):043707, 2012.
- [150] Pablo D. Garcia, Carlos R. Guerrero, and Ricardo Garcia. Nanorheology of living cells measured by afm-based force-distance curves. *Nanoscale*, 12:9133–9143, 2020.
- [151] J. S. Villarrubia. Algorithms for scanned probe microscope image simulation, surface reconstruction, and tip estimation. *J Res Natl Inst Stand Technol*, 102(4):425–454, 1997.
- [152] S. J. Fang, S. Haplepete, W. Chen, C. R. Helms, and Hal Edwards. Analyzing atomic force microscopy images using spectral methods. *Journal of Applied Physics*, 82(12):5891–5898, 1997.
- [153] R H Geiss, M Kopycinska, and D C Hurley. Wear of si cantilever tips used in atomic force acoustic microscopy. *Microscopy and Microanalysis*, 11(S02):364–365, 2005.
- [154] Vahid Vahdat, David S. Grierson, Kevin T. Turner, and Robert W. Carpick. Mechanics of interaction and atomic-scale wear of amplitude modulation atomic force microscopy probes. *ACS Nano*, 7(4):3221–3235, April 2013.
- [155] S. Hudlet, M. Saint Jean, C. Guthmann, and J. Berger. Evaluation of the capacitive force between an atomic force microscopy tip and a metallic surface. *Eur. Phys. J. B*, 2(1):5–10, 1998.
- [156] Matthew James. Hamaker constant and tip radius determination in dynamic atomic force microscopy. Master's thesis, Delft University of Technology, 2019.

- [157] Rafael Tadmor, Ronald E. Rosensweig, Joseph Frey, and Jacob Klein. Resolving the puzzle of ferrofluid dispersants. *Langmuir*, 16(24):9117–9120, November 2000.
- [158] Kevin Cooper, Anand Gupta, and Stephen Beaudoin. Simulation of the adhesion of particles to surfaces. *Journal of Colloid and Interface Science*, 234(2):284–292, 2001.
- [159] Qin Li, Victor Rudolph, Bernhard Weigl, and Alan Earl. Interparticle van der waals force in powder flowability and compactibility. *International Journal of Pharmaceutics*, 280(1):77–93, 2004.
- [160] Younjin Min, Mustafa Akbulut, Kai Kristiansen, Yuval Golan, and Jacob Israelachvili. The role of interparticle and external forces in nanoparticle assembly. *Nature Materials*, 7(7):527–538, 2008.
- [161] Sean G Fronczak, Jiannan Dong, Christopher A Browne, Elizabeth C Krenek, Elias I Franses, Stephen P Beaudoin, and David S Corti. A new "quasi-dynamic" method for determining the hamaker constant of solids using an atomic force microscope. *Langmuir*, 33(3):714–725, 2017.
- [162] B. Gady, D. Schleef, R. Reifengerger, and D. S. Rimai. The interaction between micrometer-size particles and flat substrates: A quantitative study of jump-to-contact. *The Journal of Adhesion*, 67(1-4):291–305, 1998.
- [163] Shuiqing Hu, Stephen Howell, Arvind Raman, Ron Reifengerger, and Matthew Franchek. Frequency domain identification of tip-sample van der waals interactions in resonant atomic force microcantilevers. *Journal of Vibration and Acoustics*, 126(3):343–351, 2004.
- [164] S. M. Cook, T. E. Schaffer, K. M. Chynoweth, M. Wigton, R. W. Simmonds, and K. M. Lang. Practical implementation of dynamic methods for measuring atomic force microscope cantilever spring constants. *Nanotechnology*, 17(9):2135, 2006.
- [165] Keivan Asadi, Jun Yu, and Hanna Cho. Nonlinear couplings and energy transfers in micro- and nano-mechanical resonators: intermodal coupling, internal resonance and synchronization. 376(2127):20170141.
- [166] Eyal Buks and Bernard Yurke. Mass detection with a nonlinear nanomechanical resonator. *Phys. Rev. E*, 74:046619, Oct 2006.
- [167] Yukihiro Tadokoro, Hiroya Tanaka, and M. I. Dykman. Driven nonlinear nanomechanical resonators as digital signal detectors. *Scientific Reports*, 8(1):11284, 2018.
- [168] Chun Zhao, Mohammad H. Montaseri, Graham S. Wood, Suan Hui Pu, Ashwin A. Seshia, and Michael Kraft. A review on coupled mems resonators for sensing applications utilizing mode localization. 249:93 – 111.
- [169] Dario Antonio, Damian H. Zanette, and Daniel Lopez. Frequency stabilization in nonlinear micromechanical oscillators. 3(1):806.

- [170] Robin J. Dolleman, Pierpaolo Belardinelli, Samer Hourii, Herre S. J. van der Zant, Farbod Alijani, and Peter G. Steeneken. High-frequency stochastic switching of graphene resonators near room temperature. *Nano Letters*, 19(2):1282–1288, 2019.
- [171] Yukihiro Tadokoro and Hiroya Tanaka. Highly sensitive implementation of logic gates with a nonlinear nanomechanical resonator. *Phys. Rev. Applied*, 15:024058, Feb 2021.
- [172] Z. Leghtas, S. Touzard, I. M. Pop, A. Kou, B. Vlastakis, A. Petrenko, K. M. Sliwa, A. Narla, S. Shankar, M. J. Hatridge, M. Reagor, L. Frunzio, R. J. Schoelkopf, M. Mirrahimi, and M. H. Devoret. Confining the state of light to a quantum manifold by engineered two-photon loss. 347(6224):853–857.
- [173] Stav Zaitsev, Oleg Shtempluck, Eyal Buks, and Oded Gottlieb. Nonlinear damping in a micromechanical oscillator. *Nonlinear Dynamics*, 67(1):859–883, 2012.
- [174] Alexander Croy, Daniel Midtvedt, Andreas Isacsson, and Jari M. Kinaret. Nonlinear damping in graphene resonators. *Phys. Rev. B*, 86:235435, Dec 2012.
- [175] X. Dong, M. I. Dykman, and H. B. Chan. Strong negative nonlinear friction from induced two-phonon processes in vibrational systems. *Nature Communications*, 9(1):3241, 2018.
- [176] Juan Atalaya, Thomas W. Kenny, M. L. Roukes, and M. I. Dykman. Nonlinear damping and dephasing in nanomechanical systems. *Phys. Rev. B*, 94:195440, Nov 2016.
- [177] Johannes Guttinger, Adrien Noury, Peter Weber, Axel Martin Eriksson, Camille Lagoin, Joel Moser, Christopher Eichler, Andreas Wallraff, Andreas Isacsson, and Adrian Bachtold. Energy-dependent path of dissipation in nanomechanical resonators. *Nature Nanotechnology*, 12(7):631–636, 2017.
- [178] Qianxiao Li, Felix Dietrich, Erik M. Bollt, and Ioannis G. Kevrekidis. Extended dynamic mode decomposition with dictionary learning: A data-driven adaptive spectral decomposition of the koopman operator. *Chaos: An Interdisciplinary Journal of Nonlinear Science*, 27(10):103111, 2017.
- [179] Bethany Lusch, J. Nathan Kutz, and Steven L. Brunton. Deep learning for universal linear embeddings of nonlinear dynamics. *Nature Communications*, 9(1):4950, 2018.
- [180] Andreas Mardt, Luca Pasquali, Hao Wu, and Frank Noe. Vampnets for deep learning of molecular kinetics. *Nature Communications*, 9(1):5, 2018.
- [181] Maziar Raissi, Paris Perdikaris, and George Karniadakis. Multistep neural networks for data-driven discovery of nonlinear dynamical systems. 01 2018.
- [182] Christoph Wehmeyer and Frank Noe. Time-lagged autoencoders: Deep learning of slow collective variables for molecular kinetics. *The Journal of Chemical Physics*, 148(24):241703, 2018.

- [183] Pantelis R. Vlachas, Wonmin Byeon, Zhong Y. Wan, Themistoklis P. Sapsis, and Petros Koumoutsakos. Data-driven forecasting of high-dimensional chaotic systems with long short-term memory networks. *Proceedings of the Royal Society A: Mathematical, Physical and Engineering Sciences*, 474(2213):20170844, 2018.
- [184] Hiromi Yasuda, Koshiro Yamaguchi, Yasuhiro Miyazawa, Richard Wiebe, Jordan R. Raney, and Jinkyu Yang. Data-driven prediction and analysis of chaotic origami dynamics. *Communications Physics*, 3(1):168, 2020.
- [185] Zhong Yi Wan, Pantelis Vlachas, Petros Koumoutsakos, and Themistoklis Sapsis. Data-assisted reduced-order modeling of extreme events in complex dynamical systems. *PLOS ONE*, 13(5):1–22, 05 2018.
- [186] James Bradbury, Stephen Merity, Caiming Xiong, and Richard Socher. Quasi-recurrent neural networks. *CoRR*, abs/1611.01576, 2016.
- [187] Daniel S. Wastl, Alfred J. Weymouth, and Franz J. Giessibl. Optimizing atomic resolution of force microscopy in ambient conditions. *Phys. Rev. B*, 87:245415, Jun 2013.
- [188] Sergio Santos, Victor Barcons, Hugo K. Christenson, Daniel J. Billingsley, William A. Bonass, Josep Font, and Neil H. Thomson. Stability, resolution, and ultra-low wear amplitude modulation atomic force microscopy of dna: Small amplitude small set-point imaging. *Applied Physics Letters*, 103(6):063702, 2013.
- [189] Chia-Yun Lai, Sergio Santos, and Matteo Chiesa. Systematic multidimensional quantification of nanoscale systems from bimodal atomic force microscopy data. *ACS Nano*, 10(6):6265–6272, 2016.
- [190] F. Jamitzky, M. Stark, W. Bunk, W. M. Heckl, and R. W. Stark. Chaos in dynamic atomic force microscopy. *Nanotechnology*, 17(7):S213–20, 2006.
- [191] S. Hu and A. Raman. Chaos in atomic force microscopy. *Phys Rev Lett*, 96(3):036107, 2006.





# ACKNOWLEDGEMENTS

This thesis is the culmination of 4 years of my life condensed into 150 pages. If you made it to the end '*Bravo!*'. If you enjoyed reading it, then I suspect you are showing symptoms of a PhD - '**P**atiently **H**oping for a **D**egree'. Jokes aside, even if one person reads or browses through this thesis and finds it interesting then the 4 years of effort I had put in it was worth it. Just like every other aspect of life, this thesis wouldn't be possible without all the help and support from my friends, colleagues and family. Thus, it is time to bring all those background supporters to the foreground and thank each one of them for helping me on my journey. I have taken the liberty to sprinkle this acknowledgement with some anecdotes to make it personal, I hope it conveys my gratitude to each and every one of you.

First and foremost, like every sapling needs ample amount of water and nutrition to bear strong roots, each doctoral candidate requires a strong, supporting and caring promotor. In my case I was lucky enough to get two amazing people **Farbod** and **Urs** as my promotors. I am truly grateful for your guidance throughout my doctoral candidacy. Both of you were pivotal for my success. Thank you for letting me explore different research directions within the field and supporting my crazy ideas to build a '*Frankenstein*' AFM. I have learnt a lot through some of my successes and even more so from the failures and in the end I truly felt like a full-fledged researcher. This would not have been possible without your unconditional trust and support, so thank you!

**Farbod**, we both started our TU Delft journey around the same time in 2015. I had just joined as a master student at PME and you had joined as an assistant professor. During my masters, I remember attending your course on 'Engineering dynamics' and thinking '*this is one of the fun courses I have had this year*'. Little did I know back then that I will become a teaching assistant for the same course for almost 4 years in a row. If someone asks me how did I end up doing a PhD with Farbod? My answer would be '*fate*'. It was due to a series of events where my industrial master thesis got delayed, there was only one thesis topic left with Farbod and I had to take it in order to graduate (*he only told me later that initially nobody took this topic because it was hard! fell right into it eh?*). But I had a wonderful time working on my master thesis with you and in the end I even ended up getting a PhD position within the group and that's how I became the first ever PhD in Alijani Lab.

In the last 5 years I have known you, I have seen you grow our lab and competence at a tremendous pace from having just one PhD (me) to having more than dozen PhDs and post-docs at one point. Your passion and dedication always baffled me but at the same time inspired me to work harder. Your growing research interests from MEMS & NEMS to AFM, 2D membranes, mass sensing and bacterial motion detection application makes me wonder whether you had 48 hours per day compared to the rest of us. It is impressive to see how much our group has grown under your supervision. It was truly an inspiring journey and I am happy that I was part of the group right from its inception. During

my doctoral candidacy you have given me immense support as a mentor, guardian, and as a well-wisher and I couldn't have asked for a better person as my daily supervisor. You have constantly pushed me to be at my best. This thesis is the culmination of all those days, where we argued about the quality of figures in the article, changing each individual sentences within an abstract to create an impact and constantly looking out for novel ideas to incorporate in our research. Looking back I realize that it is due to those discussions that I became more competent and more mature in my approaches. Thank you for taking me under your wing and nurturing my growth in academia.

**Urs**, I believe you were the bedrock of our project. I still remember when you sent me an email right after my masters to have an interview for my Phd and we grabbed a coffee together and discussed in length about what it means to pursue a doctoral education and what it means for the society. I knew right then that I would be in good care. If Farbod was dynamic in his approach, you were the calm, collected, solid foundation that steered our project in the right directions with your vision. Every time I used to meet you for our monthly updates, I used to come out of the discussion feeling energized and with a sort of euphoria that made me feel that I was progressing. I realize now that I felt that way because you showed innocent interest in every small result I had and always asked me what would happen if I did things differently. This motivated me to try so many different things which are all obvious to you from the amount of cantilever order requests you have got in the last 4 years. You always encouraged me to take vacations and breaks from work so that I don't burn out and always checked up on me to make sure I was doing okay. Thank you for all the kind words and gestures, it helped me get through my cognitive slumps. I was lucky to get two of the best supervisors who complemented each other's teaching styles and became one of the biggest factors for my successful doctoral candidacy at Delft.

Next, I would like to sincerely thank the members of the defense committee who had to sit and read my entire dissertation. I am honored to defend my thesis in front of such renowned world experts in the field of AFM, MEMs & NEMs and Nonlinear dynamics. I look forward to our discussions during the defense and eager to learn of your opinion on my work. Here, I say a few words about the committee members:

**Professor Arvind Raman**, we met each other for the first time during the user committee meeting for the NICE TIP TAP project. It had only been 6 months since I started my PhD research and I was preparing a manuscript based on your work from 2 decades ago. I was amazed by your contribution to the field of AFM especially in making use of nonlinear dynamics to uncover the true potential of AFM back in late 2000's. When I met you during the committee meeting, I quickly realized how humble and gentle you were but still astounded by the fact that you remembered your work from 20 years ago to the tiniest details. We had a very fruitful discussion both online and offline. Thank you for agreeing to be part of the defense committee.

**Professor Ricardo Garcia**, our first chance encounter was in Delft, 2019 during the PhD defense of another colleague from PME. It was such a humbling experience when Urs introduced me to you and we briefly spoke about my research. You were immediately appreciative of the importance of looking at AFM from a nonlinear dynamics perspective and how it can complement the conventional physics perspective and make the field of AFM even more interesting. Thanks to your kind words, I was emboldened to continue

my research in the same direction. I cannot emphasize enough your immense contribution to the field of dynamic AFM and multi-harmonic AFM, I have referred to your work countless times to get meaningful insights during my PhD. Thank you for being part of the committee and I hope to see even more amazing ideas from your group.

**Professor Andrei Metrikine**, thank you for agreeing to be part of my defense committee. The work your group is doing in understanding the dynamics of offshore pipelines, tunnels and wind turbines is inspiring for the future energy market. Coincidentally, you were also part of my master defense committee, I look forward to having a fruitful discussion during the doctoral defense.

**Professor Fred van Kuelen**, thank you for agreeing to be the reserve member of the committee. I have had the privilege of interacting with you during my masters in several courses. I always tried to inculcate some of your thinking and behavior into my own academic thought process. I still remember during the mechanical analysis for engineers course, you said that you preferred a lazy persons answer because he or she comes up with a creative way of tackling the problem. It made me realize sometimes the simple answers give you more insight than a full blown deep dive into a problem. Once again, thanks for being part of the committee.

**Peter**, you were one of my master thesis supervisor together with Robin. It was my very first interaction with you as a master student and I remember everything, you and Robin were discussing going above my head. I was like *'what did I get myself into'*, but soon enough you helped me understand particularly difficult physics based concepts by breaking them down to simpler topics. Thanks to your constant support, I had a smooth sailing during my masters. But it was when I joined DMN group as a PhD that I truly realized how vast your knowledge and research interests were spreading from fundamental studies in 2D materials to different sensing applications in NEMS and MEMS. It is truly baffling to see you holding up a conversation in different areas of science so easily and makes me wonder how you keep yourself updated. Actually, what is even more baffling is how you don't seem to age at all!. I remember when we were at Lausanne for NMC conference and you were standing next to my poster and a professor casually asked you which year are you in your PhD. It was funny, but you told me it wasn't the first time someone mistook you for a student. Please tell me your anti-ageing secret.

But honestly, I enjoyed discussing with you on various scientific topics related to 2D membranes, machine learning and AFM but even more so our social and cultural topics like *'how to raise kids to be independent'* and *'how you need to be a little eccentric and quirky to be a professor'*. During my time at PME, I have seen you grow our DMN group into an excellent research group with diverse disciplines. I am convinced that under your leadership and vision our group will reach newer heights in the coming years and no matter where I am, I will always be proud that I was part of the DMN group.

**Pierpaolo**, you were my mentor and buddy who taught me a lot in nonlinear dynamics and coached me in the ways of academia. Everyone knows you are an amazing researcher but what is even more amazing is the kind human being you are. I have personally seen the dedication, passion and the kindness you would show when it came to teaching students irrespective of how overloaded you were with your own work. If there is one person who should be in academia, I firmly believe it to be you because with you as a teacher the future of the next generation of students is secure. I cannot count the

number of times you have helped me debug my codes and the number of time you listened to me complain, you have been there to console me and guide me on the right path but also share the pain of getting rejected by journals we were so hopeful for. I am extremely happy that I started my PhD under your wing and together with Banafsheh you both postdocs raised the bar so high that in pursuit of it I became a much better researcher so, thanks for that. However, I still hold you responsible for my cryptic coding skills..like master the student right? I still can't decipher what we did in the mathematica code for the cluster but hey! it works, so I follow your advice here: 'if it ain't broke don't fix it'.

I can go on and on about our adventures in PME, from late night work to early morning white board discussions, from politics of academia to discussing 'one piece' manga that your kids love so much. I have seen your highs and lows, but no matter what, the passion you had for research and teaching never waned. I am happy that you got a position closer to your family back in Italy, you deserved it. I have no doubt that you will only see new heights in your career (*Gomu Gomu no Roketto!*) and nurture younger generation of students towards a brighter future. It was truly an honor working with you and sharing all those experiences. Without you, I wouldn't have made it to the stage I am currently and I am grateful that I had you as my colleague, mentor and friend during my doctoral journey.

Next I would like to thank the user committee members of the NICE TIP TAP project **Paul, Richard, Patrick, Jordi, Edin, and Anne**. Thank you all for spending your time and energy to make sure the project deliverables remained relevant to the current industry requirements and standards. It was thanks to your efforts that the project was a success.

Next are the faculty of PME department who have supported me during my PhD. **Murali**, thanks for all the advice on how to supervise master students and the discussions about the AFM application in mechano-biology. Also, thanks a lot for getting the super expensive JPK AFM, without this equipment I would have had a lot more tough time with my research. **Alejandro**, thanks for collaborating on our viscoelasticity project, your insights helped a lot in streamlining the project and obtain interesting results. Also, I'm a big fan of your jokes, i find them really funny, It was always fun to have discussions with you. **Gerard**, thanks for collaborating on the Hamaker constant and KPFM project. I was so happy to be able to have one more person in the department with whom I could discuss nitty gritty technical details of AFM. You always had the most critical and technical questions during the project and it was a pleasure working with you.

Finally, **Miguel**, thanks for collaborating with us on the machine learning project. I learnt about the vast number of applications possible with machine learning and artificial intelligence and I am convinced that one way or another every one's life will be intertwined with AI in future. Thanks to your insights and guidance I was able to publish my article and also learn about ML which proved to be quite useful during my job hunts. I wish you all success and hope you all get lots of funding to keep churning out the amazing research and foster the future generations of PhD's within the department.

The next group of people I want to thank are the ones who are mandatory for every PhD to taste success. These are my faculty's technical support staff, **Rob, Bradley, Gideon, Patrick and Spiridon**, I can't thank you guys enough for sticking with my crazy requests for the last 4 years. I have probably dropped by your offices more than I did to

my supervisors. You all have been extremely supportive both in making changes to my experimental setup and also to order parts. Without you guys I am sure I would have struggled a lot during my candidacy. A special mention to **Rob** and **Spiridon**, since you both were more involved to get my setup up and running during my first year which helped me get confidence and keep the momentum going. I wish you all good luck with your careers and see you all at my defense.

Now is the turn of non-technical support staff, **Lisette**, **Marianne**, **Birgit**, **Corrine** and our financial guru **Marli**, thank you all for helping us during the course of NICE TIP TAP project with all sorts of administrative work. Our research went smoothly knowing that the project planning and management were under your capable hands. **Lisette**, thank you for helping me out for my guest registration and Visa. **Marianne**, **Birgit**, **Corrine**, thank you for all the HR related help you saved me a ton of time when I was not getting any answers from central HR. Finally, **Marli**, thanks for all the instant answers to my endless financial questions related to Baan code and project codes and expense claims; you are truly the financial guru of our department.

To all the remaining faculty members, even though I have not had much interaction with every one of you, I keep hearing great things from other PhD's in their research so I am sure our department is in safe hands and I will keep reading about your work in future. If I have left out any names please know that it was not intentional and my memory might have slipped but I will always remember your contribution.

Next up are my office mates from 3mE, without you guys I wouldn't have remained sane during my PhD. I believe every PhD candidate needs friends and colleagues with whom you can relax and talk about 'non-sense' topics that have no relation to science and technology. Our legendary coffee break discussions and our 'last supper' sized lunches made my PhD more memorable.

I will start with the two penguins, my paranympths **Ata** and **Irek**. **Ata**, you were my room-office mate (if that is even a word!). You got the most coveted desk in all of PME, where you could play chess all day and quickly change your screen to matlab when Farbod walked in. *Oops was it a secret?* But it doesn't matter because you are so smart that you used to get work done in half the time of others, the nature comms and nano letters publications are the proof. We used to discuss at length about gaming, stocks and crypto and it was truly fun times. Thanks for agreeing to be my paranympth and please read the propositions really slow so that I can come up with possible answers. You are almost at the end of your PhD and I am not worried because you are one of the most capable researchers within our group and I am sure you will ace it. So all the best for your final sprint and know that '*abi*' is here for you.

Next up is the Polish-Dutch penguin **Irek** or should I call you '*Eityrek?*', you were barely in your second year and you had already made a breakthrough in sensing field with your bacterial motion research. It was so fascinating to see your cutting edge research coming to fruition. I am sure you will have a smooth sailing in your final year with the results you have amassed so far. We became good friends during the covid lockdown, where it used to be mostly you and me in the office complaining about our experimental results, covid lockdowns and dutch politics like we were experts. Man we complained a lot about a lot of things; *oh, wait a minute have I become dutch?* I still find it funny that you described the weather in Poland once as "*In Poland winter is more wintery and sum-*

*mer is more summery*". It was hilarious. Irek, you are a dependable friend, who doesn't think twice to stand up for his friends which was apparent during the summer school dinner incident and I hope you stay the same. Since I am now more in Eindhoven and you in Delft, time to switch houses!. I know you will be incredibly successful in your career so I am rooting for you and your future company. All the best with the final stage of your PhD and you can always rely on me for any help.

**Tomás**, you were a super-postdoc working on several different projects related to micro-resonators, duffing oscillators, PID controllers and even AFM research on cells, you have incredible knowledge on several different fields and you are always working hard. Congratulations on becoming an assistant professor at EWI. The next super-postdoc is **Satadal**, the plant whisperer and microelectronics expert. In our day to day coffee breaks, your broad knowledge in biology, chemistry and physics was incredible to witness. You were always curious to know more about any research topics we used to discuss and expand your knowledge on other subjects. I guess that's why you are a super-postdoc. I wish you the best of luck with your plantenna project and also your future entrepreneurial plans. I have spent many lunches with you both discussing from Spanish-catalonia politics to football to various interpretations of covid statistics. In future, I am convinced that you both will make great PI's and supervisors. We will stay in touch and get together often to discuss more random things going on in the world, prost!.

**Livia**, I am still amazed as to how a postdoc ended up publishing more than 10 articles in a completely new field compared to your PhD. To top it off you did all that with a new born baby, you are simply incredible. We shared JPK AFM setup for our research and ended up teaching each other tricks and tips to have good results, so thanks for that. I am happy to see you at your new position in TU Eindhoven, which means I will bump into you more often in the train on some mornings. I wish you success with your research and see you on Monday morning at 7?.

**Banafsheh**, thanks for warning me about the third year PhD slump! It is real and it can be hard even if you know it is coming. Thanks to your heads up I was able to wade through it. I keep reading about the amazing work you and **Mohammad** are doing at Amber Implants. I wish you good luck and success with your company.

**Robin**, thanks for mentoring me during my master thesis. I learnt from the best and strived to meet that expectations. I was proud to be able to contribute to your research a tiny bit during masters and it was together with you that I got my first publication so thanks for that. I know you will make an amazing PI in future. Good luck with your graphene research.

**Arthur**, thanks for driving home the viscoelasticity paper. Without your simulations it would not have been possible. You never cut any corners and always took the moral high ground when it came to showcasing your results, which is a rare quality in academia. It was a pleasure working with you. I wish you all the best with your future career. **Andre**, the kick boxer postdoc, thanks for getting me Silicon and Diamond samples for my research. Now that you are at ASML, lets meet more often. Be careful not to get any more black eye from your training sessions!. Let's stay in touch. **Dongil**, thanks for teaching me Bayesian optimization, and congratulations on starting a new position as Postdoc at Sandia National Laboratories. I wish you good luck with your research. **Mar-**



**tin, Hadi and Vijayendra**, I did not get enough time to get to know you guys during my last year of PhD. But I wish you guys success with your academic careers.

Now on to my fellow PhDs!, **Matthijs**, how do you have a perfect anecdote for every situation is beyond me; It doesn't matter what the discussion is you come and say "*The one time I was backpacking with my buddies in France...*" or "*We were hiking in Germany when suddenly..*". It was fun to hear the different experiences you have had and discuss them during lunch. I hear that your research is going well, I wish you good luck with your preparations for your PhD defense. **Minxing**, I am absolutely sure *if a robot bites you, you will not become a robot zombie! but trust me, you will get robot superpowers!* It was a lot of fun discussing crypto with you and hearing about your crazy economic theories. I know you are writing several articles at a time so i wish you good luck and also success with the rest of your PhD.

**Curry** a.k.a **Hanqing Liu** a.k.a the league of legends shifu, don't worry your secret is safe with me!. You are a hard worker, I have seen you in office even on Saturdays and Sundays working non-stop. Thanks for all the Chinese dinners and the special green tea. We have had some fun conversations about China and had some good laughs over lunches. I hope you will keep the promise of showing me around in China one day! Keep up with the good work and all the best with your PhD journey. **Xianfeng** a.k.a the levitation master, you have done extremely well in your PhD and the number of publications you have is the proof. We had fun during the engineering dynamics as teaching assistants and thanks for helping me grade 300 odd students every year. I know you are looking for Jobs in Industry and I wish you good luck with your job hunt. Hit me up if you need any help and all the best for your defense preparations. **Yong**, we both started writing our dissertations around the same time but you managed to finish it in just two weeks and I took 2 months!. It is nice that you joined ASML and now we can easily catch up in train and complain about the long commute to work.

**Martin Lee**, I remember you as the guy who put electrodes in the mouse brain. It was your first presentation at DMN and I was so impressed looking at that picture. After that you kept on surprising everyone with your amazing cleanroom skills and even more so with your unending list of publications. Good luck with your academic career in Munich and hope to see you around. **Makars**, the guy who is bringing back all the soviet era theoretical 2D structures to life through his research. You are so passionate about your work that you would turn any conversation into a discussion about physics. Your brilliance and dedication shows in your research and needs no words to explain. I wish you the best with your research in the other part of the world.

**Saleh**, there was so much cultural similarities between Iran and India that we used to agree on most 'idiotic' things followed in our respective countries and laugh at them all the time. You had some tough luck with your experimental setup but you pulled through it and got some nice results. It shows your dedication and commitment to the work. I know that you are preparing for your PhD defense so good luck with that (*break the curse!*). I am sure you and **Mahnaz** will have a brighter future in your careers. Stay in touch!. **Andrea**, thanks for helping me out with PhD council works. You seem to be a better fit over there than me. You already have amazing results in your research so keep up the good work and churn out the papers. **Ali**, I hope your graphene related research is going well. Good luck with your manuscript preparations and the rest of your PhD.

**Alkisti, Eleonor** and **Cristina**, you guys were the fun PhD's of PME. You all were social and made the new PhDs feel more at home with your warm hospitality. Thanks for that. **Alkisti**, I know you are enjoying your work at ASML since the last time I saw you, you were smiling from ear to ear. **Christina**, I hope you are enjoying your work in Italy as well. **Eleonor**, thanks for teaching me Nanosurf AFM during my first year and I hope your recovery is going well. **Enrique**, I am sorry that I completed overhauled your experimental setup and made it into one of a kind hybrid AFM. Thanks a lot for taking time from your work to teach me about the setup in the initial days. It helped me a ton!. I hope you are enjoying your work at CAF.

**Gurhan, Rajit, Vibhas, Stijn, Sabiju, Zhichao (MNE), Arnoud, Nils, and Zichao (DMN)** thank you guys for all the fun discussions and interactions. I wish you all good luck with the rest of your PhD. Now to the mechatronics guys who let me bunk in their room for last two months of writing my dissertation, **Ali, Xinxin, Abdullah, Malte, Jelle, and Nima**, thank you and I wish you all success with your PhD.

Being part of the PhD council of 3mE was a fun experience. I had the opportunity to interact with the PhD's of different departments within 3mE and brainstorm ideas and frameworks to further strengthen our graduate school. **Vilborg, Eline, Bart, Ankur, Andrea, Hongpeng, Pieter, Alina, Costanza, Zongcheng** and **Padmaja**, thanks you all for the fun sports events, lunch and info lectures on thesis printing (*I made use of their discount code successfully!*) and pub quizzes. By being part of the council I realized how diverse every PhD's problems can be and how we need a strong university connections to help each of them get through their issues. It also made me realize how Covid can easily exacerbate the already stressful PhD journey and create mental breakdowns for PhD's. But thanks to you guys, we had regular virtual coffee meetups, games and surveys to make sure everyone within our department could get the help and social interaction they needed. Finally, **Mascha**, thanks for chairing the council meetings and giving us the reign to handle these varied issues. Without your unconditional support and encouragement it would not have been possible.

Now moving on to my master students, **Casper**, you were a diligent student who had a tough master thesis topic but you aced it by handling both experiments and simulations. Kudos to you. You were a well-rounded master student who needed minimum supervision. Your work made it into this thesis and we also managed to publish a paper out of it so congratulations!. I wish you good luck with your industrial career at prodrive technologies. **Matthew**, you had some tough luck with the experimental setup but still you managed to write an excellent master thesis. You have very good understanding of mathematics that helps you easily understand relatively difficult concepts and you also possess amazing coding skills. Let's turn your thesis into a publication soon!. I already know that you are enjoying your work at ASML but I like how you are also following your passion for teaching by making youtube tutorial videos on nonlinear dynamics. Keep up the good work! and spread the knowledge on nonlinear dynamics!. **Hidde**, although officially you weren't my student, I still learnt a lot on GPR by collaborating with you. I wish you success in your career at ASML.

And now time to thank my friends, **Shrinivas**, you have been an amazing roommate for the last 4 years thanks for that. From the endless F1 conspiracy theories and gossip from paddock to gruelling leg days at the gym and blisters at bouldering, I have enjoyed



your company thoroughly. You are really smart and I am sorry for all the times I took advantage of your cleaning OCD at home. I wish you all the best with your upcoming defense and your postdoc at Karlsruhe!. We need to also plan for that trek in black forest.

**Ankur**, my partner in crime at ASML. First of all I should address you as Dr. Ankur, now that you have defended your PhD successfully. I am grateful to have a wonderful friend like you. Thanks for all the fun night outs, get-togethers and the 'phd council' events (only we know why we joined the council). On behalf of everyone from my state, please don't talk in Kannada. It's too hilarious and someone taught you only the 'swear' words. Congratulations to you and **Krishti** on your first house in Netherlands; now I don't have to be wary of NS railways running on time!. I wish you both success in your careers and life endeavours. And also Salud! to many more mischiefs at ASML.

**Arvind**, my other crime partner from ASML. I can't believe you ended up in Netherlands for your PhD but I am glad that you did. I feel like you are still the same goofy, nerdy, smarta\*\* you were during our pre-university times. When I move to Eindhoven you are tagging along with me for gym and bouldering, we shall embark on Mission Muscular Arvind 2023!. Thanks for listening to my rants and also joining in on them at times. Good luck with your career at ASML and your other upcoming big plan.

**Martina**, first of all sorry I borrowed your penguin word for paronyms or as we academics call it '*derived inspiration*' from you (I am doing air quotes). You have a cool research topic but I am sorry that I keep forgetting about the details of it and you have to explain it every time we meet. I want to thank you and Irek for showing me the best pizza and ice cream place in Eindhoven. Good luck with your PhD. **Uddhav**, I have no idea how you are friends with almost everyone and know all about their life stories. It is always fun hanging out with you, I wish you the best of luck with your final year of PhD. **Lili, Aryn, Vaishnavi** and **Pritish**, my long lost friends, I am happy that joining ASML got you guys back in touch. Let's keep up the regular dinner meets and anecdotes sharing sessions. We have lot of catching up to do!.

**Alok** and **Arun**, thanks for checking up on me from time to time from India and also thanks for all the dinner parties and lunches whenever I come to India for vacation. I always feel relieved to talk to you guys and reminisce about our engineering days and all the foolhardy things we did in MSRIT. I know that both of you will be part of my life forever and I am grateful to have friends like you on whom I can rely on during difficult times. I wish you guys immense success in your careers and life endeavours.

Now for the ex and present 'LAMinates', **Manoj, Ram, Srikanth, Ajay, Naveen** and **Lakshminarayana**, thanks for the beautiful and fun memories while working at LAM Research. It wouldn't have been nearly as much enjoyable without you guys. I look forward to visiting India each year thanks to you guys. We discovered most of the Bangalore pubs, eateries and hangouts during those two years of working together (that's where all my salary went eh?!<sup>+</sup>). I know for sure you all will excel in your respective careers and I wish you guys the best of luck.

**Yogesh, Ranju** and **Arju**, my gaming buddies. You all kept me sane during the covid times with Monster Hunting, Nioh and Genshin Impact. The countless number of hours we spent farming for rare materials and gems for our builds is insane. I think I have crooked fingers thanks to all the button mashing we did during our playthroughs. Look-

---

<sup>+</sup>Manoj, I know what you are thinking, don't say it!

ing forward to many more such days!. Happy button mashing!.

**Tanvi**, let me just tell you that you are way too wise for your years. I am amazed by how multi-talented you are from academic research to your mouth watering cooking skills. You do all this while travelling all over the world; it makes me a little jealous but more happy that I have someone of your incredible calibre as a friend. We share a strange telepathy right from the Goethe Institute times that continued all the way to Netherlands and Sweden. I don't know how you call me or ping me at exactly the right time but let's keep it going. Thanks for all the late night calls and discussions on life, relationships, human psychology, and all the other fun stories<sup>†</sup>. It made my PhD a bit less stressful. Now that you are in the last leg of your own PhD journey, I wish you success and know that, I am here for you if you need to talk about anything. Cheers to many more years of our growing friendship!.

**Sharmilee**, my chaddi dost, my only non-techie lawyer friend. You have been my friend since kindergarten (how long is too long?) and we have been there for each other during many ups and downs of life. Thank you for your constant support in all aspects of my life; you have seen me at my best and my worst, and stuck by me all this while. From listening to my boring 'gyaan' sharing and NRI ranting to watching random movies with me and reciting 'Friends' dialogues; I have many beautiful memories of Bangalore thanks to you. You are more fun than anyone or anything I know. I couldn't have asked for a better friend than you. You are simply amazing!. Even after I moved to Netherlands, you have always been there as a solid support on my side that I can lean on during my difficult times, thank you for that. Keep being this incredible, chill and energetic person you are and let's continue this friendship for another 40 years\*, what say you?.

Finally, In the last four years, if there is someone whom I should definitely thank for my success that would be you **Alekhyia**. This whole journey could not have been possible if it wasn't for you. This entire thesis would not be sufficient to convey my adoration and gratitude for you and your contribution to my success. I can write tales about how patient, kind and empathetic you were and how many personal sacrifices you made for my plans. I wish we could have travelled around Europe more and made even more memories to take home with. I am sorry for all the trouble I caused you. You have taught me a lot outside academia. Know that no matter what, I will be there for you if you need me. I wish you all the health and happiness in the world.

Last but not least a few words for my family. **Abhishek**, my brother, you were forced to step up and care for the family as soon as I left India. I am sorry for putting you through this responsibility sooner than you expected, but you have handled it beautifully. I have seen you grow from a teenager to a responsible adult in a short period of time especially when the Covid wave hit India. Thank you for everything you have done. Know that there is no one path for success and everyone's definition of success will be different. You are the protagonist of your life, so carve your own path. Don't worry, If you do fall down, I will be there to pick you up. Regardless of what I asked of you, you have never refused me; I am blessed to have an understanding and supporting brother like you. Know that I will always support you and stand by you. I am looking forward to seeing your success in future.

---

<sup>†</sup> I swear I will install Instagram the day you install Tiktok.

\*Please continue guarding my secrets and please don't tell anyone about the 'injection' incident in school.

To my beloved mom and dad, sorry I could not find a way to write this in kannada directly but I hope this will do. **Appa**, naanu modhalane sala masters ge antha bandhaaga neevu eshto dinagala kaala sariyaagi nidhhe madirlilla. Naanu phone madidhaagella neevu kannalli neeru thumbikondiddha dinagalu nanage nenapidhe. Nanna geluvige, nimma aase aakaankshegallannu badhiyalli ittu nimma dhudimenu kooda bali kotti nannannu illige kalisiddhakke, nanna hruthpoorvaka dhanyavaadhagalu. Nimage husharilladhidhaaga naanu nimma pakaadhalli iralilla, adhakke nannannu kshamisi. Appa nimage baruthidda pudigaasannu varshagala kaala koodi haki nannannu odhodhikke antha vidheshakke kalisiddhakke nanna vandhanegalu. Nimma thyagavannu naanu yavattu mareyodhilla. **Amma**, naanu yavaga phone madidhru naanu oota madudhna ilva annodhe ninagondhu chinthe. Ninna mugdhatheye ninage alankaara. Naanu chikkavanaagiddhaaga, vidhyabhyasada mele ondhu reethiya aasakthi, uthsaaha barodhikke neene kaarana. Neenu aduge maadtha nanage helikotta paatagala parinamadhindha ivattu naanu intha dodda mattadhalli ninthidhini, idhakke naanu ninage chira runi. chikkandhinindhalu aidhu hattu roopayiyannu sasive jeerige dabbi yalli bachittu nanage thindhi thinisugalannu kodisthidde. Ninna aa preethi matthu vathsalya nannannu ivatthigu aarogyavaagi ittidge. Nimmibara preethi, vishawasa matthu thyagadha guruthige ivattu naanu ee nanna geluvannu nimmibbara hesarige arpisuthidhene. Matthomme, nanna hruthpoorvaka dhanyavaadhagalu.

As I am writing these last few lines, I realize that I am standing on the precipice with borrowed strength, the strength in the form of friends, family and colleagues who are holding me up with their invisible hands and guiding me forward. It is ironic that we often think PhD as a solitary journey while in reality, we get support from so many lives around us, each contributing to our growth along the journey. For this, I express my sincere gratitude to each and every one of you who made this journey less arduous and gave me so many happy memories that, I almost forgot getting a PhD can be hard. Although my thesis ends here, I will continue to learn new things throughout my life and discover the endless opportunities that life has to offer. Once again a final thank you from the bottom of my heart.

Abhilash Chandrashekar  
Delft, September 2022



# CURRICULUM VITÆ

## **Abhilash CHANDRASHEKAR**

30-06-1991      Born in Bangalore, India.

### EDUCATION

2009–2013      Bachelor of Technology in Mechanical Engineering  
M.S.Ramaiah Institute of Technology, Bangalore, India

2013-2015      Design Engineer  
LAM Research Pvt Ltd, Bangalore, India

2015-2017      MSc Precision and Microsystems Engineering(cum laude)  
Delft University of Technology, Delft, The Netherlands

Thesis:          Opto-thermally Excited Parametric Resonance in Monolayer  
Graphene Nano-Drum Resonators.

Promotors:      Prof. dr. P. G. Steeneken, Dr. F. Alijani

2017-2021      PhD. Mechanical Engineering  
Delft University of Technology, Delft, The Netherlands

Thesis:          Nonlinear Dynamic Atomic Force Microscopy.

Promotors:      Prof. dr. U. Staufer, Dr. F. Alijani



# LIST OF PUBLICATIONS

## JOURNAL ARTICLES

7. **A. Chandrashekar\***, M. James\* P. Belardinelli, G. Verbiest, U. Staufer, F. Alijani, *Hamaker constant and tip radius determination in dynamic atomic force microscopy* manuscript under preparation.
6. **A. Chandrashekar\***, A. Givois\* P. Belardinelli, C. L. Penning, A. M. Aragón, U. Staufer, F. Alijani, *Sensitivity of viscoelastic characterization in multi-harmonic atomic force microscopy* Under review, Preprint: arXiv:2206.04017.
5. P. Belardinelli, **A. Chandrashekar**, F. Alijani, S. Lenci, *Machine learning to probe modal interaction in dynamic atomic force microscopy* Mechanical Systems and Signal Processing, Volume 179, 109312, (2022).
4. **A. Chandrashekar**, P. Belardinelli, M. A. Bessa, U. Staufer, F. Alijani, *Quantifying nanoscale forces using machine learning in dynamic atomic force microscopy*, Nanoscale Advances, 4, 2134-2143 (2022).
3. **A. Chandrashekar**, P. Belardinelli, S. lenci, U. Staufer, F. Alijani, *Mode Coupling in Dynamic Atomic Force Microscopy*, Physical Review Applied 15, 024013 (2021).
2. **A. Chandrashekar**, P. Belardinelli, U. Staufer, F. Alijani, *Robustness of attractors in tapping mode atomic force microscopy*, Nonlinear Dynamics, volume 97, 1137–1158 (2019).
1. R. J. Dolleman, S. Hourri, **A. Chandrashekar**, F. Alijani, H. S. J. van der Zant and P.G. Steeneken, *Opto-thermally excited multimode parametric resonance in graphene membranes*, Scientific Reports 8, 9366 (2018).

## CONFERENCE PROCEEDINGS

1. P. Belardinelli, **A. Chandrashekar**, F. Alijani, S. Lenci, *Non-smooth dynamics of tapping mode atomic force microscopy* Proceedings of the ASME 2022 International Design Engineering Technical Conferences & Computers and Information in Engineering Conference, (2022).

---

\*These authors contributed equally.

